**UNIVERSITY OF SOUTHAMPTON**

FACULTY OF ENGINEERING, SCIENCE AND MATHEMATICS

INSTITUTE OF SOUND AND VIBRATION RESEARCH

# PREDICTION AND CONTROL OF SOUND PROPAGATION IN TURBOFAN ENGINE BYPASS DUCTS

by

Christopher James Brooks

A thesis submitted in partial fulfillment for the degree of
Doctor of Engineering

September 2007

UNIVERSITY OF SOUTHAMPTON

ABSTRACT

FACULTY OF ENGINEERING, SCIENCE AND MATHEMATICS
INSTITUTE OF SOUND AND VIBRATION RESEARCH

Doctor of Engineering

# PREDICTION AND CONTROL OF SOUND PROPAGATION IN TURBOFAN ENGINE BYPASS DUCTS

by Christopher James Brooks

This thesis contains original research into the propagation of sound in acoustically lined ducts with flow. The motivation for this work is the requirement to predict the sound attenuation of acoustic liners in the bypass duct of modern turbofan aeroengines. The liners provide the most effective means with which to suppress the rear fan noise. It is therefore important to make the best possible use of the available lined area by optimising the liner configuration. A set of analytic and numerical methods for predicting the liner attenuation performance have been developed, which are suitable for use in intensive liner optimisation studies, or as preliminary design tools.

Eigenvalue solvers have been developed to find modal solutions in rectangular ducts with uniform flow and annular ducts with sheared flow. The solvers are validated by replicating results from the scientific literature and the Finite Element method. The effect of mean core flow radial profile and boundary layers on the mode eigenfunctions and axial decay rates are considered. It is shown that solutions for thin boundary layer flows converge to those based on the commonly used slip flow boundary condition. It is demonstrated that realistic flow profiles should be used to assess acoustic mode propagation in bypass ducts. The flow profile can have strong effects upon low order modes and surface waves, and in fact at high frequencies, the profile can affect all the modes.

Mode-matching schemes are developed to assess the power attenuation performance and modal scattering of finite length liners. The results of the schemes are used to show that refraction of sound by boundary layers increases attenuation at high frequency. Power attenuation is higher where the mean core flow gradient refracts sound towards the liner. It is found that asymmetric liners can provide improved attenuation, depending on the direction of the mean flow shear gradient.

The optimisation of axially-segmented liners for single and multi-mode sources is demonstrated. It is found that potentially large improvements in the attenuation of tonal noise is possible, whilst benefits for broadband noise are more difficult to achieve.

# Contents

# List of Figures

# List of Tables

**DECLARATION OF AUTHORSHIP**

I, CHRISTOPHER JAMES BROOKS, declare that the thesis entitled,

PREDICTION AND CONTROL OF SOUND PROPAGATION
IN TURBOFAN ENGINE BYPASS DUCTS

and the work presented in the thesis are both my own, and have been generated by me as the result of my own original research. I confirm that:

- this work was done wholly or mainly while in candidature for a research degree at this University;
- where any part of this thesis has previously been submitted for a degree or any other qualification at this University or any other institution, this has been clearly stated;
- where I have consulted the published work of others, this is always clearly attributed;
- where I have quoted from the work of others, the source is always given. With the exception of such quotations, this thesis is entirely my own work;
- I have acknowledged all main sources of help;
- where the thesis is based on work done by myself jointly with others, I have made clear exactly what was done by others and what I have contributed myself;
- parts of this work have been published as:

A. J. Kempton, C. J. Brooks, A. McAlpine, and C. R. McAleer. Andante wp3.2 report on optimised bypass-duct liner design - d3.2.1. Rolls-Royce Internal Noise Report INR90519, Rolls-Royce plc., 2006.

C. J. Brooks. Axially-segmented acoustic liners for turbofan engine bypass ducts: A method for preliminary design iterations and optimisation. In *Institute of Acoustics Spring Conference 2006*, University of Southampton, Southampton, United Kingdom, 2006.

C. J. Brooks and A. McAlpine. Sound transmission in ducts with sheared mean flow. In *13th AIAA/CEAS aeroacoustics conference*, AIAA-2007-3545, 2007.

Signed:

Date:

# Acknowledgements

This thesis is the result of four years of extremely interesting work in the field of aircraft noise. It's realisation would not have been possible without the continued support of many different people.

First and foremost, I would like to thank my academic supervisor, Dr Alan McAlpine, for his excellent support, guidance and encouragement over the course of my study. I am the first in what will surely be a long line of doctoral candidates that benefit from his astute tutorship. Secondly, I must thank my industrial supervisor, Dr Andrew Kempton. His knowledge on the subject of aircraft noise is second only to his infectious enthusiasm, both of which are second only to his sharp wit!

I would like to acknowledge the generous financial support of the Engineering and Physical Sciences Research Council (EPSRC) through the UK Engineering Doctorate Scheme, and the Noise Engineering department at Rolls-Royce plc. through the University Technology Centre (UTC) in Gas Turbine Noise at the ISVR. I would also like to thank the Noise Engineering department at Rolls-Royce plc. for accommodating me during my time in Derby.

My thanks to the thesis examiners, Dr Edward Rademaker from NLR and Professor Jeremy Astley from ISVR, for the time they have willingly given up to appraise my work.

After seven enjoyable years in total at the ISVR, with a few stints at Rolls-Royce, I have had the pleasure of meeting many interesting people with whom I have shared many stimulating discussions about our fascinating world of acoustics. There are of course too many people to list, but since it is always nice to see your name in print, I shall list some here! Vincent Hii Jui Ta, Chris Lowis, Chris Ham, Phil McLaughlin, Emmet English, Dr Fabrice Castres, Mahdi Azarpeyvand, Iansteel Achunche, Benoit Parcelier, Vincent Jurdic, Claire McAleer, Eugene Deane, Dr Qiduo Zhou, Alessandro Bassetti, Juan Battaner-Moro, Dr Matt Wilkinson, Gary, Dr TzePei Chong, Pal Mannerheim, Munham Park, Chan and Sally Lee, Dr Phil Joseph, John Coupland, Hillary Barton, Neville Pollard, Dr Romy Morvaunt, Luigi De Mercato, Dr Paul Strange, Alastair Moore, Kevin Brichford, Dr Shahrokh Shahpar, Dr Rod Self, Dr Brian Tester, Dr Gwenael Gabard, Dr Rie Sugimoto, Dr Neil Ferguson, Maureen Mew, Sue Brindle, Dr Malcolm Smith, Joao Carillho, Marco Muleri, Dr Keith Holland, Peter Bartlett, Pam Philipson, Professor Chris Morfey....the list goes on.

Finally, I would like to thank my family, especially my mother and father who were always pleased to see me when I turned up at their door after cycling home, even when covered head-to-toe in the mud of the South Downs! And to my grandfather, who reminds me that he started work on the Lancashire factory roofs at 14. Yes, I am 11 years late.....but better late than never!

Christopher James Brooks, September 2007

# Nomenclature

$(\hat{\mathbf{i}}, \hat{\mathbf{j}}, \hat{\mathbf{k}})$ Cartesian unit vector notation

$(\hat{\mathbf{r}}, \hat{\theta}, \hat{\mathbf{x}})$ Cartesian unit vector notation

$(\tilde{x}, \tilde{y}, \tilde{z})$ dimensional Cartesian coordinate system

$(x, y, z)$ non-dimensional Cartesian coordinate system

$\alpha_{m,n}$ lined duct eigenvalue

$\beta$, $\beta_d$, $\beta_{-d}$, $\beta_h$ non-dimensional specific acoustic admittance, top or casing wall admittance, bottom wall admittance, hub wall admittance

$\chi$ three-dimensional rectangular duct mode eigenfunction

$\delta$ non-dimensional boundary layer thickness

$\delta^*$ non-dimensional boundary layer displacement thickness

$\Delta_{\text{PWLR}}$ sound power reflection loss [dB]

$\Delta_{\text{PWL}}$ sound power transmission loss [dB]

$\delta_{m,n}$ Kronecker's delta, has a value of one if $m = n$ and of zero if $m \neq n$

$\epsilon_w$ non-dimensional wall normal radial acoustic particle displacement

$\eta$ integration parameter

$\hat{E}_{m,n}$ incident mode complex amplitude

$\hat{p}$ dimensional modal acoustic pressure

$\hat{R}_{m,n}$ modal reflection factor

$\hat{T}_{m,n}$ modal transmission factor

$\hbar$ hub-to-tip ration $h/d$

$\kappa_{m,n}$, $\mu_{m,n}$ non-dimensional rigid or lined duct transverse wavenumber

$\Lambda$ normalisation constant

$\mathfrak{K}$ Wiener-Hopf kernel function

$\Psi$ mode eigenfunction

$\Re$, $\Im$ real part, imaginary part

$\rho_0$ density of air

$\rho_{m,n}$ total reflection coefficient

$\rho_{m,r,n}$ modal reflection coefficient

$\tau_{m,n}$ total transmission coefficient

$\tau_{m,r,n}$ modal transmission coefficient

$\tilde{\omega}$ dimensional angular frequency

$\tilde{\mathbf{u}}$ dimensional acoustic particle velocity; Cartesian $(\tilde{u}, \tilde{v}, \tilde{w})$, cylindrical $(\tilde{r}, \tilde{w}, \tilde{u})$

$\tilde{p}$ dimensional time-harmonic acoustic pressure

$\tilde{t}$ dimensional time

$A^{\pm}_{m,n}$, $B^{\pm}_{m,n}$ modal coefficients *superscript*, left or right running modes, *subscript*, mode numbering

$b$ dimensional rectangular duct half width

$c_0$ speed of sound

$CF$ combined frequency cost function

$D$ non-dimensional liner cavity depth

$d$ dimensional rectangular duct half height or dimensional annular duct outer radius

$h$ dimensional annular duct inner radius

$i$ $\sqrt{-1}$

$I, II, III, \ldots$ duct segment numbering

$J_m$ Bessel function of the first kind

$k_0$ non-dimensional acoustic wavenumber

$k_{co}$ modal cut-off frequency

$k^{\pm}_{m,n}$, $\alpha^{\pm}_{m,n}$ non-dimensional rigid or lined duct axial wavenumber; *superscript*, left or right running modes

$k_z$ $z$ transverse wave number

$k_z$ non-dimensional $z$ transverse wavenumber

$L$ horizontal distance between bypass nozzle and wing trailing edge

$l$ non-dimensional duct segment length

$M$ Mach number

$m$ azimuthal mode order

$M_r$ non-dimensional liner facing sheet mass inertance

$N$ number of transverse mode include in the mode-matching

$n$ radial mode order

$N_c$ number of cut-on modes

$p$ non-dimensional modal acoustic pressure

$R$, $R_f$ resistance, final resistance

$R_a$, $R_p$ average duct radius, adjusted duct radius

$R^{\pm}_{m,n}$,$S^{\pm}_{m,n}$ mode coefficients

$S$ total number of liner segments

$s$ control volume surface

$U_0$ dimensional axial flow velocity

$V$ control volume

$v_w$ non-dimensional wall normal radial acoustic particle velocity

$W$ weighting function

$W^{\pm}$ total sound power

$W^{\pm}_{m,n}$ modal sound power

$X$, $X_f$ reactance, final reactance

$x^I$, $x^{II}$, ... axial location of liner segment interfaces

$Y_m$ Neumann function

$Z$,$Z_d$,$Z_{-d}$, $Z_h$ non-dimensional specific acoustic impedance, top or casing wall impedance, bottom wall impedance, hub wall impedance

**u** non-dimensional acoustic particle velocity; Cartesian $(u, v, w)$, cylindrical $(v, w, u)$

$I^{\pm}_{x\,m,n}$ local instantaneous axial modal intensity

BPF blade passing frequency

# Chapter 1

# Introduction

The increasing volume of commercial air traffic across the globe poses serious environmental issues with regard to aircraft emissions. Noise emissions from the aircraft engines and airframe are a chief concern when dealing with the impact of airports on their surrounding environment. In light of increasingly stringent noise emissions rules, the challenge for aeroengine manufacturers is that noise guarantees for future engine and airframe combinations can be met. This requires noise prediction methods that can generate predictions of the radiated sound, to a high level of confidence.

The engine noise can be broadly categorised into tonal noise generated by the regular cyclical motion of the turbomachinery blades, and broadband noise generated by pressure fluctuations associated with turbulent air flow. For early aeroengine designs, broadband noise from the exhaust jet was the dominant source. However, over the past twenty years design considerations have meant the ratio of bypassed air mass to combustor air mass, or *bypass ratio*, has increased. The majority of modern commercial aircraft are powered by high bypass ratio (HBPR) turbofan engines. The result has been a reduction in jet exhaust velocity and its associated noise. Consequently, the contributions from other noise sources, such as the fan, turbine and core, now dominate at certain engine conditions. Since no single source is dominant over all engine conditions, the contributions from all the major noise sources must be evaluated to gain an accurate prediction of the total engine noise.

A key method for controlling the sound field generated by the internal noise sources is the use of acoustic treatment in the engine ducts, both inlet and bypass. The most common form of the treatment used is a perforated resistive facing sheet attached to a honeycomb cell structure with a rigid backing plate. The design and layout of the acoustic treatment within the duct systems is driven by its contribution to the engine achieving the desired EPNL (Effective Perceived Noise Level, the ISO standard subjective measure of aircraft noise), whilst minimising the economic penalty. This means that the treatment must have the appropriate attenuation characteristics, at different engine power conditions, whilst achieving this within specified length and weight limits. Thus, the determination of the appropriate treatment design is a complicated task, and is

often a decision heavily based on experience. The use of modelling to determine the optimum design is dependent upon the accuracy of the model, and inevitably on the available computational resources, and is severely restricted by the number of parameters involved. In order to construct an effective, yet feasible optimisation scheme, a simplified model must be constructed for the acoustic propagation from the source to the far-field.

The work in this thesis concerns the prediction of acoustic propagation within the bypass duct, especially the attenuation performance of acoustic treatment on the duct walls. This work has been undertaken in collaboration with the Noise Department at Rolls-Royce plc. The collaboration has involved part-funding by the company, and has also allowed the author to conduct a substantial proportion of the research whilst based within the Noise Department at Rolls-Royce plc., Derby, UK. The company's interest in this work is the requirement to reduce the rear fan noise contribution to the measured EPNL, which is part of the aircraft noise certification criteria. Since passive duct liner treatment provides the most effective means with which to reduce this source, it is important to make the best possible use of the lined area available in the duct. This requires the optimisation of the liner configuration with the use of models to predict the in-duct sound field. Acoustic propagation in the bypass duct is a complex problem involving non-uniform viscous mean flows, three-dimensional geometries, and tonal and broadband sources of sound. Solutions to idealised models of the problem are developed in this work, which are suitable for use in intensive liner optimisation studies, or as preliminary design tools.

## 1.1 Planning and progress

The Engineering Doctorate Scheme advocates that research is undertaken in close collaboration with the industrial sponsor. Thus, over the four year period of this study, the author's time has been divided between the University Technology Centre (UTC) in Gas Turbine Noise at the ISVR, and the Noise Engineering department at Rolls-Royce plc. An overview of the research work time plan is shown in figure (1.1). Regular quarterly meetings were conducted between the author, and the academic and industrial supervisors to review and plan the research work. The work plan shows a progression from initial investigations into rectangular duct eigenvalue solvers to the ultimate aim of predicting finite length liner performance in sheared flows. Work involving optimisation and CFD was undertaken by the author at Rolls-Royce, taking advantage of the solution methods and computing resources available there. In addition, a smaller project covering jet noise installation effects and coaxial jet noise prediction was undertaken in three months of Year 1 at Rolls-Royce. This work provided the author with experience in different, but closely related, aspects of the engine exhaust noise problem. Parts of this work were reported in the author's mini-thesis [1], but are not reported here.

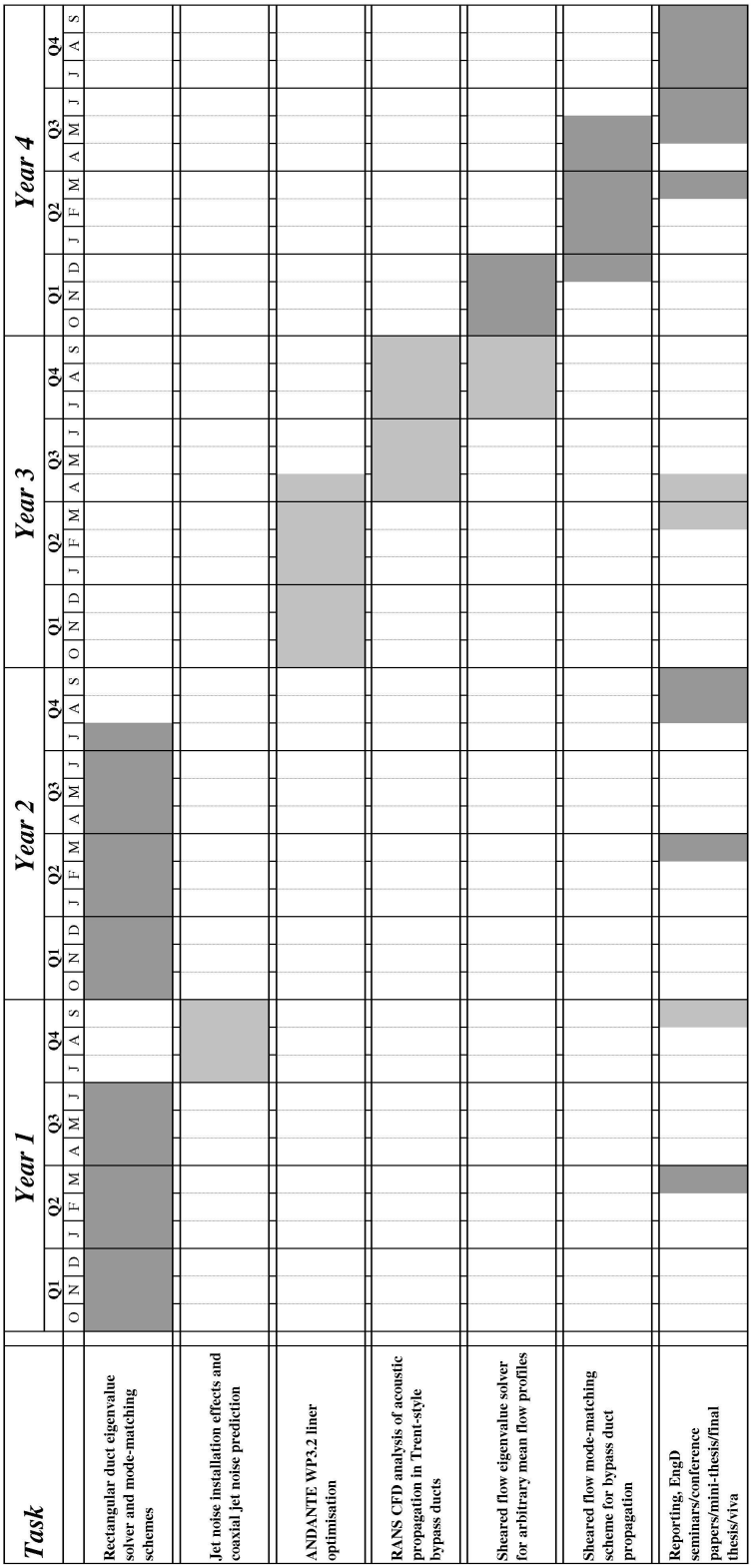


FIGURE 1.1: *Research workplan. Tasks in dark grey undertaken at ISVR, tasks in light grey undertaken at Rolls-Royce.*

## 1.2 Review of literature

The vast amount of research in the field of duct acoustics since the 1960s has resulted in its synonymous association with the aircraft engine industry. Several reviews of the collective research effort illustrate the depth and breadth of field to date [2, 3, 4]. Three broad categories of methods developed to solve the propagation problem can be identified: empirical, theoretical and computational methods. An empirical approach was required in the early years before theoretical models were readily available. These were typically derived for low flow speed ventilation duct applications [5]. However, this was superceded in the 1960s and 70s by the successful establishment of robust theoretical models for idealised geometries and flow fields. The majority of methods followed the pioneering work of Tyler and Sofrin [6], who considered the sound field within the engine duct in terms of acoustic modes, which provide solutions of the wave equation or its variants. The ultimate success of this approach, which achieved surprisingly good agreement with experimental results , [7, 8, 9, 10], led to the development of more realistic, and thus more complex models. The development of numerical models since the 1970s based on finite difference, weighted residual and finite element methods provided capabilities that were much better suited to modelling realistic geometries and flows. However, the computational speed and memory requirements for such models typically restricts their use to the final design stage and to low or mid frequency applications.

The typical starting point for theoretical duct propagation models is the simplification of the inlet and bypass geometry to axisymmetric cylindrical and annular ducts of infinite length and axial uniformity. Further simplification of the bypass duct at high hub-to-tip radius ratios to a rectangular duct was used by Snow and Lowson [9], and Yurkovich [10]. The high speed non-uniform flows present in the duct systems can be approximately modelled by a uniform radial velocity profile [7, 8]. The inclusion of acoustic treatment at the duct walls requires the formulation of boundary conditions in terms of the acoustic impedance of the treatment. It is widely agreed that the correct condition at the wall is the continuity of normal particle displacement [11]. The treatment universally used in the industry is the locally reacting resonator type liner, the complex impedance of which is typically modelled using semi-empirical relations [8, 12]. The resulting boundary-value problem reduces to a complex transcendental eigenvalue equation, the solution of which has been the subject of many research papers.

Determination of the lined duct eigenvalues is not a simple task due to the topography of the eigenvalue equation, and the complex arithmetic that is involved. In early attempts several researchers, such as Molloy and Honigman [13] and Morse and Ingard [14], focussed on the zero mean flow problem, producing charts relating the wall impedance to the eigenvalues, but without solving the eigenvalue equation explicitly. The first attempts at solving the equation directly involved the use of power series expansions [15, 16], but ultimately more successful methods have utilised numerical integration and iteration techniques. A simple Newton-Raphson iteration method was implemented by Ko [8], Christie [17] and Yurkovich [10], where the corresponding rigid duct eigenvalues were used as initial values for the routine. The convergence of the routine

in certain instances is very much dependent upon the initial values, and is known to be unreliable due to the topography of the function, and the presence of multiple eigenvalues. Motsinger et. al. [12] based their solution on a similar iteration method, but with a higher order of convergence, termed Bailey's method. In an attempt to ensure correct convergence the initial values were chosen by dividing the modal regions into subregions using the charts of Morse and Ingard [14], and the iterations proceeded in incremental steps from the converged no flow eigenvalues. The authors indicated that the routine is reliable, accurate and fast, but also noted that the method was not infallible. A clear disadvantage of this method is that a one-to-one relationship between the rigid duct eigenvalues and the lined duct eigenvalues is lost. Other researchers, such as Mechel [18], have favoured the use of Muller's method, which has the disadvantage of requiring three intial values, but the advantages of not requiring gradients, thereby avoiding problems with multiple roots, and the ability to affect the direction in which the method searches for solutions.

In an effort to circumvent the need for analysing the modal regions, Eversman [19, 20] developed an integration scheme to solve the eigenvalue equation. The scheme employed a fourth-order Runge-Kutta integration, with a variable step size, and a Newton-Raphson routine to refine the solutions where required. It was noted that particular attention was still required for multiple eigenvalues, although no indication was made of how this could be dealt with. The author also noted the presence of extra solutions which were characterised by having large imaginary components. These solutions were identified by Tester [21], Rienstra [22] and Rienstra and Peake [23], as surface wave solutions, the mode eigenfunctions of which decay exponentially in the transverse direction away from the duct walls. Rienstra [22] deduced that there are at most four surface wave solutions (eight in rectangular or annular ducts): two acoustic surface waves which are present both with and without flow (four in rectangular or annular ducts), and two hydrodynamic surface waves which only occur with flow (four in rectangular or annular ducts). These solutions are typically hard to find, and consequently are often missed using the solution methods mentioned above. A method was described in [22] which allowed for the surface wave solutions to be accurately traced from the rigid duct eigenvalues.

The acoustic surface wave was shown by Cremer [24] and Tester [25] to be important in the optimisation of acoustic liners. The maximum attenuation of the least attenuated mode, by a uniform liner of reasonable length, was shown to occur for impedances where the lowest order mode pair coalesce, that is essentially a double eigenvalue. Approximate expressions for optimum impedances were given. However, due to the large rate of change of attenuation rates around the optimum value, the practical application of the expressions is unreliable. In addition, the short lengths of ducts typically seen in aircraft engines means that reflections from the liner edges will affect the optimum impedance. This was shown to be true by Unruh [26], Unruh and Price [27], and Koch [28] who also demonstrated that an optimum finite length liner of given impedance could in theory lead to more attenuation than a longer length liner of the same impedance.

Finite length liners have been investigated analytically, numerically, and experimentally by several researchers. Two analytic techniques have been employed, namely: mode-matching and

Wiener-Hopf. The Wiener-Hopf technique can provide analytic solutions to problems with separable geometry but mixed boundary conditions. It was successfully applied to lined rectangular ducts with rigid side walls in the absence of flow by Koch [28], and in the presence of a uniform flow by Koch and Mohring [29]. The authors were able to predict the sound attenuation of finite length uniform and two-segment liners with symmetric and asymmetric linings and examine various liner parameter variations. Although a powerful technique, its application to more realistic aeroengine duct models, such as non-uniform or sheared flows and variable geometry, is limited since it is not clear whether the necessary extensions could be carried out.

The mode-matching technique is a well known method for formulating boundary-value problems in waveguide theory [30]. The first application of the technique to aeroengine duct systems was made by Lansing and Zorumski [31], which represented the first in a series of extensive analytical and experimental studies of axially-segmented liners supported by NASA in the 1970s [32, 33, 12, 34, 35]. The technique is more amenable than the Wiener-Hopf technique to the practical purpose of liner performance predictions, since relatively simple extensions have been demonstrated for variable geometries [36, 37]. A potential disadvantage is that in contrast to the Wiener-Hopf technique, the mode-matching formulation in the presence of a mean flow does not provide direct control over the edge conditions at the liner leading and trailing edges. However, the inclusion of a suitably high number of modes, and by simply keeping a check on the convergence rate of the modal amplitudes, appears to suffice when comparing the experimental results of Sawdy et. al. [34] to their corresponding mode-matching solutions. A numerical approach to mode-matching was undertaken by Hii [38], where the eigenvalue problem was solved using the Finite Element Method for ducts of arbitrary cross-section and non-uniform impedance boundaries. An improved technique of matching mass and momentum at liner discontinuities was demonstrated to provide better agreement with full FE solutions than the traditional matching of pressure and axial particle velocity. The FEM is a much more flexible method than the analytic approach. However, the accuracy of the method is highly dependent upon mesh resolution, and becomes computationally expensive at high frequencies.

The incentive to use axially-segmented liners in aeroengine applications is the possibility of obtaining extra attenuation bandwidth, not only from judicious tuning of the liner depths, but also by taking advantage of finite length effects, and beneficial modal energy redistribution at the liner impedance discontinuities [39, 40, 34]. The optimisation of such liners inevitably involves an increased parameter space, and it is widely agreed that the performance of segmented liners is heavily dependent upon the incident modal content. The optimisation study carried out by Sawdy et. al. [34] found that local optimum impedances for a three-segment liner were a strong function of the source content. It was noted that in using this property it may be possible to construct a multi-segment liner that was relatively insensitive to the incident modal content. A zero flow optimisation study by Baumeister [40] concluded that while segmented liners were more effective than uniform liners at high frequencies, and could certainly outperform uniform liners at low frequencies in plane wave mode only situations, the practical considerations of

uncertainty in optimum impedances mean little advantage is found. The large degradation in performance of multisegment liners that are sensitive to the modal input was also demonstrated.

It is noted that most of the analytic duct propagation studies cited above have dealt with symmetric liner configurations, and all have restricted their analysis to even mode excitation. Little has been published on the subject of asymmetric liners. However, an eigenvalue solver for two dimensional ducts with uniform mean flow was presented by Abdelhamid [41], and a mode-matching procedure for a single asymmetrical liner segment in the absence of mean flow was given by Ochmann and Donner [42], with brief results presented by Ochmann [43]. The analysis of Mechel [44] indicated that the favourable attenuation qualities of odd modes compared to even modes highlights the possibilities of using asymmetrical liners to redistribute modal energy from poorly attenuated even modes to well attenuated odd modes. Therefore, the inclusion of asymmetric liner segments in an axially-segmented liner could provide an extra modal conditioning tool. A mathematical model describing the mode-matching technique for asymmetrical lining configurations with uniform mean flow was presented by Unruh [26]. However, the model was only applied to a single lining segment with one of the segment walls being rigid, and with a plane wave sound source. This is in fact equivalent to a symmetrically lined duct of twice the height, with only even modes included in the matching.

The modal methods described above, for the uniform flow or no flow cases, are based on closed form modal solutions of the convected wave equation. The modelling of acoustic propagation in arbitrary sheared flows requires numerical solution of the governing Linearised Euler Equations (LEE). Currently, the only methods available for assessing acoustic propagation in lined ducts with rotational mean flows are specialised Finite Element Methods (FEM) [45, 46, 47] and LEE Computational Aeroacoustics (LEE-CAA) schemes [48, 49]. Both methods are restricted to low and mid frequencies, and have a high computational cost which precludes them from use in intensive optimisation studies. To obtain time-harmonic modal solutions, the LEE may be solved for a parallel sheared flow of constant density and sound speed in the manner described first by Pridmore-Brown [50]. Here a second order equation in the transverse pressure is obtained for a specific axial wavenumber. Alternative wave variable formulations were later highlighted by Tester [51] and Smith [52], who noted that, as opposed to other wave variables, a formulation in pressure and radial particle displacement did not involve flow gradient terms. Several researchers have assessed the effects of boundary layer profiles [51, 53, 54] on individual mode solutions by solving the Pridmore-Brown equation using various methods. Common conclusions were that upstream modes are more affected by mean flow shear than downstream modes, and attenuation by acoustic liners is enhanced for downstream propagation and degraded for upstream propagation.

## 1.3 Aims, motivation and claim to originality

The research presented in this thesis, and the research proposal outlining future work in Chapter (9), primarily covers the subject of analytical modelling of in-duct acoustic propagation in the bypass duct of a modern HBPR turbofan engine.

The propagation of sound in the bypass duct is a very complex problem. To begin with, a description of the source of sound is often unknown in detail, and will consist of both tonal and broadband components. The geometry of the duct is highly three-dimensional with a slowly varying axial curvature accentuated by the turbine hump, and non-axisymmetry due to the presence of the pylon and lower bifurcation. In addition, there may be abrupt changes in the type of acoustic liner (e.g. SDOF, 2DOF), rigid splices, service hatches and heat exchangers located on the walls. The in-duct flow field after the outlet guide vanes (OGVs) will generally have little swirl, but can have significant radial non-uniformity. Boundary layer growth and the curved duct geometry mean that significant variation in the flow field is possible along the axial length. The character of the flow field can affect the propagation of sound through refraction and convection, and ultimately affect the attenuation levels achieved by acoustic liners.

The key aim of this work is to provide simplified, yet representative models of acoustic propagation in bypass ducts for use in the optimisation of acoustic treatments, and as a computationally inexpensive design tool. In this thesis, the early chapters concentrate on the development of axisymmetric modal methods where the duct cross-section is assumed to be axially constant and the mean flow uniform, but the wall impedances are allowed to be discontinuous. Such methods provide insight into the modal structure of the in-duct sound field, the scattering effects of the liner discontinuities, and here are utilised for liner optimisation. The later chapters extend these methods to deal with the effects of a radially sheared flow on the acoustic propagation in the duct, and ultimately, the effects upon the performance of finite length liners for the attenuation of tonal and broadband sources.

The original contributions of this thesis are as follows:

- A robust eigenmode solver is developed for asymmetrically lined rectangular ducts with uniform flow, using a combination of the tracking techniques of Eversman [19] and Rienstra [22].
- A semi-analytic mode-matching method is developed to assess asymmetric liners of finite length in rectangular ducts with uniform flow. It is shown that mass and axial momentum must be matched in order to accurately resolve the pressure field at wall impedance discontinuities. In addition, the suitability of hydrodynamic surface waves in resolving wall pressure singularities at the wall impedance discontinuities is demonstrated.
- Viscous and inviscid Computational Fluid Dynamics (CFD) methods are used to investigate acoustic propagation in rigid walled bypass ducts with realistic flow fields. It is

shown that scattering of modal energy is highest in the region around the turbine hump. In addition, non-uniform inlet flows are shown to result in more scattering than uniform inlet flows.

- A robust eigenmode solver is developed for asymmetrically lined annular ducts with arbitrary sheared mean flow. It is shown that non-uniform flow profiles can strongly affect low order modes and surface waves. Boundary layer refraction effects become stronger with increasing frequency for all modes.

- The convergence of mode solutions for boundary layer flows to the slip flow solutions is confirmed by solving coupled equations in pressure and radial particle displacement.

- A mode-matching method is developed for predicting acoustic propagation in lined annular ducts of constant cross-section, containing inviscid, parallel sheared flow. This scheme represents a simple and fast solution method for assessing liner performance in uniform ducts with rotational flows, which was previously only obtainable using specialised and computationally expensive FE methods or LEE solvers.

- The presence of boundary layers is shown to increase power transmission loss at high frequencies, whilst the behaviour of modal scattering is shown to vary with boundary layer thickness.

- The effects of several flow profiles on liner attenuation and scattering are investigated. It is shown that the direction of the mean flow gradient can have a strong effect on liner attenuation, particularly for single mode sources.

- Finite liner length effects upon power attenuation are shown to be most significant for single mode sources and differences between flow profiles are limited to low order modes.

- In an optimisation study, asymmetric liners are shown to potentially provide higher attenuation rates than symmetric liners, depending on the direction of the mean flow shear gradient.

## 1.4 Outline of contents

The analysis begins in Chapter (2) where the governing eigenvalue equations are derived for acoustic modes in asymmetrically lined rectangular ducts containing uniform mean flow. A numerical scheme for obtaining the eigenvalues is presented and validated. Mode solutions of three-dimensional rectangular ducts are often used to approximate the modes of annular ducts, and this approximation is assessed here. The chapter concludes with an analysis of surface wave modes using asymptotics.

In Chapter (3) a mode-matching scheme is developed to assess sound power attenuation and modal scattering in axially-segmented rectangular ducts with uniform flow. The eigenmode

solver of Chapter (2) is used to provide mode eigenfunctions and wavenumbers for a traditional scheme, which matches pressure and axial particle velocity, and an improved scheme, which matches mass and axial momentum across liner discontinuities. Both schemes are assessed against each other, the Wiener-Hopf technique and FE solutions. The issues of liner edge conditions and hydrodynamic surface waves in the matching schemes are discussed.

The mode-matching schemes and eigenmode solvers are used in a liner optimisation study in Chapter (4). Several optimisation algorithms are used for a series of cases. A single frequency optimisation exercise is presented, aimed at determining the optimum resistance and reactance values for sound power attenuation of uniform and multi-segment liners. Examples of optimisation of attenuation performance over a specified frequency bandwidth are presented. Here, design parameters of resistance, liner cavity depth and liner segment length are used to optimise up to four liner segments for single mode and multi-mode sources.

In Chapter (5), high fidelity CFD methods are used to investigate the mean and acoustic flow fields for a realistic bypass duct geometry. Inviscid and viscous solutions on quasi-axisymmetric meshes are used to investigate the effects of boundary layer growth, realistic inflow conditions and duct curvature effects on acoustic propagation.

In Chapter (6) the equations governing acoustic mode propagation in lined annular ducts with inviscid, parallel mean flow are derived for a number of wave variables. A computational scheme to solve the governing equations is described, which is based on a shooting method involving the eigenvalue tracking procedure used in Chapter (2). The effects of the radial flow profile on the acoustic mode spectrum are assessed for realistic conditions. The convergence of mode solutions in linear and one-seventh power law boundary layer flows to the uniform slip flow solutions is investigated. In addition, the change with frequency of the mode spectrum for a selection of boundary layers and non-uniform core flows are assessed.

In Chapter (7) the mode-matching scheme of Chapter (3) is extended in order to assess the performance of axially-segmented liners in annular ducts containing parallel sheared flows of arbitrary profile. The scheme is validate against FE solutions for uniform flow and the inclusion of vortical modes in the matching is discussed.

The effects of flow profile on finite length liner attenuation are assessed in Chapter (8). The convergence of linear boundary layer flow solutions to the uniform slip flow case is investigated. Boundary layer effects upon the power attenuation spectrum and modal scattering are assessed for thin and thick linear boundary layers. Solutions for several core flow profiles are also investigated. Finite length effects are investigated since liner segments within real aeroengine ducts can vary significantly in length. Finally, a contour plot optimisation exercise is carried out to determine how the optimum liner impedance varies with flow profile. Both symmetric and asymmetric single segment liners are assessed for single and multi-mode sources.

Chapter (9) contains the conclusions of the research, and outlines areas of future work.

# Chapter 2

# Eigenvalue problems for rectangular ducts with uniform flow

## 2.1 Theory for a two-dimensional duct

This chapter outlines the theory and methods used to calculate the sound field within uniform rectangular ducts with subsonic uniform mean flow.

First, the problem of propagation of sound in a uniform two-dimensional duct of height $2d$ with a wall lining admittance $\beta$ is examined. The rectangular geometry with a Cartesian coordinate system $(\tilde{x}, \tilde{y})$ used in this case is shown in Figure (2.1). Well-known waveguide theory allows a modal breakdown of the in-duct sound field into modal sources of harmonic time dependance $e^{i\tilde{\omega}\tilde{t}}$ that can propagate upstream and downstream.
Starting with the convected wave equation in pressure

$$\left[\frac{\partial}{\partial \tilde{t}} + U_0 \frac{\partial}{\partial \tilde{x}}\right]^2 \tilde{p} - c_0^2 \left(\frac{\partial^2}{\partial \tilde{x}^2} + \frac{\partial^2}{\partial \tilde{y}^2}\right) \tilde{p} = 0 \,. \tag{2.1}$$

A time harmonic pressure field is assumed, of the form

$$\tilde{p}(\tilde{x}, \tilde{y}, \tilde{t}) = \hat{p}(\tilde{x}, \tilde{y}) e^{i\tilde{\omega}\tilde{t}} \,, \tag{2.2}$$

and the variables are made dimensionless as follows:

$$x = \frac{\tilde{x}}{d}, \qquad t = \frac{c_0 \tilde{t}}{d}, \qquad k_0 = \frac{\tilde{\omega} d}{c_0}, \qquad p = \frac{\hat{p}}{\rho_0 c_0^2}, \qquad \mathbf{u} = \frac{\hat{\mathbf{u}}}{c_0} \,. \tag{2.3}$$

Substituting into equation (2.1) leads to the convected Helmholtz equation

$$\left[ik_0 + M\frac{\partial}{\partial x}\right]^2 p - \left(\frac{\partial^2}{\partial x^2} + \frac{\partial^2}{\partial y^2}\right) p = 0 \,. \tag{2.4}$$

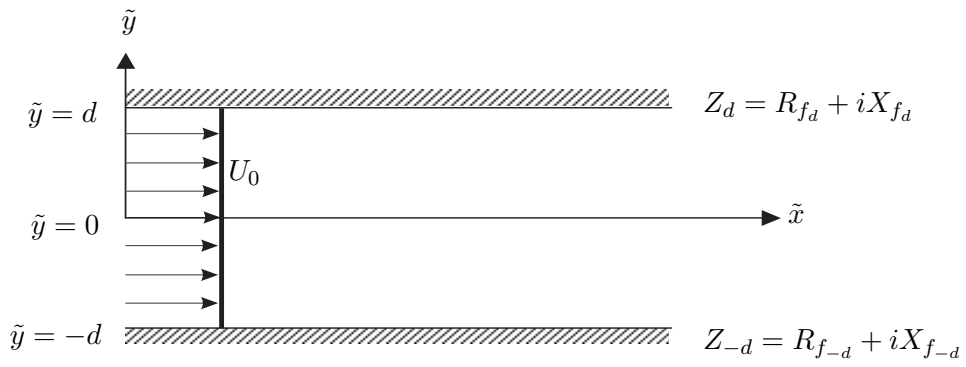


FIGURE 2.1: *Geometry and liner impedance notation for a two-dimensional lined duct with uniform mean flow.*

Modal solutions are found by separation of variables, and are of the form

$$p_n(x, y) = \Psi_n(y) e^{-ik_n x} \,, \tag{2.5}$$

where the eigenfunction describing the transverse variation of the mode is given by

$$\Psi_n(y) = \Lambda_n \left[ R_n \cos \kappa_n y + S_n \sin \kappa_n y \right] \,. \tag{2.6}$$

The normalisation constant $\Lambda_n$ is determined so that

$$\frac{1}{2} \int_{-1}^{1} \Psi_n \Psi_{n'}^* \mathrm{d}y = \delta_{nn'} \,. \tag{2.7}$$

The dispersion relation between the $n$th mode non-dimensional eigenvalue $\kappa_n$ , the corresponding non-dimensional axial wavenumber $k_n$, and the non-dimensional free space wavenumber $k_0$, is

$$\kappa_n^2 = \left[ k_0 - k_n M \right]^2 - k_n^2 \,. \tag{2.8}$$

The dispersion relation can be rearranged to give the axial wavenumber in terms of the mode eigenvalue

$$\frac{k_n}{k_0} = \frac{1}{1 - M^2} \left( -M \pm \left[ 1 - \left( 1 - M^2 \right) \left( \frac{\kappa_n}{k_0} \right)^2 \right]^{\frac{1}{2}} \right) \,. \tag{2.9}$$

The eigenvalues are determined following application of the wall boundary conditions. The boundary condition at $y = \pm 1$ for the case of a duct with rigid walls is that the acoustic particle velocity normal to the wall is zero. The boundary condition is determined by application of the acoustic momentum equation in the $y$-direction, and leads to

$$\frac{\partial p}{\partial y} = 0 \qquad \text{at } y = \pm 1 \,. \tag{2.10}$$

The mode eigenvalues $\kappa_n$ are therefore defined by

$$\sin \kappa_n y \cos \kappa_n y = 0 \,, \tag{2.11}$$

where

$$\kappa_n = \frac{(n-1)\pi}{2} \qquad \text{for } n = 1, 2 \ldots \,. \tag{2.12}$$

Solutions corresponding to even and odd modes respectively are

$$\kappa_n = 0, \pi, 2\pi \ldots \qquad \kappa_n = \frac{\pi}{2}, \frac{3\pi}{2}, \frac{5\pi}{2} \ldots \,. \tag{2.13}$$

The modal coefficients $R_n$ and $S_n$ are determined through application of the boundary conditions at $y = \pm 1$. For a rigid walled duct the coefficients are given by,

$$R_n = \cos(\kappa_n) \,, \qquad y = \pm 1, \tag{2.14}$$

$$S_n = \pm \sin(\kappa_n) \,, \qquad y = \pm 1. \tag{2.15}$$

The normalisation constant $\Lambda_n$ is given by

$$\Lambda_n = \begin{cases} 1 & n = 1 \,, \\ \sqrt{2} & n > 1 \,. \end{cases}$$

The axial wavenumber determines the travelling wave nature of the modal solutions, and its value depends upon $\kappa_n$, $k_0$ and $M$. The axial wave number is real for

$$\left(1 - M^2\right) \left(\frac{\kappa_n}{k_0}\right)^2 < 1 \,, \tag{2.16}$$

where the positive sign choice in Equation (2.9) corresponds to a right running mode, and the negative sign corresponds to a left running mode. The axial wavenumber becomes complex when

$$\left(1 - M^2\right) \left(\frac{\kappa_n}{k_0}\right)^2 > 1 \,. \tag{2.17}$$

In this case modal solutions of Equation (2.4) are evanescent modes that decay exponentially with axial distance given by

$$p_n(x, y) = \Psi_n(y) e^{-i\Re(k_n)x} e^{\pm \Im(k_n)x} \,. \tag{2.18}$$

In Equation (2.9), by taking the principle value of the square root in the lower half plane, the significance of the sign choice in Equation (2.18) is more straightforward, as exponentially growing solutions are avoided, by assuming the positive sign indicates a mode propagating in the positive $x$-direction, and the negative sign indicates a mode propagating in the negative $x$-direction. It may be shown through energy considerations that these modes carry no acoustic power and are referred to as being *cut-off* [55].

The duct is assumed to be of infinite length in the axial direction, hence there exist uncoupled solutions for upstream and downstream propagating modes as no termination reflections are permitted [56]. Therefore, the appropriate sign choice in Equation (2.9) is required to correctly define propagation or decay in either axial direction which leads to the designation of $k_n^+$ or $k_n^-$ to indicate solutions in the positive or negative $x$-direction. The appropriate modal solutions propagating in positive and negative $x$-directions are of the form

$$p_n^+(x,y) = \Psi_n^+(y)e^{-ik_n^+ x}\,, \tag{2.19}$$

$$p_n^-(x,y) = \Psi_n^-(y)e^{-ik_n^- x}\,, \tag{2.20}$$

where the general solution for the duct sound field is given by the Fourier modal sum

$$p(x,y) = \sum_{n=0}^{\infty} \Psi_n^+(y)e^{-ik_n^+ x} + \sum_{n=0}^{\infty} \Psi_n^-(y)e^{-ik_n^- x}\,. \tag{2.21}$$

Extension of the theory to the calculation of mode eigenvalues in a duct with lined walls requires the use of more complicated wall boundary conditions at $y = \pm 1$. The liner is assumed to be locally reacting with non-dimensional specific acoustic impedance $Z$ defined as

$$Z = \frac{z}{\rho_0 c_0} = \frac{p}{\pm v_w} \qquad \text{at } y = \pm 1\,, \tag{2.22}$$

where $v_w$ is the normal wall particle velocity. Continuity of particle displacement at each wall yields the Ingard-Myers boundary conditions [11, 57], which in terms of the non-dimensional admittance $\beta = 1/Z$ are given by

$$\frac{\partial p}{\partial y} = \mp ik_0\beta\left(1 - i\frac{M}{k_0}\frac{\partial}{\partial x}\right)^2 p \qquad \text{at } y = \pm 1\,. \tag{2.23}$$

Modal solutions are again of the form

$$p_n(x,y) = \Lambda_n\left[R_n \cos\mu_n y + S_n \sin\mu_n y\right] e^{-i\alpha_n x}\,, \tag{2.24}$$

where $\mu_n$ is the non-dimensional transverse lined duct eigenvalue, and $\alpha_n$ is the non-dimensional axial lined duct wavenumber. The modal coefficients $R_n$ and $S_n$ for a lined duct are given by

$$R_n = \cos(\mu_n) + \frac{ik_0\beta_{d,-d}}{\mu_n}\left(1 - M\frac{\alpha_n}{k_0}\right)^2 \sin(\mu_n)\,, \qquad y = \pm 1, \tag{2.25}$$

$$S_n = \pm\sin(\mu_n) \mp \frac{ik_0\beta_{d,-d}}{\mu_n}\left(1 - M\frac{\alpha_n}{k_0}\right)^2 \cos(\mu_n)\,, \qquad y = \pm 1. \tag{2.26}$$

Application of the boundary conditions to each modal solution yields the transcendental eigenvalue equation

$$\mu_n \tan 2\mu_n + \frac{(k_0\beta)^2}{\mu_n}\left(1 - M\frac{\alpha_n^\pm}{k_0}\right)^4 \tan 2\mu_n - i2k_0\beta\left(1 - M\frac{\alpha_n^\pm}{k_0}\right)^2 = 0\,. \tag{2.27}$$

Alternatively, the separate eigenvalue equations for even and odd eigenfunctions are given by

$$(\mu_n)\tan\mu_n - i\beta k_0\left(1 - M\frac{\alpha_n^{\pm}}{k_0}\right)^2 = 0\,, \tag{2.28}$$

$$(\mu_n)\,\mathrm{cot}\mu_n + i\beta k_0\left(1 - M\frac{\alpha_n^{\pm}}{k_0}\right)^2 = 0\,. \tag{2.29}$$

It should be noted that the eigenvalue equation for even modes will also apply to the problem of a duct of height $d$ with one wall rigid and the other wall lined with admittance $\beta$.

For cases where the top wall lining admittance $\beta_d$ differs from that of the bottom wall lining admittance $\beta_{-d}$ the eigenvalue equation becomes

$$\begin{aligned}\mu_n\tan 2\mu_n + \frac{k_0^2\beta_d\beta_{-d}}{\mu_n}\left(1 - M\frac{\alpha_n^{\pm}}{k_0}\right)^4\tan 2\mu_n \\ -ik_0\beta_d\left(1 - M\frac{\alpha_n^{\pm}}{k_0}\right)^2 - ik_0\beta_{-d}\left(1 - M\frac{\alpha_n^{\pm}}{k_0}\right)^2 = 0\,.\end{aligned} \tag{2.30}$$

Equation (2.30) is equivalent to Equation (2.27) when $\beta_d = \beta_{-d}$, and to Equation (2.11) when $\beta_d = \beta_{-d} = 0$.

Determination of the eigenvalues of any of the above eigenvalue equations is not simple because of the complex topography of the function for which the zeros are sought, and the complex arithmetic that is involved. A numerical scheme has been developed where the eigenvalue problem is transformed into a differential equation and the eigenvalues are found using an initial-value-problem approach following the type of procedure proposed by Eversman [19].

## 2.2 The numerical method applied to the two-dimensional case

Firstly the eigenvalue $\mu/k_0$ and wall lining admittance $\beta$ are assumed to be functions of a parameter $\eta$. Differentiation of the eigenvalue problem with respect to $\eta$ yields a single ordinary differential equation (ODE). If the admittance function $\beta(\eta)$ is prescribed over $0 < \eta < 1$, then $\mu/k_0$ may be found by integrating the differential equation over the same limits. If the value $\beta(0)$ is prescribed as the rigid-wall admittance, then the initial value is determined from the known rigid-wall eigenvalue sequence

$$\frac{\kappa_n}{k_0} = \frac{(n-1)\pi}{2k_0} \qquad \text{for } n = 1, 2\ldots\,. \tag{2.31}$$

The solution of the ODE at $\eta = 1$ is the eigenvalue for the condition $\beta(1)$, $k_0$, $M$, where $\beta(1)$ is the given wall lining admittance.

The choice of the admittance function $\beta(\eta)$ is determined by the value of the wall lining admittance. The value of the wall lining admittance determines the number and location of surface

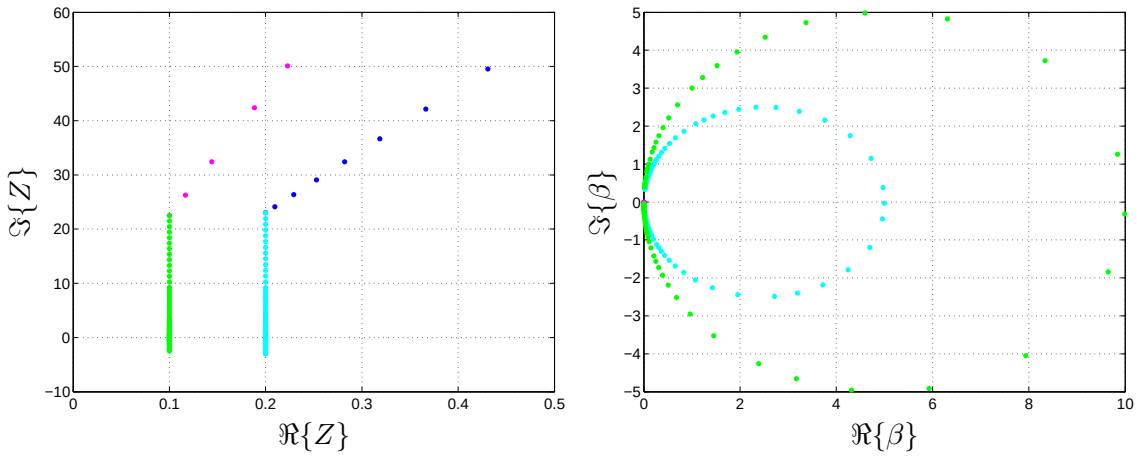


(a) Impedance plane.

(b) Admittance plane.

FIGURE 2.2: *Admittance and impedance contours taken for the tracing of mode* $n = 1$ *from the rigid wall case to the asymmetrically lined case.* •*, bottom wall admittance contour;* •*, top wall admittance contour;* •*, bottom wall impedance contour;* •*, top wall impedance contour;*.$R_{f_d} = 0.2$, $X_{f_d} = -3$, $R_{f_{-d}} = 0.1$, $X_{f_{-d}} = -2.5$.

wave modes, which can be hard to find. Where surface waves are not present the admittance function is identical to that used by Eversman [19]

$$\beta(\eta) = \eta\beta_f \,, \tag{2.32}$$

where $\beta_f$ is the required admittance. However, where surface waves are present a method suggested by Rienstra [22] is used so that all surface waves may be found. The method defines an impedance function, $Z(\eta)$, along a contour parallel to the imaginary axis in the complex impedance plane starting from $Z = R + i\infty$ for $M > 0$, or $Z = R - i\infty$ for $M = 0$, to the required impedance, $Z_f$. The proposed method uses a combination of the schemes suggested by Eversman and Rienstra, where an impedance function is defined such that both the wall impedances for an asymmetrically lined duct are taken into account, and tracking through the impedance plane occurs in such a way that all the surface waves can be found. The tracking of the top and bottom wall impedances occurs sequentially, so that the gap between successive eigenvalues is minimised, reducing the risk of instability in the scheme. The impedance function must begin from a region where surface waves do not exist, so Rienstra's method must be implemented for the first wall impedance by tracking from $Z = R_{f_d} \pm i\infty$ to $Z = R_{f_d} + iX_{f_d}$, and then for the second wall impedance by tracking from $Z = R_{f_{-d}} \pm i\infty$ to $Z = R_{f_{-d}} + iX_{f_{-d}}$.

For computational purposes a value of $X_\infty = \pm 20$ for the starting reactance is assumed to be sufficiently large to represent a contour beginning at $\pm i\infty$. This represents a change from a rigid to a nearly rigid wall impedance for both walls, which requires the inclusion of an additional step in the impedance function since the initial eigenvalues used for both walls are no longer close enough to ensure correct convergence. The step from rigid to nearly rigid wall impedance occurs in a region where surface waves do not occur, so Eversman's method is used to track the first wall impedance from rigid to $Z = R_{f_d} \pm iX_\infty$, and the second wall impedance from rigid

to $Z = R_{f_{-d}} \pm iX_\infty$. An example of the total impedance tracking path, with the four component paths, for an asymmetrically lined duct is presented in figure (2.2a) in the impedence plane, and in figure (2.2b) in the admittance plane.

## 2.3 The structure of the computational scheme

The structure of the computational scheme for the general case of an asymmetrically lined duct with uniform flow has five main components:

1. **Calculate the rigid-wall eigenvalue.**
   The calculation of the eigenvalues for the case of one wall rigid and one wall lined is undertaken using the even modes of a symmetrically lined duct of height $4d$ in order to reduce computation time and complexity. The rigid-wall eigenvalues are therefore defined as
   $$\frac{\mu_n}{k_0} = \frac{(n-1)\pi}{2k_0} \qquad \text{for } n = 1, 2 \dots , \tag{2.33}$$
   and the eigenvalue problem being solved is
   $$k_0 \left(\frac{\mu_n}{k_0}\right) \tan 2k_0 \left(\frac{\mu_n}{k_0}\right) = i\beta k_0 w^2 , \tag{2.34}$$
   $$w = \frac{1 \mp M\left[1 - \left(1 - M^2\right)\left(\frac{\mu_n}{k_0}\right)^2\right]^{\frac{1}{2}}}{1 - M^2} . \tag{2.35}$$
2. **Calculate the eigenvalue for the case of one wall rigid and the other with lining impedance $Z = R_{f_d} + iX_\infty$.**
   The rigid-wall eigenvalues are used as initial values for the initial-value-problem, where the admittance function is given by
   $$\beta_d(\eta) = \eta\beta_{f_d} \qquad \text{where } \beta_{f_d} = \frac{1}{R_{f_d} + iX_\infty}, \tag{2.36}$$
   and differentiation of Equation (2.34) yields the ODE
   $$\frac{d}{d\eta}\left(\frac{\mu}{k_0}\right) = \frac{i\omega^2\beta_{f_d}}{\tan 2k_0\left(\frac{\mu}{k_0}\right) + k_0\left(\frac{\mu}{k_0}\right)\sec^2 2k_0\left(\frac{\mu}{k_0}\right) \mp \frac{i2\beta_d w M\left(\frac{\mu}{k_0}\right)}{\sqrt{v}}} , \tag{2.37}$$
   $$v = 1 - \left(1 - M^2\right)\left(\frac{\mu}{k_0}\right)^2 . \tag{2.38}$$
3. **Calculate the eigenvalue for the case of one wall rigid and the other with the required lining impedance $Z_{f_d} = R_{f_d} + iX_{f_d}$.**
   Upon integration of Equation (2.37) the computed nearly rigid wall eigenvalues are used

as initial values for the initial-value-problem where the impedance function as suggested by Rienstra is given by

$$Z_d(\eta) = R_{f_d} + i\left[X_\infty - \eta\left(X_\infty - X_{f_d}\right)\right] . \tag{2.39}$$

The ODE for the problem is then

$$\frac{d}{d\eta}\left(\frac{\mu}{k_0}\right) = \frac{w^2\left(X_{f_d} - X_\infty\right)}{Z_d^2 \tan 2k_0\left(\frac{\mu}{k_0}\right) + Z_d^2 k_0\left(\frac{\mu}{k_0}\right)\sec^2 2k_0\left(\frac{\mu}{k_0}\right) \mp \frac{i2Z_d w M\left(\frac{\mu}{k_0}\right)}{v^{\frac{1}{2}}}} , \tag{2.40}$$

which upon integration yields the eigenvalues for the case of one wall hard and the other with the required lining impedance $Z_{f_d} = R_{f_d} + iX_{f_d}$. The eigenvalues are then used as initial values for the asymmetrically lined case.

4. **Calculate the eigenvalue for the case of one wall with lining impedance $Z = R_{f_{-d}} + iX_\infty$ and the other with the required impedance $Z_{f_d}$.**
The eigenvalue problem for the asymmetrically lined case with upper wall lining admittance $\beta_d$ and lower wall lining admittance $\beta_{-d}$ is written as

$$k_0\left(\frac{\mu}{k_0}\right)\tan 2k_0\left(\frac{\mu}{k_0}\right) - ik_0 w^2\beta_d$$

$$-ik_0 w^2\beta_{-d} + \frac{k_0 w^4\beta_d\beta_{-d}}{\left(\frac{\mu}{k_0}\right)}\tan 2k_0\left(\frac{\mu}{k_0}\right) = 0 , \tag{2.41}$$

$$w = \frac{1 \mp M\left[1 - \left(1 - M^2\right)\left(\frac{\mu_n}{k_0}\right)^2\right]^{\frac{1}{2}}}{1 - M^2} . \tag{2.42}$$

The initial-value-problem is then set up where the admittance function for the lower wall lining is prescribed as

$$\beta_{-d}(\eta) = \eta\beta_{f_{-d}} \qquad \text{where } \beta_{f_{-d}} = \frac{1}{R_{f_{-d}} + iX_\infty}, \tag{2.43}$$

and the upper wall admittance is held at the required admittance $\beta_{f_d} = 1/\left(R_{f_d} + iX_{f_d}\right)$ yielding the ODE

$$\frac{d}{d\eta}\left(\frac{\mu}{k_0}\right) = \frac{\mathfrak{N}_A}{\mathfrak{D}_A} , \tag{2.44}$$

where

$$\mathfrak{N}_A = iw^2\beta_{f_{-d}} - \frac{w^4\beta_d\beta_{f_{-d}}\tan 2k_0\left(\frac{\mu}{k_0}\right)}{\left(\frac{\mu}{k_0}\right)} ,$$

$$\mathfrak{D}_A = \tan 2k_0\left(\frac{\mu}{k_0}\right) + 2k_0\left(\frac{\mu}{k_0}\right)\sec^2 2k_0\left(\frac{\mu}{k_0}\right) \mp \frac{i2w\beta_d M\left(\frac{\mu}{k_0}\right)}{\sqrt{v}}$$

$$\mp \frac{i2w\beta_{-d}M\left(\frac{\mu}{k_0}\right)}{\sqrt{v}} + \frac{w^4\beta_d\beta_{-d}\tan 2k_0\left(\frac{\mu}{k_0}\right)}{\left(\frac{\mu}{k_0}\right)}$$

$$\cdot\left[\frac{2k_0\left(\frac{\mu}{k_0}\right)\sec^2 2k_0\left(\frac{\mu}{k_0}\right)}{\tan 2k_0\left(\frac{\mu}{k_0}\right)} - \frac{1}{\left(\frac{\mu}{k_0}\right)} \pm \frac{4M\left(\frac{\mu}{k_0}\right)}{w\sqrt{v}}\right] .$$

5. **Calculate the eigenvalue for the case of one wall with the required lining impedance $Z_{f_{-d}} = R_{f_{-d}} + iX_{f_{-d}}$ and the other with the required impedance $Z_{f_d}$.**
   Upon integration of Equation (2.44) the eigenvalues are once again used as initial values for the initial-value-problem where the lower wall impedance function is given by

$$Z_{-d}(\eta) = R_{f2} + i\left[X_\infty - \eta\left(X_\infty - X_{f_{-d}}\right)\right] , \tag{2.45}$$

   and the upper wall is held at the required impedance $Z_{f_d}$ yielding the ODE

$$\frac{d}{d\eta}\left(\frac{\mu}{k_0}\right) = \frac{\mathfrak{N}_Z}{\mathfrak{D}_Z} , \tag{2.46}$$

   where

$$\mathfrak{N}_Z = -\frac{w^2\left(X_\infty - X_{f_{-d}}\right)}{Z_{-d}^2} - \frac{iw^4\tan 2k_0\left(\frac{\mu}{k_0}\right)\left(X_\infty - X_{f_{-d}}\right)}{Z_{-d}^2 Z_{f_d}\left(\frac{\mu}{k_0}\right)} ,$$

$$\mathfrak{D}_Z = \tan 2k_0\left(\frac{\mu}{k_0}\right) + 2k_0\left(\frac{\mu}{k_0}\right)\sec^2 2k_0\left(\frac{\mu}{k_0}\right)$$

$$\mp \frac{i2wM\left(\frac{\mu}{k_0}\right)}{Z_{f_d}\sqrt{v}} \mp \frac{i2wM\left(\frac{\mu}{k_0}\right)}{Z_{-d}\sqrt{v}} + \frac{w^4\tan 2k_0\left(\frac{\mu}{k_0}\right)}{Z_{f_d}Z_{-d}\left(\frac{\mu}{k_0}\right)}$$

$$\cdot\left[\frac{2k_0\left(\frac{\mu}{k_0}\right)\sec^2 2k_0\left(\frac{\mu}{k_0}\right)}{\tan 2k_0\left(\frac{\mu}{k_0}\right)} - \frac{1}{\left(\frac{\mu}{k_0}\right)} \pm \frac{4M\left(\frac{\mu}{k_0}\right)}{w\sqrt{v}}\right] .$$

   Upon integration the ODE yields the eigenvalues for the case of one wall with lining impedance $Z_{f_d} = R_{f_d} + iX_{f_d}$ and the other with lining impedance $Z_{f_{-d}} = R_{f_{-d}} + iX_{f_{-d}}$.

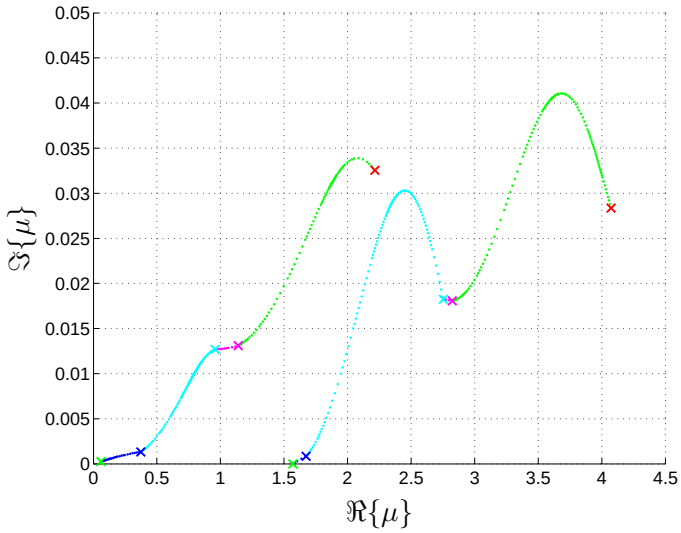


FIGURE 2.3: *Tracking of the positive $x$-direction propagating mode eigenvalues ($n = 1, 2$) with adaptive step size, showing the four component admittance/impedance contour sections. Colours correspond to the admittance/impedance contours in figure (2.2).* $k_0 = 18$, $M = 0.5$, $R_{f_d} = 0.2$, $X_{f_d} = -3$, $R_{f_{-d}} = 0.1$, $X_{f_{-d}} = -2.5$.

## 2.4 Implementation of the scheme

A fourth/fifth order Runge-Kutta-Fehlberg [58] adaptive step size integration routine has been applied to each of the ODEs that have been derived. A simple Newton-Raphson iteration has been used after the integration of each of the ODEs to maintain the accuracy of the eigenvalue at each step during the scheme.

It was noted by Eversman [19] that Equation (2.37) becomes singular when stepping away from the rigid-wall eigenvalue $\kappa/k_0 = 0$, but assuming small $\beta_d$ and $\mu/k_0$ the first step away from the eigenvalue can be made by

$$\frac{\mu}{k_0} = \left[\frac{i\triangle\beta_{f_d}}{2k_0}\right]^{\frac{1}{2}} \frac{1 \pm M}{1 - M^2}\,, \tag{2.47}$$

where $\triangle$ is the initial step away from $\eta = 0$.
An example of the path taken by two low order mode eigenvalues over the $\mu$ plane is shown in Figure (2.3), where the four colours represent the paths taken using the four impedance contours. The dots indicate the value of the eigenvalue at each integration step, whilst the crosses indicate the eigenvalue having been refined using the Newton-Raphson iteration. The smooth tracking of the eigenvalues demonstrates the stability of the integration scheme. The requirement for the rigid to nearly rigid components in the impedance contour is shown to be justified since the corresponding eigenvalue tracking paths (i.e. blue dots) can constitute a substantial amount of the total tracking pathlength.
The tracking paths of the first forty-four mode eigenvalues are presented in Figure (2.4), where the four tracking paths which move far away from the real axis are those of the surface wave

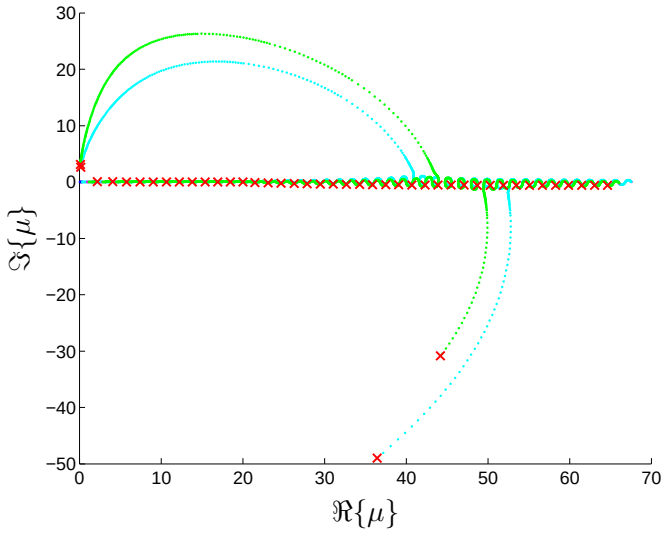


FIGURE 2.4: *Tracking of the first forty-four positive $x$-direction propagating mode eigenvalues. Colours correspond to the admittance/impedance contours in figure (2.2).* $k_0 = 18$, $M = 0.5$, $R_{f_d} = 0.2$, $X_{f_d} = -3$, $R_{f_{-d}} = 0.1$, $X_{f_{-d}} = -2.5$.

modes. Each surface wave mode is localised to either the inner or outer wall, which can be deduced from the tracking contours, either cyan or green respectively.
The independent integration variable is $\eta$, which is directly related to either the complex admittance or the reactance, so it is possible to investigate the variation in the dependant variable $\mu$ over the integration limits, and the variation in the adaptive integration step size. The two plots in Figure (2.5) show the value of $|\mu|$ over the integration limits of the reactance contours of top and bottom walls. The spacing of the dots indicates the step size chosen by the Runge-Kutta-Fehlberg routine in order to maintain the desired accuracy. The genuine acoustic modes show generally smooth integration paths, with a strong clustering of integration points for $\Im\{Z\} < 2$. However, there are regions of strong change in $|\mu|$ over the reactance contours where acoustic modes transition into surface wave modes (in red). It is noted from figure (2.5a) that the bottom wall localised surface wave modes are virtually unaffected by the introduction of the top wall impedance. There is a strong clustering of integration points at the transition points of the surface wave modes and this behaviour appears to be reciprocated in the acoustic modes in the vicinity of the surface wave modes as demonstrated in figure (2.6), which shows the plot range $[-3\ 2\ 38\ 55]$ of figure (2.5b). These observations demonstrate that the use of an adaptive step size integration routine is extremely useful for maintaining stability in the tracking methods and will prove useful for defining tracking contours in shooting methods developed later on.

## 2.5 Validation of the scheme for the two-dimensional case

The numerical scheme has been validated against published data from Eversman [20], and by comparison of results from a Finite Element (FE) code [38]. This includes flow and no flow

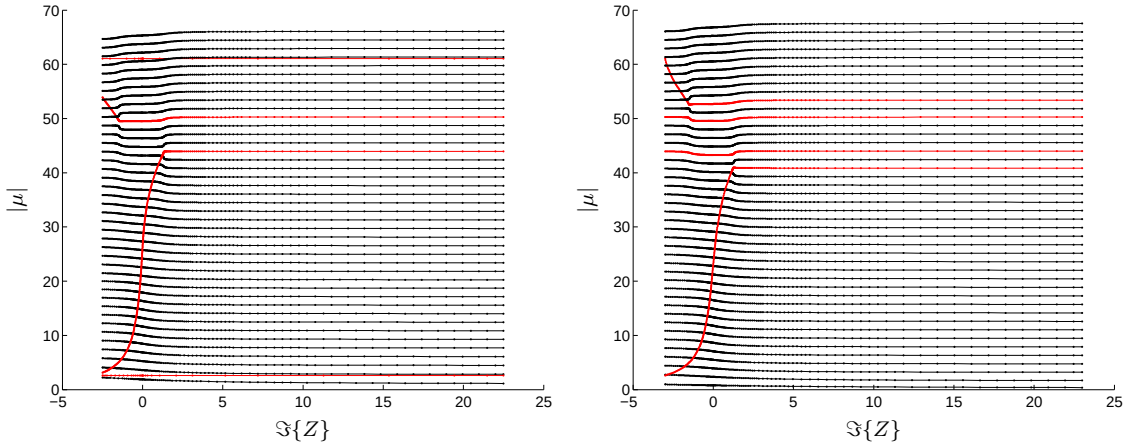


(a) Top wall impedance contour.

(b) Bottom wall impedance contour.

FIGURE 2.5: *Mode eigenvalue and Runge-Kutta-Fehlberg integration step size variation over the two reactance contours for the first 44 radial modes, with surface wave modes (red) and dots indicate the solution at each step.* $k_0 = 18$, $M = 0.5$, $R_{f_d} = 0.2$, $X_{f_d} = -3$, $R_{f_{-d}} = 0.1$, $X_{f_{-d}} = -2.5$.

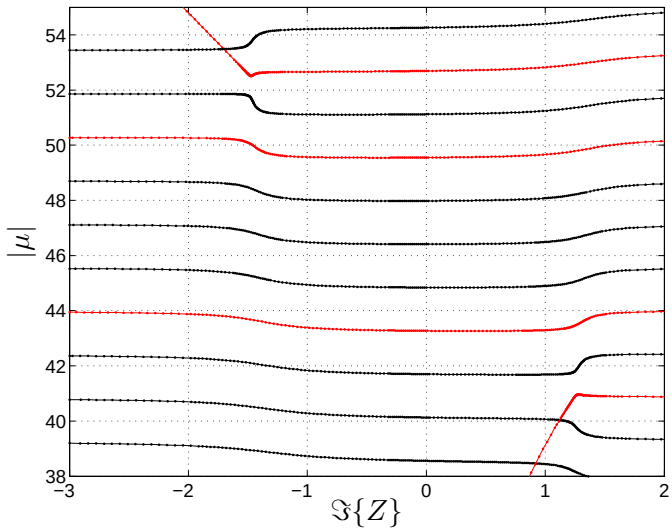


FIGURE 2.6: *Runge-Kutta-Fehlberg integration step size variation for casing impedance contour showing plot range [-3 2 38 55] of figure (2.5b), with surface wave modes (red).* $k_0 = 18$, $M = 0.5$, $R_{f_d} = 0.2$, $X_{f_d} = -3$, $R_{f_{-d}} = 0.1$, $X_{f_{-d}} = -2.5$.

cases, and symmetrically and asymmetrically lined ducts. The first validation case uses published data from Eversman [20] for a flow duct with one wall rigid and one wall lined. Two lining admittances were prescribed; $\beta = 0.72 + i0.42$ is located in a region where surface waves exist , and $\beta = 0.72 - i0.42$ is located in a region where surface waves do not exist. The results and validation data are presented in Tables (2.1) and (2.2) in terms of the axial wavenumber and the residual achieved by substitution of the computed eigenvalue into

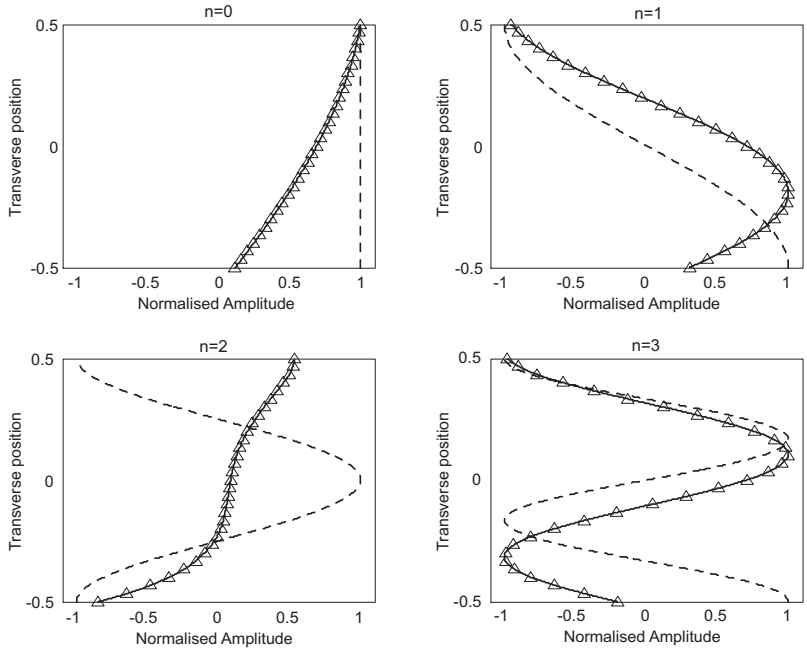


FIGURE 2.7: *Mode shapes for a rigid-wall duct (dashed line) and a duct lined on one wall (solid line - result determined from numerical scheme, △ - result from FE code) with admittance* $\beta = 0.72 + i0.42$, $k_0 = 0.5$, $M = -0.5$.

Equation (2.30). All the required modes were successfully calculated, including surface waves, with an accuracy of $10^{-11}$.
The first four mode shapes for the duct with lining admittance $\beta = 0.72 + i0.42$ are shown in Figure (2.7). The surface wave mode $n = 2$ decays exponentially away from the lined wall, whilst the other modes are slightly modified forms of the corresponding rigid duct mode shapes.

The second validation case uses results from a FE code for an asymmetrically lined duct with and without flow. The top wall admittance $\beta_d$ is located in a region where surface waves exist, but the bottom wall admittance $\beta_{-d}$ is located in a region where surface waves do not exist. The results and validation data for the flow case are presented in Table (2.3) and for the no flow case in Table (2.4).

## 2.6 Extension of the scheme to a three-dimensional duct

The analysis of the two-dimensional problem can be extended to the three-dimensional problem of a duct of height $2d$ and width $2b$, with rigid sidewalls, and asymmetric lining on top and bottom walls, with relatively little adjustment to the computational scheme. The rectangular geometry with Cartesian coordinate system $(x, y, z)$ chosen for this system is shown in Figure (2.8), where $z = \tilde{z}/d$. The governing equation is the three-dimensional

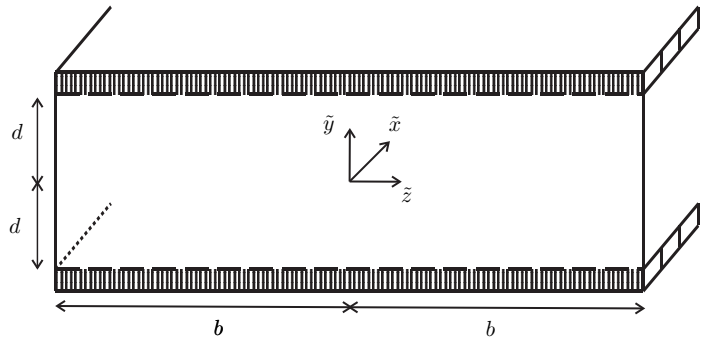


FIGURE 2.8: *Geometry and coordinate system for a three-dimensional duct*

convected Helmholtz equation

$$\left[ik_0 + M\frac{\partial}{\partial x}\right]^2 p - \nabla^2 p = 0\,, \tag{2.48}$$

the modal solutions of which have the form,

$$p_{m,n}(x,y,z) = \chi_{m,n}(y,z)e^{-ik_{m,n}x}\,. \tag{2.49}$$

The $(y,z)$ transverse variation of the mode is given by

$$\chi_{m,n}(y,z) = \Lambda_{m,n}\Psi_{m,n}(y)\left[R_m \cos k_{z_n} z + S_m \sin k_{z_n} z\right]\,, \tag{2.50}$$

and the normalisation constant $\Lambda$ is determined from

$$\frac{d}{4b}\int_{-b/d}^{b/d}\int_{-1}^{1} \chi_{m,n}\chi^*_{(m,n)'}\mathrm{d}y\mathrm{d}z = \delta_{(mn)(mn)'}\,. \tag{2.51}$$

The dispersion relation for the problem is defined as

$$\kappa^2_{m,n} = [k_0 - k_{m,n}M]^2 - k^2_{m,n} - k^2_{z_m}\,. \tag{2.52}$$

Boundary conditions on the duct sidewalls at $z = \pm b/d$ are set as

$$\frac{\partial p}{\partial z} = 0, \tag{2.53}$$

with the additional phase condition of $p(y,-b/d) = p(y,b/d)$. This phase condition is prescribed in order to enable a rectangular duct approximation to an axi-symmetric annular duct, such that the $z$ transverse mode variation is directly comparable to the annular duct $\theta$ mode variation. This transformation is described further in the next section (2.7).
The $z$ transverse wave number $k_{z_m}$ is given by

$$k_{z_m} = \frac{m\pi d}{b} \qquad \text{for } m = 0,1,2\ldots \tag{2.54}$$

The normalisation constant $\Lambda_{m,n}$ for a rigid walled duct is given by,

$$\Lambda_{m,n} = \begin{cases} 1 & m = 0, n = 1\,, \\ \sqrt{2} & m > 0, n = 1 \text{ or } m = 0, n > 1\,, \\ 2 & m > 0, n > 1\,. \end{cases}$$

Application of the boundary conditions for the top and bottom walls yields the eigenvalue problem which is identical to Equation (2.30), but where the axial wave number is now defined as

$$\frac{k_{m,n}}{k_0} = \frac{1}{1-M^2}\left(-M \pm \left[1-\left(1-M^2\right)\left[\left(\frac{\kappa_n}{k_0}\right)^2 + \left(\frac{k_{z_m}}{k_0}\right)^2\right]\right]^{\frac{1}{2}}\right)\,. \tag{2.55}$$

The theory discussed for the solution of the two-dimensional problem may now be applied with the $z$ transverse wave number included in the formulation. The first step away from the rigid-wall eigenvalue $\kappa/k_0 = 0$ can now be made by

$$\frac{\mu}{k_0} = \left[\frac{i\triangle\beta_{f1}}{2k_0}\right]^{\frac{1}{2}} w\,, \tag{2.56}$$

$$w = \frac{1 \mp M\left[1-\left(1-M^2\right)\left(\frac{k_{z_m}}{k_0}\right)^2\right]^{\frac{1}{2}}}{1-M^2}\,. \tag{2.57}$$

The method and structure of the scheme used to compute the eigenvalues is identical to that used for the two-dimensional case. Validation of the scheme for the three-dimensional case was made against a FE formulation, and numerical solution of the no flow problem in the $(y, z)$ plane using the commercial partial differential equation (PDE) solver MATLAB PDE toolbox. Validation data for an asymmetrically lined duct without flow is presented in Table (2.5), where data from both the FE solution and PDE toolbox are provided. Data for an asymmetrically lined duct with flow is presented in Table (2.6), with data from the FE solution also provided. Comparisons of the validation results demonstrate excellent agreement.

## 2.7 Rectangular approximation to an annular duct

The approximation of acoustic propagation in an annular duct using the three-dimensional rectangular duct model described above has been used previously by several researchers [10, 59, 60, 61]. The premise of the approximation is that at high hub-to-tip ratios $\hbar$, the mode eigenfunctions of the rectangular duct closely resemble those of the annular duct. The radial mode eigenfunctions of the annular duct are a linear combination of Bessel and Neumann functions

$$\Psi_{m,n}(r) = R_{m,n}J_m(\kappa_{m,n}r) + S_{m,n}Y_m(\kappa_{m,n}r)\,, \tag{2.58}$$

and by observing the principal asymptotic forms of these functions as $(\kappa_{m,n}r) \to \infty$ ([62], p.364) it is seen that trigonometric functions are recovered, indicating the similarity to the

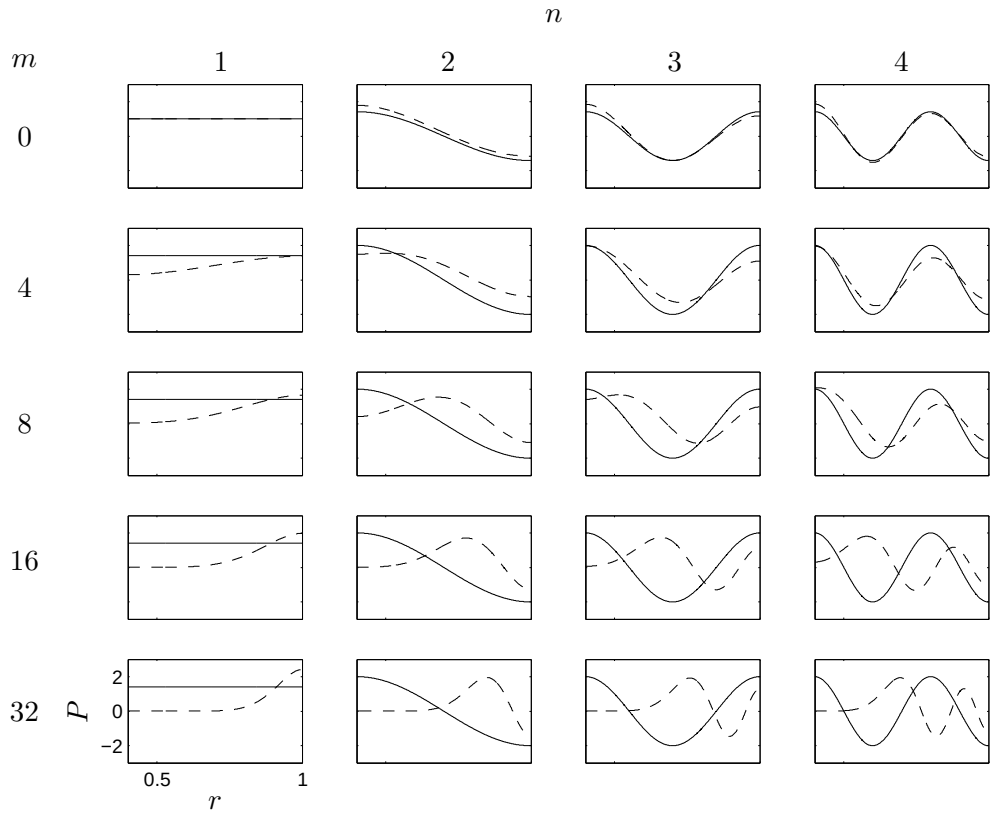


FIGURE 2.9: *Comparison of rectangular (solid lines) and annular (dashed lines) rigid duct modes.* $k_0 = 21.24925$, $\hbar = 0.4$, $M = 0$.

rectangular case,

$$J_m(\kappa_{m,n}r) \sim \sqrt{\frac{2}{\pi\kappa_{m,n}r}}\cos\left(\kappa_{m,n}r - \frac{m\pi}{2} - \frac{1}{4}\right),$$
$$Y_m(\kappa_{m,n}r) \sim \sqrt{\frac{2}{\pi\kappa_{m,n}r}}\sin\left(\kappa_{m,n}r - \frac{m\pi}{2} - \frac{1}{4}\right),$$
$$\text{as } \kappa_{m,n}r \to \infty\,. \tag{2.59}$$

A comparison of rigid rectangular and annular duct mode eigenfunctions at increasing hub-to-tip ratio $\hbar$ is presented in Figures (2.9), (2.10) and (2.11). It can be seen that agreement does indeed improve as $\hbar \to 1$. The agreement becomes worse as $m$ is increase, but improves as $n$ is increased.

Another important assumption is that the approximated modal cut-off frequencies (or cut-off ratios) also compare better with the true annular duct values with increasing hub-to-tip ratio. The modal cut-off frequency for an annular geometry is defined as

$$k_{\text{co}} = \left|\kappa^{\circledcirc}_{m,n}\right|\sqrt{1-M^2}\,, \tag{2.60}$$

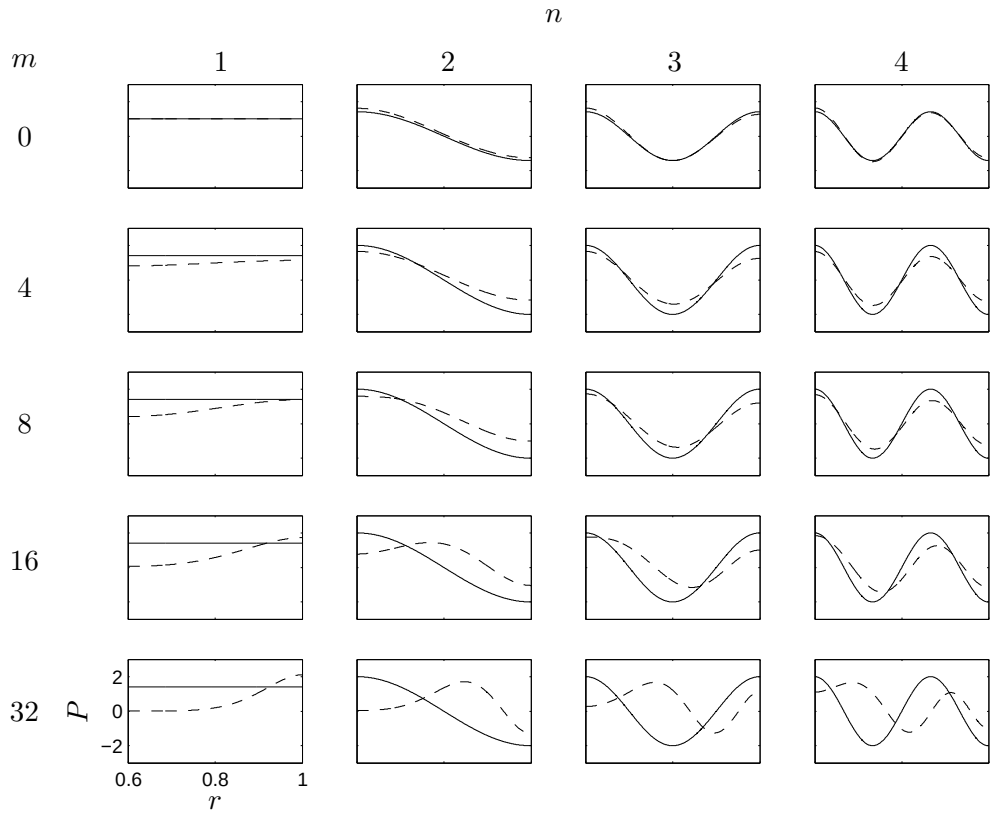


FIGURE 2.10: *Comparison of rectangular (solid lines) and annular (dashed lines) rigid duct modes.* $k_0 = 21.24925$, $\hbar = 0.6$, $M = 0$.

whereas, for a rectangular geometry it is defined as

$$k_{\text{co}} = \left| \sqrt{\kappa^{\square 2}_{m,n} + k^2_{z_m}} \right| \sqrt{1 - M^2} \, . \tag{2.61}$$

The cut-off frequency in the rectangular duct is dependent upon the $z$ transverse wave number component, $k_z$, which is determined using the duct width, $b$. The usual choice for the duct width is by taking the duct circumference at an average radius, $R_a$, given by

$$R_a = \frac{\hbar + 1}{2} \, , \tag{2.62}$$

such that the wave number is

$$k_{z_m} = \frac{m}{2R_a} \, . \tag{2.63}$$

However, in the annular duct the azimuthal wave number component does not appear explicitly in the cut-off frequency expression since it is inherent in the annular eigenvalue, $\kappa^{\circledcirc}_{m,n}$ [63]. The error in modal cut-off frequency given by the rectangular approximation compared to the true annular duct value, defined as $(k^{\square}_{co} - k^{\circledcirc}_{co})/k^{\circledcirc}_{co}$, is shown in Figures (2.12a), (2.12b) and (2.12c) for increasing hub-to-tip ratio. In general, a positive error means fewer modes are predicted to be cut-on at a given frequency, and vice versa. It can be seen that the approximation error reduces as the hub-to-tip ratio increases. It is also noted that the error for

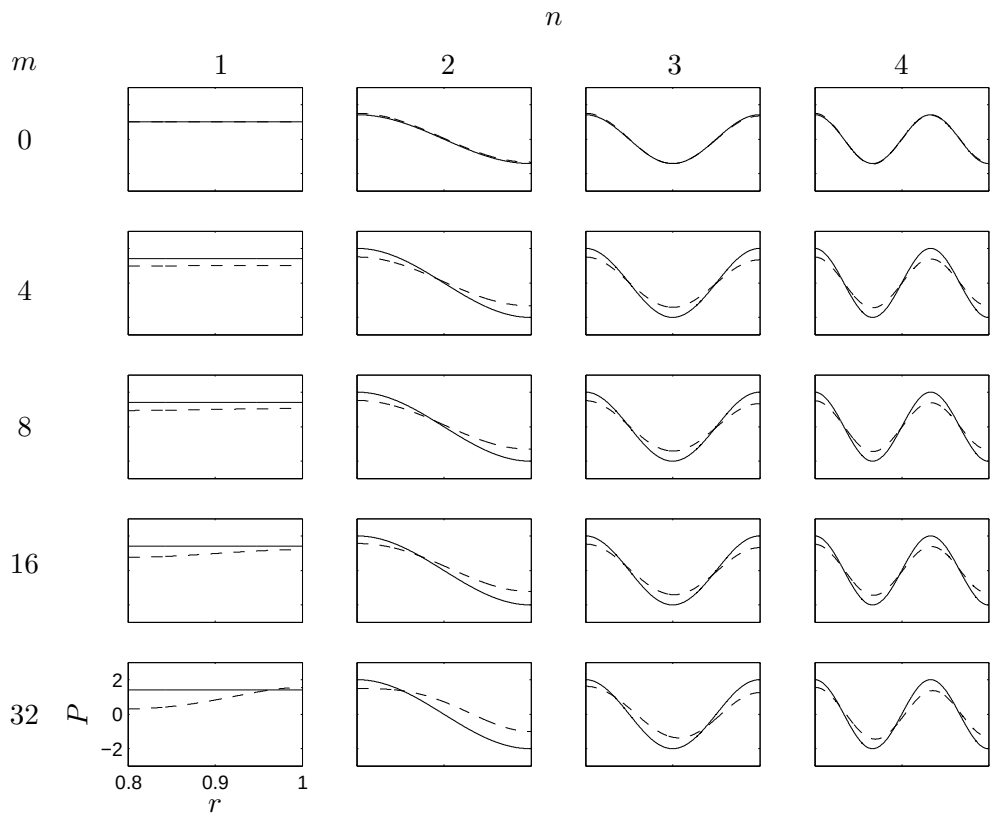


FIGURE 2.11: *Comparison of rectangular (solid lines) and annular (dashed lines) rigid duct modes.* $k_0 = 21.24925$, $\hbar = 0.8$, $M = 0$.

the modes $n > 1$ collapses faster than for the lowest radial order mode, $n = 1$, which was also seen to have the mode eigenfunction least well represented as $m$ is increased.

It is also of interest to compare the situation for the rectangular approximation of lined duct modes. In a lined duct the modal cut-off ratio no longer defines whether or not a mode transmits acoustic power, since all modes have complex axial wave numbers. However, it provides an indication of how well the mode propagates. An example of the error in modal cut-off frequency for a lined duct is shown in Figures (2.13a), (2.13b) and (2.13c) for increasing hub-to-tip ratio. As before, the error reduces as hub-to-tip ratio increases with the low order modes having the greatest error.

It is possible to artificially alter the cut-off ratio of the rectangular duct modes by judicious choice of the duct width, $b$ [59]. Equating the modal cut-off frequencies for the annular and rectangular geometries gives

$$\left|\kappa^{\circledcirc}_{m,n}\right| = \left|\sqrt{\kappa^{\square 2}_{m,n} + k^2_{z_m}}\right| \ . \tag{2.64}$$

It is the lowest radial order mode, $n = 1$, having the largest cut-off ratio that is of interest, so the inequality is reduced to

$$\left|\kappa^{\circledcirc}_{m,n}\right| = |k_{z_m}| = \left|\frac{m\pi d}{b}\right| \ . \tag{2.65}$$

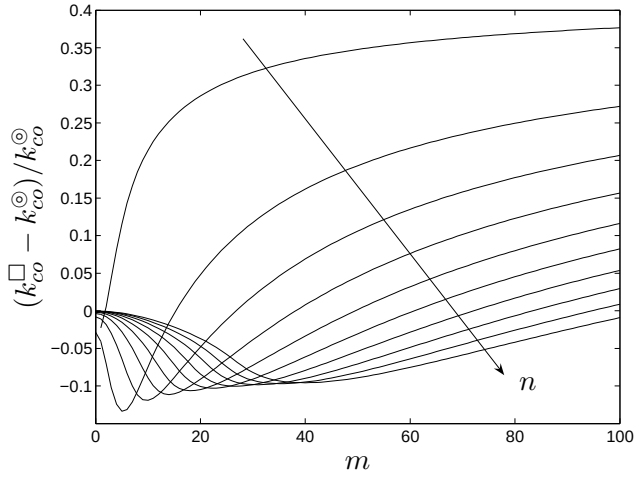


(a) $\hbar = 0.4$.

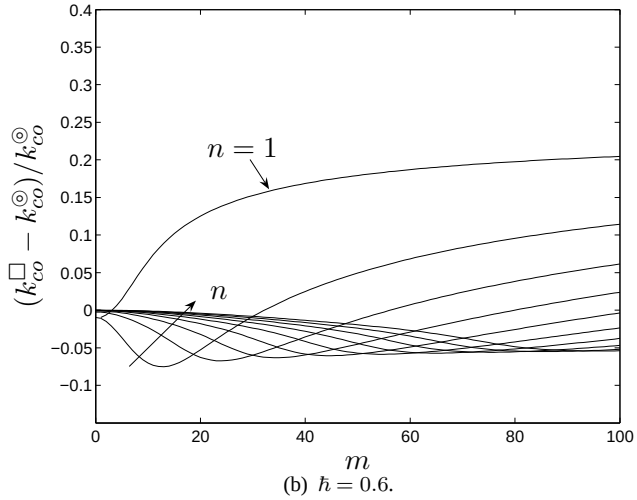


(b) $\hbar = 0.6$.

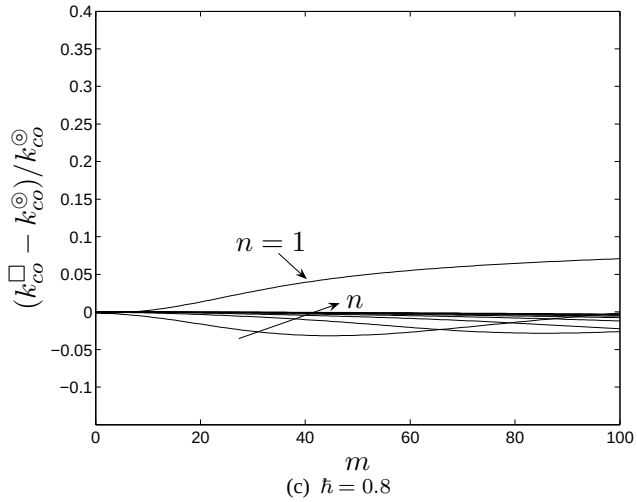


(c) $\hbar = 0.8$

FIGURE 2.12: *Error in modal cut-off frequencies using the rectangular approximation for rigid duct modes.* $m = 0$ *to* $100$, $n = 1$ *to* $11$, $M = 0$.

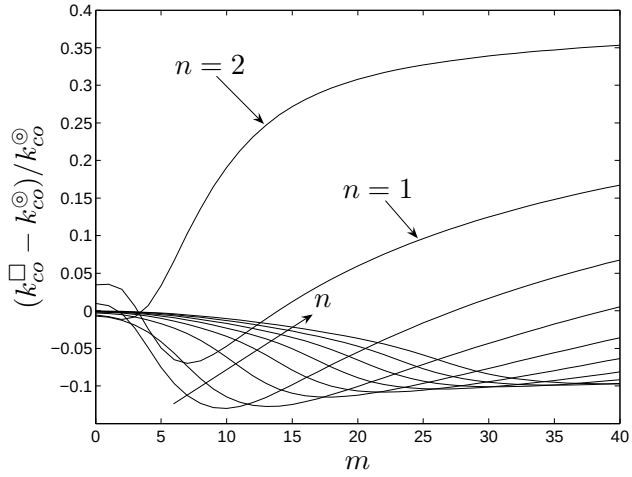


(a) $\hbar = 0.4$.

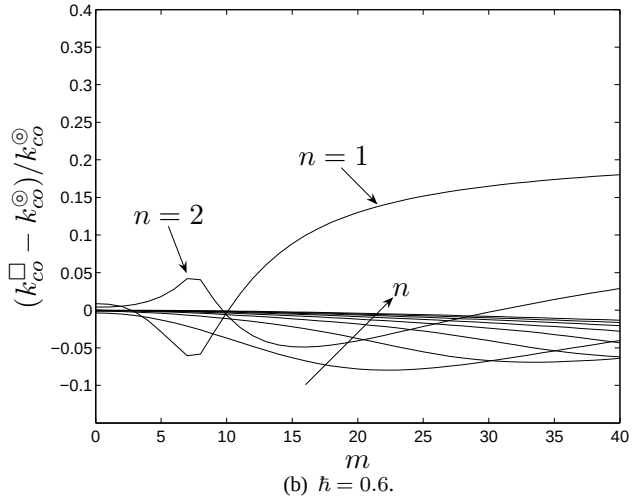


(b) $\hbar = 0.6$.

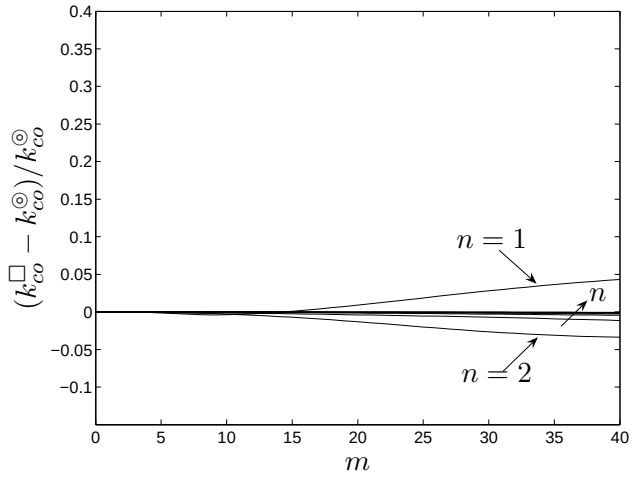


(c) $\hbar = 0.8$.

FIGURE 2.13: *Error in modal cut-off frequencies using the rectangular approximation for lined duct modes.* $k_0 = 21.25$, $Z_d = Z_{-d} = 2 - i$, $m = 0$ *to* $40$, $n = 1$ *to* $11$, $M = 0$.

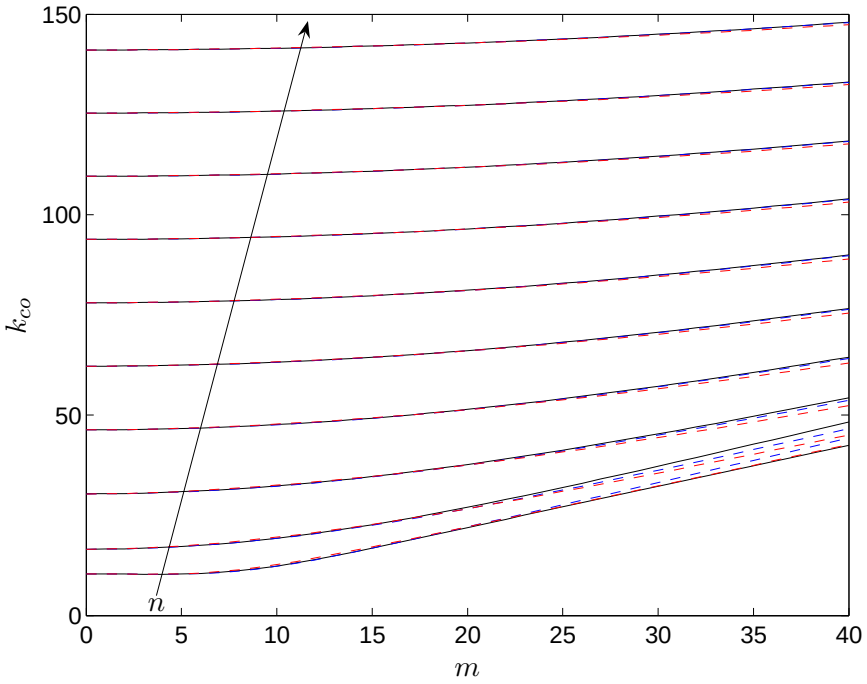


FIGURE 2.14: *Modal cut-off frequencies using the rectangular approximation for lined duct modes. Annular duct (black solid), Rectangular* $b = \pi R_a$ *(blue dashed), Rectangular* $b = \pi R_p$ *(red dashed).* $k_0 d = 21.25$, $Z_d = Z_{-d} = 2 - i$, $m = 0$ *to* $40$, $n = 1$ *to* $11$, $\hbar = 0.8$, $M = 0$.

The duct width is now chosen, using the rigid annular duct eigenvalue, $\kappa_{m,0}$, to be

$$b = \pi R_p = \left| \frac{m\pi d}{\kappa_{m,0}} \right| . \tag{2.66}$$

An example of the effect this adjustment has upon the modal cut-off frequencies is presented in Figure (2.14) for a lined duct with high hub-to-tip ratio. It is seen that the lowest order radial mode approximation is improved especially at higher azimuthal orders, but the approximation is adversely affected for higher order radial modes. The adjustment will not be used in the examples presented here due to the inaccuracy at higher order modes, and that annular duct eigenvalues are required to be calculated.

## 2.8 Surface waves

Lined duct modes at high frequency were classified into two categories by Rienstra [22]: genuine acoustic modes resulting from the finite duct geometry , and surface waves that exist near the impedance wall surface, independent of duct geometry. Surface wave dynamics are quite different from genuine acoustic modes, and are therefore more difficult to find. For parameters typical of aircraft engine duct problems, surface wave modes can appear at low radial mode orders with higher than typical axial decay rates, which could have a significant impact on acoustic liner performance. In addition, their unusual mode eigenfunctions can

enhance mode scattering in finite length acoustic liners, which is the subject of discussion in future chapters. Thus, it is important that these mode solutions are found in a robust manner. The implementation of Rienstra's impedance contour method in the eigenvalue scheme detailed previously was designed specifically to deal with these mode solutions.
Surface wave modes can be identified by $\mu_{m,n}$ having a large imaginary part, and can have large axial decay rates. Such modes can be seen in the axial wave number plot in Figure (2.15), where the majority of the modes are acoustic, forming a typical 'cut-on/cut-off' family of modes, with the surface waves located far away from the family of acoustic modes.
Approximate solutions for surface waves can be found in the high frequency limit by assuming $\Im\{\mu_{m,n}\}$ is large in the eigenvalue equations (2.27), (2.28), (2.29) and (2.30). Developing the approximate equations following [22], we introduce the Doppler corrected definitions,

$$\varsigma = \sqrt{1-M^2}\,, \qquad \hat{X} = \frac{x}{\varsigma}\,, \qquad k_0 = \varsigma\Omega\,, \qquad \mu = \Omega\gamma\,, \qquad \alpha = \frac{\Omega}{\varsigma}(\sigma - M)\,. \quad (2.67)$$

Noting that $\tan\Omega\gamma \to \pm i$ for $\Im\{\Omega\gamma\} \to \pm\infty$, the odd and even mode eigenvalue equations (2.28) and (2.29) can both be approximated by

$$(1-M\sigma)^2 \mp \varsigma^3 Z\gamma = 0\,. \quad (2.68)$$

On taking the second term to the right-hand side and squaring both sides, a quartic equation in $\sigma$ is found indicating there are four surface wave solutions. If there is no mean flow (i.e. $M = 0$) then there are just two possible solutions. The odd and even eigenvalue equations produce identical approximate equations. Applying the same analysis to the combined equation (2.27) produces the approximate equation given by

$$\left[(1-M\sigma)^2 \mp \varsigma^3 Z\gamma\right]^2 = 0\,, \quad (2.69)$$

from which eight surface wave solutions are possible, including multiplicity.
For the symmetrically lined duct no flow case, the approximate eigenvalue solutions are given by

$$\mu = k_0\gamma = \frac{k_0}{Z}\,. \quad (2.70)$$

The asymptotic solution is plotted against the exact solution in figure (2.16) and demonstrates excellent agreement. The approximate equation for an asymmetrically lined duct is given by

$$\left[(1-M\sigma)^2 \mp \varsigma^3 Z_{-d}\gamma\right]\left[(1-M\sigma)^2 \mp \varsigma^3 Z_d\gamma\right] = 0\,, \quad (2.71)$$

which is identical to that found by Rienstra for an asymmetrically lined annular duct [22]. The analysis of Rienstra covering the regions and numbers of surface waves in the impedance plane ([22], p.127) provides an explanation of the strong variation in $\mu$ when integrating over reactance, noted previously in figure (2.6), for the surface waves. The boundaries of the regions containing additional surface wave modes, as derived by Rienstra, coincide with the reactances in figure (2.6) where transition from acoustic modes to surface wave modes occurs

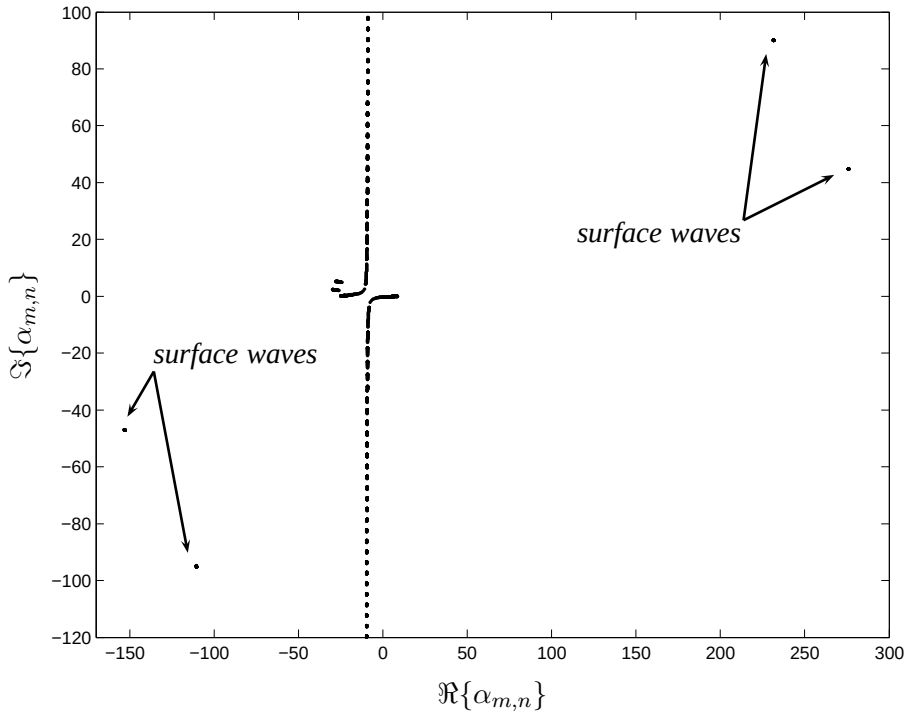


FIGURE 2.15: *Example axial wave number spectrum showing genuine acoustic modes and surface wave modes.* $k_0 = 6.37$, $Z_d = 2 - 4i, Z_{-d} = 1 - 5i$, $m = 0$ *to* $40$, $n = 1$ *to* $61$, $\hbar = 0.8$, $M = 0.5$.

($\Im\{Z\} \approx \pm 1.4$). In this example eight surface wave modes are possible, and the mode eigenfunctions of the positive propagating modes are presented in figure (2.17). The first two modes are acoustic surface wave modes, whilst the second two are hydrodynamic surface wave modes.

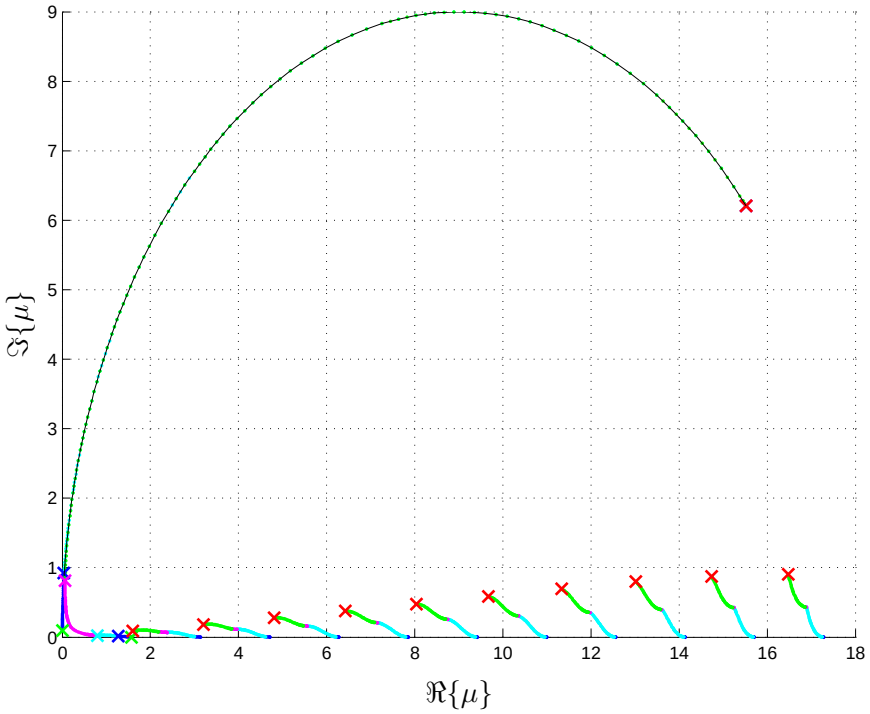


FIGURE 2.16: *Comparison of asymptotic surface wave mode approximation (black line) with exact solutions for a no flow case.* $k_0 = 18$, $M = 0$, $R_{f_d} = 1$, $X_{f_d} = -0.4$, $R_{f_{-d}} = 1$, $X_{f_{-d}} = -0.4$.

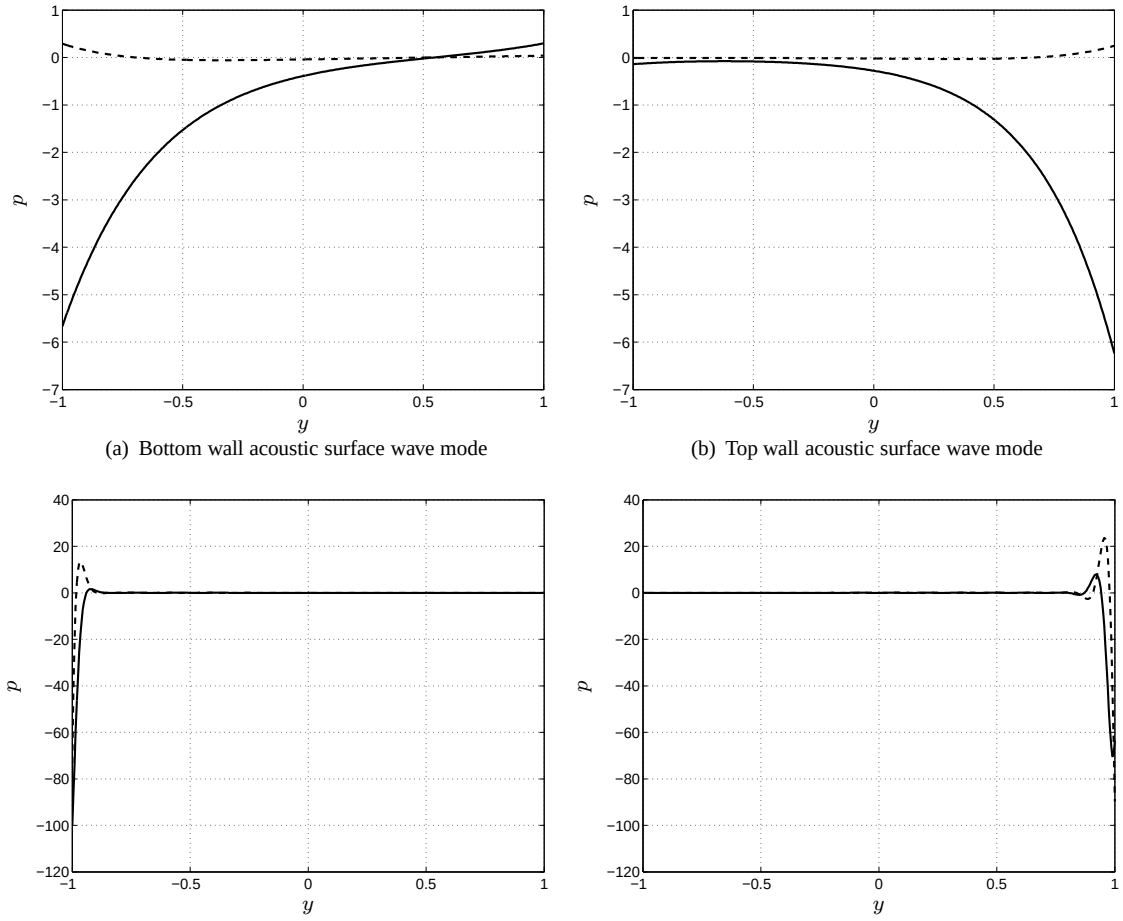


(a) Bottom wall acoustic surface wave mode

(b) Top wall acoustic surface wave mode

(c) Bottom wall hydrodynamic surface wave mode

(d) Top wall hydrodynamic surface wave mode

FIGURE 2.17: *Downstream propagating surface wave mode eigenfunctions.* —, $\Re\{P\}$; $--$, $\Im\{P\}$. $k_0 = 18$, $M = 0.5$, $R_{f_d} = 0.2$, $X_{f_d} = -3$, $R_{f_{-d}} = 0.1$, $X_{f_{-d}} = -2.5$.

## 2.9 Summary

- An eigenvalue solver for asymmetrically lined rectangular ducts in the presence of a uniform mean flow has been outlined.
- The solver uses the nonlinear initial-value-problem formulation of Eversman [19] to obtain the eigenvalues in a robust manner.
- The capture of surface wave solutions is assured by implementing the impedance contour approach of Rienstra [22] in combination with the admittance tracking of Eversman [19, 20].
- The solver was validated against benchmark solutions from the literature [20] and finite element solutions [38].

TABLE 2.1: *First ten axial wave numbers with residual values and validation data for a two-dimensional lined duct;* $M = -0.5$, $k_0 = 0.5$, $\beta = 0.72 + i0.42$.

| Mode | Axial wave number $\alpha_n$ | Residual | Axial wave number $\alpha_n$ from Eversman [20] | Axial wave number $\alpha_n$ from FE [38] |
|---|---|---|---|---|
| $0^+$ | $1.52374-i1.01082$ | 7.7826e-011 | $1.524-i1.011$ | $1.524-i1.011$ |
| $0^-$ | $-0.77164+i0.12579$ | 9.2526e-011 | $-0.772+i0.126$ | $-0.772+i0.126$ |
| $1^+$ | $0.67873-i4.53837$ | 9.4774e-011 | $0.679-i4.538$ | $0.679-i4.538$ |
| $1^-$ | $0.89692+i2.22619$ | 8.2610e-011 | $0.897+i2.226$ | $0.897+i2.226$ |
| $2^+$ | $-5.91842-i4.07768$ | 3.2062e-011 | $-5.918-i4.078$ | $-5.918-i4.078$ |
| $2^-$ | $1.29084+i5.63647$ | 6.6208e-011 | $1.291+i5.636$ | $1.291+i5.636$ |
| $3^+$ | $0.46488-i8.50142$ | 1.6104e-011 | $0.465+i8.501$ | $0.465-i8.501$ |
| $3^-$ | $1.17817+i9.02529$ | 2.1832e-011 | $1.178+i9.025$ | $1.178-i9.025$ |
| $4^+$ | $0.45531-i12.31711$ | 2.4301e-011 | $0.455-i12.317$ | $0.455-i12.317$ |
| $4^-$ | $1.04193+i12.59280$ | 9.7770e-011 | $1.042+i12.593$ | $1.042+i12.593$ |
| $5^+$ | $0.47699-i16.04607$ | 6.9773e-011 | $0.477-i16.046$ | $0.477-i16.047$ |
| $5^-$ | $0.95539+i16.21324$ | 9.5529e-011 | $0.955+i16.213$ | $0.955+i16.214$ |
| $6^+$ | $0.49971-i19.73430$ | 9.5107e-011 | $0.500-i19.734$ | $0.500-i19.736$ |
| $6^-$ | $0.89961+i19.84609$ | 9.3339e-011 | $0.900+i19.846$ | $0.900+i19.848$ |
| $7^+$ | $0.51903-i23.40160$ | 8.9883e-011 | $0.519-i23.402$ | $0.519-i23.405$ |
| $7^-$ | $0.86135+i23.48153$ | 9.1088e-011 | $0.861+i23.482$ | $0.861+i23.485$ |
| $8^+$ | $0.53491-i27.05699$ | 7.8200e-011 | $0.535-i27.057$ | $0.535-i27.064$ |
| $8^-$ | $0.83366+i27.11697$ | 8.9087e-011 | $0.834+i27.117$ | $0.834+i27.124$ |
| $9^+$ | $0.54795-i30.70505$ | 3.5506e-012 | $0.548-i30.705$ | $0.548-i30.718$ |
| $9^-$ | $0.81276+i30.75171$ | 8.8732e-011 | $0.812+i30.752$ | $0.813+i30.765$ |

TABLE 2.2: *First ten axial wave numbers with residual values and validation data for a two-dimensional lined duct;* $M = -0.5$, $k_0 = 0.5$, $\beta = 0.72 - i0.42$.

| Mode | Axial wave number $\alpha_n$ | Residual | Axial wave number $\alpha_n$ from Eversman [20] | Axial wave number $\alpha_n$ from FE [38] |
|---|---|---|---|---|
| $0^+$ | $1.28779 - i0.53174$ | 5.0556e-011 | $1.288 - i0.532$ | $1.288 - i0.532$ |
| $0^-$ | $-0.6049 + i0.19319$ | 2.108e-011 | $-0.605 + i0.193$ | $-0.605 + i0.193$ |
| $1^+$ | $-0.27112 - i4.6194$ | 3.3004e-011 | $-0.271 - i4.619$ | $-0.271 - i4.619$ |
| $1^-$ | $0.25691 + i2.42175$ | 8.2322e-011 | $0.257 + i2.422$ | $0.257 + i2.422$ |
| $2^+$ | $-1.70761 - i4.82454$ | 3.4737e-011 | $-1.708 - i4.824$ | $-1.708 - i4.824$ |
| $2^-$ | $0.76201 + i5.90588$ | 8.1507e-011 | $0.762 + i5.906$ | $0.762 + i5.906$ |
| $3^+$ | $0.10895 - i8.97452$ | 8.684e-011 | $0.109 - i8.975$ | $0.109 - i8.975$ |
| $3^-$ | $0.85911 + i9.39006$ | 1.3796e-011 | $0.859 + i9.39$ | $0.859 + i9.390$ |
| $4^+$ | $0.28768 - i12.68452$ | 5.5437e-011 | $0.288 - i12.684$ | $0.288 - i12.685$ |
| $4^-$ | $0.86424 + i12.92002$ | 2.4226e-011 | $0.864 + i12.92$ | $0.864 + i12.920$ |
| $5^+$ | $0.37928 - i16.33718$ | 9.4626e-011 | $0.379 - i16.337$ | $0.379 - i16.338$ |
| $5^-$ | $0.84754 + i16.48798$ | 8.5933e-011 | $0.848 + i16.488$ | $0.848 + i16.489$ |
| $6^+$ | $0.43543 - i19.97405$ | 4.5898e-011 | $0.435 - i19.974$ | $0.435 - i19.976$ |
| $6^-$ | $0.82824 + i20.07818$ | 5.4198e-012 | $0.828 + i20.078$ | $0.848 + i20.080$ |
| $7^+$ | $0.47339 - i23.6051$ | 2.7741e-011 | $0.473 - i23.605$ | $0.473 - i23.609$ |
| $7^-$ | $0.81088 + i23.68103$ | 1.1115e-011 | $0.811 + i23.681$ | $0.811 + i23.685$ |
| $8^+$ | $0.50076 - i27.23368$ | 7.8043e-011 | $0.501 - i27.234$ | $0.501 - i27.247$ |
| $8^-$ | $0.79616 + i27.29138$ | 8.8168e-011 | $0.796 + i27.291$ | $0.796 + i27.298$ |
| $9^+$ | $0.52141 - i30.86114$ | 7.658e-011 | $0.521 - i30.861$ | $0.521 - i30.874$ |
| $9^-$ | $0.78382 + i30.90641$ | 2.0792e-011 | $0.784 + i30.906$ | $0.784 + i30.920$ |

TABLE 2.3: *First four axial wave numbers with residual values and validation data for a two-dimensional asymmetrically lined duct;* $M = 0.4$, $k_0 = 9.3915$, $\beta_d = 0.2813 + i0.1210$, $\beta_{-d} = 0.72 - i0.42$.

| Mode | Axial wave number $\alpha_n$ | Residual | Axial wave number $\alpha_n$ from FE [38] |
|---|---|---|---|
| $0^+$ | $13.32735 - i0.17745$ | 1.0387e-010 | $13.327 - i0.178$ |
| $0^-$ | $-31.03822 + i0.04288$ | 9.6317e-011 | $-31.038 + i0.043$ |
| $1^+$ | $12.99759 - i0.25997$ | 1.1321e-010 | $12.998 - i0.260$ |
| $1^-$ | $-30.21476 + i0.18634$ | 1.9798e-010 | $-30.215 + i0.186$ |
| $2^+$ | $12.07437 - i0.39058$ | 1.3303e-010 | $12.073 - i0.391$ |
| $2^-$ | $-28.74385 + i0.49013$ | 1.4643e-010 | $-28.743 + i0.491$ |
| $3^+$ | $10.59577 - i0.56321$ | 1.5061e-010 | $10.596 - i0.563$ |
| $3^-$ | $-26.30835 + i1.09528$ | 1.9118e-010 | $-26.308 + i1.095$ |

TABLE 2.4: *First four axial wave numbers with residual values and validation data for a two-dimensional asymmetrically lined duct without flow;* $M = 0.0$, $k_0 = 9.3915$, $\beta_d = 0.2813 + i0.1210$, $\beta_{-d} = 0.72 - i0.42$.

| Mode | Axial wave number $\alpha_n$ | Residual | Axial wave number $\alpha_n$ from FE [38] |
|---|---|---|---|
| $0^+$ | 17.91849$-i$0.68213 | 1.1811e-010 | 17.919$-i$0.682 |
| $0^-$ | $-$17.91849$+i$0.68213 | 1.1811e-010 | $-$17.919$+i$0.682 |
| $1^+$ | 8.90489$-i$1.70311 | 1.5596e-010 | 8.904$-i$1.704 |
| $1^-$ | $-$8.90489$+i$1.70311 | 1.5596e-010 | $-$8.904$+i$1.704 |
| $2^+$ | 18.23024$-i$0.13267 | 1.5731e-010 | 18.230$-i$0.133 |
| $2^-$ | $-$18.23024$+i$0.13267 | 1.5731e-010 | $-$18.230$+i$0.133 |
| $3^+$ | 17.09317$-i$0.51076 | 1.3029e-010 | 17.093$-i$0.511 |
| $3^-$ | $-$17.09317$+i$0.51076 | 1.3029e-010 | $-$17.093$+i$0.511 |

TABLE 2.5: *Axial wave numbers in order of the first ten most accurate solutions from the PDE solver, with residual values and validation data, for a three-dimensional asymmetrically lined duct without flow;* $M = 0.0$, $k_0 = 9.24$, $k_0 b/d = 18.48$, $\beta_d = 0.2813 + i0.1210$, $\beta_{-d} = 0.72 - i0.42$.

| Mode m | Mode n | Axial wave number $\alpha_n$ | Residual | Axial wave number $\alpha_n$ from numerical solution | Axial wave number $\alpha_n$ from FE [38] |
|---|---|---|---|---|---|
| 0 | 2 | 18.23024$-i$0.13267 | 1.5731e-010 | 18.2302$-i$0.1327 | 18.230$-i$0.133 |
| 1 | 2 | 18.16244$-i$0.13316 | 1.5731e-010 | 18.1624$-i$0.1332 | 18.162$-i$0.133 |
| 2 | 2 | 17.95752$-i$0.13468 | 1.5731e-010 | 17.9574$-i$0.1349 | 17.958$-i$0.135 |
| 0 | 0 | 17.91849$-i$0.68213 | 1.1811e-010 | 17.9188$-i$0.6828 | 17.918$-i$0.682 |
| 1 | 0 | 17.8496$-i$0.68476 | 1.1811e-010 | 17.85$-i$0.6853 | 17.850$-i$0.685 |
| 2 | 0 | 17.64135$-i$0.69284 | 1.1811e-010 | 17.6419$-i$0.6932 | 17.642$-i$0.693 |
| 3 | 2 | 17.61069$-i$0.13733 | 1.5731e-010 | 17.6103$-i$0.1377 | 17.611$-i$0.137 |
| 3 | 0 | 17.28873$-i$0.70698 | 1.1811e-010 | 17.2894$-i$0.7071 | 17.290$-i$0.707 |
| 4 | 2 | 17.11332$-i$0.14132 | 71.5731e-010 | 17.1122$-i$0.1419 | 17.112$-i$0.142 |
| 0 | 3 | 17.09317$-i$0.51076 | 1.3029e-010 | 17.0921$-i$0.5117 | 17.093$-i$0.511 |

TABLE 2.6: *First five axial wave numbers, with residual values and validation data, for a three-dimensional asymmetrically lined duct with flow;* $M = 0.4$, $k_0 = 9.3915$, $k_0 b/d = 18.78$, $\beta_d = 0.2813 + i0.1210$, $\beta_{-d} = 0.72 - i0.42$.

| Mode m | Mode n | Axial wave number $\alpha_n$ | Residual | Axial wave number $\alpha_n$ from FE [38] |
|---|---|---|---|---|
| $0^+$ | $0^+$ | 13.32735$-i$0.17745 | 1.0388e-010 | 13.327$-i$0.178 |
| $0^-$ | $0^-$ | $-$31.03822$+i$0.04288 | 9.7054e-011 | $-$31.038$+i$0.043 |
| $0^+$ | $1^+$ | 12.99759$-i$0.25997 | 1.1319e-010 | 12.998$-i$0.260 |
| $0^-$ | $1^-$ | $-$30.21476$+i$0.18634 | 1.9818e-010 | $-$30.215$+i$0.186 |
| $0^+$ | $2^+$ | 12.07437$-i$0.39058 | 1.3303e-010 | 12.073$-i$0.391 |
| $0^-$ | $2^-$ | $-$28.74385$+i$0.49013 | 1.4632e-010 | $-$28.743$+i$0.491 |
| $1^+$ | $0^+$ | 13.26049$-i$0.17862 | 1.0509e-010 | 13.261$-i$0.179 |
| $1^-$ | $0^-$ | $-$30.97165$+i$0.04309 | 9.635e-011 | $-$30.972$+i$0.043 |
| $1^+$ | $1^+$ | 12.93070$-i$0.26156 | 1.1037e-010 | 12.931$-i$0.262 |
| $1^-$ | $1^-$ | $-$30.14560$+i$0.18732 | 1.9635e-010 | $-$30.146$+i$0.187 |

# Chapter 3

# Axially-segmented liners in rectangular ducts with uniform mean flow

## 3.1 The mode-matching method

This chapter outlines a theoretical technique for calculating the performance of axially-segmented wall linings in rectangular ducts with uniform flow. A semi-analytic method known as *mode-matching* is used to analyse the propagation of sound in an infinite flow duct which contains multiple acoustically lined segments.

The mode-matching technique is a well-known method for formulating boundary-value problems in waveguide theory [30]. The first application of the technique to jet engine duct systems was made by Lansing and Zorumski [31], which represented the first in a series of extensive analytical and experimental studies of axially-segmented wall linings supported by NASA in the 1970s [32, 33, 12, 34, 35]. The geometry used in the studies by Motsinger et al. [12, 32] and Sawdy et al. [34, 33] was a two-dimensional rectangular duct, with symmetrical lining configurations with up to three segments aligned axially, whilst Zorumski [35] dealt with axisymmetric ducts. A mathematical model describing the mode-matching technique for asymmetrical lining configurations was outlined by Unruh [26]. However, the model was only applied to a single lining segment with one of the segment walls being rigid, and with a plane wave source. This is in fact equivalent to a symmetrically lined duct of twice the height, with only even modes included in the matching.

The geometry, as shown in Figure (3.1), considered in the mathematical analysis contained here is a three dimensional rectangular flow duct, with an asymmetric lining configuration. A mode-matching method is summarised for a single lining segment, then the method is extended to include multiple segments.

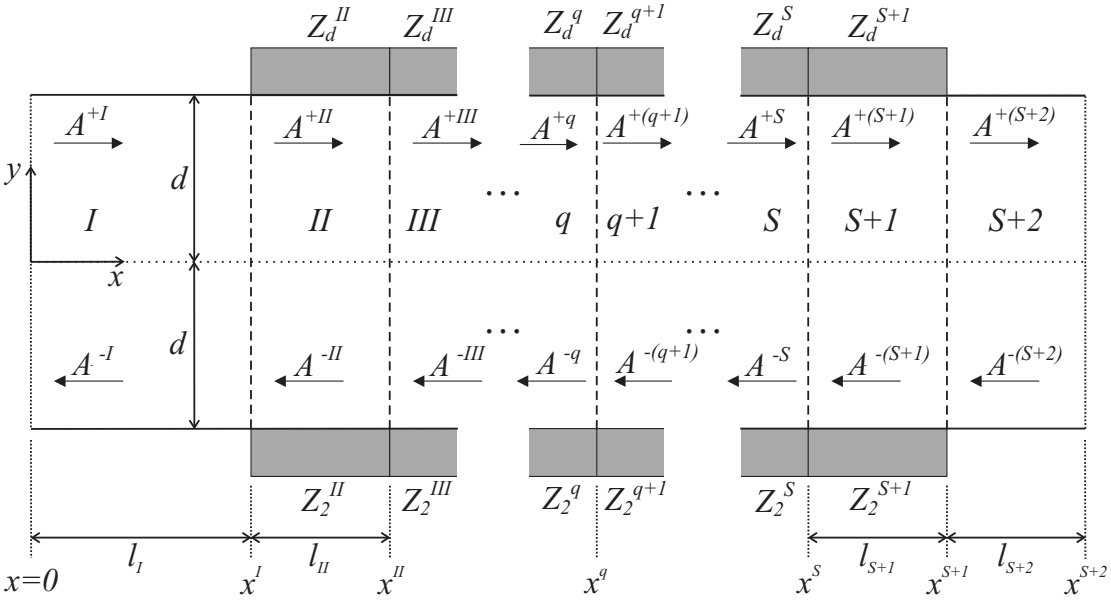


(a) Axial section

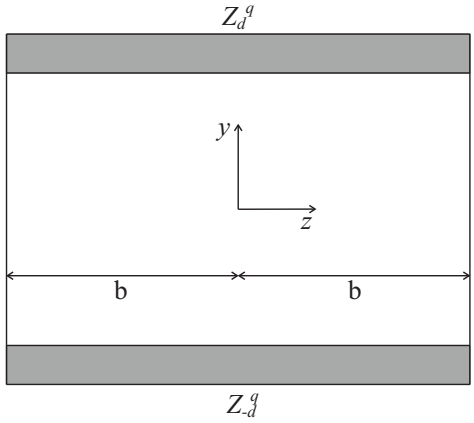


(b) Transverse section

FIGURE 3.1: *Geometry and notation for a three dimensional duct with axially-segmented wall linings*

## 3.2 Mode-matching theory for a single asymmetric liner segment

The basis of the mode-matching method described here is the condition of continuity of acoustic pressure and axial particle velocity over the interface planes where the duct wall impedance changes [31]. Since the pressure and axial particle velocity can be expressed in terms of analytic functions, for simple uniform duct geometries, a simple and computationally fast mode-matching scheme can be constructed. The theoretical basis for such a method is presented here for a three-dimensional rectangular duct with a single asymmetric liner segment located between rigid duct sections.

The basis of the analysis is the acoustic field in a three-dimensional duct with uniform flow. Since the acoustic properties of the lined sections are constant across the duct $z$ transverse direction, there will be no scattering between modes of different order $m$. Therefore, without

loss of generality, the mode-matching scheme is restricted to a fixed order $m$, and the solution for the pressure field can be expressed as a superposition of modal solutions for fixed $m$. The non-dimensional harmonic pressure field is then expanded as a sum of left $(+)$ and right $(-)$ travelling acoustic modes in the rigid and lined duct sections respectively as

$$p_m(x,y,z) = \sum_{n=1}^{\infty} \left[ A^+_{m,n} \Psi^+_{m,n}(y) e^{-ik^+_{m,n}x} + A^-_{m,n} \Psi^-_{m,n}(y) e^{-ik^-_{m,n}x} \right] \cos k_{z_m} z \,, \tag{3.1}$$

$$p_m(x,y,z) = \sum_{n=1}^{\infty} \left[ A^+_{m,n} \Psi^+_{m,n}(y) e^{-i\alpha^+_{m,n}x} + A^-_{m,n} \Psi^-_{m,n}(y) e^{-i\alpha^-_{m,n}x} \right] \cos k_{z_m} z \,. \tag{3.2}$$

For the problem of a single lined segment in a rigid duct the internal pressure field is divided into three regions $I$,$II$ and $III$. The pressure fields in the three regions are expressed by the following superposition of modal solutions, where the $e^{i\omega t}$ and $\cos k_{z_m} z$ terms have been omitted for convenience:

$$p^I_m(x,y) = \sum_{n=1}^{\infty} \left[ A^{+I}_{m,n} \Psi^{+I}_{m,n}(y) e^{-ik^+_{m,n}x} + A^{-I}_{m,n} \Psi^{-I}_{m,n}(y) e^{-ik^-_{m,n}x} \right] \,, \tag{3.3}$$

$$p^{II}_m(x,y) = \sum_{n=1}^{\infty} \left[ A^{+II}_{m,n} \Psi^{+II}_{m,n}(y) e^{-i\alpha^+_{m,n}x} + A^{-II}_{m,n} \Psi^{-II}_{m,n}(y) e^{-i\alpha^-_{m,n}x} \right] \,, \tag{3.4}$$

$$p^{III}_m(x,y) = \sum_{n=1}^{\infty} \left[ A^{+III}_{m,n} \Psi^{+III}_{m,n}(y) e^{-ik^+_{m,n}x} + A^{-III}_{m,n} \Psi^{-III}_{m,n}(y) e^{-ik^-_{m,n}x} \right] \,. \tag{3.5}$$

The acoustic field within each duct section satisfies the momentum equation, in non-dimensional form

$$\left[ \frac{\partial}{\partial t} + M \frac{\partial}{\partial x} \right] \hat{\mathbf{u}} = -\nabla \hat{p} \,, \tag{3.6}$$

which relates the acoustic particle velocity $\hat{\mathbf{u}} = \{\hat{u}, \hat{v}, \hat{w}\}$ to the acoustic pressure $\hat{p}$. The current mode-matching method only requires consideration of the axial component of the acoustic particle velocity fields, which for the three regions are expressed by the following modal expansions:

$$u^I_m(x,y) = \sum_{n=1}^{\infty} \left[ B^{+I}_{m,n} \Psi^{+I}_{m,n}(y) e^{-ik^+_{m,n}x} + B^{-I}_{m,n} \Psi^{-I}_{m,n}(y) e^{-ik^-_{m,n}x} \right] \,, \tag{3.7}$$

$$u^{II}_m(x,y) = \sum_{n=1}^{\infty} \left[ B^{+II}_{m,n} \Psi^{+II}_{m,n}(y) e^{-i\alpha^+_{m,n}x} + B^{-II}_{m,n} \Psi^{-II}_{m,n}(y) e^{-i\alpha^-_{m,n}x} \right] \,, \tag{3.8}$$

$$u^{III}_m(x,y) = \sum_{n=1}^{\infty} \left[ B^{+III}_{m,n} \Psi^{+III}_{m,n}(y) e^{-ik^+_{m,n}x} + B^{-III}_{m,n} \Psi^{-III}_{m,n}(y) e^{-ik^-_{m,n}x} \right] \,. \tag{3.9}$$

Using the momentum equation, the time harmonic axial particle velocity can be related to the time harmonic acoustic pressure by

$$\hat{u}_{m,n} = \frac{k_{m,n}}{(k_0 - k_{m,n}M)}\hat{p}_{m,n} \, . \tag{3.10}$$

Therefore, the modal amplitude coefficients in the rigid and lined duct sections respectively are related by

$$B^{\pm}_{m,n} = \frac{k^{\pm}_{m,n}}{\left(k_0 - k^{\pm}_{m,n}M\right)}A^{\pm}_{m,n} \, , \qquad \text{and} \qquad B^{\pm}_{m,n} = \frac{\alpha^{\pm}_{m,n}}{\left(k_0 - \alpha^{\pm}_{m,n}M\right)}A^{\pm}_{m,n} \, . \tag{3.11}$$

In the present problem, continuity of pressure and axial particle velocity is required at the leading and trailing edges, $x = x^I$ and $x^{II}$, of the liner. The residual errors that must be minimised are:

$$\begin{aligned} p^{II} - p^I, \qquad u^{II} - u^I \qquad &\text{at} \qquad x = x^I \, , \\ p^{III} - p^{II}, \qquad u^{III} - u^{II} \qquad &\text{at} \qquad x = x^{II} \, . \end{aligned} \tag{3.12}$$

The residual errors are minimised by means of the Galerkin method of weighted residuals, which uses the assumption that the eigenfunctions of the adjoining duct regions form a complete set [26]. This ensures that the residual errors are orthogonal to each eigenfunction in the modal expansion, and as the eigenfunctions form a complete set, the residual must be zero. The eigenfunctions of a rigid wall section are the weighting functions used to force the matching residuals to zero, since they are known to be complete and orthogonal, with and without the presence of a uniform mean flow. The modal expansions of the pressure and axial particle velocity fields are truncated at $n = N$, where $N$ must be chosen such that the near field in the vicinity of the matching interface planes is well resolved [64]. The following matching equations for the acoustic pressure and axial particle velocity are then obtained at the liner leading edge interface $x = x^I$

$$\begin{aligned} \int_{-1}^{1} W_{m,l}(y) \left[p^{II}_m(x^I, y) - p^I_m(x^I, y)\right] \mathrm{d}y = 0 \, , \\ \int_{-1}^{1} W_{m,l}(y) \left[u^{II}_m(x^I, y) - u^I_m(x^I, y)\right] \mathrm{d}y = 0 \, . \end{aligned} \tag{3.13}$$

where the weighting functions $W_{m,l}$ are the corresponding rigid duct eigenfunctions given by

$$W_{m,l} = \cos\left(\kappa_{m,l}\right)\cos\left(\kappa_{m,l}y\right) + \sin\left(\kappa_{m,l}\right)\sin\left(\kappa_{m,l}y\right), \qquad l = 1, \ldots N \, . \tag{3.14}$$

Substituting for the modal expansions, and rewriting, results in matching equations of reduced form, given by

$$\sum_{n=1}^{N}\left[A^{+II}_{m,n}e^{-i\alpha^{+}_{m,n}x^{I}}c^{+}_{ln}\right]+\sum_{n=1}^{N}\left[A^{-II}_{m,n}e^{-i\alpha^{-}_{m,n}x^{I}}c^{-}_{ln}\right]$$
$$-\sum_{n=1}^{N}\left[A^{+I}_{m,n}e^{-ik^{+}_{m,n}x^{I}}a_{ln}\right]-\sum_{n=1}^{N}\left[A^{-I}_{m,n}e^{-ik^{-}_{m,n}x^{I}}a_{ln}\right]=0 \tag{3.15}$$

$$\sum_{n=1}^{N}\left[A^{+II}_{m,n}e^{-i\alpha^{+}_{m,n}x^{I}}d^{+}_{ln}\right]+\sum_{n=1}^{N}\left[A^{-II}_{m,n}e^{-i\alpha^{-}_{m,n}x^{I}}d^{-}_{ln}\right]$$
$$-\sum_{n=1}^{N}\left[A^{+I}_{m,n}e^{-ik^{+}_{m,n}x^{I}}b_{ln}\right]-\sum_{n=1}^{N}\left[A^{-I}_{m,n}e^{-ik^{-}_{m,n}x^{I}}b_{ln}\right]=0 \tag{3.16}$$

$$l=1,\dots N \qquad n=1,\dots N\,,$$

where

$$a_{ln}=\int_{-1}^{1}W_{m,l}(y)\Psi^{I}_{m,n}(y)dy\,, \tag{3.17}$$

$$c^{\pm}_{ln}=\int_{-1}^{1}W_{m,l}(y)\Psi^{\pm II}_{m,n}(y)dy\,. \tag{3.18}$$

the above integrals are evaluated, taking advantage of the orthogonality of the mode eigenfunctions, and the result is given in Appendix (A). The momentum equation is used to rewrite the acoustic particle velocity modal amplitudes as

$$b^{\pm}_{ln}=\frac{k^{\pm}_{m,n}}{\left(k_0-k^{\pm}_{m,n}M\right)}a_{ln}\,, \tag{3.19}$$

$$d^{\pm}_{ln}=\frac{\alpha^{\pm}_{m,n}}{\left(k_0-\alpha^{\pm}_{m,n}M\right)}c^{\pm}_{ln}\,. \tag{3.20}$$

It is now convenient to write the matching equations at the liner leading edge $x=x^{I}$ in a combined matrix form

$$\left(\begin{array}{c|c}\mathbf{a}^{+}_{I} & \mathbf{a}^{-}_{I}\\ \hline \mathbf{b}^{+}_{I} & \mathbf{b}^{-}_{I}\end{array}\right)\left(\begin{array}{c}\mathbf{A}^{+I}\\ \hline \mathbf{A}^{-I}\end{array}\right)=\left(\begin{array}{c|c}\mathbf{c}^{+}_{I} & \mathbf{c}^{-}_{I}\\ \hline \mathbf{d}^{+}_{I} & \mathbf{d}^{-}_{I}\end{array}\right)\left(\begin{array}{c}\mathbf{A}^{+II}\\ \hline \mathbf{A}^{-II}\end{array}\right) \tag{3.21}$$

where the matrix elements are detailed in Appendix (A).
An identical analysis is applied to construct the combined matrix matching equations at the liner trailing edge $x=x^{II}$ which is given by

$$\left(\begin{array}{c|c}\mathbf{a}^{+}_{II} & \mathbf{a}^{-}_{II}\\ \hline \mathbf{b}^{+}_{II} & \mathbf{b}^{-}_{II}\end{array}\right)\left(\begin{array}{c}\mathbf{A}^{+III}\\ \hline \mathbf{A}^{-III}\end{array}\right)=\left(\begin{array}{c|c}\mathbf{c}^{+}_{II} & \mathbf{c}^{-}_{II}\\ \hline \mathbf{d}^{+}_{II} & \mathbf{d}^{-}_{II}\end{array}\right)\left(\begin{array}{c}\mathbf{A}^{+II}\\ \hline \mathbf{A}^{-II}\end{array}\right)\,. \tag{3.22}$$

The combined matrix equations (3.21) and (3.22) then form a system of $4N$ equations which are used to evaluate the $4N$ unknown coefficients.

### 3.2.1 An Iterative scheme for obtaining modal amplitudes

The linear equations (3.21) and (3.22) can be solved directly [31], however the system can often be ill-conditioned. This is due to the potentially large variation in modal axial decay rates. In order to overcome potential problems, an iterative scheme as used by Cummings [65] and Rienstra [66] is utilised to solve the system of equations for the unknown coefficients. In order to achieve this, the combined matrix equations are written in a slightly altered form, with the axial decay rates listed separately in a diagonal matrix. The matching equations for fixed $m$ at the liner leading edge $x = x^I$, and trailing edge $x = x^{II}$, are respectively

$$\begin{pmatrix} \mathbf{a}_{ln} & -\mathbf{c}^-_{ln} \\ \mathbf{b}^+_{ln} & -\mathbf{d}^-_{ln} \end{pmatrix} \begin{pmatrix} e^{-ik^+_{m,n}x^I} & 0 \\ 0 & e^{-i\alpha^-_{m,n}(x^I - x^{II})} \end{pmatrix} \begin{pmatrix} \mathbf{A}^{+I}_{m,n} \\ \mathbf{A}^{-II}_{m,n} \end{pmatrix} = \\ = \begin{pmatrix} \mathbf{c}^+_{ln} & -\mathbf{a}_{ln} \\ \mathbf{d}^+_{ln} & -\mathbf{b}^-_{ln} \end{pmatrix} \begin{pmatrix} \mathbf{A}^{+II}_{m,n} \\ \mathbf{A}^{-I}_{m,n} \end{pmatrix} , \tag{3.23}$$

$$\begin{pmatrix} \mathbf{c}^+_{ln} & -\mathbf{a}_{ln} \\ \mathbf{d}^+_{ln} & -\mathbf{b}^-_{ln} \end{pmatrix} \begin{pmatrix} e^{-i\alpha^+_{m,n}(x^{II} - x^I)} & 0 \\ 0 & e^{-ik^-_{m,n}(x^{II} - x^{III})} \end{pmatrix} \begin{pmatrix} \mathbf{A}^{+II}_{m,n} \\ \mathbf{A}^{-III}_{m,n} \end{pmatrix} = \\ = \begin{pmatrix} \mathbf{a}_{ln} & -\mathbf{c}^-_{ln} \\ \mathbf{b}^+_{ln} & -\mathbf{d}^-_{ln} \end{pmatrix} \begin{pmatrix} \mathbf{A}^{+III}_{m,n} \\ \mathbf{A}^{-II}_{m,n} \end{pmatrix} . \tag{3.24}$$

The combined matrix equations can be written in terms of the $2N \times 2N$ transfer matrices, $\mathbf{T}_I$ and $\mathbf{T}_{II}$, which relate the pressure and axial particle velocity at the liner interfaces, $x = x^I$ and $x = x^{II}$ respectively, as follows:

$$\begin{pmatrix} \mathbf{A}^{+II} \\ \mathbf{A}^{-I} \end{pmatrix} = \mathbf{T}_I \begin{pmatrix} \mathbf{A}^{+I} \\ \mathbf{A}^{-II} \end{pmatrix} , \tag{3.25}$$

$$\begin{pmatrix} \mathbf{A}^{+III} \\ \mathbf{A}^{-II} \end{pmatrix} = \mathbf{T}_{II} \begin{pmatrix} \mathbf{A}^{+II} \\ \mathbf{A}^{-III} \end{pmatrix} . \tag{3.26}$$

The coefficients $\mathbf{A}^{-I}$, $\mathbf{A}^{+II}$, $\mathbf{A}^{-II}$ and $\mathbf{A}^{+III}$ are initially set to zero, whilst the coefficients $\mathbf{A}^{+I}$ are determined from the source and the coefficients $\mathbf{A}^{-III}$ are chosen according to how the duct termination is modelled. Where an anechoic termination is assumed, the coefficients $\mathbf{A}^{-III}$ are set to zero. The iteration proceeds by first using equation (3.25) to calculate $\mathbf{A}_{+II}$ and $\mathbf{A}_{-I}$, then using this result to calculate $\mathbf{A}_{+III}$ and $\mathbf{A}_{-II}$ using (3.26). A new iteration may then proceed by using the revised value for $\mathbf{A}_{-II}$. The process is then repeated until the variation in the coefficients is less than a specified tolerance. Generally it is found that very few iterations are required for the coefficients to converge sufficiently.

## 3.3 Mode-matching theory for multiple liner segments

The extension of the mode-matching method from single to multiple axial segments $S$ is a relatively simple exercise [26, 34]. Matching equations for each of the $q = I, II \ldots S+1$ liner segment interfaces can be written as

$$\begin{pmatrix} \mathbf{c}^{+q} & -\mathbf{c}^{-(q+1)} \\ \mathbf{d}^{+q} & -\mathbf{d}^{-(q+1)} \end{pmatrix} \begin{pmatrix} e^{-i\alpha^{+q}(x_{q+1}-x_q)} & 0 \\ 0 & e^{-i\alpha^{-(q+1)}(x_{q+1}-x_{q+2})} \end{pmatrix} \begin{pmatrix} \mathbf{A}^{+q} \\ \mathbf{A}^{-(q+1)} \end{pmatrix} = \\ = \begin{pmatrix} \mathbf{c}^{+(q+1)} & -\mathbf{c}^{-q} \\ \mathbf{d}^{+(q+1)} & -\mathbf{d}^{-q} \end{pmatrix} \begin{pmatrix} \mathbf{A}^{+(q+1)} \\ \mathbf{A}^{-q} \end{pmatrix}, \tag{3.27}$$

or in terms of the transfer matrix as

$$\begin{pmatrix} \mathbf{A}^{+(q+1)} \\ \mathbf{A}^{-q} \end{pmatrix} = \mathbf{T}_q \begin{pmatrix} \mathbf{A}^{+q} \\ \mathbf{A}^{-(q+1)} \end{pmatrix}. \tag{3.28}$$

This leads to a coupled system of $(2S+2)\,N$ equations with $(2S+2)\,N$ unknown coefficients $\mathbf{A}^{\pm q}$, which are solved using the iteration scheme described in the previous section.

## 3.4 Alternative mode matching method for ducts with uniform flow

Recently, an alternative mode matching method for ducts with uniform flow was proposed by Hii [38] and Astley et al. [67]. The basis of this method is continuity of mass and axial momentum at the liner interface matching plane, as opposed to the pressure and axial particle velocity formulation described previously. Continuity is enforced by taking weighted forms of the mass and axial momentum equations over a vanishingly small control volume around the matching plane. In this way, finite contributions to the matching from line integrals on the duct walls at the matching plane are recovered. These contributions appear to improve the mode matching solutions, in particular the near field at the wall at the matching plane where a discontinuous pressure field is apparent [67].

In this section the alternative mode matching method is applied to the case of a three dimensional rectangular duct with uniform flow. The analysis begins with the acoustic continuity and axial momentum equations, which in Cartesian coordinates are

$$\left[ik_0 + M\frac{\partial}{\partial x}\right] p + \frac{\partial u}{\partial x} + \frac{\partial v}{\partial y} + \frac{\partial w}{\partial z} = 0\,, \tag{3.29}$$

$$\left[ik_0 + M\frac{\partial}{\partial x}\right] u + \frac{\partial p}{\partial x} = 0\,. \tag{3.30}$$

Firstly, the weighted form of the continuity equation (3.29) is taken over a control volume $V$

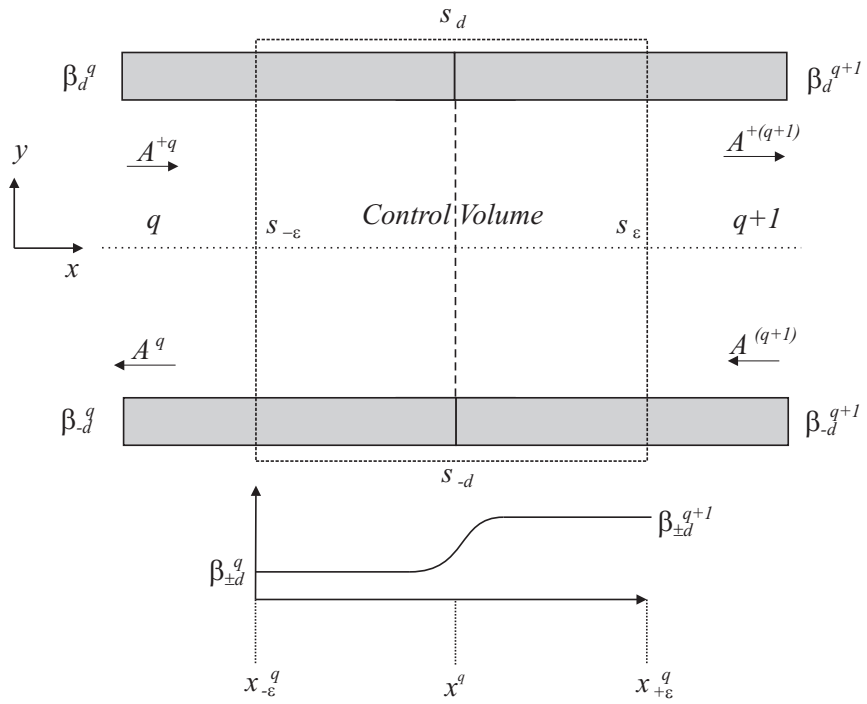


FIGURE 3.2: *Geometry and notation for the matching plane axial section. The admittance varies smoothly between* $x = x^q_{-\varepsilon}$ *and* $x = x^q_{+\varepsilon}$.

around the liner interface matching plane, as shown in figure (3.2), to give

$$\int_V ik_0 Wp - v\frac{\partial W}{\partial y} - w\frac{\partial W}{\partial z}\mathrm{d}V + \int_V \nabla \cdot [WMp + Wu, Wv, Ww]\,\mathrm{d}V = 0\,, \tag{3.31}$$

where the weighting function is the rigid duct mode eigenfunction given by

$$W_{m,n}(y,z) = [\cos(\kappa_{m,l})\cos(\kappa_{m,l}y) + \sin(\kappa_{m,l})\sin(\kappa_{m,l}y)]\cos(k_{z_m}z), \quad n = 1, \ldots N. \tag{3.32}$$

Applying Gauss' divergence theorem to transform the second volume integral into a surface integral gives

$$\int_V ik_0 Wp - v\frac{\partial W}{\partial y} - w\frac{\partial W}{\partial z}\mathrm{d}V + \int_s [WMp + Wu, Wv, Ww]\cdot \mathrm{d}\mathbf{s} = 0\,. \tag{3.33}$$

The surface integral is split into six integrals, so the integral over the control volume surface is equivalent to

$$\begin{aligned}
&\int_s [WMp + Wu, Wv, Ww] \cdot \mathrm{d}\mathbf{s} = \\
&-\int_{s_{-\epsilon}} WMp + Wu \,\mathrm{d}s_x + \int_{s_\epsilon} WMp + Wu \,\mathrm{d}s_x \\
&-\int_{s_{-d}} Wv \,\mathrm{d}s_y + \int_{s_d} Wv \,\mathrm{d}s_y \\
&-\int_{s_{-b/d}} Ww \,\mathrm{d}s_z + \int_{s_{b/d}} Ww \,\mathrm{d}s_z \,.
\end{aligned} \tag{3.34}$$

The boundary conditions on the duct walls are

$$w = 0 \qquad \text{on } z = \pm b/d \tag{3.35}$$

$$v = \pm \left[ ik_0 + M\frac{\partial}{\partial x} \right] \frac{\beta p}{ik_0} \qquad \text{on } y = \pm 1 \,. \tag{3.36}$$

On substituting the boundary conditions for $v$ and $w$, the integrals over the side walls vanish, whilst the integrals over the lined walls can be split into a surface integral and a line integral in the following manner

$$\begin{aligned}
-\int_{s_{-d}} Wv \,\mathrm{d}s_y &= \int_{s_{-d}} W\beta_d p \,\mathrm{d}s_y + \int_{s_{-d}} \frac{\partial}{\partial x}\left[\frac{WM\beta_d p}{ik_0}\right] \mathrm{d}s_y \\
&= \int_{s_{-d}} W\beta_d p \,\mathrm{d}s_y + \int_{-b/d}^{b/d} \left[\frac{WM\beta_d p}{ik_0}\right]_{-\epsilon}^{\epsilon} \mathrm{d}z \,,
\end{aligned} \tag{3.37}$$

$$\begin{aligned}
\int_{s_d} Wv \,\mathrm{d}s_y &= \int_{s_d} W\beta_{-d} p \,\mathrm{d}s_y + \int_{s_d} \frac{\partial}{\partial x}\left[\frac{WM\beta_{-d} p}{ik_0}\right] \mathrm{d}s_y \\
&= \int_{s_d} W\beta_{-d} p \,\mathrm{d}s_y + \int_{-b/d}^{b/d} \left[\frac{WM\beta_{-d} p}{ik_0}\right]_{-\epsilon}^{\epsilon} \mathrm{d}z \,.
\end{aligned} \tag{3.38}$$

The full weighted form of the continuity equation over the control volume $V$ can now be expressed as

$$\begin{aligned}
&\int_V ik_0 Wp - v\frac{\partial W}{\partial y} - w\frac{\partial W}{\partial z} \mathrm{d}V \\
&-\int_{s_{-\epsilon}} WMp + Wu \,\mathrm{d}s_x + \int_{s_\epsilon} WMp + Wu \,\mathrm{d}s_x \\
&+\int_{s_{-d}} W\beta_d p \,\mathrm{d}s_y + \int_{-b/d}^{b/d} \left[\frac{WM\beta_d p}{ik_0}\right]_{-\epsilon}^{\epsilon} \mathrm{d}z \\
&+\int_{s_d} W\beta_{-d} p \,\mathrm{d}s_y + \int_{-b/d}^{b/d} \left[\frac{WM\beta_{-d} p}{ik_0}\right]_{-\epsilon}^{\epsilon} \mathrm{d}z = 0 \,.
\end{aligned} \tag{3.39}$$

In order to obtain a matching equation at the liner interface plane the limit $\epsilon \to 0$ is applied to

equation (3.39). In this limit the volume integral and the surface integrals at the walls $y = \pm 1$ will vanish, so long as any singularities in p and **u** at $(x = 0, y = \pm 1)$ are less than $O(1/\epsilon^2)$ and $O(1/\epsilon)$ respectively. Recognizing that any $z$ transverse dependence can be dropped without loss of generality, the weighted form of the continuity equation is then

$$\int_{-1}^{1} W(y)M\left[p(y)^{II} - p(y)^{I}\right]\,\mathrm{d}y + \int_{-1}^{1} W(y)\left[u(y)^{II} - u(y)^{I}\right]\,\mathrm{d}y + \frac{W(1)M}{ik_0}\left[\beta_{-d}^{II}p(1)^{II} - \beta_{-d}^{I}p(1)^{I}\right] + \frac{W(-1)M}{ik_0}\left[\beta_{d}^{II}p(-1)^{II} - \beta_{d}^{I}p(-1)^{I}\right] = 0\,. \quad (3.40)$$

The next step is to take the weighted form of the axial momentum equation (3.30) over the control volume $V$, to give

$$\int_V ik_0 W u\,\mathrm{d}V + \int_V \nabla\cdot\left[WMu + Wp, 0, 0\right]\,\mathrm{d}V = 0\,. \quad (3.41)$$

As before, the surface integral is split into six integrals and, on taking the limit $\epsilon \to 0$ and dropping the $z$ transverse dependence, the resulting matching equation for axial momentum is

$$\int_{-1}^{1} W(y)\left[p(y)^{II} - p(y)^{I}\right]\,\mathrm{d}y + \int_{-1}^{1} W(y)M\left[u(y)^{II} - u(y)^{I}\right]\,\mathrm{d}y = 0\,. \quad (3.42)$$

Equations (3.40) and (3.42) are the matching equations to be applied at the liner interface matching planes. The linear system of equations can be formed into the matrix matching equations given by equation (3.27) in the manner detailed in the previous sections.

### 3.4.1 Liner edge conditions and hydrodynamic surface waves

It is noted that the matching equations (3.40) and (3.42) reduce to those given in equations (3.13) of the pressure and axial particle velocity matching method in the absence of a mean flow. With mean flow, the above analysis is analogous to that of Möhring and Eversman [68] where conservation of the Blokhintzev acoustic energy equation is applied to a control volume extending over a duct containing a finite length liner. The resulting energy conservation equation contains terms local to the liner edges, which are analogous to the third and fourth terms in equation (3.40) resulting from line integrals over the lined duct walls. These terms are interpreted by Möhring and Eversman as acoustic sources or sinks at the liner edges, since they represent the difference between the summed outgoing and incident energy fluxes, and the rate of work done on the liner within the control volume, which extends from $x = x_{+\epsilon}^{I}$ to $x_{-\epsilon}^{II}$ and $y = -1$ to 1. However, Quinn and Howe [69] pointed out that by taking these control volume limits from $x = x_{-\epsilon}^{I}$ to $x = x_{+\epsilon}^{II}$, effectively outside the liner edges, the contributions from the edge terms disappear from the energy conservation equation, thus cannot represent sources or sinks.

The analysis of Möhring and Eversman neglects the singularity in the axial gradient of wall normal displacement $\partial\epsilon_w/\partial x = \partial(\beta p/ik_0)/\partial x$ at the liner edges, which stems from the slip

flow boundary condition. This singular behaviour is included explicitly in the mass-momentum matching equations within integrals over the lined wall surfaces.

Two difficulties occur when attempting to resolve the singularities using the mode-matching method. The first is that although $\partial\varepsilon_w/\partial x$ is singular at the liner edges, $\varepsilon_w$, $p$ and $\mathbf{u}$ are generally finite and non-zero [68, 70]. In order for the volume and surface integrals to vanish as assumed for $\epsilon \to 0$, they must be no more singular than $O(\epsilon^{-2})$. This is in agreement with the wall streamline condition in the Wiener-Hopf analysis of Rienstra and Peake [71] when assuming all modes are stable. However, within the mode-matching procedure there is no way to enforce this minimum edge condition, rather it is left until after the solution is computed to check whether the modal amplitudes produce suitably converged liner edge displacements. In practise, it is found that varying the number of cut-off modes in the matching can assist in this process. Highly cut-off modes are very localised, having no effect on the field away from the liner interface plane, and so can contribute to resolving any singular behaviour at the walls. However, their contributions to the field within the duct at the matching planes are highly oscillatory and minimising the field residuals away from the walls, whilst trying to resolve wall singularities can prove to be troublesome. The issues in resolving higher order modes are seen in the validation section of this chapter (in the form of highly oscillatory behaviour localised at the matching planes) and were previously noted in a mode-matching technique by Nijboer [72, 73].

The second difficulty involves the presence of hydrodynamic surface wave modes, which occur for certain $k_0$, $M \neq 0$ and $Z$. Rienstra [22] showed that, under certain conditions, one of these modes (per impedance and azimuthal order) is a downstream running instability, with an invariably large growth rate for impedances away from the real axis [74]. Whether the presence of this mode is physically realistic is a subject for discussion [29, 71, 74, 75]. Rienstra and Peake [71] found that it is possible that such a mode can have genuine acoustic effects upon the mode scattering at a rigid-lined duct interface using a Wiener-Hopf solution. However, Rienstra and Tester [74] reasoned that including unstable modes in the field description within the lined duct section is futile, and somewhat against the assumption of small perturbations made in the linearised model used here. In addition, the Ingard-Myers boundary condition [11, 57] assumes small deflections of the wall streamline, thus large deflections would be unacceptable and, judging by the wall localised nature of the surface wave modes, this may well be the case. Here we take the approach of Rienstra and Tester by assuming that all modes decay in the direction of travel, thus the downstream running instability mode becomes an upstream running damped mode.

A further difficulty encountered with the hydrodynamic surface waves is that their exponential behaviour at the wall can cause conditioning problems when attempting to invert the matrix on the right-hand-side of matrix matching equation (3.27). The problem stems from attempting to integrate the weighted surface wave eigenfunctions using equations (A.2) when $|\Im\{\mu_{m,n}\}| \gg 1$, which is often the case for hydrodynamic surface waves. The value of the integrands become exponentially large. In attempting to circumvent this problem it is possible

to write the hydrodynamic surface wave eigenfunction as a complex exponential for $|\Im\{\mu_{m,n}\}| \gg 1$ by noting that

$$\begin{aligned}\Psi_n(y) &= R_n \cos\kappa_n y + S_n \sin\kappa_n y \,, \\ &= \cos\kappa_n y \pm i \sin\kappa_n y \,, \\ &= e^{\pm i\kappa_n y} \,. \end{aligned} \tag{3.43}$$

The mode eigenfunctions may then be normalised to their wall values before integrating. This requires the normalisation of the surface wave mode to the wall on which it is localised, of which prior knowledge is required. It is possible to infer this from the behaviour of the mode eigenvalue in the tracking procedure of the eigenvalue solver detailed in the previous chapter (2). A surface wave mode eigenvalue will vary rapidly along the impedance contour of the wall to which it is localised, and is hardly affected by the impedance contour of the opposite wall.

In parts of this work the hydrodynamic surface waves may be ignored for four reasons. The first being that the unstable modes are included as decaying modes, which may have an effect on the scattering [71]. The second is that these modes have very large decay rates, so do not contribute to the field away from the liner interface planes. The third is that the mode order of these modes is rather hard to predict, and generally occur at very high mode orders, which would require the cumbersome calculation of very many modes. The final reason is that, for practical purposes, they may need to be excluded in order to perform a matrix inversion in the matching procedure. In addition, it will be seen in the following validation sections that, their exclusion does not appear to have any perceptible effect on the power transmission.

## 3.5 Expressions for induct sound power

A convenient quantifier of the performance of acoustic liners in ducts is the sound power transmission loss $\Delta_{PWL}$, i.e. the difference between the incident acoustic power and the transmitted acoustic power. This is calculated by comparing acoustic powers in rigid walled sections either side of the lined region. Several expressions for sound power in flow ducts are available in the literature [76, 77], and for this study the more widely used definition of Morfey [76] is chosen. The axial component of the local instantaneous modal intensity is defined as

$$I_{x\,m,n}^{\pm} = \frac{|\,p^{\pm}{}_{m,n}\,|^2}{2\rho_0 c_0}\left[\left(1+M^2\right)\Re\left\{\frac{\rho_0 c_0 u^{\pm}{}_{m,n}}{p^{\pm}{}_{m,n}}\right\} + M\left(1+\left|\frac{\rho_0 c_0 u^{\pm}{}_{m,n}}{p^{\pm}{}_{m,n}}\right|^2\right)\right] . \tag{3.44}$$

The modal sound power is found by integrating $I_x$ over the duct cross-section, to give

$$W_{m,n}^{\pm} = \int_{-b}^{b}\int_{-d}^{d} I_{x\,m,n}^{\pm}\, dy\, dz. \tag{3.45}$$

The average axial acoustic intensity of a duct mode is then

$$\langle I^{\pm}_{x\ m,n} \rangle_s = \frac{W^{\pm}_{m,n}}{s} \ , \tag{3.46}$$

where $s = 4bd$ is the duct cross-sectional area. The total sound power $W^{\pm}$ is found by summing the modal powers of all the cut-on modes $N_c$

$$W^{\pm} = \frac{db}{\rho_0 c_0} \sum_{n=1}^{N_c} \varepsilon_{m,n} |A^{\pm I}{}_{m,n}|^2 \left[ \left(1 + M^2\right) Re\{\varpi^{\pm}_{m,n}\} + M \left(1 + |\varpi^{\pm}_{m,n}|^2\right) \right] \ , \tag{3.47}$$

where

$$\varpi^{\pm}_{m,n} = \frac{k^{\pm}_{m,n}}{k_0 - k^{\pm}_{m,n} M} \ , \qquad \varepsilon_{m,n} = \begin{cases} 4 & m = 0,\ n = 1 \\ 1 & m \neq 0,\ n \neq 1 \\ 2 & otherwise \end{cases} \ .$$

The sound power transmission loss, in decibels, is then given by

$$\Delta_{PWL} = 10 \log_{10} \left[ \frac{W^{+I}}{W^{+(S+1)}} \right] \ . \tag{3.48}$$

## 3.6 Comparison with Wiener-Hopf solutions

A Wiener-Hopf solution [28] to the problem of a uniform symmetric liner, in the absence of flow, with an even incident mode, was coded in Fortran 90 for the purpose of validating the mode-matching method previously described. The Wiener-Hopf and mode-matching methods are known to be closely related [28] and, therefore, the former can provide a good indication of the quality of solutions given by the latter. The coding of Wiener-Hopf solutions for other liner configurations and flow was not attempted. For zero flow, this was primarily due to the mode-matching method being similar across all configurations, so the single uniform symmetric lining solution would suffice to confirm that the method was valid. Where a mean flow is present, the Wiener-Hopf solution is complicated by issues surrounding the choice of edge conditions and instability waves [78, 29]. For these reasons, benchmarking for other lining configurations and flow has been done by comparison against published results from the literature.

Extensions to the ordinary Wiener-Hopf technique [79] have been applied by Koch [28] to derive an analytic solution for the scattering of sound by multiple liner elements in the absence of flow. The basic structure of this Wiener-Hopf solution begins with the formulation of the generalised Wiener-Hopf equations for the problem. This is undertaken through application of Fourier transforms, applied with respect to the axial direction, to the governing Helmholtz equation and associated boundary conditions. The solution of the resulting generalised Wiener-Hopf equations first requires factorisation into two split functions of the Wiener-Hopf

kernel contained within the equations. The kernel is in fact a combination of the dispersion relation, and characteristic equations governing the duct regions, where the poles and zeros of the kernel correspond to the axial wavenumbers of the rigid walled and lined segments respectively. Since the required wavenumbers have already been evaluated for use in the mode-matching method, no further work was necessary in their calculation. The split functions simply separate the information for the left- and right-running modes, which is necessary in the solution since the boundary conditions are different for each direction.

The second step in the solution involves the decomposition, either by inspection or via a decomposition theorem ([79], p.13), of the generalised Wiener-Hopf equation, firstly by assuming the generalised equation to be an ordinary Wiener-Hopf equation for the liner leading edge discontinuity, and secondly by concentrating on the liner trailing edge discontinuity. Application of the residue theorem to integrals in the decomposition leads to the introduction of correction terms due to the finite length of the liner ([28], p.469). The final step in the solution is the inverse Fourier transform of the original, and now known, transform function. From this all acoustical quantities of interest can be computed.

### 3.6.1 Wiener-Hopf solution for a uniform symmetric liner in the absence of a mean flow

The following analysis for a uniform symmetric liner in the absence of a mean flow with an even incident mode uses the formulation of Koch [28]. In order to calculate the acoustical quantities of interest the transmission and reflection factors, $\hat{T}_{m,2s}/\hat{E}_{m,2r}$ and $\hat{R}_{m,2s}/\hat{E}_{m,2r}$, for each of the $N_c$ cut-on modes are required. These are given by the following equations

$$\frac{\hat{T}_{m,2s}}{\hat{E}_{m,2r}} = \frac{ie^{il^{II}2k_{m,2s}}}{(1+\delta_{s,0})\,\delta_k k_{m,2s}\mathfrak{K}^s_+\left(-\delta_k 2k_{m,2s}\right)}\left[\sum_{n=0}^{N}\frac{Q_{2n}}{\delta_k 2k_{m,2s}-2\alpha_{m,2n}}\frac{C^1_{2n}}{\hat{E}_{m,2r}}\right], \tag{3.49}$$

$$\frac{\hat{R}_{m,2s}}{\hat{E}_{m,2r}} = \frac{i}{(1+\delta_{s,0})\,\delta_k k_{m,2s}\mathfrak{K}^s_-\left(-\delta_k 2k_{m,2s}\right)}\times$$

$$\left[\frac{k_0\left(1/Z^{II}\right)}{\left(k_{m,2r}+\delta_k k_{m,2s}\right)\mathfrak{K}^s_+\left(-2k_{m,2r}\right)}+\sum_{n=0}^{N}\frac{P_{2n}}{\delta_k 2k_{m,2s}+2\alpha_{m,2n}}\frac{C^2_{2n}}{\hat{E}_{m,2r}}\right],$$

$$\delta_k=\begin{cases}1 & \Im\{k\}=0\\ -1 & \Im\{k\}\neq 0\end{cases}, \qquad 1\le r\le N_c+1, \qquad 1\le s\le N_c+1. \tag{3.50}$$

The coefficients $Q_{2n}$ and $P_{2n}$, the correction terms $C^1_{2n}$ and $C^2_{2n}$, and the kernel functions $\mathfrak{K}^s_+$ and $\mathfrak{K}^s_-$ are given in Appendix (B). If it is assumed that the source is not affected by reflections, and the exit duct is anechoically terminated, then the total transmission and reflection

coefficients are given by

$$\tau_{m,2r} = \sum_{s=0}^{N_c} \tau_{m,2r,2s} = \frac{2-\delta_{r,0}}{\delta_{k_x} k_{x_{m,2r}} 2d} \sum_{s=0}^{N_c} \frac{\delta_{k_x} k_{x_{m,2s}} 2d}{2-\delta_{s,0}} \left| \frac{\hat{T}_{m,2s}}{\hat{E}_{m,2r}} \right|^2 , \tag{3.51}$$

$$\varrho_{m,2r} = \sum_{s=0}^{N_c} \varrho_{m,2r,2s} = \frac{2-\delta_{r,0}}{\delta_{k_x} k_{x_{m,2r}} 2d} \sum_{s=0}^{N_c} \frac{\delta_{k_x} k_{x_{m,2s}} 2d}{2-\delta_{s,0}} \left| \frac{\hat{R}_{m,2s}}{\hat{E}_{m,2r}} \right|^2 . \tag{3.52}$$

The sound power transmission loss for the liner is then defined using the total transmission coefficient by

$$\Delta_{\text{PWL}} = 10\log_{10}\left(1/\tau_{m,2r}\right) . \tag{3.53}$$

### 3.6.2 Validation of the mode-matching method against Wiener-Hopf solutions in the absence of a mean flow

The first validation case is given by Koch ([28], p.473) for uniform liners of various depths, where the source is the fundamental mode. The specific impedance of the single-degree-of-freedom acoustic liner is modelled using the following

$$Z = R + i\left[k_0 M_r - \cot(k_0 D)\right] , \tag{3.54}$$

where $R$ is the facing sheet resistance, $M_r$ is the non-dimensional facing sheet mass inertance, and $D$ is the non-dimensional cavity depth. The corresponding sound power transmission loss curves presented in figure (3.3) show that results obtained using the mode-matching method compare very well with those obtained using Koch's Wiener-Hopf solutions.

The modal reflection and transmission coefficients are important parameters to determine whether the wall impedance discontinuity has been adequately modelled in the mode-matching method. The singular derivatives that appear in the solution near to the interface plane at the duct wall are not an intrinsic part of the mode-matching method procedure. Instead, it is expected that the mode-matching solution will converge to the correct value as the number of modes $N$ in the procedure is increased. The above Wiener-Hopf analysis provides an analytic description for the reflection and transmission coefficients, which are compared to the mode-matching solutions in figure (3.4). The solutions from both methods compare very well, demonstrating the adequacy of the mode-matching method when twenty cut-off modes are included in the procedure.

The calculation of the mode eigenvalues represents the majority of the computation time for the mode-matching solution, so it is of interest to see the effect of reducing the number of modes. The reflection coefficients obtained using two, ten and twenty cut-off modes are shown in Figure (3.5). The solutions are very close, even with only two cut-off modes included, and with ten modes the solution is indistinguishable from that using 20 modes. The mode-matching procedure of Sawdy et al. [34] included ten modes in total but, with the extra processing power

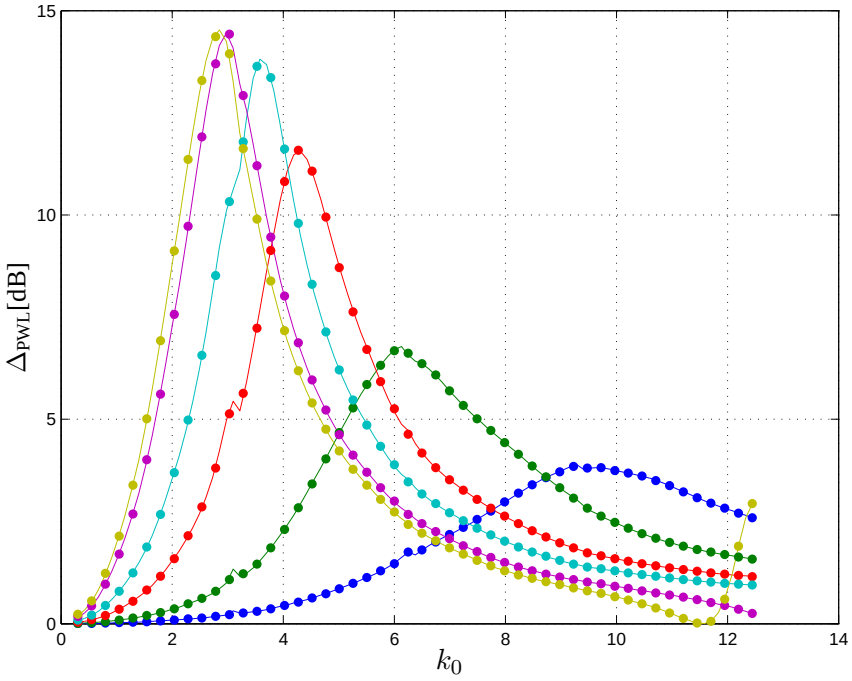


FIGURE 3.3: *Attenuation of the fundamental mode* $(0,1)$ *by uniform symmetric liners of depth* $D$*: Solid line, Wiener-Hopf solution; dots, Mode-matching solution.* —, $D = 0.0272$; —, $D = 0.054$; —, $D = 0.108$; —, $D = 0.162$; —, $D = 0.24$; —, $D = 0.272$. $d = 0.09365$*m*, $l_{II} = 4.34$, $R = 1.4$, $M_r = 0.05475$, $c_0 = 345.09$*ms*$^{-1}$, $\rho_0 = 1.21$*kgm*$^{-3}$.

now available, including all cut-on modes plus twenty cut-off modes appears adequate in terms of processing time and solution accuracy.

The second validation case is for the realistic bypass duct geometry and frequency range of a modern turbofan aeroengine, where the source is the blade passing frequency (BPF) mode (24,0). The annular bypass duct is approximated using a rectangular duct [28, 10] by imposing a periodicity condition at the side walls. Very good agreement was achieved between the Wiener-Hopf and mode-matching solutions for the sound power transmission loss, presented in Figure (3.6) against the Helmholtz number, where the (24,1) mode does not propagate below $k_0 = 6$. Agreement between the solutions is also very good for the transmission and reflection coefficients, shown in Figure (3.7), which displays results for the first four modes only, although the agreement is equally good over all the higher order cut-on modes.

## 3.7 Comparison of mode-matching methods with Finite Element solutions

This section provides a comparison of the pressure-particle velocity (PU) and mass-momentum (MM) mode-matching methods, with Finite Element (FE) solutions for two dimensional rectangular ducts with and without a uniform mean flow. Solutions for uniform and

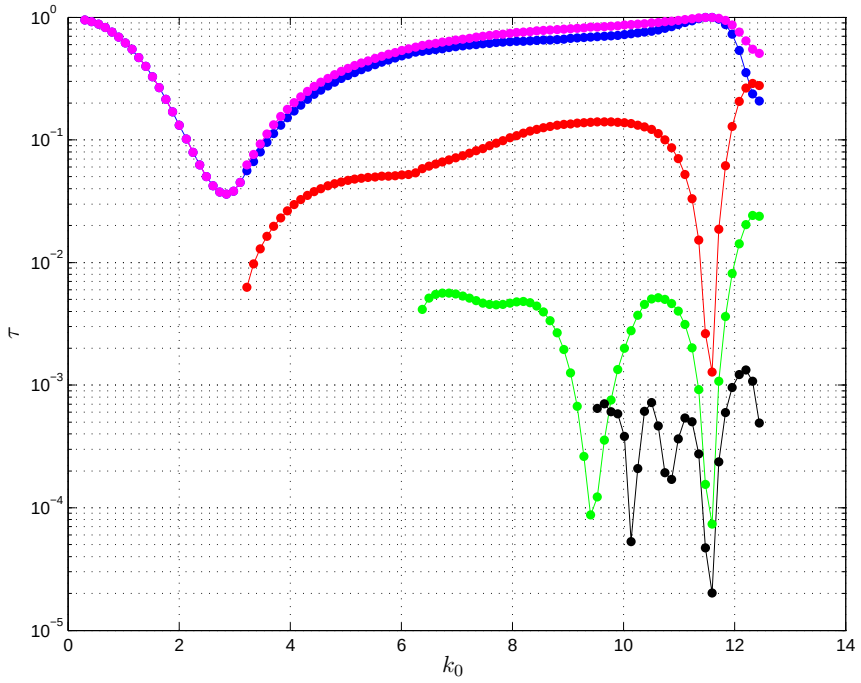


(a) Total $\tau_{m,2r}$ and modal $\tau_{m,2r,2s}$ transmission coefficients.

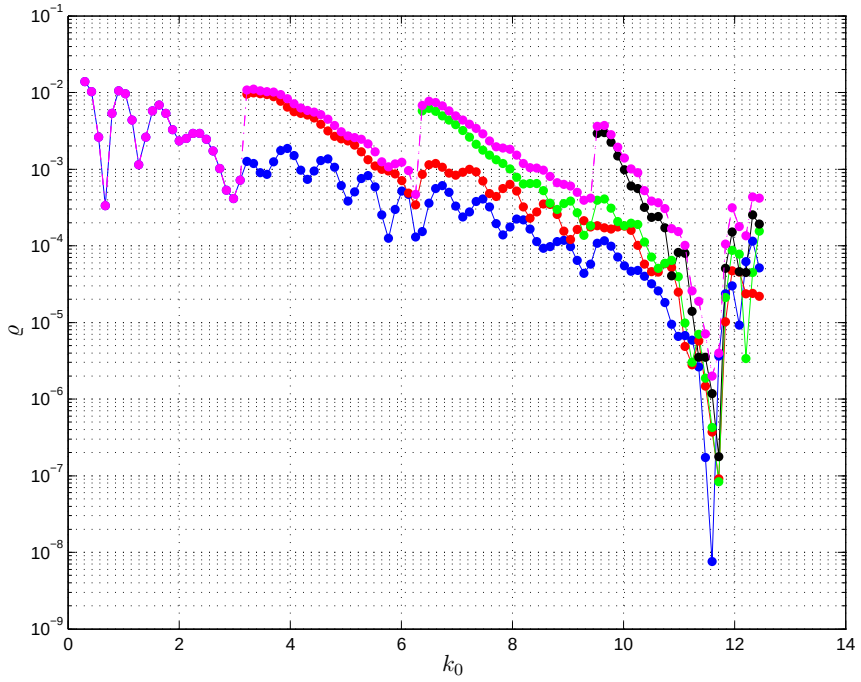


(b) Total $\varrho_{m,2r}$ and modal $\varrho_{m,2r,2s}$ reflection coefficients.

FIGURE 3.4: *Transmission and reflection coefficients for a uniform symmetric liner in the absence of a mean flow. Solid line, Wiener-Hopf solution; dots, Mode-matching solution. — , mode (0,1); —, mode (0,3); —, mode (0,5); —, mode (0,7); — ·, total.* $d = 0.09365$*m*, $l_{II} = 4.34$,$D = 0.272$, $R = 1.4$, $M_r = 0.05475$, $c_0 = 345.09$*ms*$^{-1}$, $\rho_0 = 1.21$*kgm*$^{-3}$.

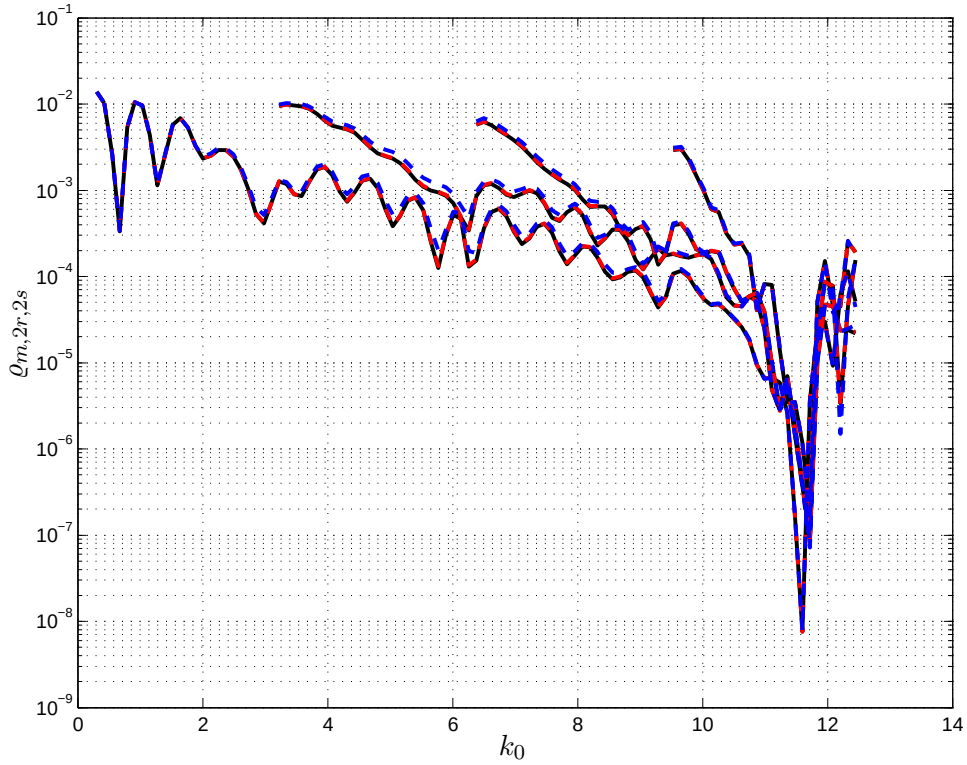


FIGURE 3.5: *Effect of truncation on reflection coefficients for a uniform symmetric liner in the absence of a mean flow. Problem parameters as Figure (3.4): (—), 20 cut-off modes; - -, 10 cut-off modes; - -, 2 cut-off modes.*

two-segment, symmetric and asymmetric liners are compared at a single frequency of $k_0 = 6.67$. Six test cases are compared here, the details of each are listed in tables (3.1) and (3.2). The geometry and impedances are chosen to be realistic of a modern high bypass ratio turbofan engine at approach for a frequency at twice the Blade Passing Frequency (BPF). The incident mode at the plane $x = 0$ in each test case is a right-running plane wave mode, $n = 1$, of unit intensity. The commercial finite element solver ACTRAN TM/2006 is used to generate solutions of the convected wave equation on a uniform, structured grid consisting of 8-noded quadrangular elements (quadratic interpolation order) [80]. Two over-specified meshes are used, for the single and two segment cases respectively, each having 58 radial and 284 axial elements.

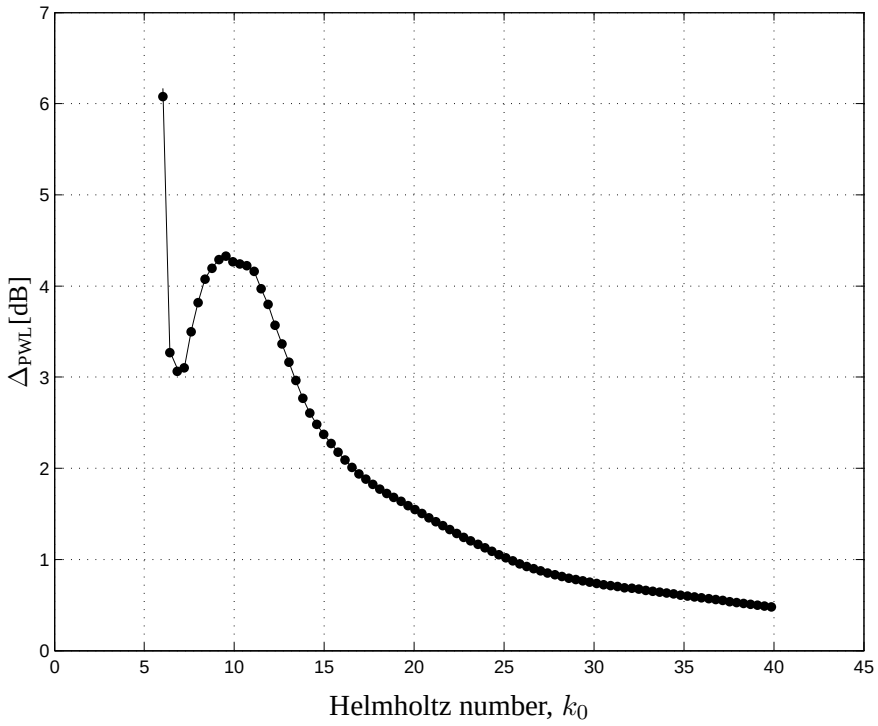


FIGURE 3.6: *Attenuation of the BPF mode* $(24, 1)$ *by a uniform symmetric liner for realistic aeroengine parameters: Solid line, Wiener-Hopf solution; dots, Mode-matching solution.* $d = 0.3\ m$, $\hbar = 0.6$, $l_{II} = 5$, $R = 3$, $M_r = 0.05475$, $D = 0.0167$, $M = 0$.

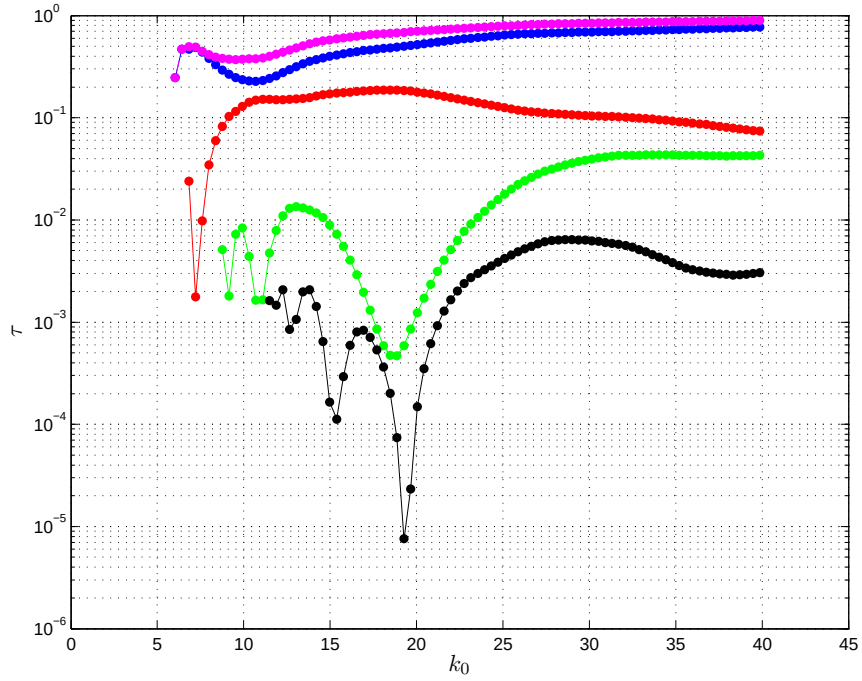


(a) Total $\tau_{m,2r}$ and modal $\tau_{m,2r,2s}$ transmission coefficients.

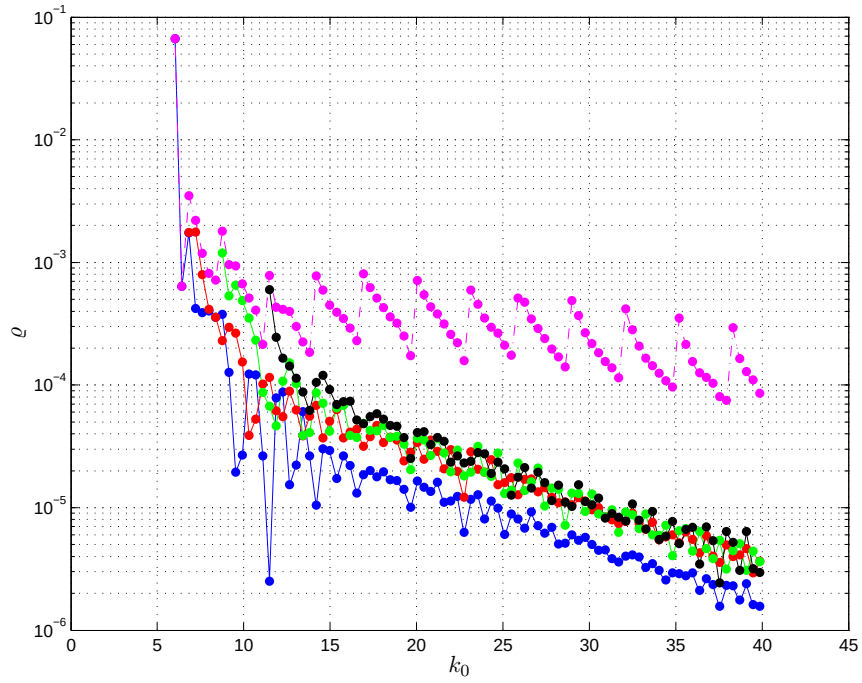


(b) Total $\varrho_{m,2r}$ and modal $\varrho_{m,2r,2s}$ reflection coefficients.

FIGURE 3.7: *Transmission and reflection coefficients of the first four cut-on modes for a uniform symmetric liner in the absence of a mean flow with a periodicity condition applied at the side walls. Solid line, Wiener-Hopf solution; dots, Mode-matching solution. —, mode (24,1); —, mode (24,3); —, mode (24,5); —, mode (24,7); — ·, total.* $d = 0.3\ m$, $\hbar = 0.6$, $L_{II} = 5$, $D = 0.0167$, $R = 3$, $M_r = 0.05475$, $c_0 = 345.09\ ms^{-1}$, $\rho_0 = 1.21\ kgm^{-3}$.

TABLE 3.1: *General conditions for 2D test cases.*

| | | |
|---|---|---|
| Helmholtz number | $k_0$ | $6.6689$ |
| Duct half height | $d$ [m] | $0.3175$ |
| Total duct length | $l_{duct}$ | $10.9606$ |
| Speed of sound | $c_0[ms^{-2}]$ | $347$ |
| Density of air | $\rho_0[kgm^{-3}]$ | $1.317$ |
| Impedance A | $Z_A$ | $1 - 9.934i$ |
| Impedance B | $Z_B$ | $1.5 - 1.255i$ |
| Impedance C | $Z_C$ | $1.05 - 0.978i$ |
| Impedance D | $Z_D$ | $1.57 - 1.314i$ |
| Leading rigid duct | $l_I$ | $0.315$ |
| Trailing rigid duct | $l_{end}$ | $0.315$ |

TABLE 3.2: *Configurations for 2D test cases.*

| | Case 1 | Case 2 | Case 3 | Case 4 | Case 5 | Case 6 |
|---|---|---|---|---|---|---|
| $M$ | $0$ | $0$ | $0$ | $0.278$ | $0.278$ | $0.278$ |
| $Z_d^I$ | $Z_A$ | $Z_A$ | $Z_B$ | $Z_C$ | $Z_C$ | $Z_D$ |
| $Z_{-d}^I$ | $Z_A$ | $Z_B$ | $Z_A$ | $Z_C$ | $Z_D$ | $Z_C$ |
| $Z_d^{II}$ | | | $Z_A$ | | | $Z_C$ |
| $Z_{-d}^{II}$ | | | $Z_B$ | | | $Z_D$ |
| $l^{II}$ | $10.3045$ | $10.3045$ | $2.0069$ | $10.3045$ | $10.3045$ | $2.0069$ |
| $l^{III}$ | | | $8.2977$ | | | $8.2977$ |

### 3.7.1 No flow test cases

In the absence of flow the PU and MM mode-matching methods are equivalent. Test *Case 1* is a single symmetric liner. Bottom and top wall pressures from the FE and mode-matching solutions are plotted in figure (3.8) and demonstrate excellent agreement. The radial pressure profiles at the matching planes $x = x^I, x^{II}$ are plotted in figure (3.9), where the mode-matching solution constructed from the mode eigenfunctions of each adjoining duct section are plotted for comparison with the FE solution. The comparison is excellent except for very slight deviations at the walls. The reflected and transmitted modal intensities are plotted in figure (3.10) and show excellent agreement. Only the even modes $n = 1, 3...$ are excited, since the problem is symmetric. Scattering of energy from the plane wave into higher order radial modes occurs, with large reflected energy levels in modes near cut-off.

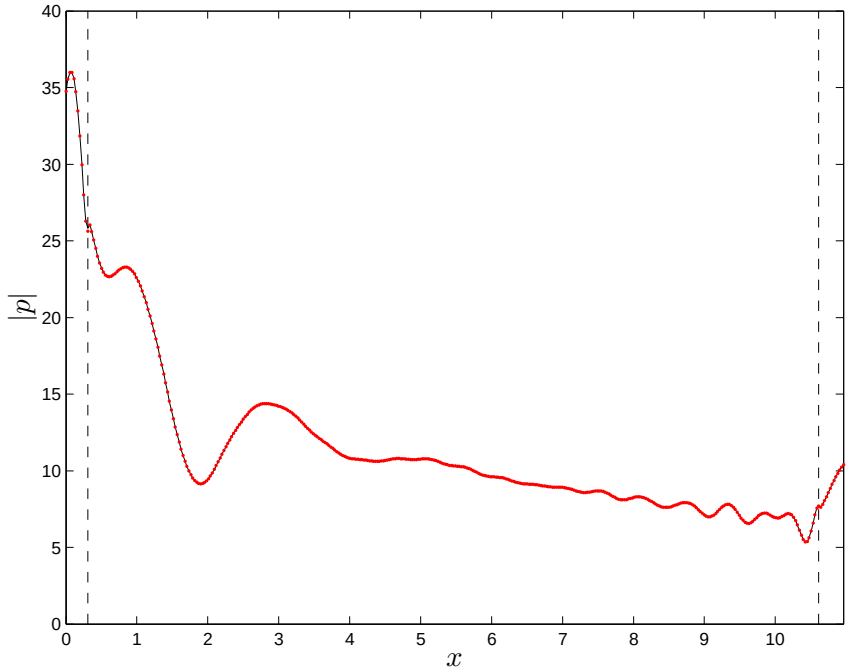


(a) Top wall pressure

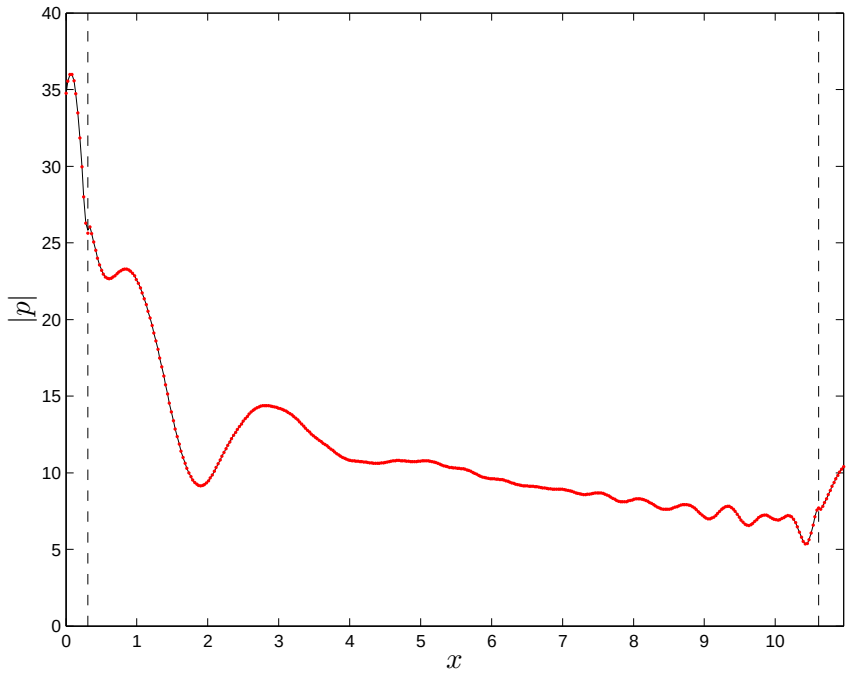


(b) Bottom wall pressure

FIGURE 3.8: *Case 1: Comparison of 2D mode matching and finite solutions for a single symmetric liner without flow. Liner interface matching planes indicated by dashed lines. Solid line, finite element solution;* •*,* $p$*-*$u$ *mode matching solution.*

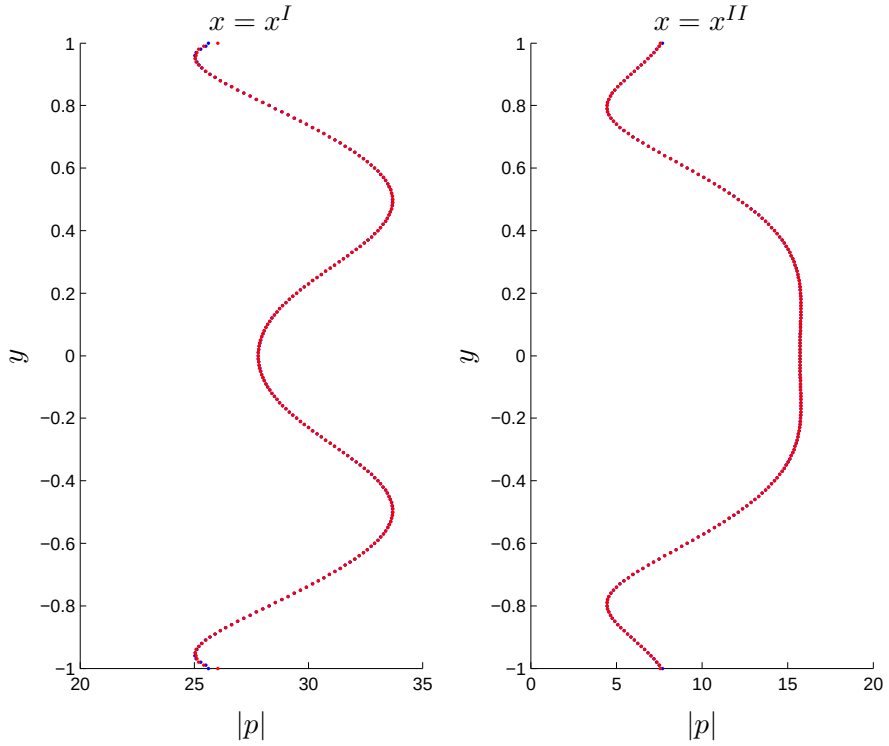


FIGURE 3.9: *Case 1: Comparison of mode matching and finite element radial pressure solutions at liner interface matching planes. Solid line, finite element solution; ●, mode matching solution (lefthand segment modes); ●, mode matching solution (righthand segment modes).*

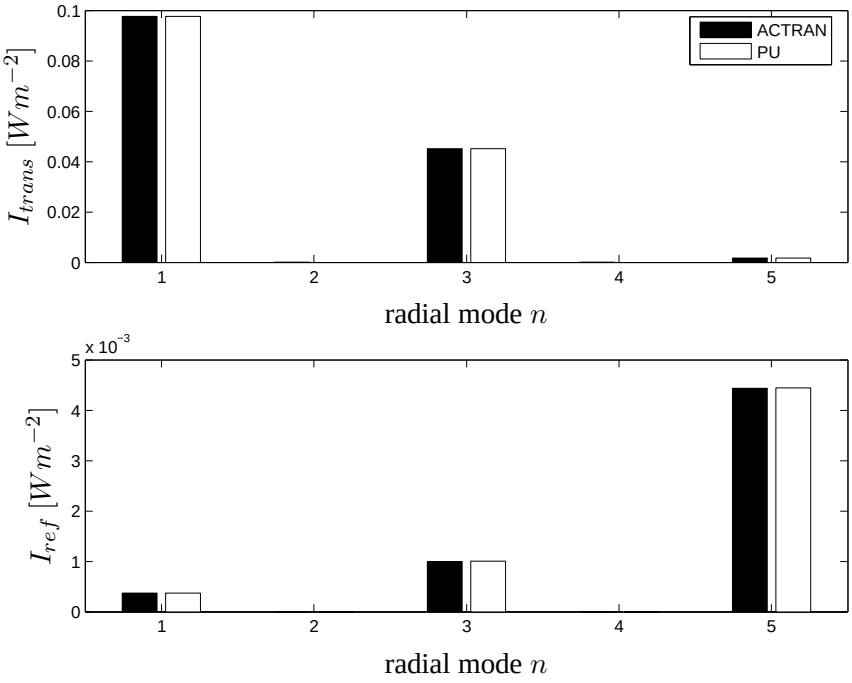


FIGURE 3.10: *Case 1: Comparison of scattered modal intensities from mode matching and finite element methods due to an incident plane wave of unit intensity. Top plot, Transmitted modal intensity; Bottom plot, Reflected modal intensity.*

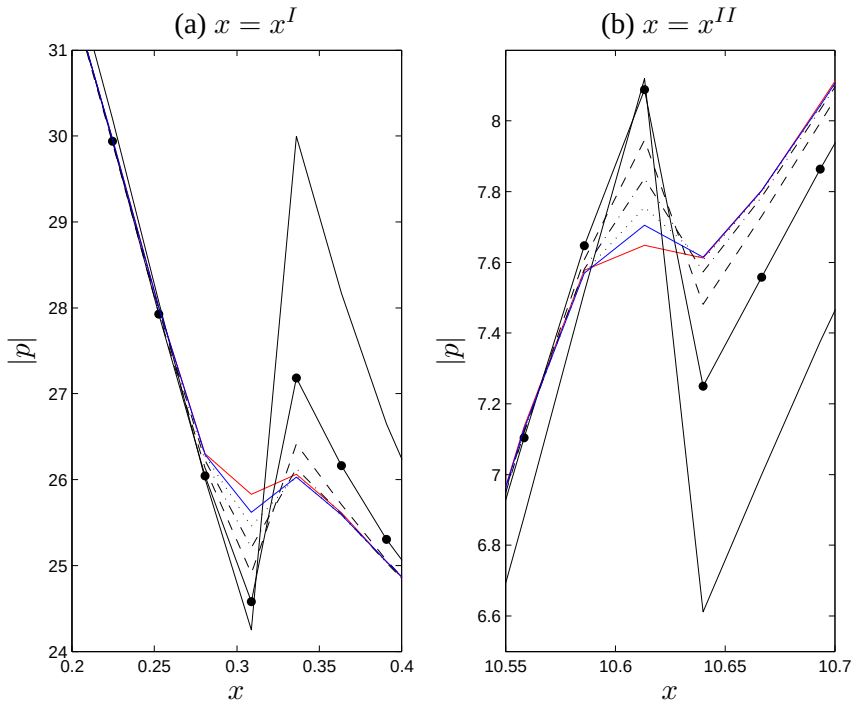


FIGURE 3.11: *Case 1: Mode matching solution convergence study. Interface matching plane casing wall pressure. (—) , $N/N_c = 1$; (-•-), $N/N_c = 2$; (- -) , $N/N_c = 3$; (— ·), $N/N_c = 5$; (· · ·), $N/N_c = 9$; (—), $N/N_c = 17$; (—), finite element solution.*

The convergence of the mode-matching method to the FE solution is checked by increasing the number of modes $N$ included in the matching process. The convergence of the casing wall pressure at the liner interface matching planes $x = x^I, x^{II}$ is presented in figure (3.11), and it is seen to converge to the FE solution as $N$ is increased. The ratio $N/N_c$ is used to compare solutions, where $N_c$ is the number of *cut-on* modes. The convergence of the radial pressure profile at the first matching plane $x = x^I$ is presented in figure (3.12). The radial pressure is constructed from both the rigid and lined duct modes, and it is seen that fair number of higher order modes must be used order to adequately reconstruct the radial pressure, especially when using lined duct modes. Finally, the error in the transmitted and reflected total intensities $I = \sum_{n=1}^{N_c} I_n$ compared with the FE solution is compared in figure (3.13), where the measure of error is calculated from

$$\text{Error} = |(I_{PU} - I_{FE}/I_{FE})| \,. \tag{3.55}$$

The error in the transmitted intensity is around 2 orders of magnitude lower than for the reflected intensity.

For *Case 2* the wall pressure solutions for a single asymmetric liner without flow are presented in appendix figure (C.1), with the corresponding scattered modal intensities shown in appendix figure (C.2), and all show excellent agreement. Energy is seen to scatter into all mode orders, since the problem is now asymmetric.

The final no flow comparison, *Case 3*, is for a two segment, asymmetric liner. The wall pressure plots in figure (3.14) show good agreement, except for the region around the second

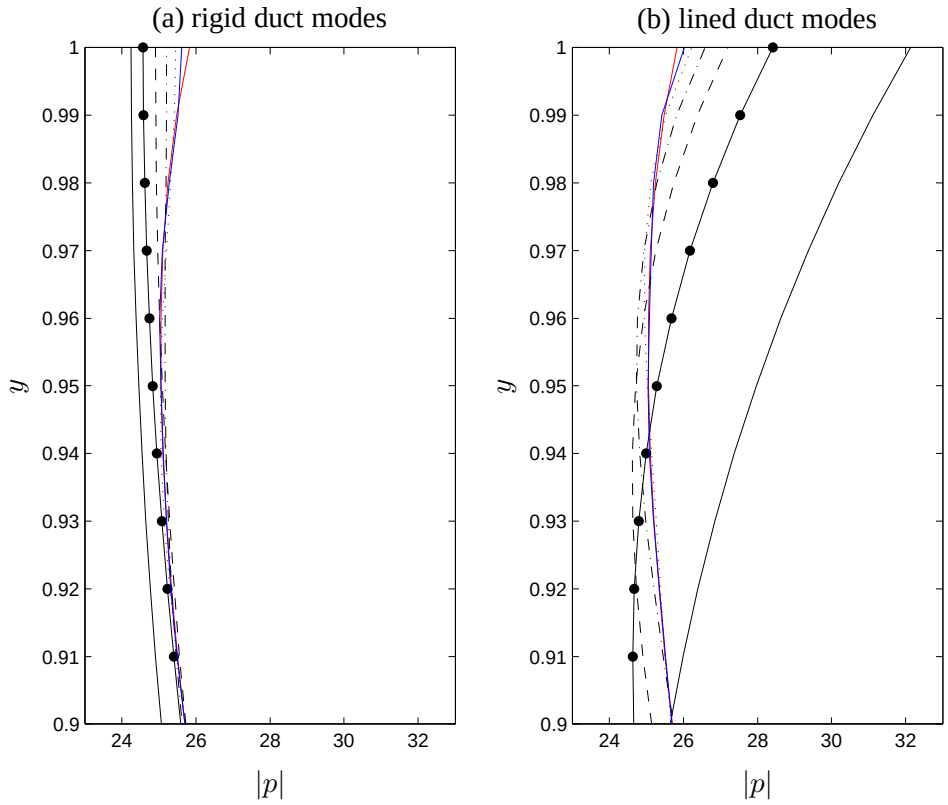


FIGURE 3.12: *Case 1: Mode matching solution convergence study. Interface matching plane* $x = x^I$ *radial pressure near the casing wall. (—),* $N/N_c = 1$*; (-•-),* $N/N_c = 2$*; (- -),* $N/N_c = 3$*; (— ·),* $N/N_c = 5$*; (· · ·),* $N/N_c = 9$*; (—),* $N/N_c = 17$*; (—), finite element solution.*

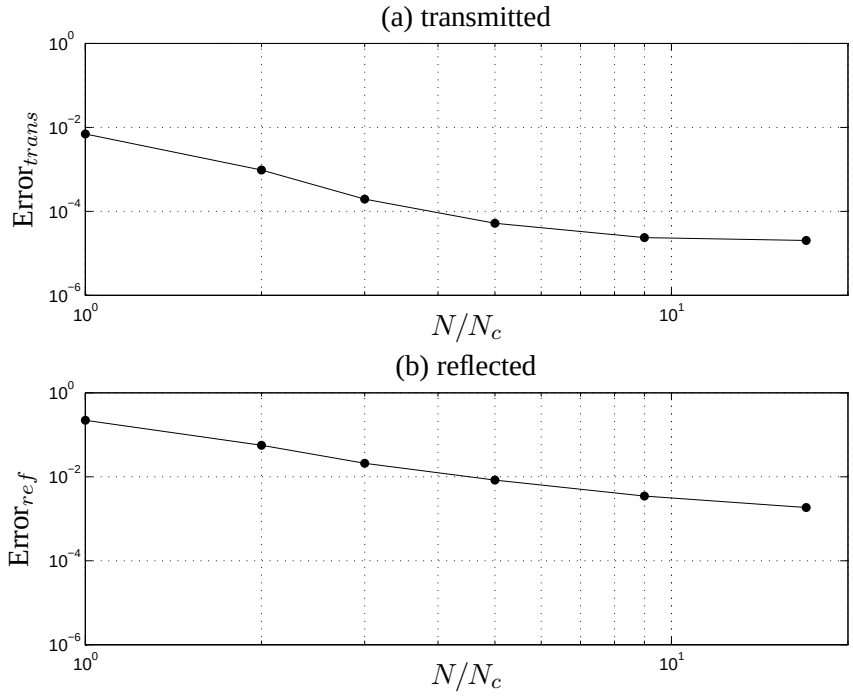


FIGURE 3.13: *Case 1: Mode matching solution convergence study. Scattered total intensity error re FE solution, Error* $= |(I_{PU} - I_{FE})/I_{FE}|$.

liner interface matching plane at $x = x^{II}$. The radial pressure profiles shown in figure (3.15) indicate that the pressure matching at $x = x^{II}$ is not as good as at the liner leading and trailing edges. A comparison of the scattered intensities plotted in figure (3.16) reveals differences of the order of 1 percent, or a difference in the sound power transmission loss of around 0.05dB.

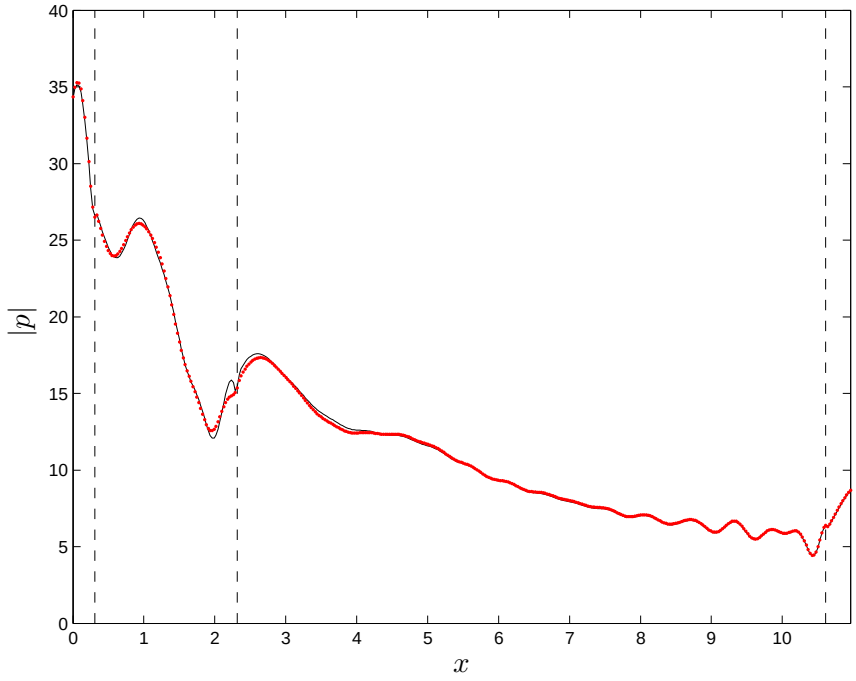


(a) Top wall pressure

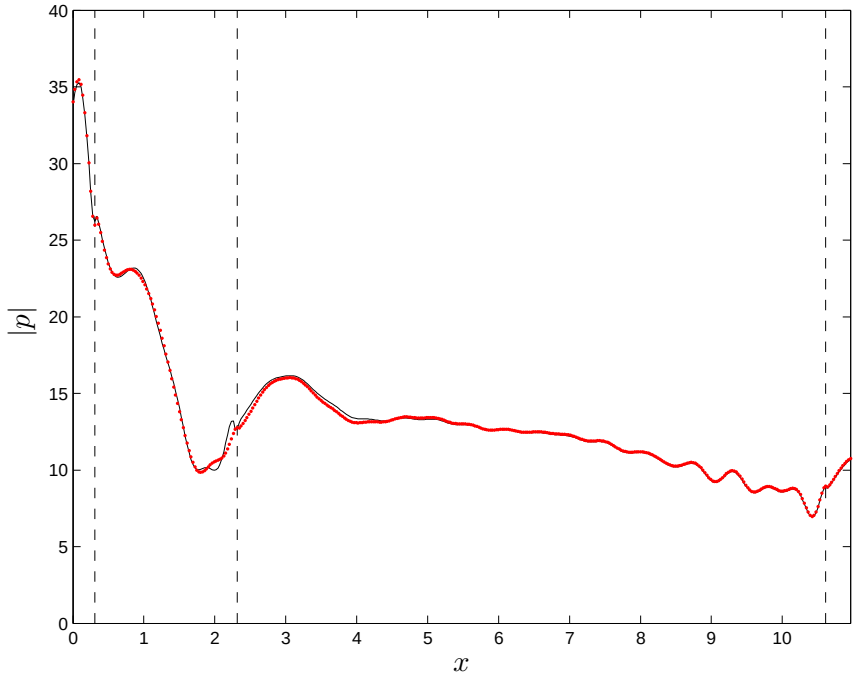


(b) Bottom wall pressure

FIGURE 3.14: *Case 3: Comparison of 2D mode matching and finite solutions for a two segment, asymmetric liner without flow. Liner interface matching planes indicated by dashed lines. Solid line, finite element solution;* •*, $p$-$u$ mode matching solution.*

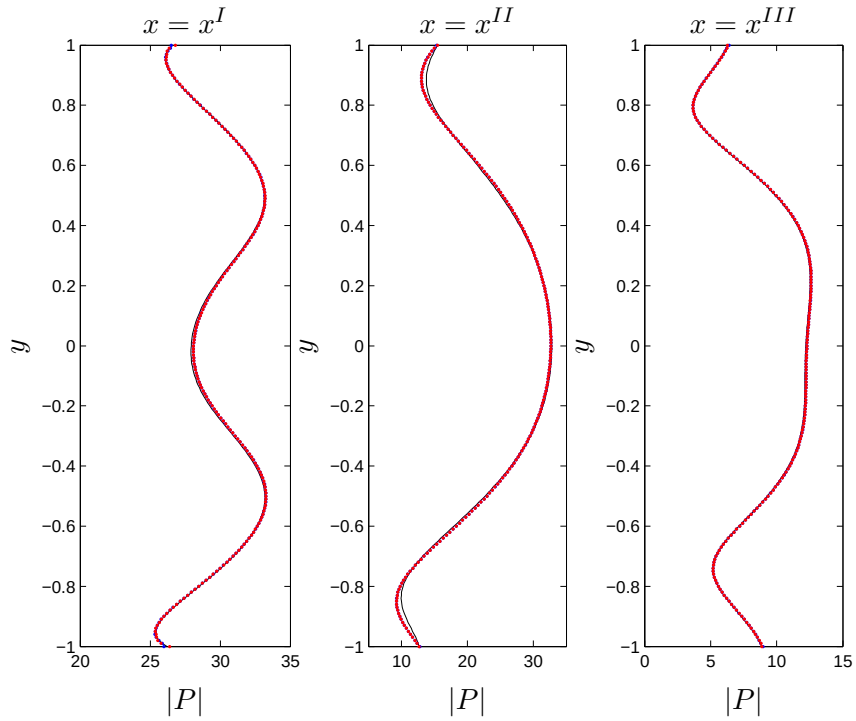


FIGURE 3.15: *Case 3: Comparison of mode matching and finite element radial pressure solutions at liner interface matching planes. Solid line, finite element solution; •, mode matching solution (lefthand segment modes); •, mode matching solution (righthand segment modes).*

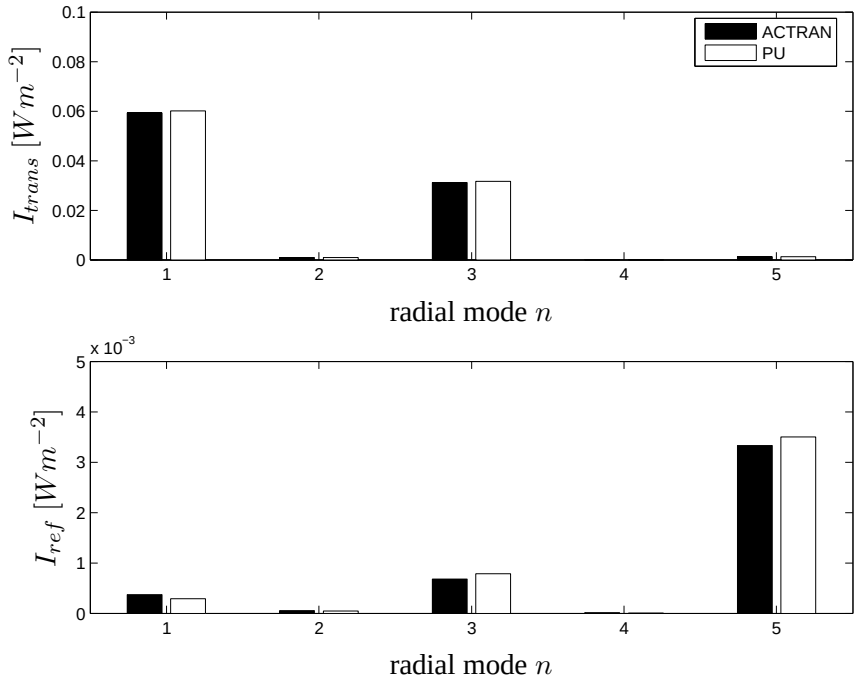


FIGURE 3.16: *Case 3: Comparison of scattered modal intensities from mode matching and finite element methods due to an incident plane wave of unit intensity. Top plot, Transmitted modal intensity; Bottom plot, Reflected modal intensity.*

### 3.7.2 Uniform flow test cases

In the presence of a uniform mean flow the mass-momentum formulation provides an alternative to the usual pressure-velocity mode-matching method. Therefore, in the test cases presented here both mode-matching solutions are compared against FE solutions. The mean flow speed is chosen to be at a realistic approach condition of $M = 0.278$. Three test cases of identical geometry to the no flow cases are presented here, with test case details provided in table (3.2).

Test *Case 4* is a single symmetric liner and the computed wall pressures are presented in figure (3.17). The finite element model predicts pressure singularities at the liner interface planes, which are poorly predicted by the PU matching, but very well predicted by the MM matching method. The computed radial pressure profiles at the matching planes are compared in figure (3.18). It is seen that the PU matching solution compares fairly well with the FE solution across most of the duct section, but the steeper pressure gradients near the walls are not captured so well. In contrast, the MM matching solution compares very well with the FE solution. High order oscillations are seen in the radial pressure profiles, which correspond to the very high order modes included in the matching. If the wall line integral terms are removed from the calculation, the result (dashed line in figure (3.18)) is identical to that of the PU matching. This indicates that the line integrals are essential to accurately determine the acoustic field. In figure (3.19), the oscillations seen in the radial pressure profiles, decay rapidly away from the liner interface planes, since the high order modes have large decay rates. This occurs in the region of the pressure singularity, indicating that high order modes are required to resolve the singularity. The scattered modal intensities are compared in figure (3.20), and show that the MM method provides a much better comparison with the FE solution than the PU method.

The convergence of the PU method against the FE solution is now checked by increasing the number of modes $N$ in the matching procedure. Convergence of the casing wall pressure at the matching planes is plotted in figure (3.21) and shows that even with many cut-off modes included, the PU method struggles to accurately predict the pressure singularity. This is confirmed in figure (3.22), by plotting the radial pressure near the casing at the first matching plane $x = x^I$ using either rigid or lined duct modes. The same convergence study was carried out for the MM method and plots of the casing wall pressure in figure (3.23) demonstrate that the pressure singularity is well resolved. However, convergence plots of the radial pressure near the casing in figure (3.24) demonstrate how the inclusion higher order modes, although helping to resolve the wall singularity, induce oscillations to the field across the matching planes. The difference in the scattered intensities computed via the mode matching methods to the FE solution are given in figure (3.25) with the MM method at least an order of magnitude closer than the PU method. From this convergence study the recommended maximum number of modes to include in the mode matching procedure is $N/N_c = 10$, so that radial matching plane oscillations are minimised, and the wall pressure singularities are at least well resolved. It should be noted that the differences in intensity are rather small, so the effects upon a sound

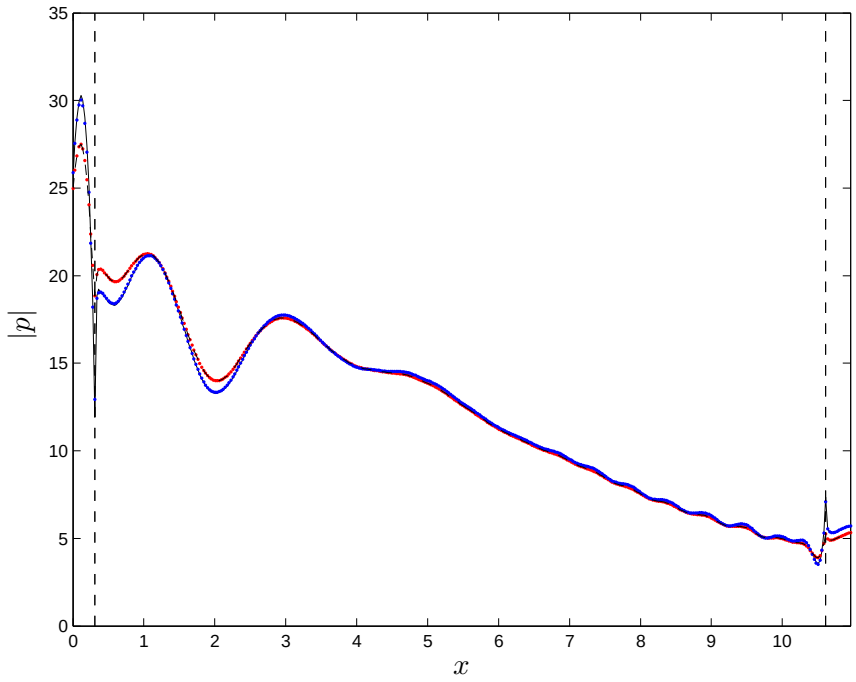


(a) Top wall pressure

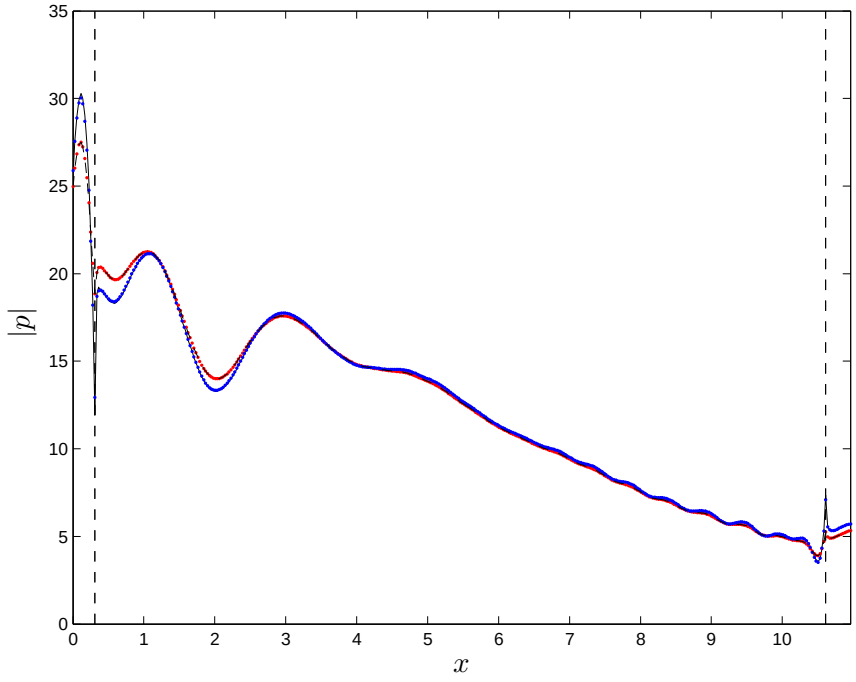


(b) Bottom wall pressure

FIGURE 3.17: *Case 4: Comparison of 2D mode matching and finite solutions for a single symmetric liner with flow. Liner interface matching planes indicated by dashed lines. Solid line, finite element solution;* ●*, $p$-$u$ mode matching solution;* ●*, mass-momentum mode matching solution; Dashed line, mass-momentum mode matching solution without wall line integrals.*

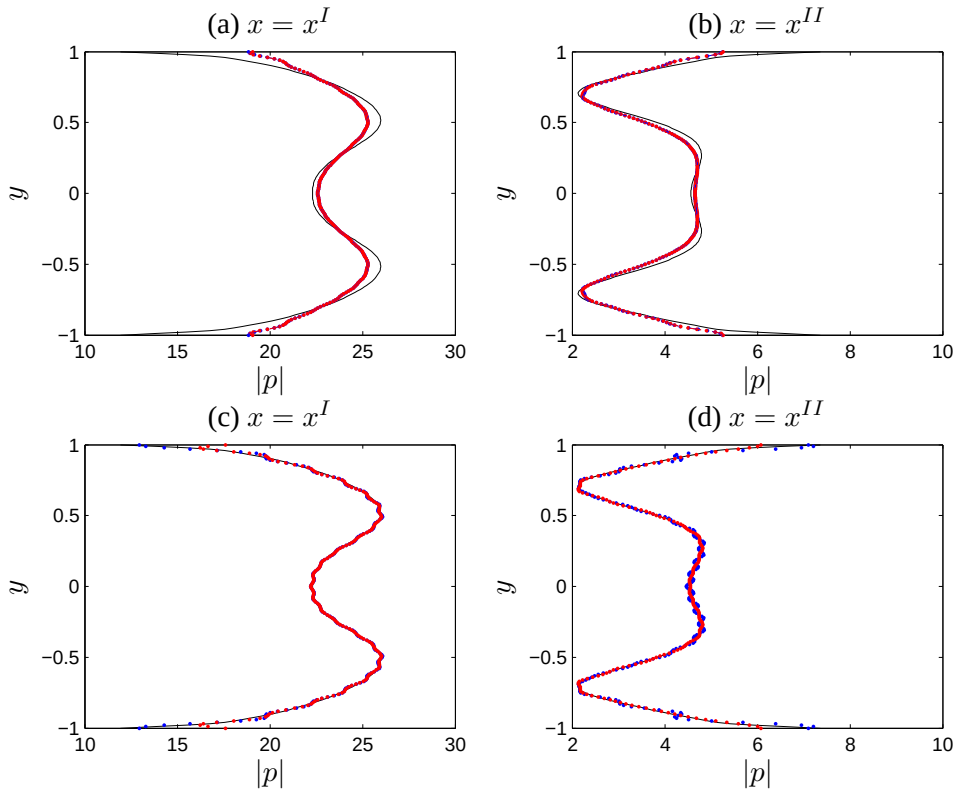


FIGURE 3.18: *Case 4: Comparison of mode matching and finite element radial pressure solutions at liner interface matching planes. (a,b), $p$-$u$ matching; (c,d), mass-momentum matching ; Solid line, finite element solution;* •*, mode matching solution (lefthand segment modes);* •*, mode matching solution (righthand segment modes).*

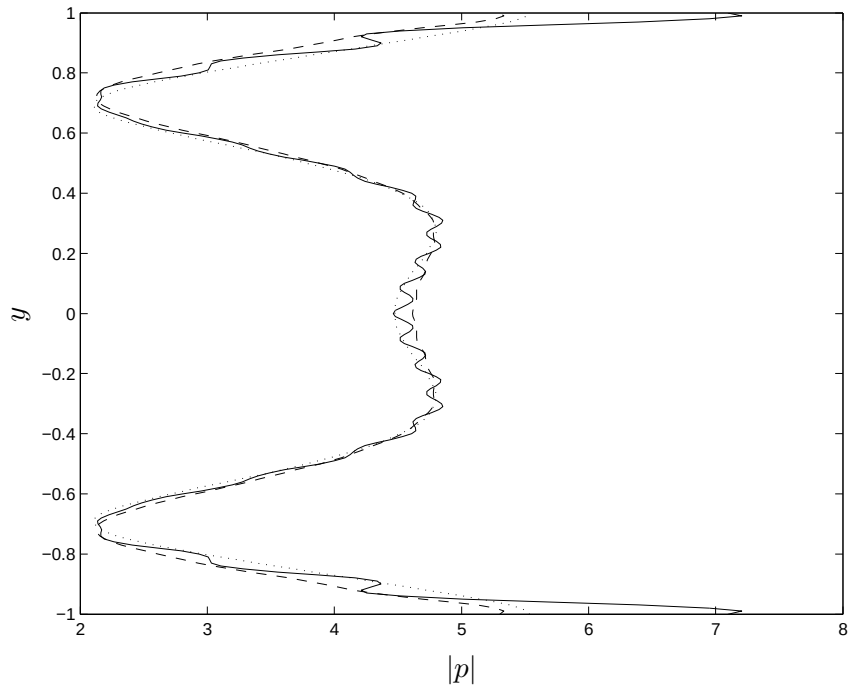


FIGURE 3.19: *Case 4: Mass-momentum matching solution for radial pressure around $x = x^{II}$. —, $x = x^{II} = 10.6133$; −−, $x = x^{II}_{-\epsilon} = 10.5859$; · · ·, $x = x^{II}_{+\epsilon} = 10.6400$.*

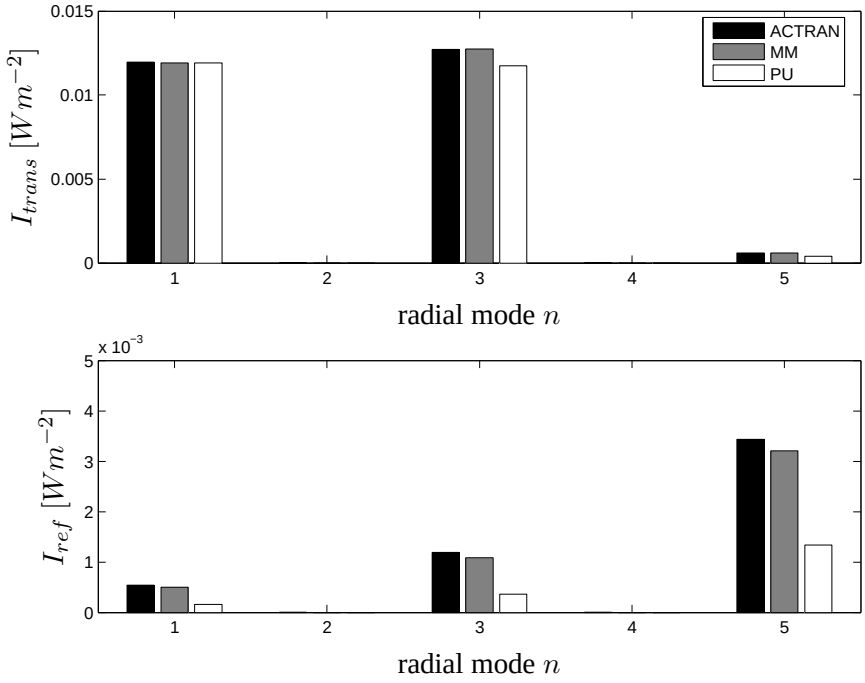


FIGURE 3.20: *Case 4: Comparison of scattered modal intensities from mode matching and finite element methods due to an incident plane wave of unit intensity. Top plot, Transmitted modal intensity; Bottom plot, Reflected modal intensity.*

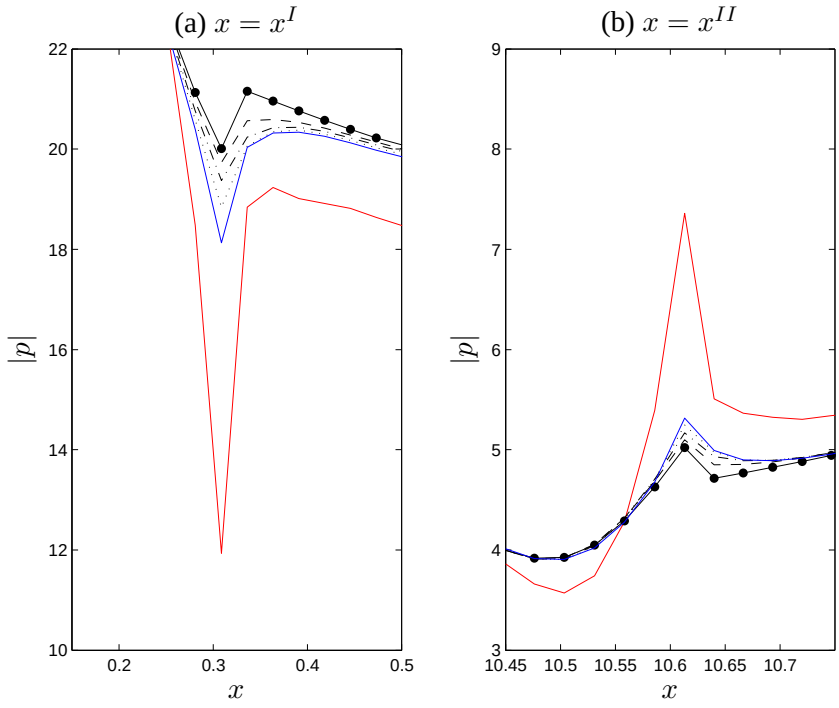


FIGURE 3.21: *Case 4: Pressure-velocity mode matching solution convergence study. Interface matching plane casing wall pressure. (-•-) ; $N/N_c = 2$, (- -) ; $N/N_c = 3$, (— ·) ; $N/N_c = 5$, (· · ·) ; $N/N_c = 9$, (—); $N/N_c = 17$, (—); finite element solution.*

power transmission loss calculation are insignificant. Therefore, for practical purposes, fewer modes may be utilised to reduce the computation time.

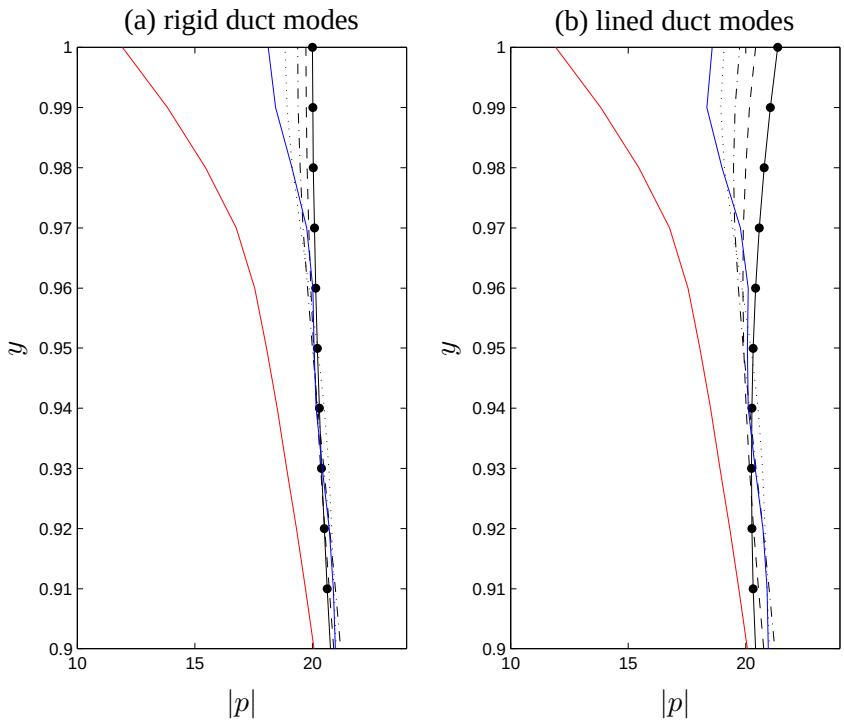


FIGURE 3.22: *Case 4: Pressure-velocity mode matching solution convergence study. Interface matching plane $x = x^I$ radial pressure near the casing wall. (-•-), $N/N_c = 2$; (- -), $N/N_c = 3$; (— ·), $N/N_c = 5$; (· · ·), $N/N_c = 9$; (—), $N/N_c = 17$; (—), finite element solution.*

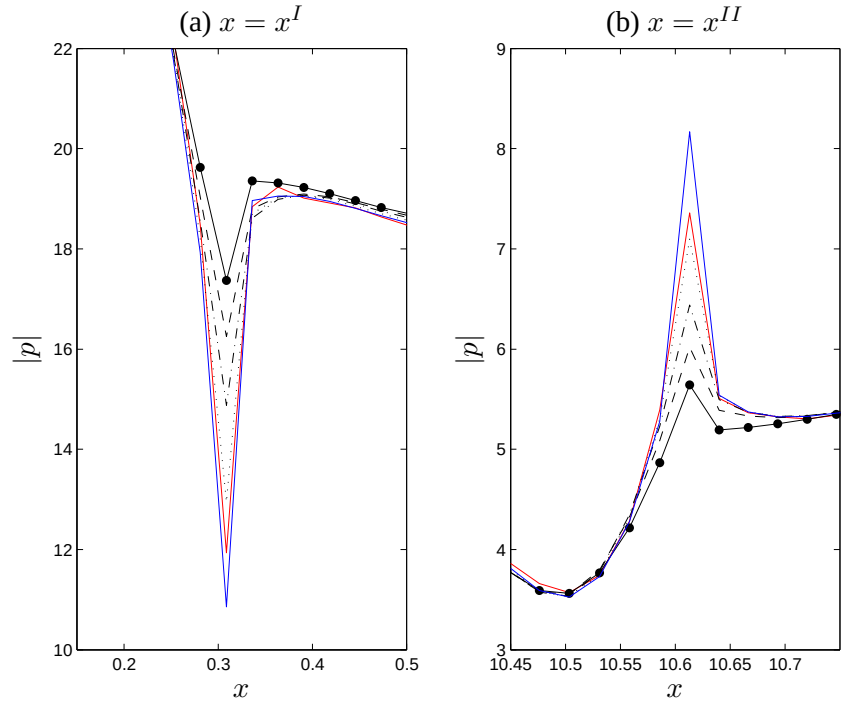


FIGURE 3.23: *Case 4: Mass-momentum mode matching solution convergence study. Interface matching plane casing wall pressure. (-•-), $N/N_c = 2$; (- -), $N/N_c = 3$; (— ·), $N/N_c = 5$; (· · ·), $N/N_c = 9$; (—), $N/N_c = 17$; (—), finite element solution.*

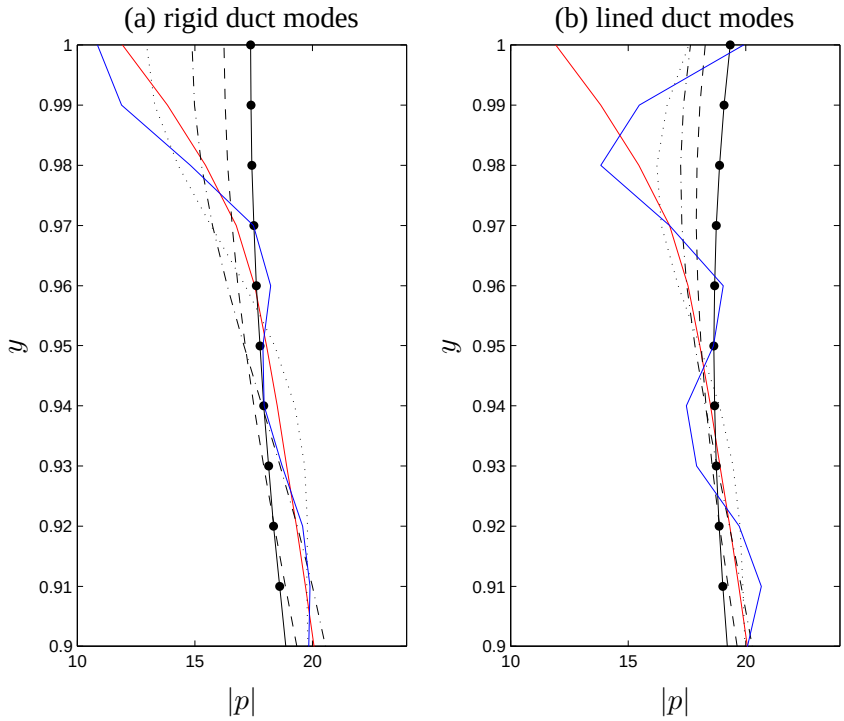


FIGURE 3.24: *Case 4: Mass-momentum mode matching solution convergence study. Interface matching plane $x = x^I$ radial pressure near the casing wall. (-•-), $N/N_c = 2$; (- -), $N/N_c = 3$; (— ·), $N/N_c = 5$; (· · ·), $N/N_c = 9$; (—), $N/N_c = 17$; (—), finite element solution.*

Wall pressure plots and matching plane radial pressure profiles for the single asymmetric liner of test *Case 5* are shown in appendix figures (C.3) and (C.4). Again, the MM matching proves to be superior to the PU matching compared with the FE solution, which is also seen in the predictions of scattered intensities shown in appendix figure (C.5).

A final comparison against the FE solution is made for the two segment, asymmetric liner with uniform flow (test *Case 6*). The wall pressure solutions are presented in figure (3.26) and show that the MM matching compares much better with the FE solution than the PU matching, especially at the matching planes. A comparison of the radial matching plane pressures in figure (3.27) confirms this. It is noted that the comparison at the second matching plane $x = x^{II}$, between the two lined sections, appears at first to be rather poorer than at the leading and trailing matching planes, between rigid and lined sections. However, it is found that the finite element solver struggles to provide an adequately converged solution, even on the currently over-specified mesh (58 by 284 quad elements). A refined mesh of 116 by 568 quad elements (equating to 55 radial and 49 axial elements per wavelength) was used to resolve the problem. The pressure and velocity potential $\phi$ solutions at the second matching plane $x = x^{II}$ compared with the mode matching solutions are shown in figures (3.28) and (3.27). It is seen that by refining the mesh the FE solution converges towards the MM mode matching solution. The velocity potential is plotted here since the FE method solves the governing equations in terms of velocity potential, thus the pressure solution is generated in post-processing involving the use of numerical gradients, which may introduce error in the pressure field. The velocity potential is calculated for the mode-matching solutions by assuming modal solutions in

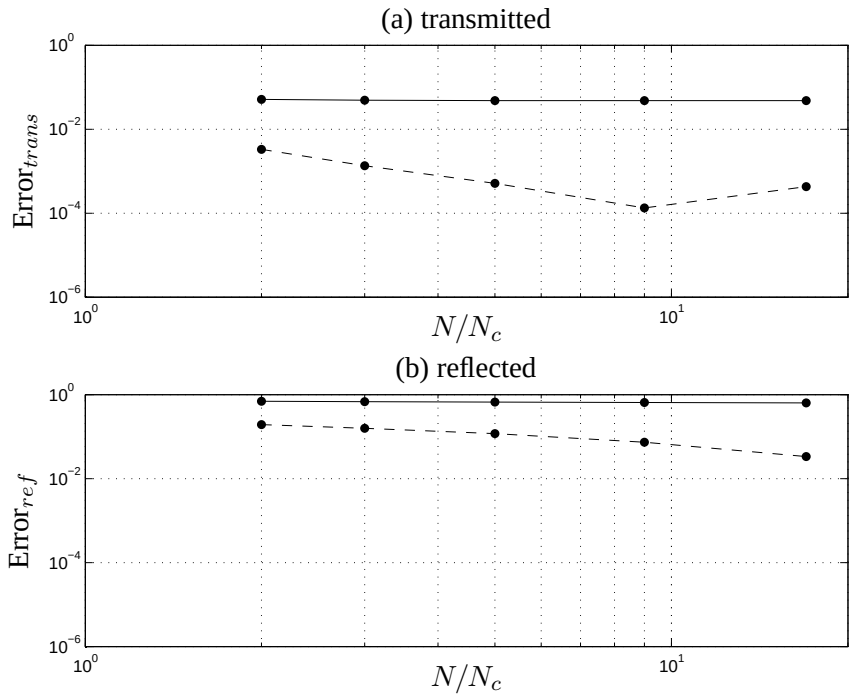


FIGURE 3.25: *Case 4: Mode matching solution convergence study. Scattered total intensity error re FE solution, Error* $= |(I_{PU} - I_{FE})/I_{FE}|$*. Solid line, p-u matching; Dashed line, mass-momentum matching.*

velocity potential form which are related to the pressure mode eigenfunction by

$$\Psi_n = -\rho_0 \frac{D\phi_n}{Dt} \ . \tag{3.56}$$

The scattered modal intensities for the case are shown in figure (3.30), and show that the refined FE and MM matching solutions produce the most favourable comparison.

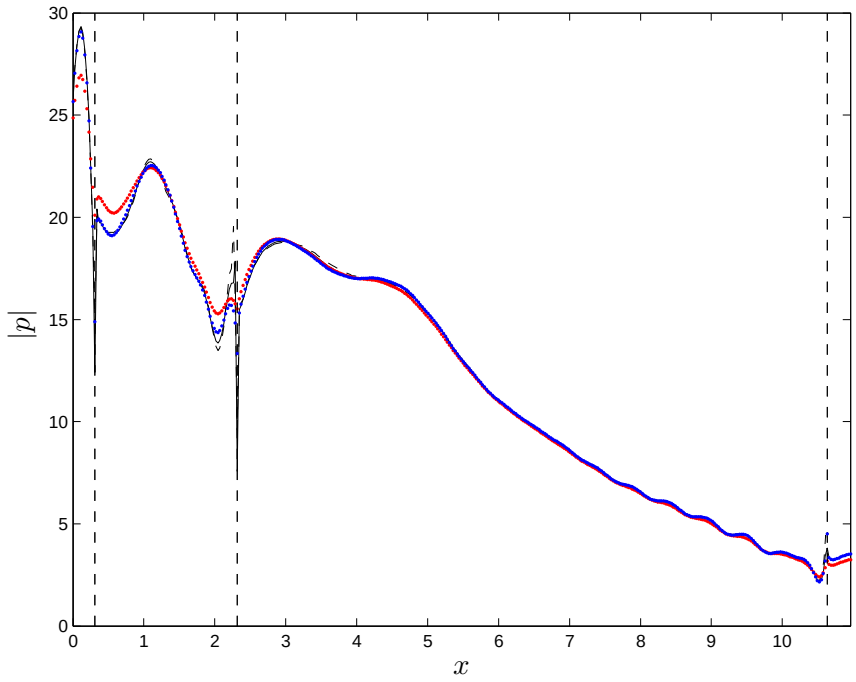


(a) Top wall pressure

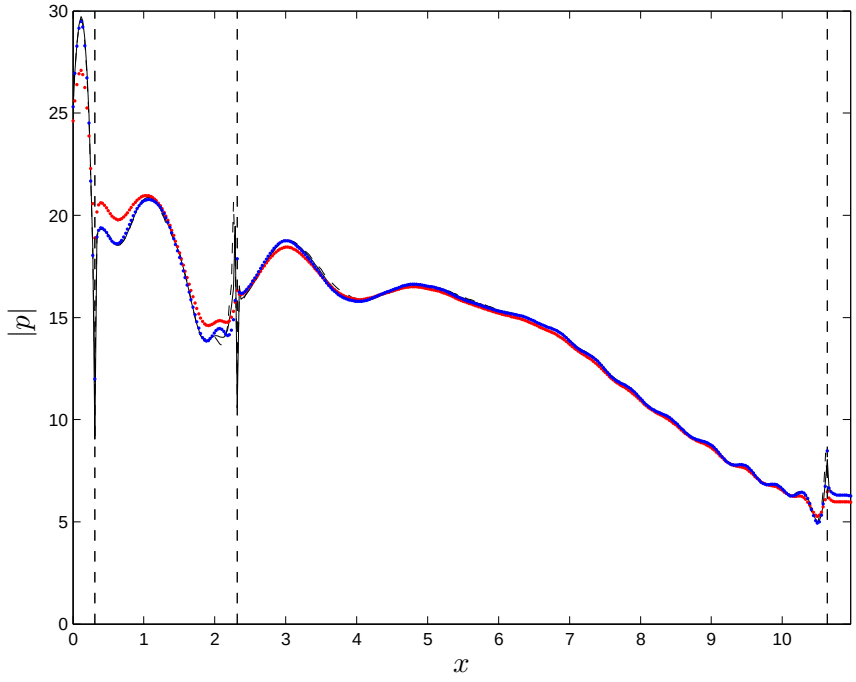


(b) Bottom wall pressure

FIGURE 3.26: *Case 6: Comparison of 2D mode matching and finite element solutions for a two segment, asymmetric liner with flow. Liner interface matching planes indicated by dashed lines. Solid line, finite element solution;* ●*, $p$-$u$ mode matching solution;* ●*, mass-momentum mode matching solution.*

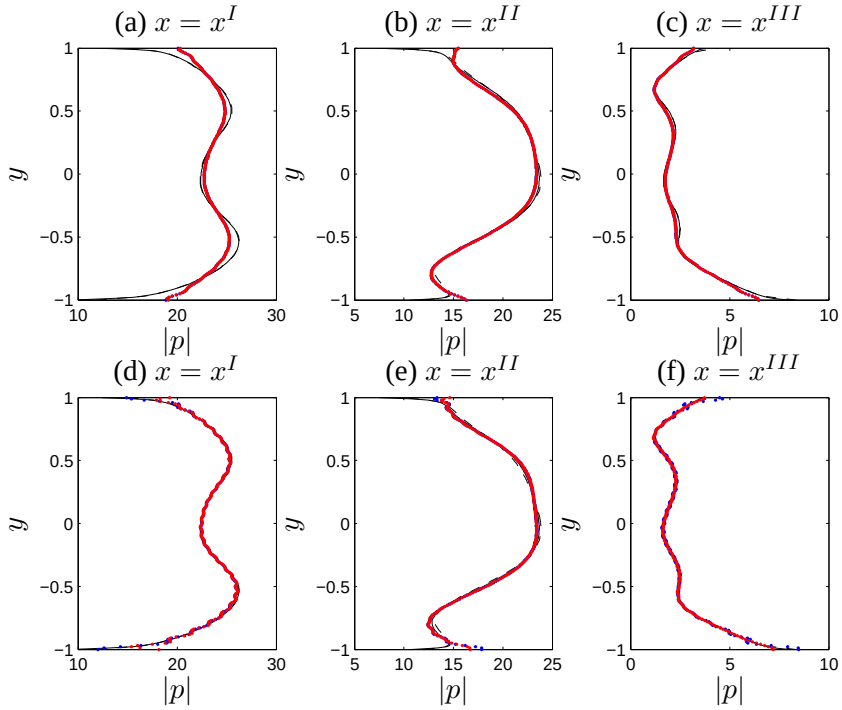


FIGURE 3.27: *Case 6: Comparison of mode matching and finite element radial pressure solutions at liner interface matching planes. (a,b,c), $p$-$u$ matching; (d,e,f), mass-momentum matching ; Solid line, finite element solution; ●, mode matching solution (lefthand segment modes); ●, mode matching solution (righthand segment modes).*

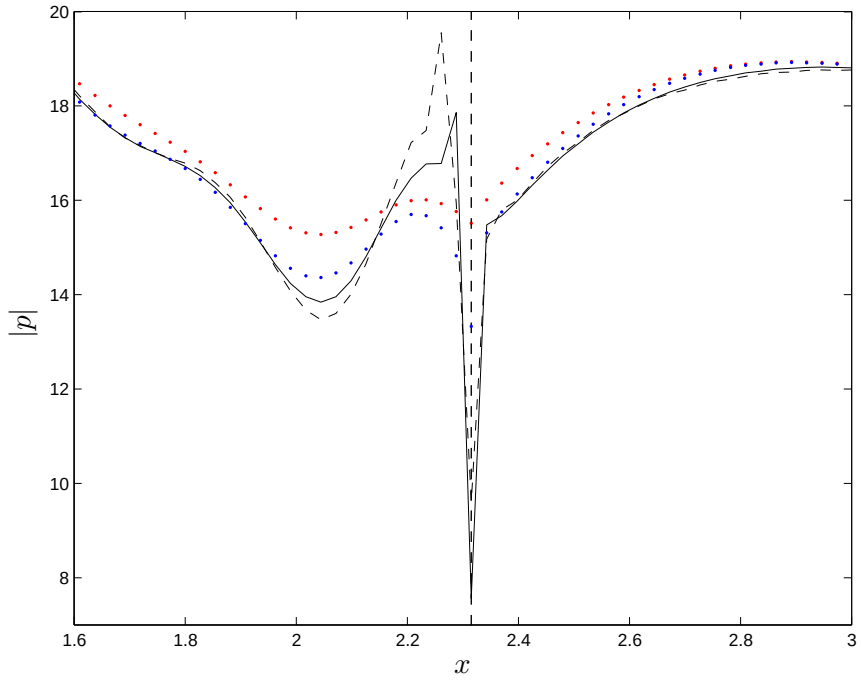


(a) Top wall pressure around $x = x^{II}$

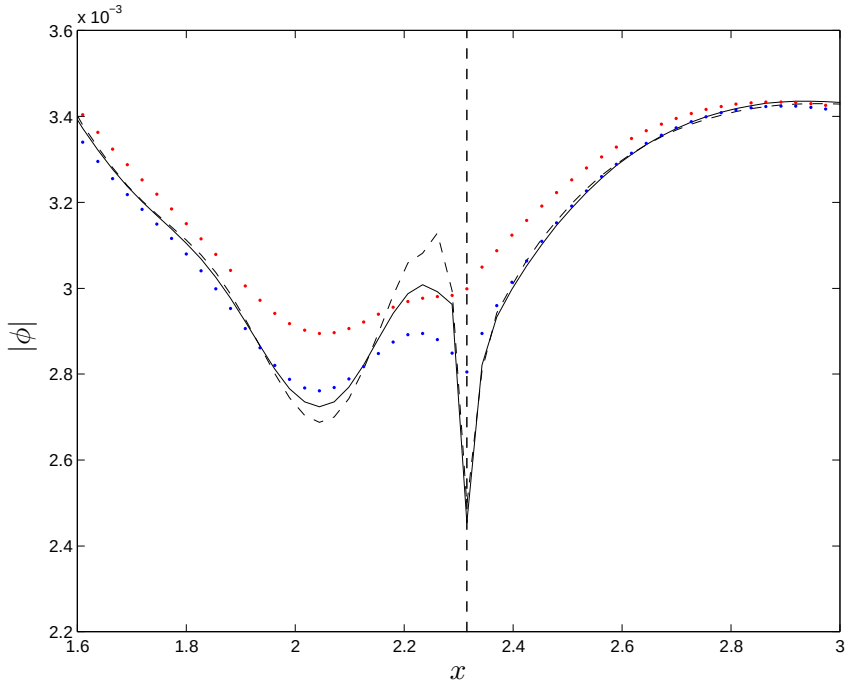


(b) Casing potential around $x = x^{II}$

FIGURE 3.28: *Case 6: Comparison of 2D mode matching and finite element solutions of pressure and potential around $x = x^{II}$ for a two segment, asymmetric liner with flow. Liner interface matching planes indicated by dashed lines. Dashed line, finite element solution; Solid line, refined finite element solution; ●, $p$-$u$ mode matching solution; ●, mass-momentum mode matching solution.*

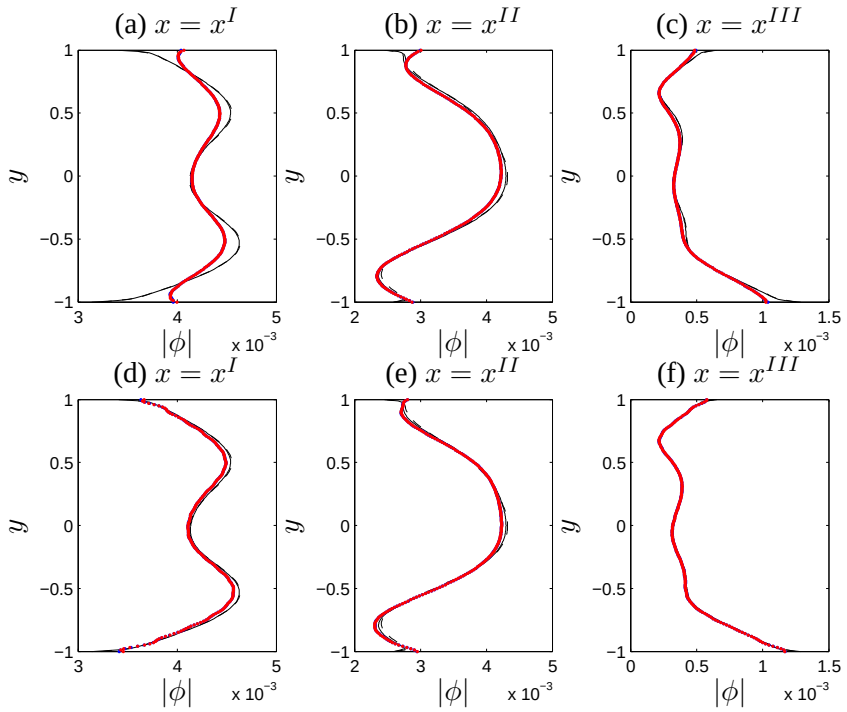


FIGURE 3.29: *Case 6: Comparison of mode matching and finite element radial potential solutions at liner interface matching planes. (a,b,c), $p$-$u$ matching; (d,e,f), mass-momentum matching ; Dashed line, finite element solution; Solid line, refined finite element solution; ●, mode matching solution (lefthand segment modes); ●, mode matching solution (righthand segment modes).*

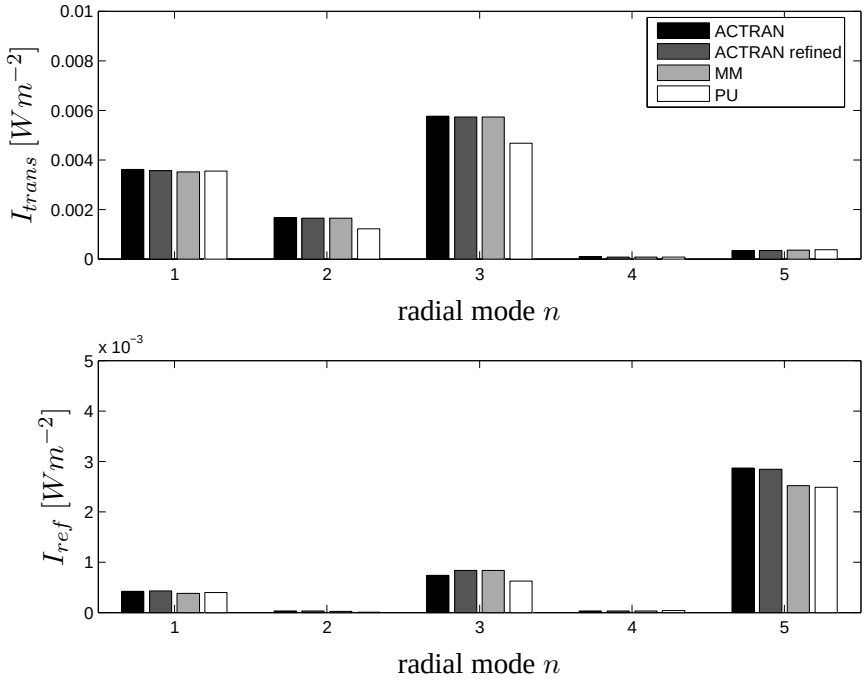


FIGURE 3.30: *Case 6: Comparison of scattered modal intensities from mode matching and finite element methods due to an incident plane wave of unit intensity. Top plot, Transmitted modal intensity; Bottom plot, Reflected modal intensity.*

### 3.7.3 Inclusion of hydrodynamic surface wave modes

In this section, the effects of including the hydrodynamic surface wave modes in the MM matching procedure are assessed. The example used is *Case 4*, but with a rigid bottom wall. The eigenvalues and axial wavenumbers of the surface wave modes are given in table (3.3), where the unstable hydrodynamic surface wave mode is included as a decaying mode in the left-running set of modes.

TABLE 3.3: *Surface wave mode solutions for Case 4 with rigid hub wall*

| Surface wave type | Transverse wavenumber $\mu_n$ | Axial wavenumber $\alpha_n$ |
|---|---|---|
| right-running acoustic | 3.8848+i4.1272 | 10.5579-i1.1921 |
| left-running acoustic | 14.9543+i6.8932 | -15.0240+i10.1510 |
| unstable hydrodynamic | 171.7040-i248.3906 | 254.8387+i178.5613 |
| stable hydrodynamic | 180.6213-i52.1542 | -58.4615-i187.5200 |

A finite element solution was obtained using an over-specified mesh (116 by 568 elements). Mass-momentum mode matching solutions were obtained with and without the hydrodynamic surface wave modes included in the matching procedure. The casing pressures around the matching planes obtained from the three solutions are compared in figure (3.31). Away from the matching planes the mode-matching solution including the hydrodynamic surface wave modes provide an improved comparison with the FE solution. The radial pressure profiles for

the top half of the duct are compared in figure (3.32). When the hydrodynamic surface wave modes are included the pressure profiles compare very well with the FE solutions away from the lined wall, with a strong reduction in the high order mode oscillations in the lined segment pressures. The scattered modal intensities are compared in figure (3.33) and demonstrate that the inclusion of the hydrodynamic surface wave modes provides the best comparison with the FE solution. The reflected intensity is improved by around 7 percent, but the transmitted intensity is hardly affected.

These results demonstrate that the hydrodynamic surface wave modes must be included to accurately reconstruct the field. The highly wall localised behaviour of these modes means that they are most suitable in reconstructing the singular behaviour of the field at the wall around the liner interface planes. Since the mode matching can be interpreted simply as an inverse 'source location' problem [67], if the source or observer are near the wall, they are in the regime of the surface wave modes. So, as Rienstra and Tester [74] noted, if they are overlooked the computed field may not be converged. This can prove problematic for numerical solutions of the field by the FE method since a mesh that is highly refined at the walls and around the liner interface planes may be required to resolve the wall localised surface wave modes and their effect upon scattering, which has been noted by Hii [38]. This is not a problem for the analytic solutions presented here.

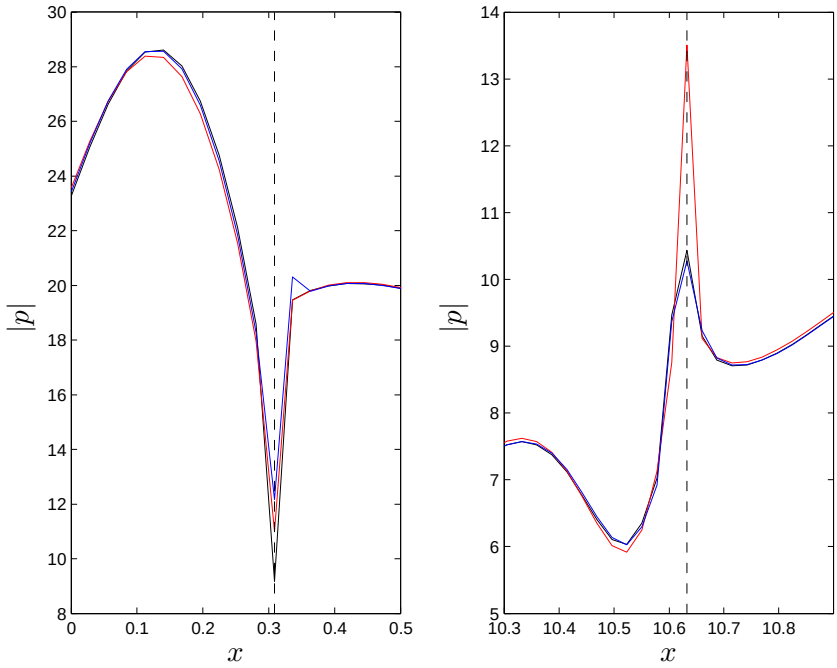


FIGURE 3.31: *Comparison of mass-momentum mode matching with and without hydrodynamic surface waves, and finite element casing pressure solutions at liner interface matching planes. —, finite element solution; —, mode-matching without hydrodynamic surface wave modes; —, mode-matching with hydrodynamic surface wave modes.*

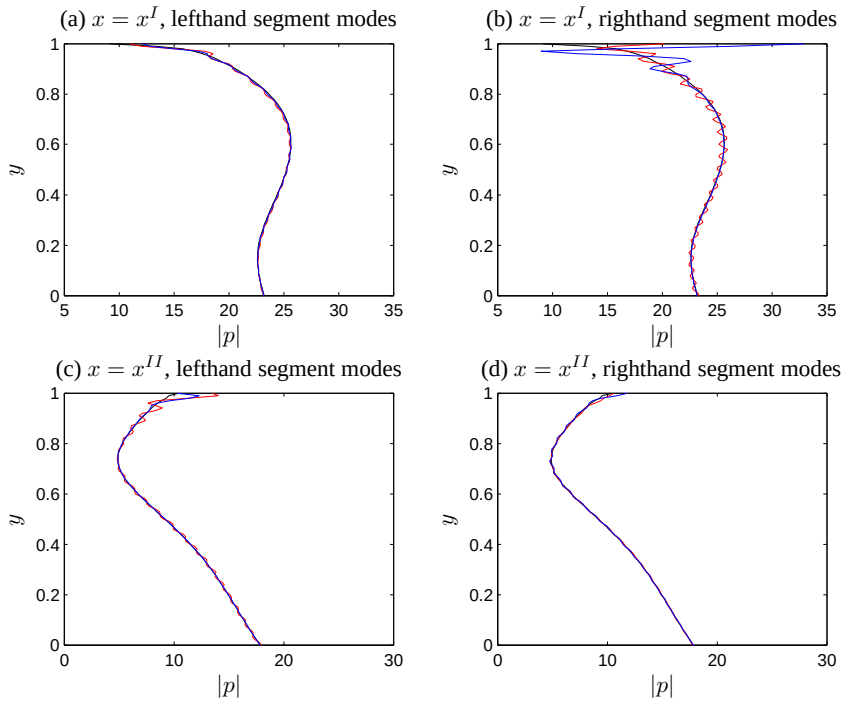


FIGURE 3.32: *Comparison of mass-momentum mode matching with and without hydrodynamic surface waves, and finite element radial pressure solutions at liner interface matching planes. —, finite element solution; —, mode-matching without hydrodynamic surface wave modes; —, mode-matching with hydrodynamic surface wave modes.*

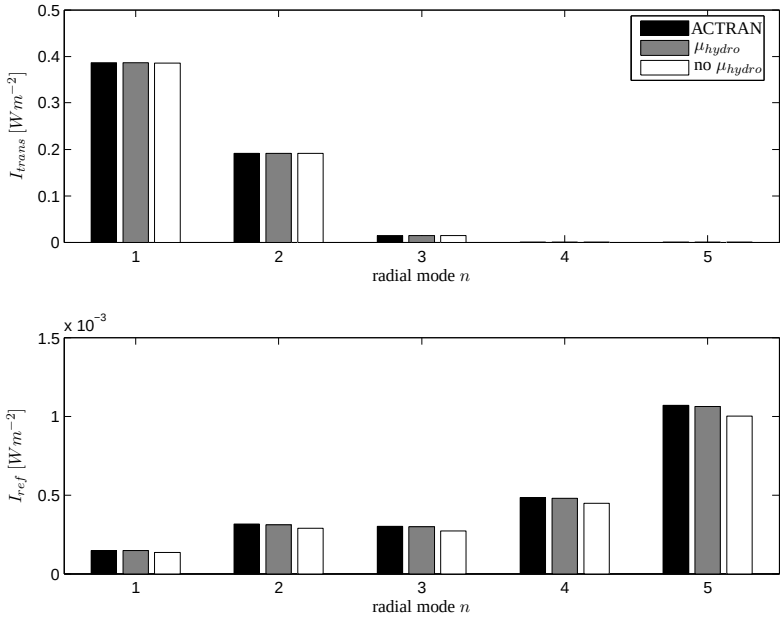


FIGURE 3.33: *Comparison of scattered modal intensities from mass-momentum mode matching with and without hydrodynamic surface waves, and finite element method due to an incident plane wave of unit intensity. Top plot, Transmitted modal intensity, Bottom plot, Reflected modal intensity.*

## 3.8 Summary

- A mode-matching method has been developed to model the propagation of sound in rectangular ducts with uniform mean flow, and a finite length asymmetric wall lining.
- By matching mass and axial momentum equations an extra matching term, related to the singularity in the axial gradient of wall displacement, is found relative to the standard pressure-velocity matching
- The method can use a single-mode or multi-mode description of the sound source
- The method was extended to include multiple liner segments of different lengths and impedances.
- A Wiener-Hopf solution by Koch [81], for a uniform symmetric liner in the absence of mean flow was outlined.
- A comparison of mode-matching and Wiener-Hopf solutions in the absence of mean flow showed excellent agreement.
- A comparison of mode-matching results with solutions from a Finite Element method found very good agreement. It was found that a highly refined finite element mesh is required to adequately resolve the field around the matching planes.

# Chapter 4

# Optimisation of bypass duct acoustic liners

Rearward propagating fan noise has become an increasingly important turbofan engine noise source with the current trend of high bypass-ratio designs. The increased size of the fan and outlet guide vanes (OGV) leads to higher tonal and broadband source levels, which become dominant sources at takeoff and approach [82]. A key method for mitigating the rearward propagating rotor-stator interaction tones [6] and fan-OGV broadband noise [83] is the use of passive attenuating acoustic liners in the bypass duct walls. The placement and design of the liners must be such that the attenuation performance is maximised over a wide frequency range, for different operating conditions and source content. A number of analytic (e.g. ray acoustics, modal methods) and computational techniques (e.g. finite element, time or frequency domain LEE, finite difference, discontinuous Galerkin methods) for acoustic propagation in lined flow ducts are available for evaluating the liner attenuation performance. However, computational cost is a limiting factor in the use of computational methods in the optimisation process. In fact, finite element methods for the convected wave equation are currently the most mature of the available methods and have only very recently begun to be used in the liner optimisation process [84, 85]. Analytic methods have seen greater use, since they are computationally cheap, but are limited to highly idealised models [86, 32, 33, 25]. However, they can give good approximations of attenuation performance over wider frequency ranges, for multi-modal source descriptions and multiple liner segments within reasonable time scales.

TABLE 4.1: *ISVR one-sixth scale no flow bypass duct rig geometry.*

| | | |
|---|---|---|
| Total liner length | $l_{lined}/d$ | 10 |
| Hub radius | $h[m]$ | 0.1191 |
| Casing radius | $r[m]$ | 0.1985 |
| Annulus half height | $d[m]$ | 0.0397 |
| Hub-to-tip ratio | $\hbar$ | 0.6 |
| Speed of sound | $c_0[ms^{-1}]$ | 343 |
| Density of air | $\rho_0[kgm^{-3}]$ | 1.21 |

In this chapter, the optimisation of uniform and axially-segmented acoustic liners for the attenuation of fan noise in turbofan bypass ducts is demonstrated. Parts of this work have contributed to a Department for Trade and Industry (DTI) sponsored research project, Aircraft Noise Disturbance Alleviation by Novel TEchnology (ANDANTE), focusing on fan noise propagation and control in bypass ducts [87]. The liner attenuation performance is calculated using the pressure-velocity mode-matching method described in chapter (3). The geometry chosen for the following studies is identical to that of the one-sixth scale bypass duct rig used at the ISVR [88], the details of which are in table (4.1). The mode-matching model is a rectangular approximation to the actual annular geometry, and the duct width $b$ is determined from the average radius $R_a$ to be

$$b/d = \pi R_a = \frac{\pi(1+\hbar)}{2} = 2.5133\ . \tag{4.1}$$

The non-dimensional specific liner impedance is that for a single-degree-of-freedom liner, which is determined using a commonly used semi-empirical model [89], given by

$$Z = R + i\left[k_0 M_r - \cot(k_0 D)\right]\ , \tag{4.2}$$

where $R$ is the facing sheet resistance, $M_r$ is the non-dimensional facing sheet mass inertance, and $D$ is the non-dimensional cavity depth.

### 4.0.1 Source assumptions

Knowledge of the fan noise source is essential to accurately predict the noise signature of this source that is heard by observers on the ground. The first stage of any prediction method is the determination of in-duct propagation, for which a modal decomposition of the source is inevitably required. However, determination of the modal structure of the tonal and broadband sources is difficult, owing to the complex source mechanisms and lack of adequate measurement techniques. Predictions for tonal noise sources have very recently been demonstrated [90], at considerable computational cost, through full three-dimensional nonlinear CFD calculations of the fan assembly. Also, experimental determination of the propagating modal sound field structure has recently been demonstrated [91, 92], and methods

for separating rotor and stator-based broadband sources have been suggested, but not implement as yet [93, 94].

Owing to these difficulties past researchers have successfully used rotor-stator interaction mode theory to determine the dominant azimuthal mode orders [6]. The assumptions for the radial mode breakdown of tones is rather more difficult, in the absence experimental results. Typically, the propagating radial modes are assumed to be uncorrelated, such that the attenuation of each mode can be calculated separately, and assigned equal energy at the source plane. Statistical analysis suggests that for single azimuthal mode orders, and where few radial modes are cut-on, random variation of the incident radial mode phases produces a non-Gaussian power attenuation at the duct exit [95, 96, 97]. The implication for in-duct propagation predictions is that, where few modes propagate, the choice of the phase of the mode is more likely to affect the power attenuation (i.e. higher standard deviation). Therefore, in the absence of a computationally expensive statistical source description, care must be taken when drawing conclusions from rotor-stator mode predictions, with few propagating modes, using an uncorrelated mode assumption.

The broadband fan noise source is typically modelled by assuming excitation of all cut-on modes in an uncorrelated manner, with equal energy per mode [98, 99]. Statistical analysis has shown that this is a reasonable assumption which improves for higher frequencies [95, 96, 97, 100]. This approach is applied to the current work, and is compared to experimental results from the ISVR one-sixth scale bypass duct rig in figure (4.1). The experimental sound power transmission loss is determined from microphone measurements at the source (reverberation chamber) and a far field polar array (anechoic chamber). Further details of the test setup and data processing can be found in Sugimoto *et al.* [88]. Four different liner configurations for an axially uniform geometry are compared: uneven liner with three matching planes; single symmetric liner; single casing liner; single hub liner [101]. Finite element solutions for the annular geometry are included for comparison. Predictions were made at a series of one-third octave band centre frequencies, with around 300 propagating modes at the highest frequency considered. The rectangular mode-matching solutions provides a good comparison with the measured data for the uneven and symmetric linings. For builds with inner or outer rigid walls the rectangular model under- and over-predicts both the FE solution and experimental data. This is due to differences in the lined areas and mode eigenfunctions between rectangular and annular ducts.

Hence, in this work multi-mode propagation is modelled by assuming an equal energy distribution per uncorrellated cut-on mode at each frequency.

## 4.1 Single segment impedance optimisation

The simplest optimisation exercise for finite length liners is that of a single, symmetric liner with a single incident mode. A common method used to determine peak attenuation and

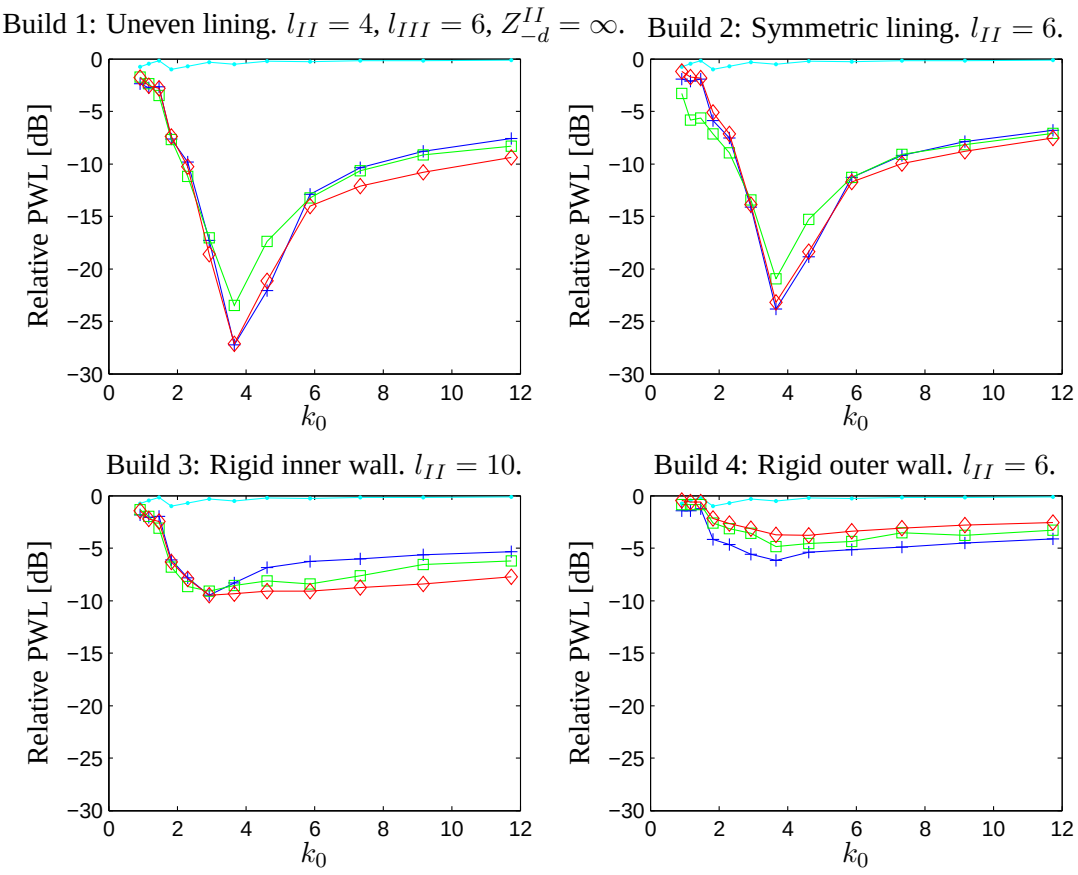


FIGURE 4.1: *Comparison of power transmission loss from mode matching and FE solutions with experimental data for lined annular ducts without flow, for a broadband noise source.* -·-, *FE end correction;* -□-, *Experiment;* -◇-, *ACTRAN FE;* -+-, *Mode-matching.*

optimum liner design is the use of isocontours of attenuation in the impedance plane, here measured in terms of the sound power transmission loss $\Delta_{PWL}$. By determining isocontours for a range of frequencies and Mach numbers the optimum liner impedances can be obtained as an empirical function of frequency, and off-optimum attenuation sensitivity can also be easily assessed [89]. Isocontours were obtained for the rig geometry at nine one-third octave frequencies between 300 Hz and 2500 Hz for a single incident mode.

Results for incident modes (0,1) and (0,3) are presented in figures (4.2) and (4.3) respectively. At low frequencies, where few modes are propagating, the location of the peak attenuation corresponds to impedances near the so-called 'Cremer optimum' of the least attenuated mode, which is indicated on the figures, along with higher order mode pair optima. Such optima were ascertained by Cremer [24] and Tester [25, 102] to correspond to branch points in the complex eigenvalue plane where certain modes coalesce, and may obtain their maximum axial decay rates according to infinite duct theory. Interestingly, even when the incident mode is of higher order, the optimum impedance still occurs near the first Cremer mode pair value. This is a direct result of the mode scattering which occurs at the liner interfaces. To demonstrate this, the scattered amplitudes due to the second even mode are plotted in figure (4.4), for the first ($Z_{C1} = 1.2903 - 1.0334i$) and second ($Z_{C2} = 0.71252 - 0.27501i$) mode pair Cremer

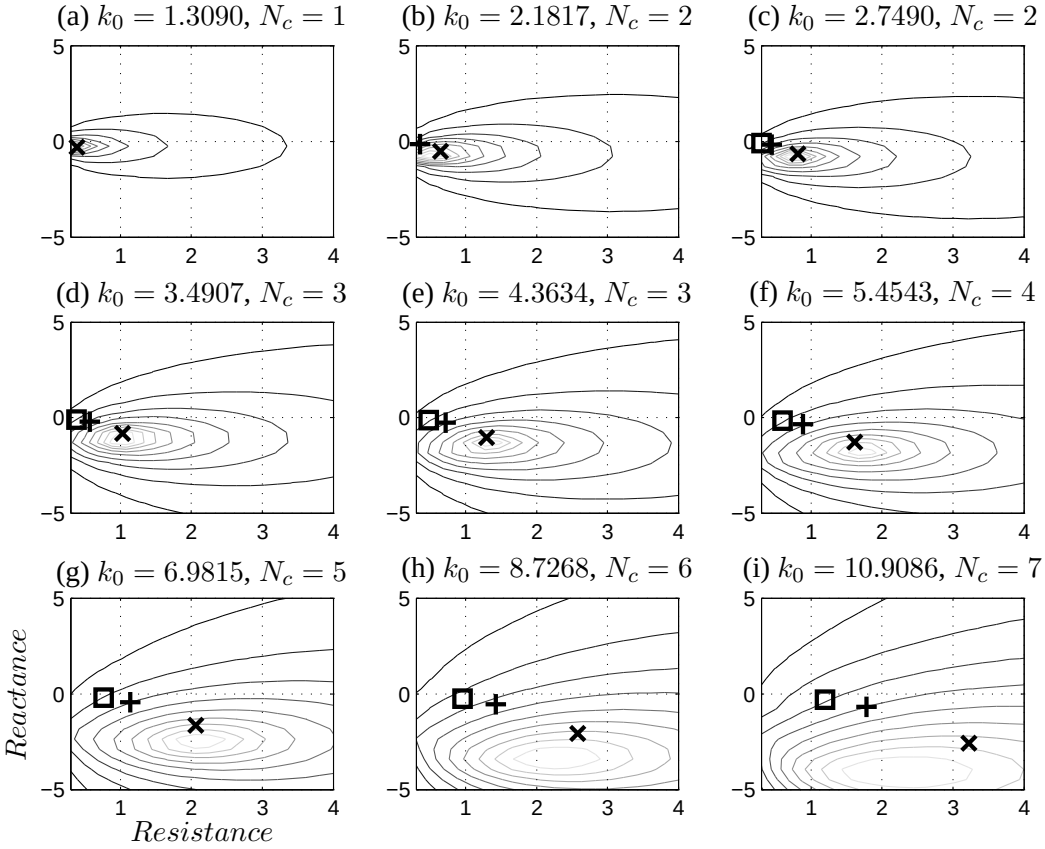


FIGURE 4.2: *Isocontours of $\Delta_{PWL}$ (normalised to the peak value) in the impedance plane for an incident plane wave mode $(0, 1)$. $\times$, 1st even mode pair Cremer optimum; $+$, 2nd even mode pair Cremer optimum; $\square$, 3rd even mode pair Cremer optimum; $l_{liner} = 10$, $M = 0$.*

TABLE 4.2: *First four right-running axial wavenumbers for impedances near 1st and 2nd Cremer mode pair optima at $k_0 = 4.3634$, $M = 0$.*

| Even mode number | $\alpha^+$ at $Z_{C1} = 1.2903 - 1.0334i$ | $\alpha^+$ at $Z_{C2} = 0.71252 - 0.27501i$ |
|---|---|---|
| 1 | $4.0368 - 0.5778i$ | $2.4106 - 3.5122$ |
| 2 | $4.0167 - 0.5994i$ | $4.0594 - 0.1172$ |
| 3 | $0.5030 - 4.1375i$ | $2.2561 - 3.6084$ |
| 4 | $0.2538 - 8.1510i$ | $0.7298 - 8.0563$ |
| $\Delta_{PWL}$ [dB] | 32.9124 | 15.9640 |

optimum impedances at $k_0 = 4.3634$. Note that $Z_{C1}$ is close to the finite length optimum demonstrated in figure (4.3b). For both impedances, a large proportion of the incident mode energy scatters into the Cremer mode pair. However, for $Z_{C2}$ the attenuation rate of the least attenuated mode, as shown in table (4.2), is much lower than the Cremer mode pair. Thus, by the end of the liner the least attenuated mode contains the highest proportion of the energy to be scattered at the trailing liner interface.

Returning to the isocontours, as the frequency and number of propagating modes increase, the optimum impedance no longer corresponds to the Cremer values. It was shown by Tester [25] that the attenuation rate [dB] of the first Cremer mode pair decreases like $20.73/k_0$, and that

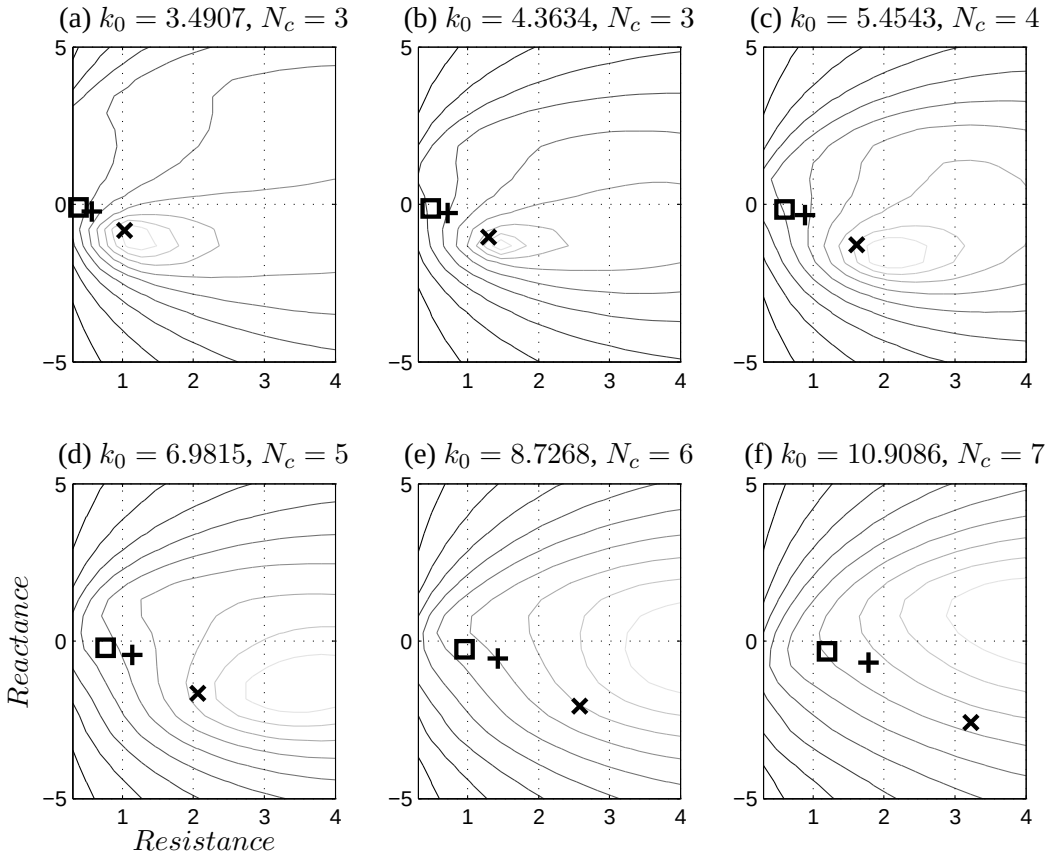


FIGURE 4.3: *Isocontours of $\Delta_{PWL}$ (normalised to the peak value) in the impedance plane for an incident even mode $(0,3)$. $\times$, 1st even mode pair Cremer optimum; $+$, 2nd even mode pair Cremer optimum; $\square$, 3rd even mode pair Cremer optimum; $l_{liner} = 10$, $M = 0$.*

attenuation rates of other higher order cut-on modes at the optimum impedance can have similar or even lower decay rates than the mode pair. The implication is that scattering into the mode pair does not necessarily provide the highest power loss with a finite length liner when higher order modes are cut-on. The finite length optima found here are away from the Cremer optima, since they allow more scattering into higher order modes in the lined section, thus a higher power attenuation is achieved. This is demonstrated in figure (4.5) by plotting the scattered modal amplitudes for impedances near the first Cremer mode pair ($Z_{C1} = 2.581 - 2.067i$) and finite length ($Z_{FL} = 2.247 - 3.421i$) optima at $k_0 = 8.7268$. For $Z_{C1}$, scattering in the lined section occurs mainly into the mode pair, but for $Z_{FL}$ a much higher proportion occurs into higher order modes. The resulting power loss is higher for $Z_{FL}$ despite the cut-on mode decay rates being lower than for $Z_{C1}$, as shown in table (4.3).

The same behaviour noted above is seen when flow is introduced. An example of isocontours of attenuation for a uniform flow $M = 0.4$ are presented in figure (4.6). The convection effect of the flow increases the downstream mode cut-on ratio, hence more downstream modes can propagate and peak attenuation rates are lower than the corresponding quiescent case.

Attenuation isocontours over the impedance plane are plotted, for a multi-mode source with

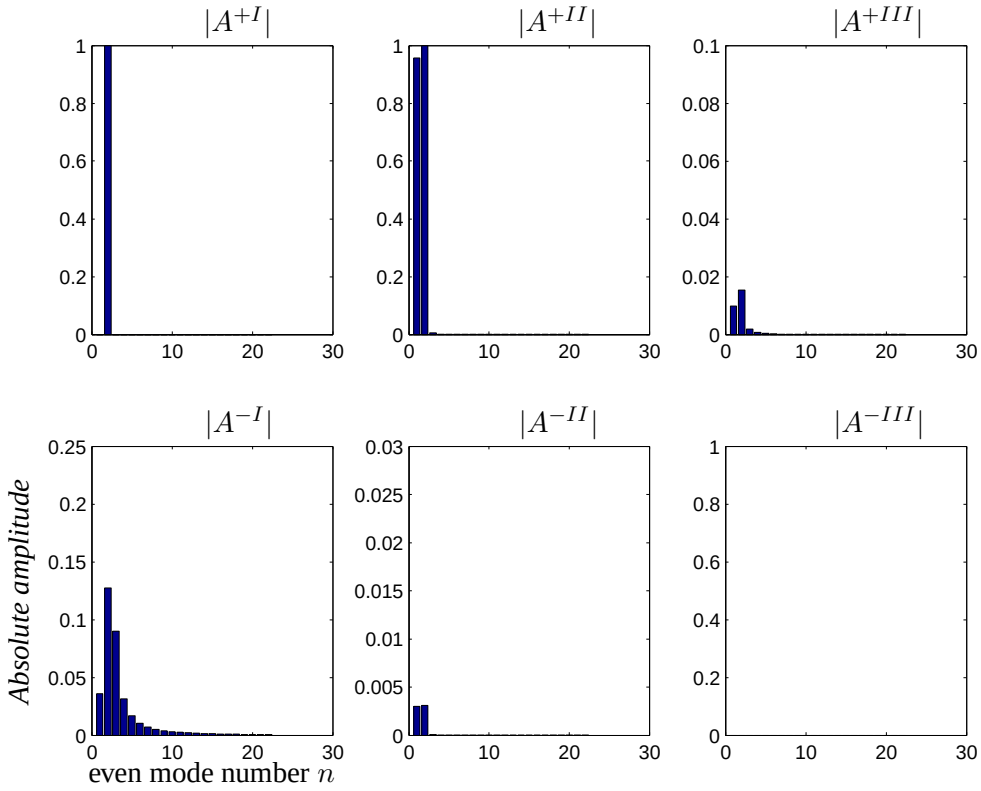


(a) Near 1st mode pair Cremer optimum impedance $Z_{C1} = 1.2903 - 1.0334i$.

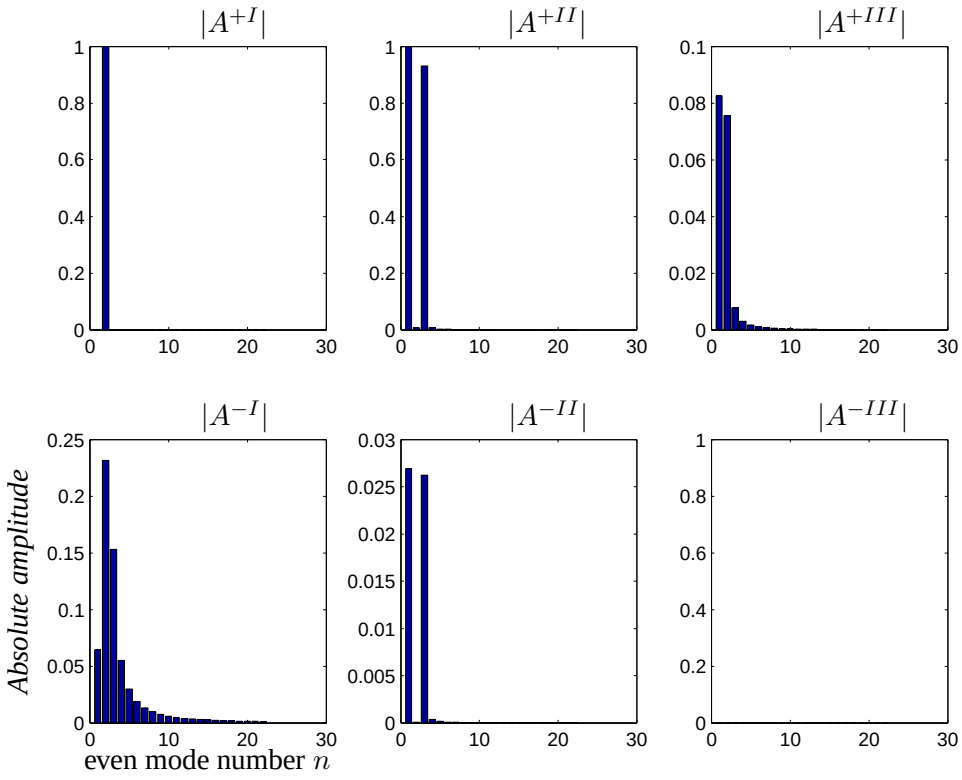


(b) Near 2nd mode pair Cremer optimum impedance $Z_{C2} = 0.71252 - 0.27501i$.

FIGURE 4.4: *Scattered even mode amplitudes for a single symmetric liner segment due to incident 2nd even mode.* $l_{II} = 10$, $M = 0$.

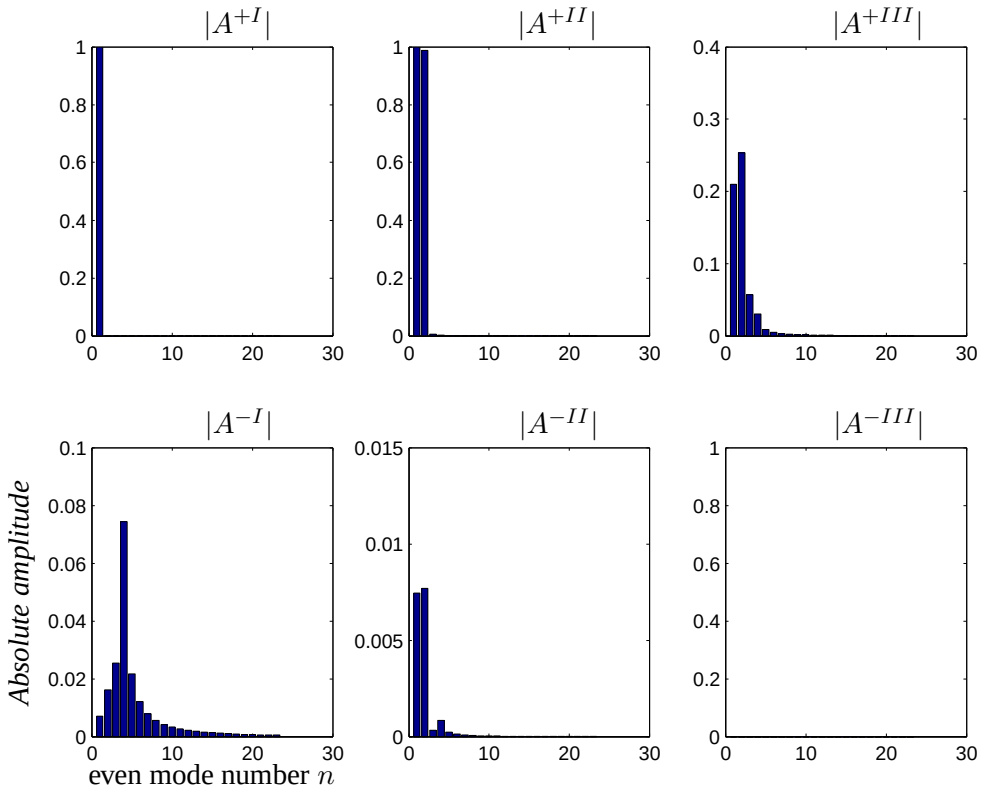


(a) Near 1st mode pair Cremer optimum impedance $Z_{C1} = 2.581 - 2.067i$.

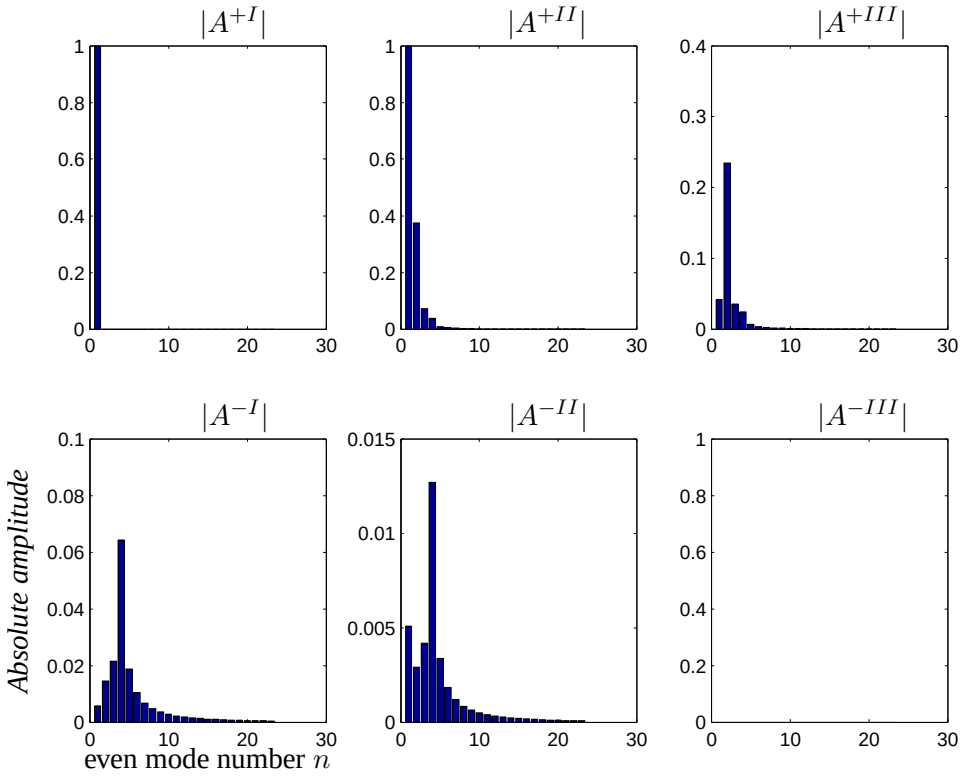


(b) Near finite length optimum impedance $Z_{C2} = 2.247 - 3.421i$.

FIGURE 4.5: *Scattered even mode amplitudes for a single symmetric liner segment due to incident plane wave mode.* $l_{II} = 10$, $M = 0$.

TABLE 4.3: *First four right-running axial wavenumbers for impedances near 1st Cremer mode pair and finite length optima at* $k_0 = 8.7268$, $M = 0$.

| Even mode number | $\alpha^+$ at $Z_{C1} = 2.581 - 2.067i$ | $\alpha^+$ at $Z_{FL} = 2.247 - 3.421i$ |
|---|---|---|
| 1 | $8.5548 - 0.2731i$ | $8.8477 - 0.2122i$ |
| 2 | $8.5406 - 0.2814i$ | $8.3830 - 0.1188i$ |
| 3 | $6.3529 - 0.3275i$ | $6.3525 - 0.1795i$ |
| 4 | $0.6642 - 3.1141i$ | $0.3814 - 3.0358i$ |
| $\Delta_{PWL}$ [dB] | 11.2443 | 15.5439 |

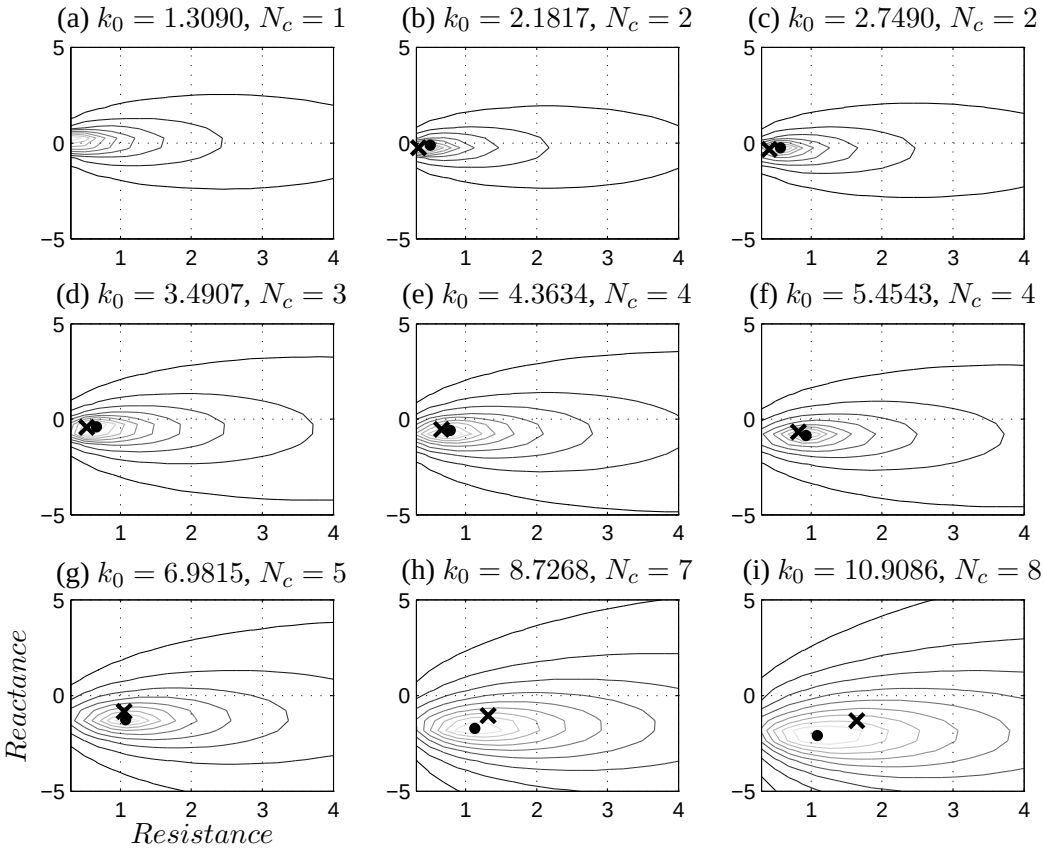


FIGURE 4.6: *Isocontours of* $\Delta_{PWL}$ *(normalised to the peak value) in the impedance plane for an incident plane wave mode* $(0, 1)$. $\times$*, 1st mode pair Cremer optimum;* $\bullet$*, DHC optimum;* $l_{liner} = 10$, $M = 0.4$.

and without flow, in figures (4.7) and (4.8) respectively. A deterministic, gradient-based optimisation method known as Dynamic Hill Climbing (DHC) [103] was used to determine the optimum impedances for plane wave and multi-mode sources with flow, which are indicated ($\bullet$) on the isocontours in figures (4.6) and (4.7) respectively. The variation in the optimum impedance with frequency is shown in figure (4.9) and demonstrates that the multi-mode optima do not correspond to those of the plane wave mode at high frequencies. Peak attenuation levels, as shown in figure (4.10), are higher than the plane wave case since the higher order incident modes are more easily attenuated. At high frequencies, the peak attenuation level is virtually independent of frequency.

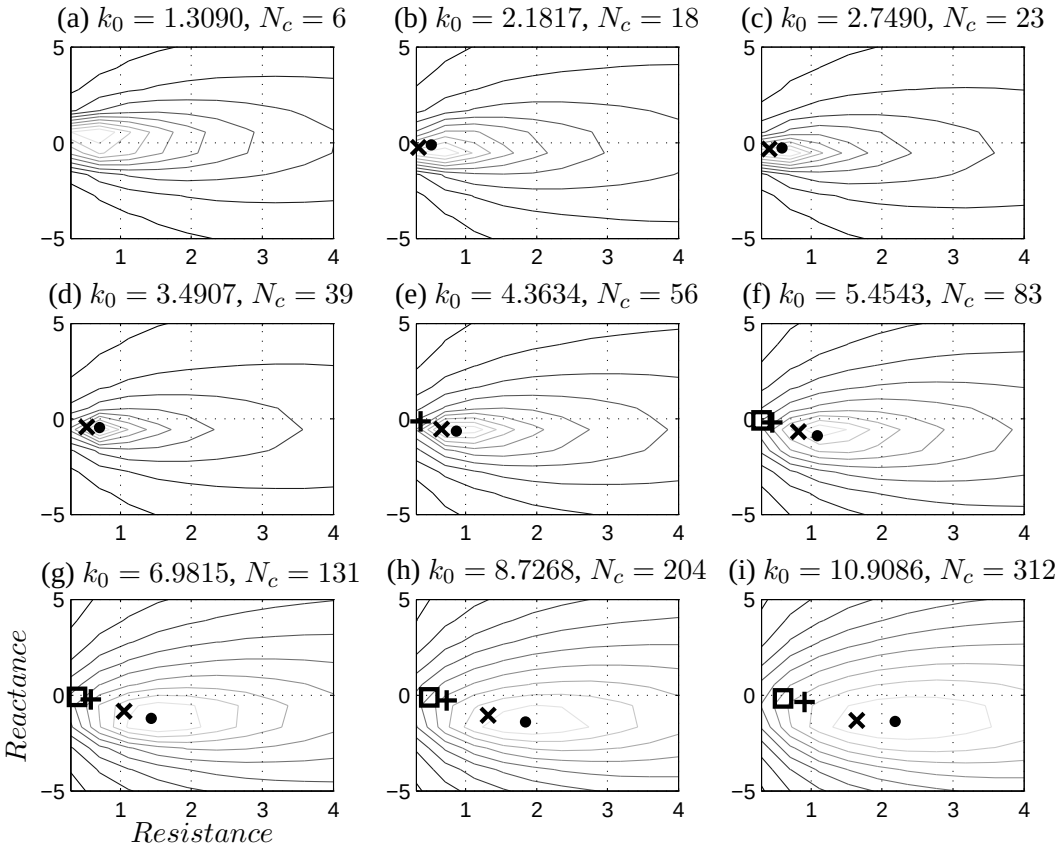


FIGURE 4.7: *Isocontours of $\Delta_{PWL}$ (normalised to the peak value) in the impedance plane for a multi-mode source. $\times$, 1st even mode pair Cremer optimum; $+$, 2nd even mode pair Cremer optimum; $\square$, 3rd even mode pair Cremer optimum; $\bullet$, DHC optimum; $l_{liner} = 10$, $M = 0.4$.*

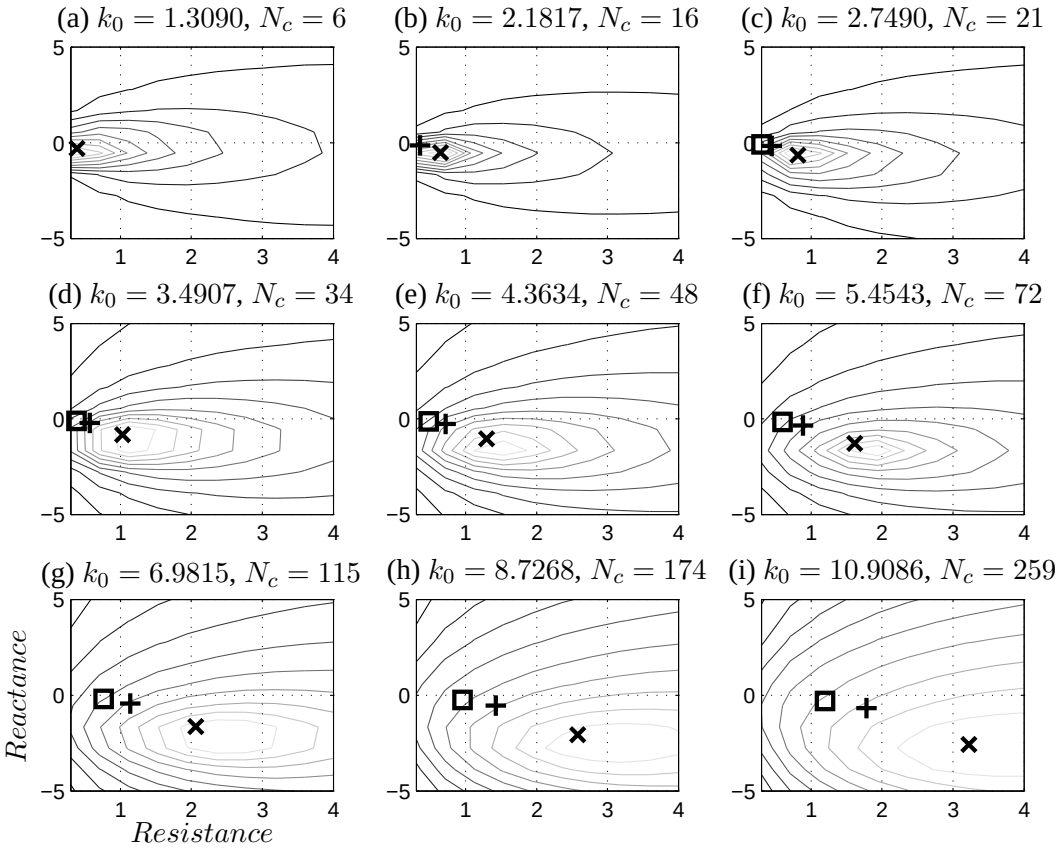


FIGURE 4.8: *Isocontours of $\Delta_{PWL}$ (normalised to the peak value) in the impedance plane for a multi-mode source. $\times$, 1st even mode pair Cremer optimum; $+$, 2nd even mode pair Cremer optimum; $\square$, 3rd even mode pair Cremer optimum; $l_{liner} = 10$, $M = 0$.*

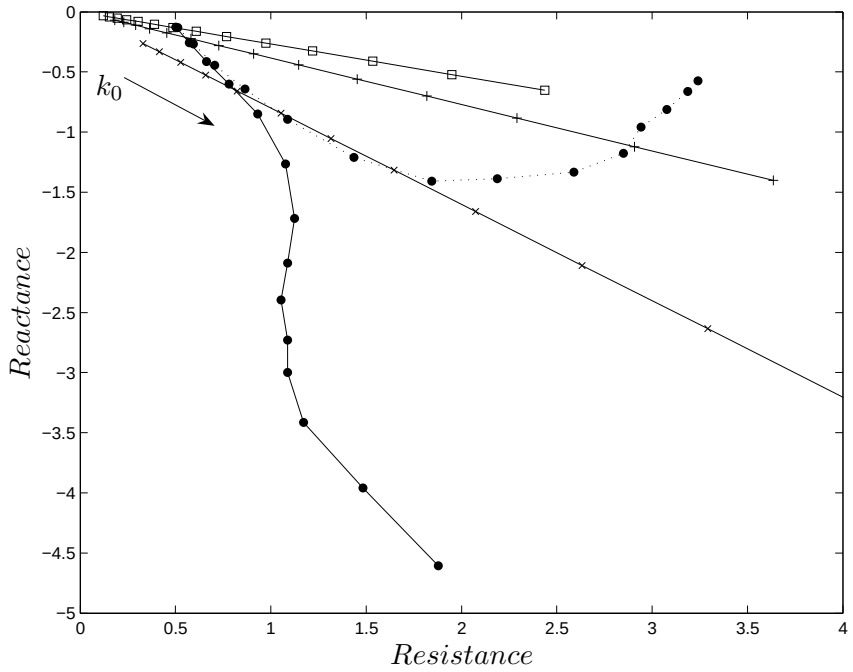


FIGURE 4.9: *Optimum impedance for increasing Helmholtz number $k_0$ (14 1/3rd-octave band centre frequencies). − • −, DHC optimum for plane wave source; · · • · ·, DHC optimum for multi-mode source; ×, 1st even mode pair Cremer optimum; +, 2nd even mode pair Cremer optimum; □, 3rd even mode pair Cremer optimum; $l_{liner} = 10$, $M = 0.4$.*

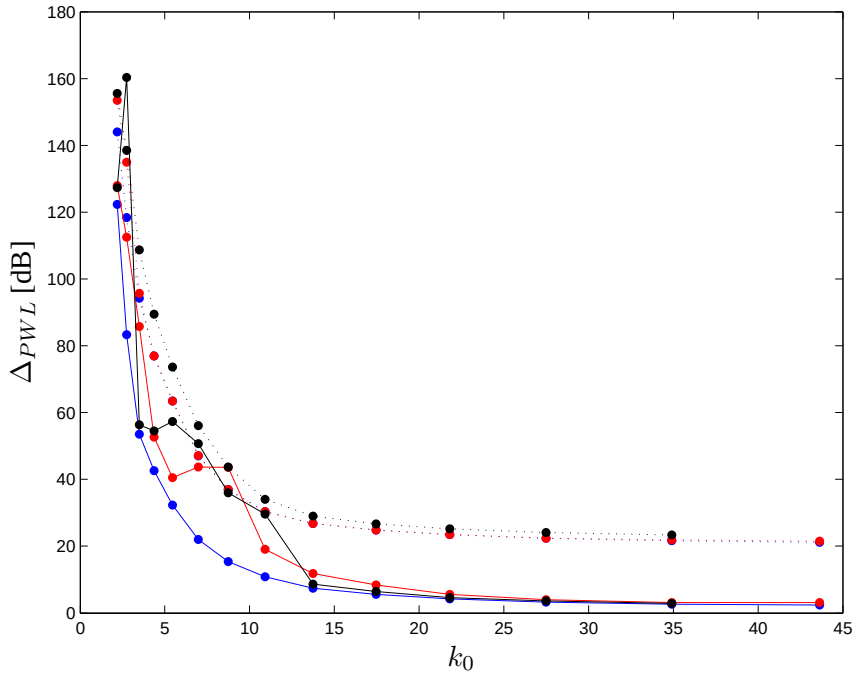


FIGURE 4.10: *Peak power transmission loss for segmented liner optimum impedances (1/3rd-octave band centre frequencies). − • −, single segment optimum for plane wave source; − • −, two-segment optimum for plane wave source; − • −, four-segment optimum for plane wave source; · · • · ·, single segment optimum for multi-mode source; · · • · ·, two-segment optimum for multi-mode source; · · • · ·, four-segment optimum for multi-mode source. $l_{liner} = 10$, $M = 0.4$.*

Examples of the DHC search pattern and convergence are presented in appendix figure (C.6) for the plane wave case at $k_0 = 8.7268$. The design parameters are constrained to $0.3 \leq R \leq 4$ and $-10 \leq X \leq 1$. The algorithm is restarted at three random points, and each time is seen to converge to the same design point.

## 4.2 Two-segment impedance optimisation

The optimisation of a liner with two symmetric segments of equal length was undertaken using a stochastic optimisation method called Adaptive Simulated Annealing (ASA) [104]. This method involves random sampling of the design space, which is important for high dimensional optimisation problems in order to avoid convergence to local optima [105]. The optimum impedances at each frequency for both plane wave and multi-mode sources are plotted in figure (4.11). For the plane wave source, the trend shown is for a leading segment of low resistance, and a trailing segment of higher resistance. This behaviour was previously noted by Baumeister [40] and Sawdy et al. [34] as being due to the preferential scattering of sound in the leading liner segment, making it susceptible to absorption in the trailing liner segment. The maximum improvement of the peak attenuation over the uniform liner is shown in figure (4.10) to occur at around $k_0 = 10$, which corresponds well with the results of Baumeister [40]. The results for the multi-mode source show improvement in peak attenuation at low frequencies, but none at high frequencies. The optimum segment impedances are virtually equivalent to the uniform liner configuration. This indicates that two-segment liners are potentially very effective for attenuating the rotor-stator interaction noise around 2BPF, but provide no benefit over uniform liners for multi-mode sources at discrete frequencies.

Examples of the ASA search pattern and convergence are presented in appendix figure (C.7) for the plane wave case at $k_0 = 8.7268$. The algorithm begins with a random walk over the design space, and progresses to a downhill search involving random moves. The search requires a large number of iterations to obtain convergence which is a known feature, and disadvantage, of the ASA method [105]. However, the algorithm is quite robust, owing to its stochastic nature, and is statistically guaranteed to provide global convergence [104].

## 4.3 Four-segment impedance optimisation

The optimisation of a liner consisting of four symmetric segments of equal length was undertaken using an Adaptive Range MultiObjective Genetic Algorithm (ARMOGA) [106, 107]. Genetic Algorithms (GA) allow for higher dimensional design spaces to be searched in a more efficient manner. This is achieved by searching from a population, rather than a single parameter set, obtained in a manner which provides good coverage of the design space. The principle behind GAs is that of Darwinian theory of natural selection, where the 'fittest' members of a population are favoured to produce offspring. Here, the cost function

evaluations required in constructing each ARMOGA population were calculated simultaneously over a number of processors on a Linux High Power Computing (HPC) cluster. A maximum of sixty generations with a population size of forty was specified, with the cost function again being the power transmission loss. The optimised impedance values are plotted in figure (4.12) where low resistances again dominate in the leading segments for the plane wave case. The peak attenuation levels are plotted in figure (4.10) and it is seen that the ARMOGA algorithm fails because levels equal to or greater than those of the optimised two-segment liner are not obtain in the plane wave case. This highlights a common problem in high dimensional optimisation problems where convergence to local optima occurs due to a variety of reasons, such as inadequate sampling of the design space or certain features of the problem (such as the rapid variations seen around the Cremer optima). Recent studies [108, 100] of segmented liners have attempted to circumvent such convergence problems by using hybrid approaches that combine surrogate models of the problem, which are intelligently constructed and updated, with a variety of search techniques. It is expected that future work involving liner optimisation will utilise such techniques in combination with parallel computing methods in order to obtain populations or design sets in an efficient manner.

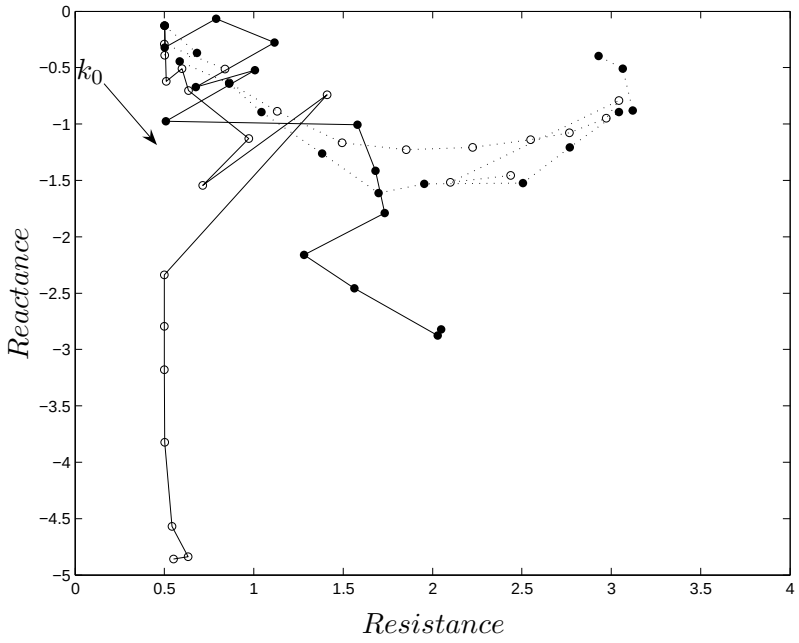


FIGURE 4.11: *Two-segment liner optimum impedances for increasing Helmholtz number $k_0$ (14 1/3rd-octave band centre frequencies).* $-\circ-$*, 1st segment ASA optimum for plane wave source;* $-\bullet-$*, 2nd segment ASA optimum for plane wave source;* $\cdot\cdot\circ\cdot\cdot$*, 1st segment ASA optimum for multi-mode source;* $\cdot\cdot\bullet\cdot\cdot$*, 2nd segment ASA optimum for multi-mode source;* $l_{liner} = 10, l_{II} = l_{III} = 5, M = 0.4$.

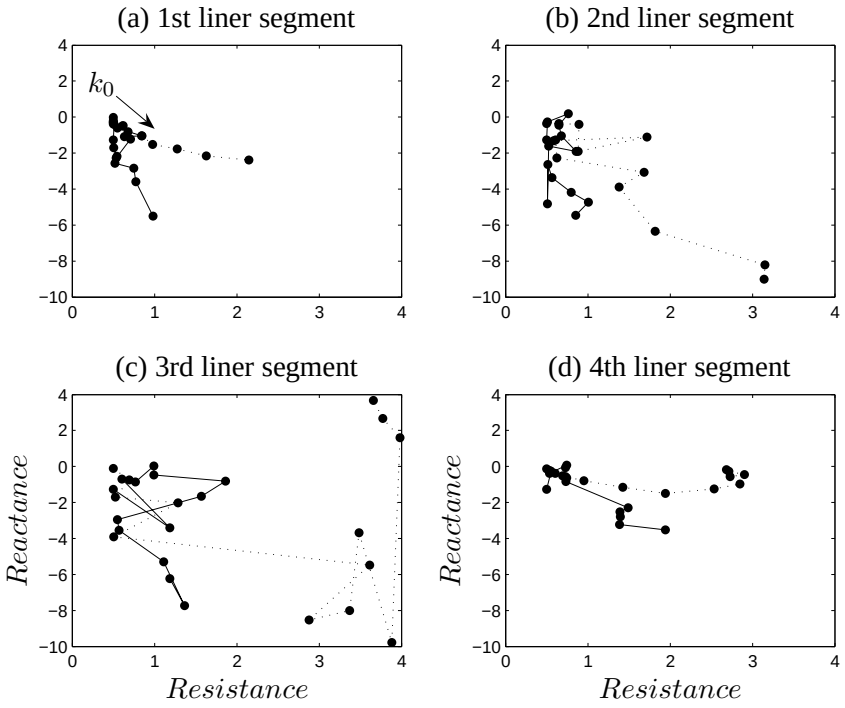


FIGURE 4.12: *Four-segment liner optimum impedances for increasing Helmholtz number $k_0$ (13 1/3rd-octave band centre frequencies). $-\bullet-$, ARMOGA optimum for plane wave source; $\cdots\bullet\cdots$, ARMOGA optimum for multi-mode source. $l_{liner} = 10$, $l_{II} = l_{III} = l_{IV} = l_V = 2.5$, $M = 0.4$.*

For the multi-mode case the largest benefits over the uniform optima are seen at low frequencies, but these are only improvements over already very large attenuation rates. Towards higher frequencies the improvement drops to around 1.5dB.

Examples of the ARMOGA search pattern and convergence are presented in appendix figure (C.8) for the plane wave case at $k_0 = 8.7268$. The search appears to be converging, but more generations are required.

## 4.4 Optimisation of SDOF liners

The optimisation simulations in the previous section are aimed at determining the optimum resistance and reactance values for sound power attenuation at individual frequencies. A common method to determine the best liner design parameters is to take a best fit from a database of the calculated optimum resistances and reactances over frequency [32]. However, in this section the optimum liner design parameters of resistance $R$ and non-dimensional liner depth $D$ are determined directly, to provide the best attenuation performance over a specific frequency range. The aim of this work was to provide optimum uniform and segmented liner designs for testing in the ISVR no flow bypass duct rig [87]. The SDOF liner model given in equation (4.2) is used to calculate the impedance, where the mass inertance is held at $M_r = 0.1259$. The optimisation is constrained to realistic values of resistance $0.5 \leq R \leq 4$

and model scale liner cavity depth $0.002\text{m} \leq D \times d \leq 0.02\text{m}$. Optimisation of axially-segmented liners was carried out for up to four liner segments, with variable liner segment lengths. The segment lengths were constrained such that the minimum length was 0.03m, and the total lined duct length was held at $l_{liner} = 10$.

### 4.4.1 Multi-mode source

In order to optimise liner performance over a frequency bandwidth, a cost function is prescribed which combines the attenuation obtained at a discrete set of frequencies. The cost function used here is calculated by assuming a source with a constant power spectrum across a discrete set of frequencies. At each frequency, the source is assumed to excite all cut-on modes with equal energy. The combined frequency cost function $CF$ is then obtained by comparing the sums of incident and transmitted modal powers,

$$CF = 10 \log_{10} \left[ \frac{\sum_f \sum_m \sum_n W^{inc}_{k_0,m,n}}{\sum_f \sum_m \sum_n W^{trans}_{k_0,m,n}} \right] . \tag{4.3}$$

The one-third octave band centre frequencies chosen to construct the cost function were $k_0 = 5.45, 8.73, 13.74, 17.45$, chosen on the basis of their importance for rotor-stator interaction noise around 2BPF and Noy weighting curves. All optimisations are carried out using the ARMOGA search algorithm, utilising a Linux computer cluster to compute the GA populations.

An isocontour plot of the $CF$ cost function over the resistance-liner depth plane, for a multi-mode source, is presented in figure (4.13), together with the ARMOGA search points. The cost function is seen to increase towards higher resistances, a trend which was seen for discrete frequency optimisation in figure (C.6), which suggests that the higher frequencies dominate the optimisation.

Optimisation of axially-segmented liners was carried out for symmetric and asymmetric liners. However, the optimisation algorithm was found to be inadequate for the asymmetric problems. Therefore, the results presented here are for the symmetric cases only, and are *not* considered to represent the global optima. The optimised resistances, liner depths and liner length ratios for one, two, three and four segment liners are presented in table (4.4). The trend seen is for at least one long segment with similar properties to the optimum single segment liner. The power attenuation spectra of the four optimised liners are presented in figure (4.14), which shows that any benefits over the optimised uniform liner are very small, or incur a penalty at other frequencies. A thin liner is prescribed in order that the high frequency attenuation is maximised (the uniform liner depth being effectively tuned to $k_0 = 17.45$).

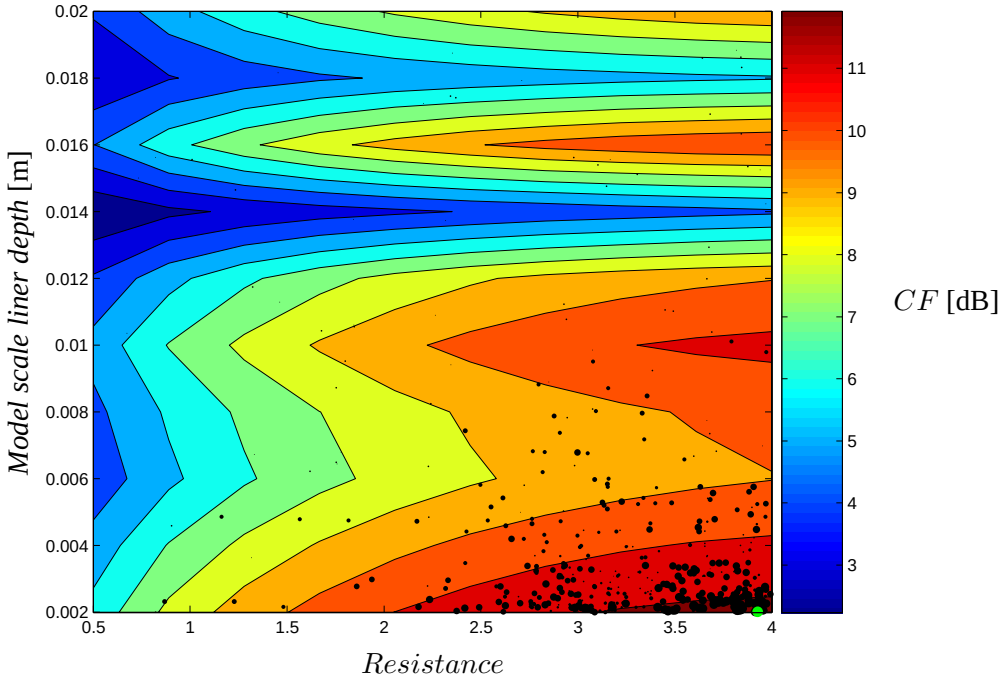


FIGURE 4.13: *Isocontours of combined frequency cost function $CF$ in the resistance-liner depth plane for a multi-mode, multi-frequency source. •, ARMOGA search points; •, ARMOGA optimum; $l_{liner} = 10$, $M = 0$.*

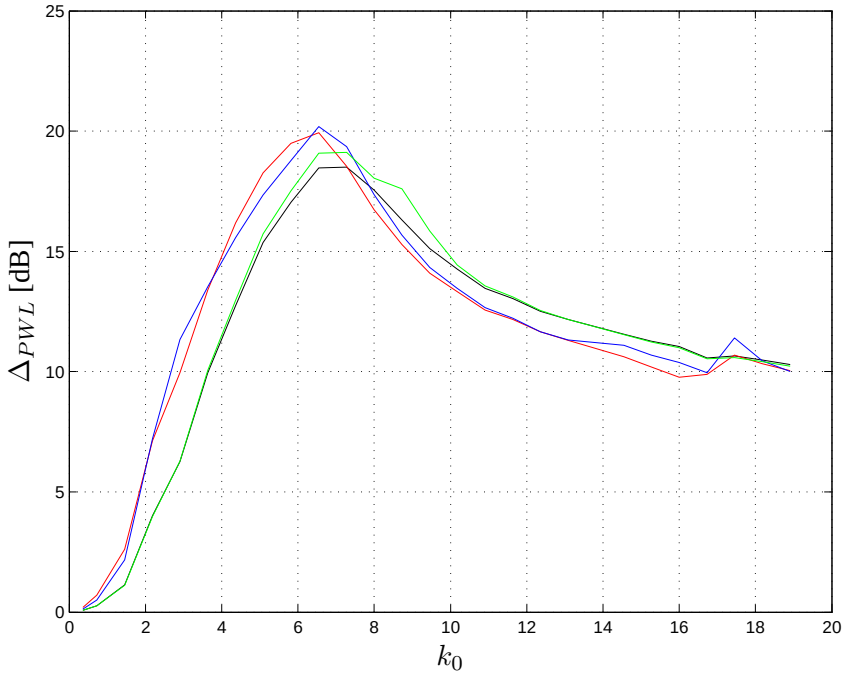


FIGURE 4.14: *Power transmission loss spectra for optimised axially-segmented symmetric liner designs for a multi-mode source. —, single segment; —, two segments; —, three segments; —, four segments; $l_{liner} = 10$, $M = 0$.*

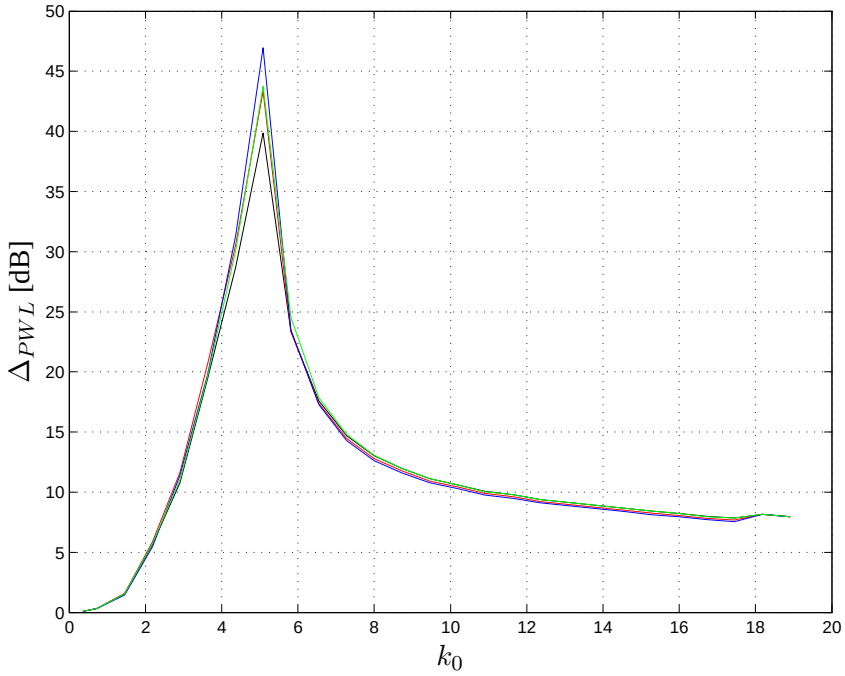


FIGURE 4.15: *Power transmission loss spectra for optimised axially-segmented symmetric liner designs for a rotor-stator interaction tonal source. —, single segment; —, two segments; —, three segments; —, four segments;* $l_{liner} = 10$, $M = 0$.

### 4.4.2 Rotor-stator interaction tonal source

Optimisation for a rotor-stator interaction tonal source was undertaken. The source is modelled by assuming an equal distribution of energy between uncorrelated cut-on radial modes at the relevant azimuthal order. The source is assumed to be generated by a twenty-four bladed fan, at a shaft rotation frequency of 145Hz, and fifty-two stator vanes. For these conditions, the interaction tone of most significance is generated at an azimuthal order $m = -4$, at 2BPF $k_0 = 5.06$, consisting of five cut-on radial modes. The optimised liner parameters are presented in table (4.5), and the trend seen is for short leading liners with low resistance followed by a long segment with a similar liner to the optimised uniform liner. The power transmission loss spectra for the optimised liners are shown in figure (4.15), and show that the multi-segment liners provide no benefit away from the target frequency of 2BPF.

### 4.4.3 Multi-objective optimisation

A multi-objective function optimisation was implemented in an effort to improve the high frequency multi-mode attenuation performance, whilst maintaining the rotor-stator interaction tone attenuation. The noise source for this case consists of a flat input power spectrum with equal energy per uncorrelated cut-on mode at four frequencies $k_0 = 5.06, 8.73, 13.74, 17.45$. The level of the $m = -4$ rotor-stator interaction tones at $k_0 = 2BPF = 5.06$ is set at 15dB above the multi-mode power level. The two cost functions are the $CF$ cost function and the

rotor-stator interaction tone power transmission loss $\Delta_{RS}$. The $\Delta_{RS}$ cost function was constrained to between 10 dB and 15dB in order to avoid results with unmeasureable attenuation levels. The ARMOGA algorithm was implemented in its multi-objective mode, and applied to symmetric liner configurations with mean flow $M = 0.4$. The optimised liner configurations are presented in table (4.6), and again the trend seen is for at least one longer segment with similar liner properties to the optimised uniform liner. Power transmission loss spectra are shown in figure (4.16) and demonstrate little improvement over a uniform liner. The spectra for the multi-mode source with and without flow are also plotted for reference, and show that the tuning frequency is simple adjusted to account for the 2BPF tonal source.

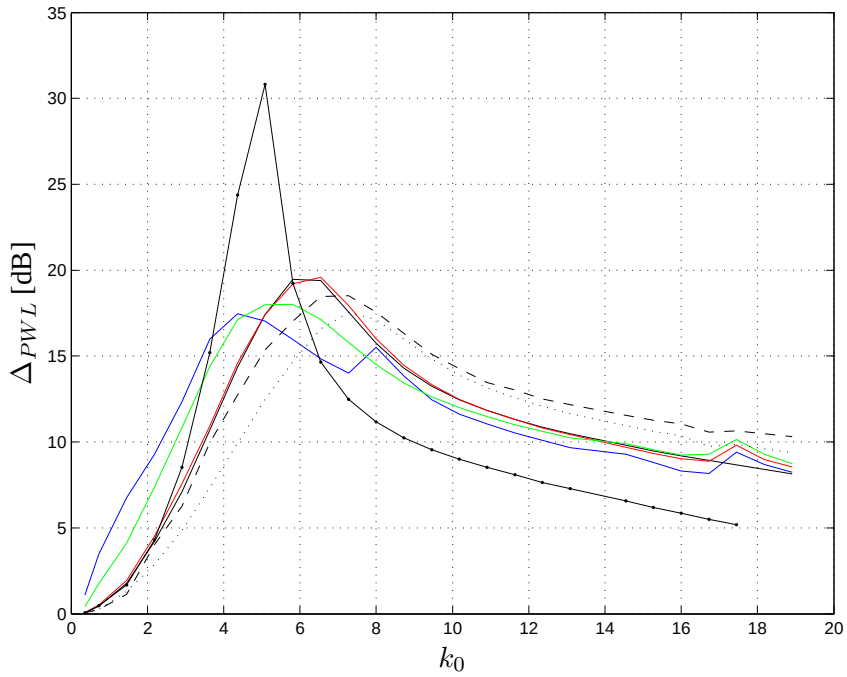


FIGURE 4.16: *Power transmission loss spectra for multi-objective optimised axially-segmented symmetric liner designs for a multi-mode source and rotor-stator interaction tonal source.* —*, single segment;* - -*,* $\Delta_{PWL}$ *optimised single segment,* $M = 0$*;* $\cdots$*,* $\Delta_{PWL}$ *optimised single segment;* -•-*,* $R = 0.8976$*,* $D = 0.1228$ *single segment;* —*, two segments;* —*, three segments;* —*, four segments;* $l_{liner} = 10$*,* $M = 0.4$*.*

The multi-objective search pattern is plotted for the two cost functions in figure (C.9). The $\Delta_{RS}$ cost function surface has a distinct optimum at $R = 0.8976$ $D = 0.1228$, whilst the $CF$ cost function has several local optima, but a similar global optima. The transmission loss spectra of this global optima is shown in figure (4.16) to have a very localised peak at 2BPF. By constraining the $\Delta_{RS}$ cost function, the final optima provides a better broadband attenuation. The algorithm convergence is shown in figure (C.10), where the mean and standard deviation of each cost function for each generation are also plotted. The ARMOGA algorithm performs a range adaptation every five generations, which corresponds to the drops seen in the cost functions. An upward trend is seen for every five generations of the $CF$ cost function over the entire optimisation period. However, this upward trend stops at around 1700 iterations for the

$\Delta_{RS}$ cost function, indicating that by this point the algorithm has reached the upper constraint of 15 dB, and concentrates upon maximising the $CF$ cost function. The optimum result is actually achieved at the 841st iteration, which indicates that, for the successive generations, the algorithm is rather inefficient for this problem.

## 4.5 Summary

- Rectangular duct mode-matching, using an uncorrelated multi-mode source assumption, compared well against experimental results for a lined annular duct.
- Optimisation of resistance and reactance was demonstrated for single and multi-segment liners for plane wave and multi-mode sources at discrete frequencies. Segmented liners can provide large benefits over uniform liners at relatively low frequencies for tonal sources. However, benefits for multi-mode sources were shown to be small.
- Optimisation of SDOF segmented liners was demonstrated using a combined frequency cost function, for both a tonal source and a multi-mode source. Segmented liners were seen to provide little benefit over uniform liners for a broadband source, since the optimisation was found to be dominated by the high frequency attenuation levels. Large benefits were possible for a tonal source.
- A multi-objective function optimisation was demonstrated for a broadband source with an interaction tone. It was found that the tonal noise attenuation level needs to be constrained in order to avoid designs that are highly localised to the frequency of the tone.

TABLE 4.4: *ARMOGA optimised resistance, liner depth and liner segment length ratios, for a multi-modal source with combined frequency cost function.* $M = 0$.

| Segments | CF cost | Segment length ratios | | | $R^{II}$ | $D^{II}$ | $R^{III}$ | $D^{III}$ | $R^{IV}$ | $D^{IV}$ | $R^{V}$ | $D^{V}$ |
|---|---|---|---|---|---|---|---|---|---|---|---|---|
| 1 | 13.03 | | | $l_{II}/l_{liner}$ | 3.927 | 0.05088 | | | | | | |
| 2 | 13.06 | | | 0.85 | 3.946 | 0.05088 | 2.634 | 0.06071 | | | | |
| | | | $l_{II}/l_{III}$ | $l_{III}/l_{liner}$ | | | | | | | | |
| 3 | 13.63 | | 0.28 | 0.165 | 1.306 | 0.24584 | 1.597 | 0.19018 | 3.504 | 0.05139 | | |
| | | $l_{II}/l_{III}$ | $l_{III}/l_{IV}$ | $l_{IV}/l_{liner}$ | | | | | | | | |
| 4 | 13.19 | 0.194 | 0.209 | 0.247 | 1.026 | 0.05189 | 2.477 | 0.06171 | 3.825 | 0.05340 | 3.832 | 0.05063 |

TABLE 4.5: *Optimised resistance, liner depth and liner segment length ratios, for a rotor-stator interaction tonal source with combined frequency cost function. $M = 0$.*

| Segments | $\Delta_{PWL}$ cost [dB] | Segment length ratios | | | $R^{II}$ | $D^{II}$ | $R^{III}$ | $D^{III}$ | $R^{IV}$ | $D^{IV}$ | $R^{V}$ | $D^{V}$ |
|---|---|---|---|---|---|---|---|---|---|---|---|---|
| 1 | 38.05 | | | $l_{II}/l_{liner}$ | 1.651 | 0.08741 | | | | | | |
| 2 | 42.14 | | | 0.0951 | 0.805 | 0.12494 | 1.653 | 0.08791 | | | | |
| | | | $l_{II}/l_{III}$ | $l_{III}/l_{liner}$ | | | | | | | | |
| 3 | 48.64 | | 0.382 | 0.293 | 0.576 | 0.13098 | 2.110 | 0.05365 | 1.497 | 0.09295 | | |
| | | $l_{II}/l_{III}$ | $l_{III}/l_{IV}$ | $l_{IV}/l_{liner}$ | | | | | | | | |
| 4 | 47.27 | 0.171 | 0.393 | 0.279 | 0.569 | 0.12695 | 0.997 | 0.10806 | 1.992 | 0.07078 | 1.596 | 0.09244 |

TABLE 4.6: *Multi-objective optimised resistance, liner depth and liner segment length ratios, for a multi-mode source and rotor-stator interaction tonal source.* $M = 0.4$.

| Segments | $CF$ cost | $\Delta_{RS}$ cost [dB] | Segment length ratios | | | $R^{II}$ | $D^{II}$ | $R^{III}$ | $D^{III}$ | $R^{IV}$ | $D^{IV}$ | $R^{V}$ | $D^{V}$ |
|---|---|---|---|---|---|---|---|---|---|---|---|---|---|
| 1 | 13.16 | 14.93 | | | $l_{II}/l_{liner}$ | 2.023 | 0.08715 | | | | | | |
| 2 | 13.42 | 14.96 | | | 0.082 | 1.008 | 0.19521 | 2.077 | 0.08086 | | | | |
| | | | | $l_{II}/l_{III}$ | $l_{III}/l_{liner}$ | | | | | | | | |
| 3 | 13.36 | 15.00 | | 0.563 | 0.685 | 1.932 | 0.09194 | 2.198 | 0.37935 | 1.857 | 0.09144 | | |
| | | | $l_{II}/l_{III}$ | $l_{III}/l_{IV}$ | $l_{IV}/l_{liner}$ | | | | | | | | |
| 4 | 13.48 | 14.86 | 0.440 | 0.366 | 0.614 | 0.704 | 0.19421 | 1.403 | 0.10025 | 2.061 | 0.08665 | 2.685 | 0.05290 |

# Chapter 5

# A RANS CFD analysis of acoustic propagation in bypass ducts with flow

Analytic methods can provide useful approximate solutions for acoustic propagation in bypass ducts for idealised uniform geometry and inviscid mean flow. However, the acoustic effects of the real curved duct geometry and non-uniform, viscous flows may only be calculated using numerical methods. Recent approaches to the problem were based upon solving the Linearised Euler Equations (LEE) on a predetermined mean flow field based on solution of the Navier-Stokes equations (viscous) or Euler equations (inviscid). Solution methods have included time and frequency domain solutions using Finite Element Methods (FEM) [109, 110], and time domain, high-order finite difference solutions [48, 49].

In this chapter, the effects of realistic mean flows upon the in-duct acoustic propagation of a 2BPF rotor-stator interaction tone is demonstrated, for a quasi-axisymmetric rigid bypass duct. A proprietary Rolls-Royce general purpose finite volume CFD code, *HYDRA*, is used to solve the governing flow equations. *HYDRA* is a suite of non-linear, linear and adjoint solvers for hybrid unstructured meshes using an efficient edge-based data structure [111, 112]. The flow equations are iterated towards steady state using a five-stage Runge-Kutta scheme, and a multigrid algorithm with preconditioning is used to accelerate convergence. The linear solver is obtained, using a fully-discrete approach, by linearising the discrete version of the nonlinear flow equations.

The aim of the work is two-fold: firstly to investigate the axial and radial variation of the mean flow, and secondly to demonstrate acoustic propagation for benchmark and realistic cases. The interest here in non-uniform mean flows is motivated by work on acoustic propagation in parallel sheared flows, which is documented in subsequent chapters. The radial profile of the mean flow is required, and it is also of interest to know the axial variation of the radial profile due to duct curvature and boundary layer growth. Acoustic solutions obtained using the linear solver can yield information on the acoustic scattering due to geometry curvature, mean flow variation, and boundary layer refraction.

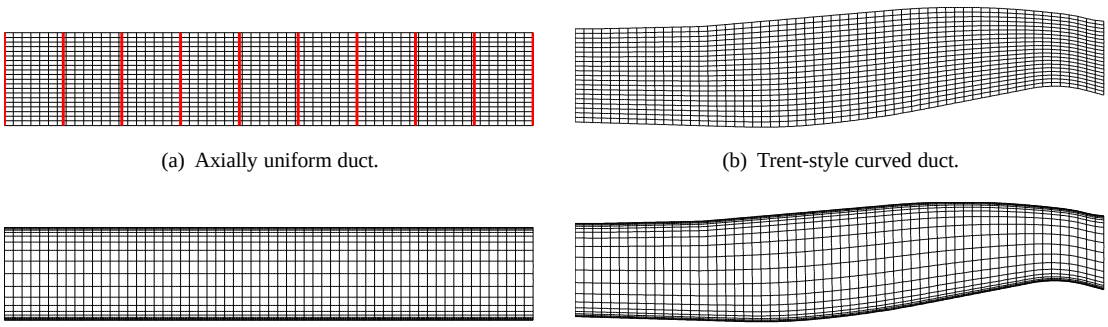

(a) Axially uniform duct.

(b) Trent-style curved duct.

(c) Axially uniform duct. Expanding grid.

(d) Trent-style curved duct. Expanding grid.

FIGURE 5.1: *Quasi-axisymmetric bypass duct mesh geometries used in the CFD study. Mesh size of 300 by 100 cells, where every fifth cell edge is plotted. Red lines indicate radial profile extraction planes.*

## 5.1 Problem specification and methods

Two quasi-axisymmetric annular bypass duct geometries were selected: an axially-uniform geometry, and a Rolls-Royce Trent-style three-quarter cowl geometry, which are shown in figure (5.1). The uniform duct geometry is determined from the average hub and casing wall radii of the curved duct, with the average hub-to-tip ratio being $\hbar = 0.62$. The total duct length is $3.28$m. The CFD meshes are quasi-axisymmetric, in the sense that the azimuthal construction of each mesh is a $1^\circ$ wedge of single cell depth. For the mean flow calculations a simple periodic boundary condition is implemented at the two azimuthal boundary planes. For acoustic calculations, since only individual azimuthal harmonics $m$ are considered, a phase-shifted periodic boundary condition is implemented at the azimuthal boundary planes, given by $e^{-im\Delta\theta}$, where $\Delta\theta = \pi/180$. A four-level multigrid is used throughout.

## 5.2 Flow field analysis

The mean flow entering the bypass duct is known to be radially non-uniform due to the fan-OGV stage [113]. The OGV stage tends to negate swirl. For this work three incident mean flow profiles are chosen: uniform mean flow, a realistic radially non-uniform mean flow with boundary layers, and a realistic radially non-uniform mean flow with wall slip conditions. The non-uniform incident mean flow is obtained from a nonlinear, steady CFD calculation for a Trent-style fan-OGV stage at an approach engine power condition [114]. The circumferentially averaged total temperature and total pressure radial profiles were extracted from the OGV passage solution, at a reasonable distance downstream of the OGV trailing edge. The corresponding Mach profiles are shown in figure (5.2). These values were then scaled and used as inlet boundary conditions for the current mean flow analysis. Inlet boundary conditions for the uniform mean flow analysis are obtained by averaging the realistic profile values, giving a total temperature $T = 307$ K, total pressure $P_t = 123000$ Pa and zero whirl angle. The outflow

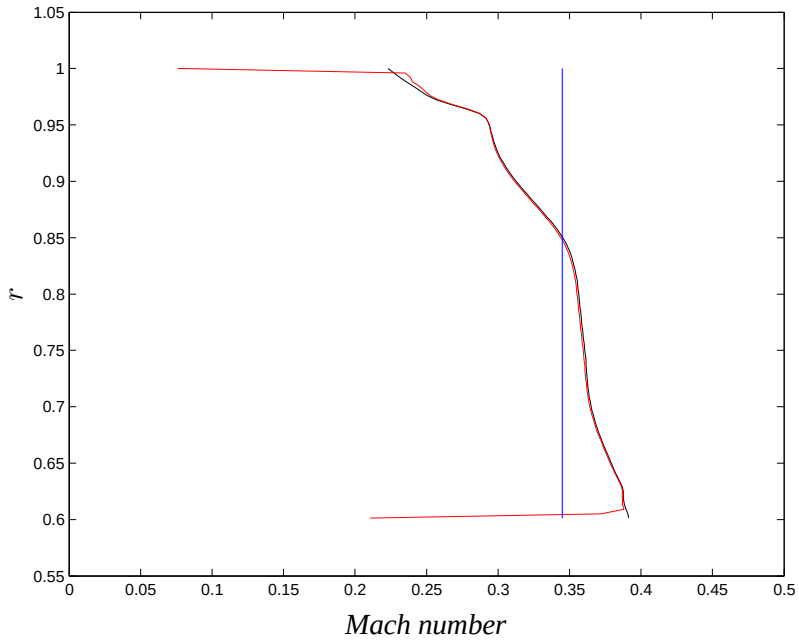


FIGURE 5.2: *Realistic inflow Mach profiles.* —, *with boundary layers;* —, *with wall slip conditions;* —, *uniform flow.*

boundary condition is static pressure $P_s = 101325$ Pa. The flow field is initialised using a uniform flow condition with density $\rho_0 = 1.279$ kg/m$^3$ and velocity $U_0 = 145$ m/s.

For both the uniform and curved geometries, both the viscous and inviscid steady flow fields are computed for the uniform inlet flow profile, and the non-uniform inlet flow profile with boundary layers. Only the inviscid flow field was solved for the non-uniform inlet flow profile with slip. For viscous flows the non-linear, viscous flow solver is used to solve the steady Reynolds Averaged Navier Stokes (RANS) equations with the Spalart-Allmaras turbulence model. An expanding mesh is used when solving the viscous flow equations, as shown in figure (5.1). For inviscid flows, the non-linear, inviscid flow solver is used to solve the steady Euler equations.

Mean flow information over the radial plane is extracted from each solution at ten axial locations indicated in figure (5.1).

### 5.2.1 Inviscid flows

Inviscid flow field Mach contours of the curved duct solutions for each inlet flow profile are shown in figure (5.3). For the uniform inlet flow case, the reduction in duct cross-section at the turbine hump results in higher flow speeds at the duct exit, and a negative flow profile gradient around the hump. However, by the duct exit, the radial profile returns to a uniform profile. This is demonstrated in the radial flow profile plots given for ten axial stations in figure (5.4). For the non-uniform inlet flows, a similar trend is seen with the exit flow profile remaining similar

(a) Uniform inlet flow.

(b) Non-uniform inlet flow with boundary layers.

(c) Non-uniform inlet flow with wall slip.

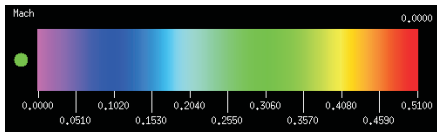


(d) Mach number scale.

FIGURE 5.3: *Mach number contours of inviscid flow solutions for the curved duct.*

to the inlet flow profile for this geometry. A distinct region of low flow velocity is found at the casing around halfway down the duct where the cross-section increases.

The uniform duct cases result in axially uniform flow fields and so are not discussed here.

### 5.2.2 Viscous flows

Viscous flow field Mach contours of the uniform duct solutions for uniform and non-uniform inlet flows are presented in figure (5.5). From the radial flow profiles shown in figure (5.6), it is seen that the boundary layer thickness increases by around 7% by the outlet plane.

The corresponding Mach contours for the curved duct case are presented in figure (5.7) and, as previously, the flow region around the turbine hump contains the greatest variation in radial flow profile as seen in figure (5.8).

## 5.3 Acoustic analysis

Using the linearised solver, the acoustic response of the flow to time-periodic excitation can be determined in the frequency domain. The acoustic source is prescribed at the inlet plane in terms of acoustic modes, where the axisymmetric azimuthal variation is maintained through phase-shifted periodic boundary conditions. Standard 1D (pointwise) characteristic boundary conditions are prescribed at the inflow and outflow boundaries. The acoustic modes are determined by solving the Pridmore-Brown equation [50], which describes sound propagation in a steady parallel inviscid non-uniform flow, using the implicit finite difference scheme of Vilenski and Rienstra [115]. The mean flow density and sound speed are assumed to be constant.

In order to investigate the nature of acoustic mode propagation through the duct it is necessary to decompose the acoustic flow into upstream and downstream propagation waves. This is undertaken using the eigenmode analysis method of Moinier and Giles [116], where the

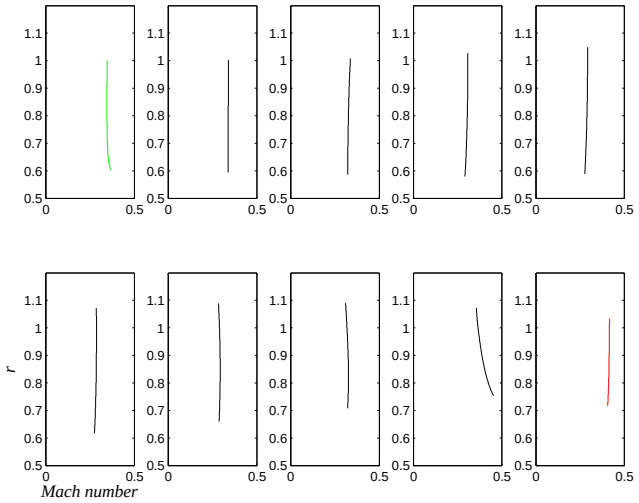


(a) Uniform inlet flow.

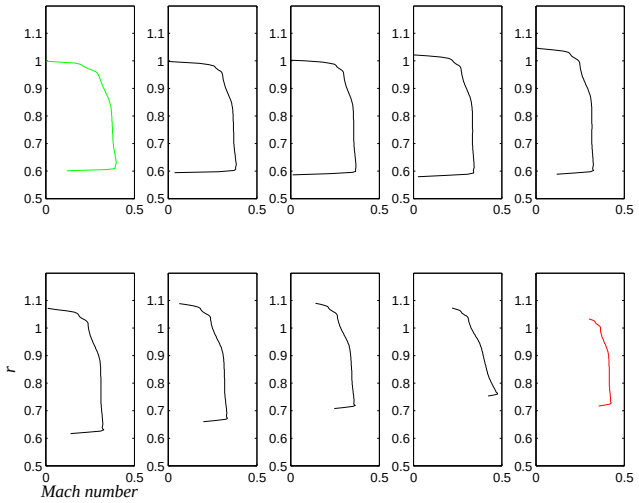


(b) Non-uniform inlet flow with boundary layers.

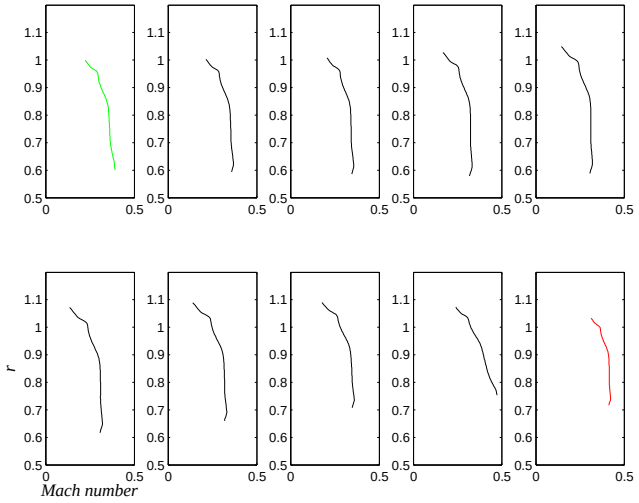


(c) Non-uniform inlet flow with wall slip.

FIGURE 5.4: *Mach number profiles at 10 axial stations of inviscid flow solutions for the curved duct. Radius normalised to inlet casing value.*

(a) Uniform inlet flow.

(b) Non-uniform inlet flow with boundary layers.

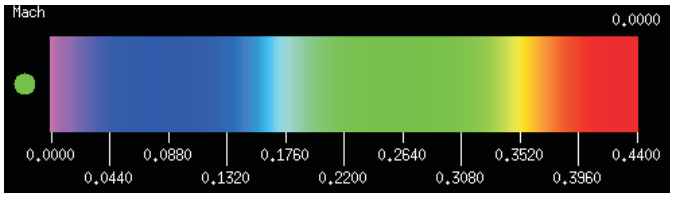


(c) Mach number scale.

FIGURE 5.5: *Mach number contours of viscous flow solutions for the uniform duct.*

discrete linear flow equations are formed into a Generalised Eigenvalue Problem (GEP), of which the eigenvectors are the approximate three-dimensional eigenmodes. The mean flow is assumed to be axially and circumferentially uniform. Acoustic, entropy and vorticity modes are recovered and are separated using a set of criteria. Modal decompositions are obtained for each solution at the ten axial planes indicated in figure (5.1). Upon obtaining the modal amplitude and eigenfunctions, the modal acoustic power flow is approximated using the formulation of Morfey [76].

In this study the incident acoustic perturbations are the 5 cut-on radial modes of the first rotor-stator interation tone $m = -4$ at 2BPF. Solutions are calculated for each incident mode in turn, so that an incoherent sum of the scattered modal powers can be obtained.

### 5.3.1 Numerical dissipation and dispersion

It is necessary to check the suitability of the mesh for performing acoustic calculations. The cell size must be fine enough such that dissipation (related to amplitude errors) and dispersion (related to phase errors) of the acoustic perturbations due to cell-to-cell numerical error is small. The unsteady solution for the propagation of mode (-4,1) in the uniform duct with uniform flow is used to determine the dissipation and dispersion errors on the chosen mesh. An orthogonal mesh of 300 by 100 cells was used, which provides around 27 axial points per

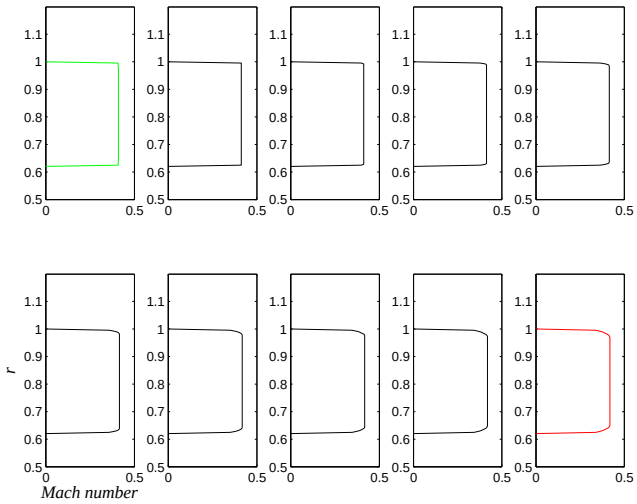


(a) Uniform inlet flow.

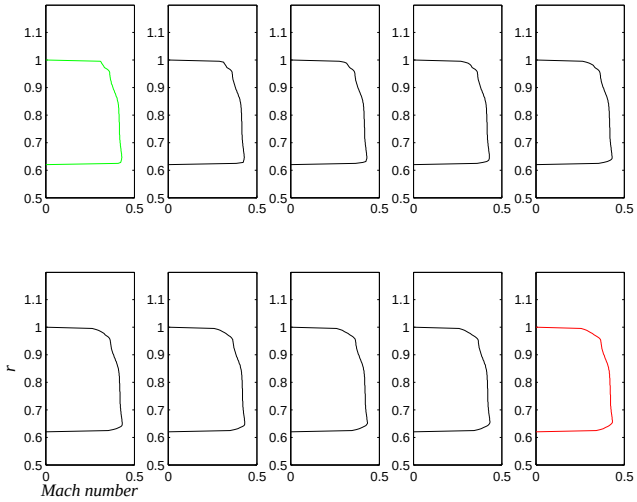


(b) Non-uniform inlet flow with boundary layers.

FIGURE 5.6: *Mach number profiles at 10 axial stations of viscous flow solutions for the uniform duct. Radius normalised to inlet casing value.*

Doppler-corrected wavelength, and 52 radial points per Doppler-corrected wavelength. Relative amplitude and phase errors along the duct axial direction are plotted in figure (5.9), and demonstrate an amplitude dissipation rate of around $0.05$ dB per Doppler-corrected wavelength. This value compares well with previous dissipation studies for the HYDRA code [117]. The corresponding power loss over the duct axial extent is 6 percent, or around 0.25dB. This value is used in subsequent power calculations to correct transmitted powers for numerical dissipation. Reflected powers are not corrected since the path length of the waves is not known a priori.

(a) Uniform inlet flow.

(b) Non-uniform inlet flow with boundary layers.

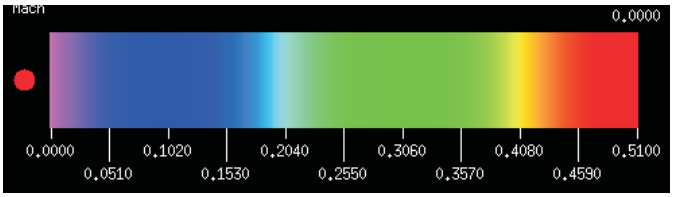


(c) Mach number scale.

FIGURE 5.7: *Mach number contours of viscous flow solutions for the curved duct.*

### 5.3.2 Mode propagation in inviscid flows

The scattered modal powers for the curved duct case with uniform inlet flow are shown in figure (5.10). Four modes are cut-on at the exit plane, compared with five at the inlet plane. A comparison of plots of the acoustic pressure for the modes (-4,1) and (-4,5) in figure (5.11) demonstrates the turning point of mode (-4,5) around the turbine hump. The modal power is reflected, as can be seen in the bar plots.

Mode scattering results of a corresponding Finite Element solution are also shown in figure (5.10), and demonstrate very good agreement with the CFD solution in the transmitted mode powers. The reflected power levels do not compare as well due to numerical dissipation in the CFD solution along the path length of the reflected waves. The axial variation in the individual and summed acoustic powers of the upstream and downstream cut-on modes is plotted is shown in figure (5.12). Mode (-4,5) is the least well cut-on mode and therefore more prone to reflection. The mode becomes cut-off around $x = 1.6$ and is strongly reflected. Most of the mode scattering occurs around the turbine hump region where both the flow field and mode cut-off ratios vary the most rapidly. The less well cut-on modes exhibit the largest amount of scattering.

The axial power variations for non-uniform inlet flow solutions with and without boundary layer velocity profiles are presented in figure (5.13) and (5.14) respectively. As seen for the

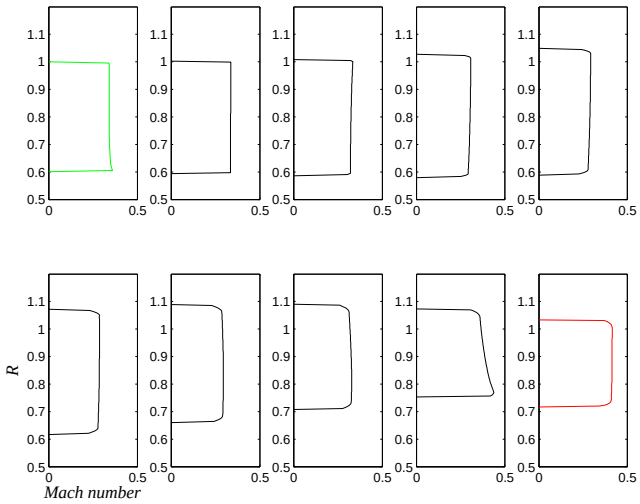


(a) Uniform inlet flow.

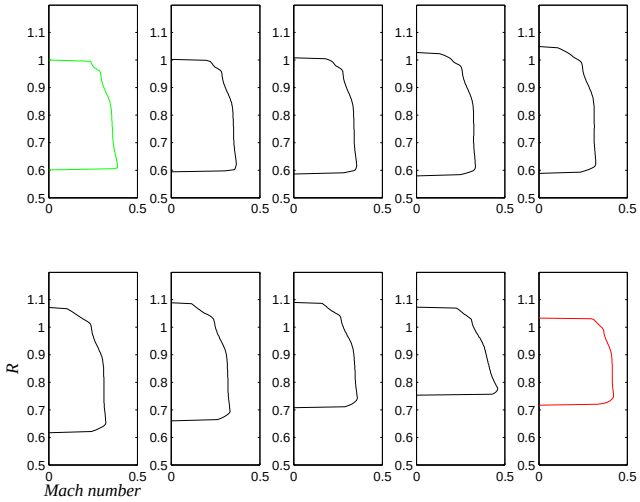


(b) Non-uniform inlet flow with boundary layers.

FIGURE 5.8: *Mach number profiles at 10 axial stations of viscous flow solutions for the curved duct. Radius normalised to inlet casing value.*

uniform inlet flow, most of the scattering occurs around the turbine hump, but more scattering is also seen before the turbine hump, and more prominently for the boundary layer inlet profile. The transmitted power at the outlet plane is lowest for the boundary layer profile.

### 5.3.3 Mode propagation in viscous flows

Axial power variations, from viscous solutions for the uniform duct with uniform and non-uniform inlet flows, are used to assess the effects of boundary layer growth on mode scattering, and are presented in figure (5.15) and (5.16), respectively. The less well cut-on modes are most affected by the boundary layer growth, and a stronger effect is seen for the non-uniform inlet flow. As the boundary layer grows, the modal energy is reflected.

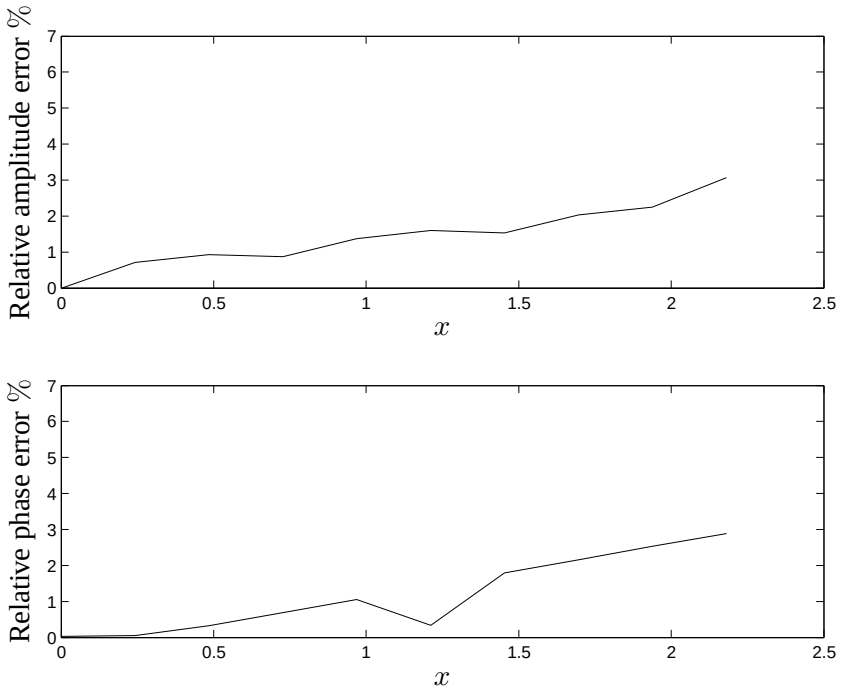


FIGURE 5.9: *Relative error in modulus and phase of mode* $(-4, 1)$ *complex amplitude in duct axial direction.*

Axial power variations for the curved duct with uniform and non-uniform inlet flows are shown in figures (5.17) and (5.18), respectively. Transmitted power levels are slightly lower than the equivalent Euler case for the less well cut-on modes. Qualitatively, the scattering is very similar for the well cut-on modes, indicating that the boundary layer effects can be adequately modelled by ignoring viscocity, but including a boundary layer velocity profile.

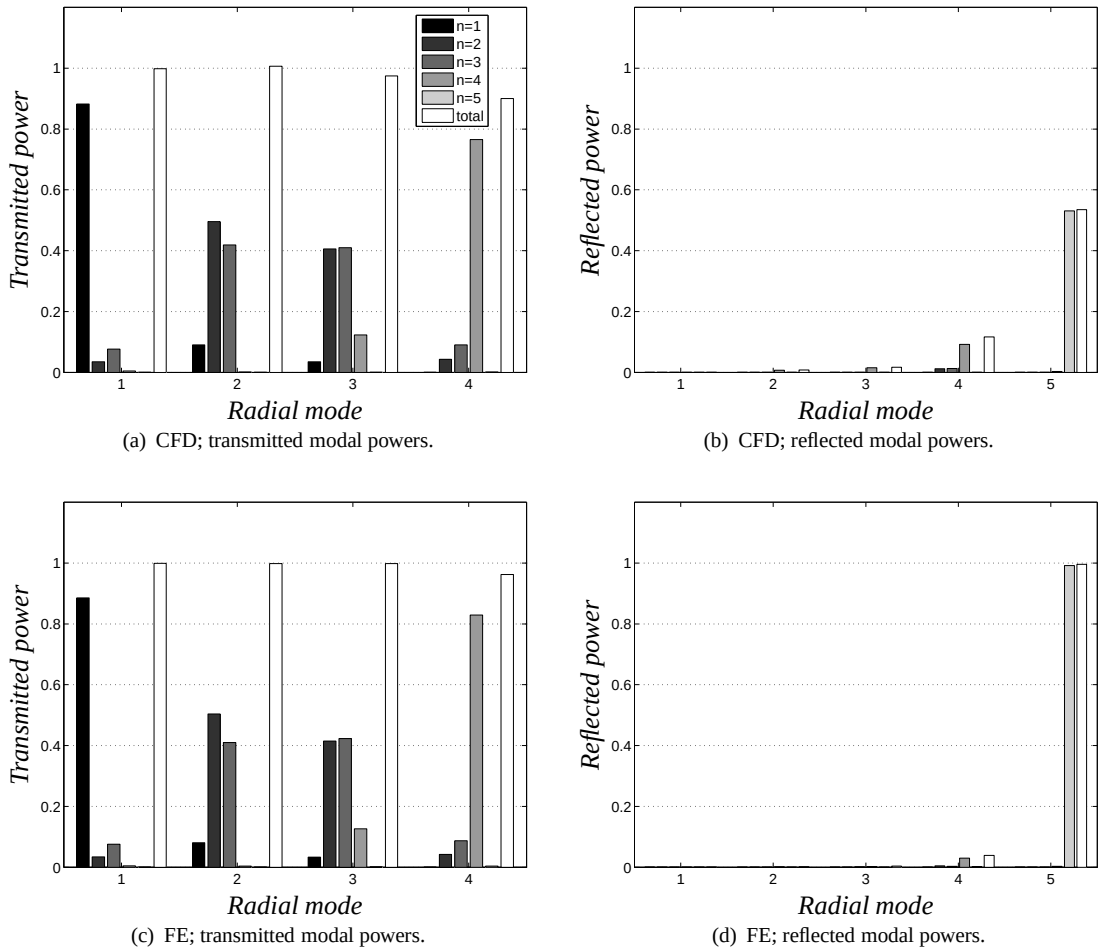


(a) CFD; transmitted modal powers.

(b) CFD; reflected modal powers.

(c) FE; transmitted modal powers.

(d) FE; reflected modal powers.

FIGURE 5.10: *Scattered modal powers from FE and CFD acoustic solutions on Euler mean flow fields, with a uniform inlet flow profile.*

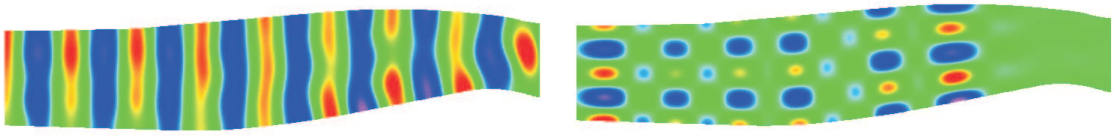

(a) $(-4, 1)$

(b) $(-4, 5)$

FIGURE 5.11: *Acoustic pressure (real part) contours for incident modes* $(-4, 1)$ *and* $(-4, 5)$ *for uniform inlet flow.*

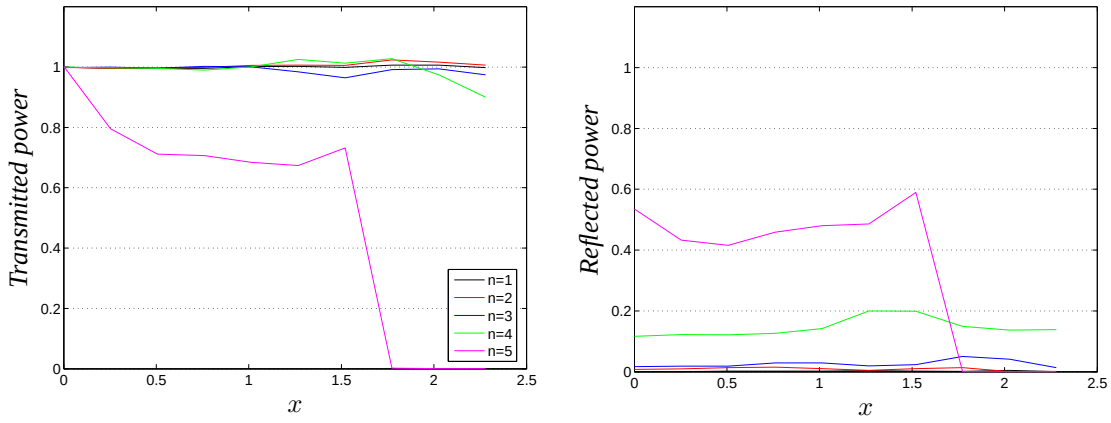


(a) Transmitted modal powers.

(b) Reflected modal powers.

(c) Total transmitted (—) and reflected (- -) powers.

FIGURE 5.12: *Axial variation in individual and summed modal powers from curved duct CFD acoustic solutions on an Euler mean flow field, with a uniform inlet flow profile.*

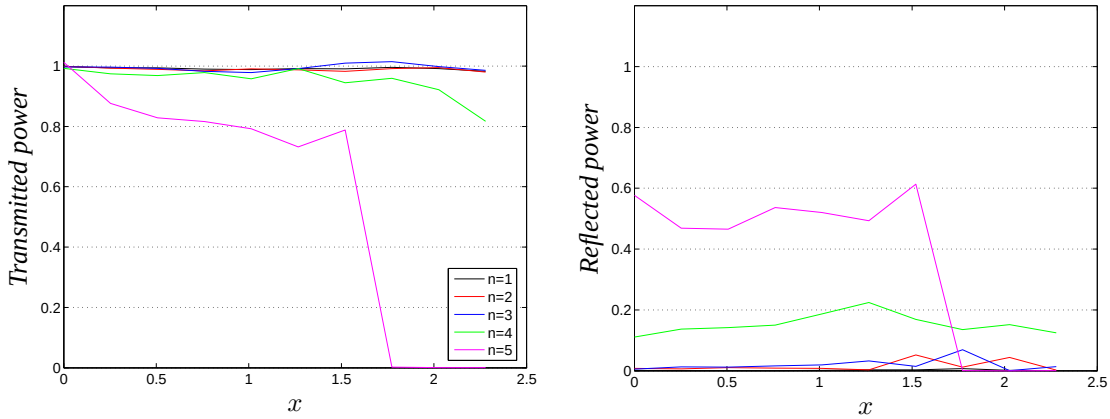


(a) Transmitted modal powers.

(b) Reflected modal powers.

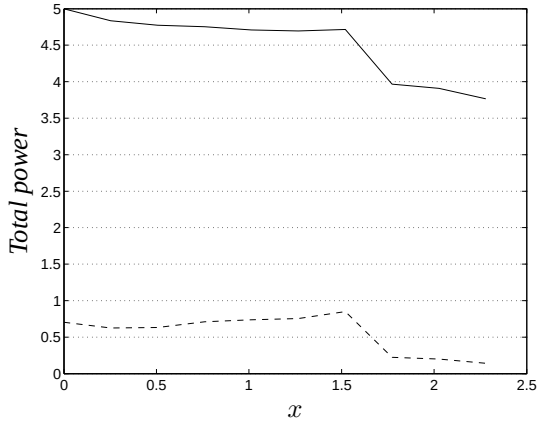


(c) Total transmitted (—) and reflected (- -) powers.

FIGURE 5.13: *Axial variation in individual and summed modal powers from curved duct CFD acoustic solutions on an Euler mean flow field, with a non-uniform inlet flow profile with boundary layers.*

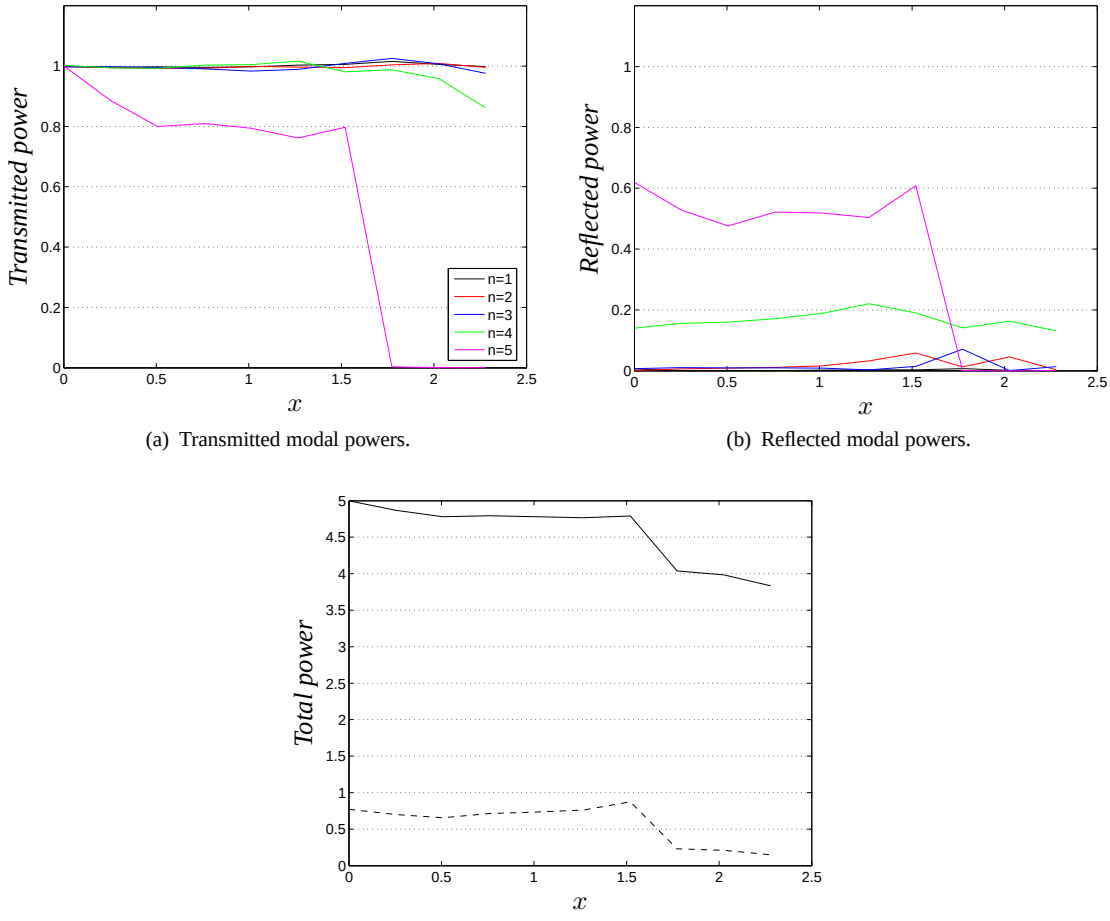


(a) Transmitted modal powers.

(b) Reflected modal powers.

(c) Total transmitted (—) and reflected (- -) powers.

FIGURE 5.14: *Axial variation in individual and summed modal powers from curved duct CFD acoustic solutions on an Euler mean flow field, with a non-uniform inlet flow profile with wall slip.*

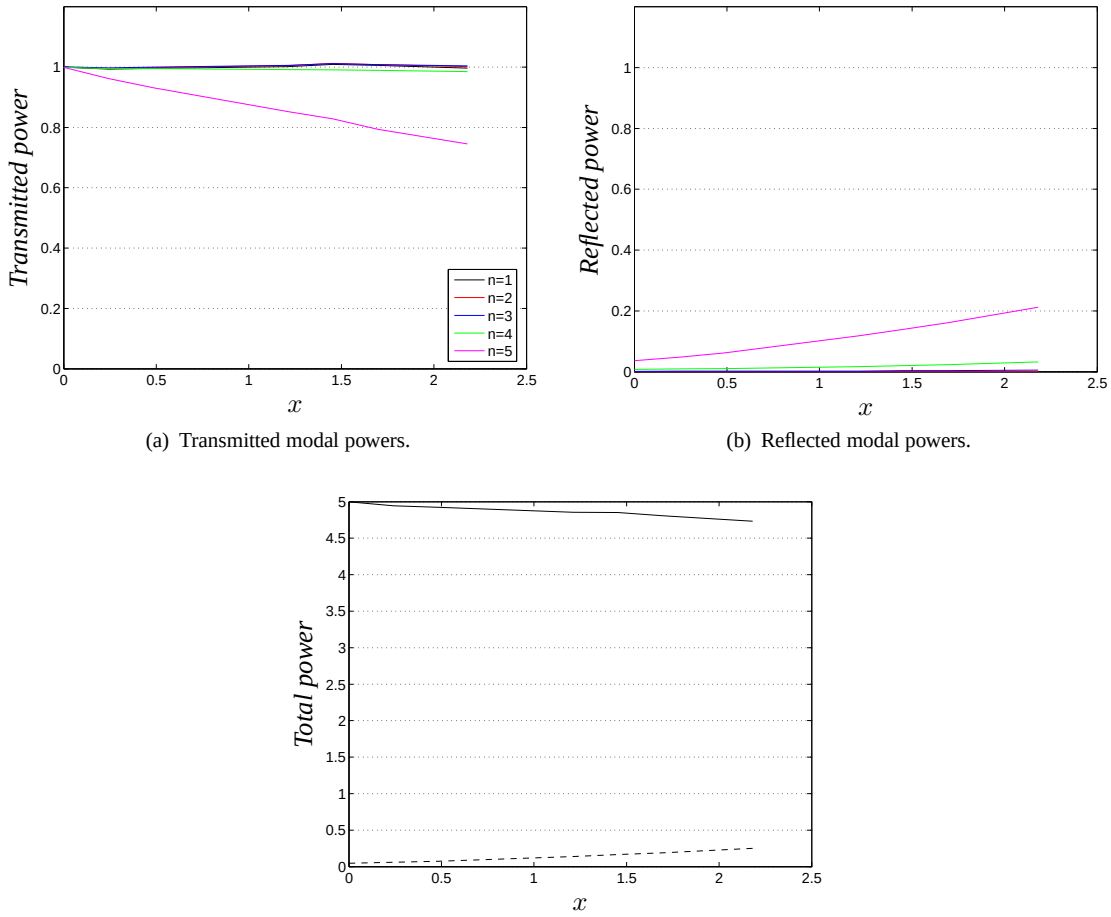


(a) Transmitted modal powers.

(b) Reflected modal powers.

(c) Total transmitted (—) and reflected (- -) powers.

FIGURE 5.15: *Axial variation in individual and summed modal powers from uniform duct CFD acoustic solutions on a viscous mean flow field, with a uniform inlet flow.*

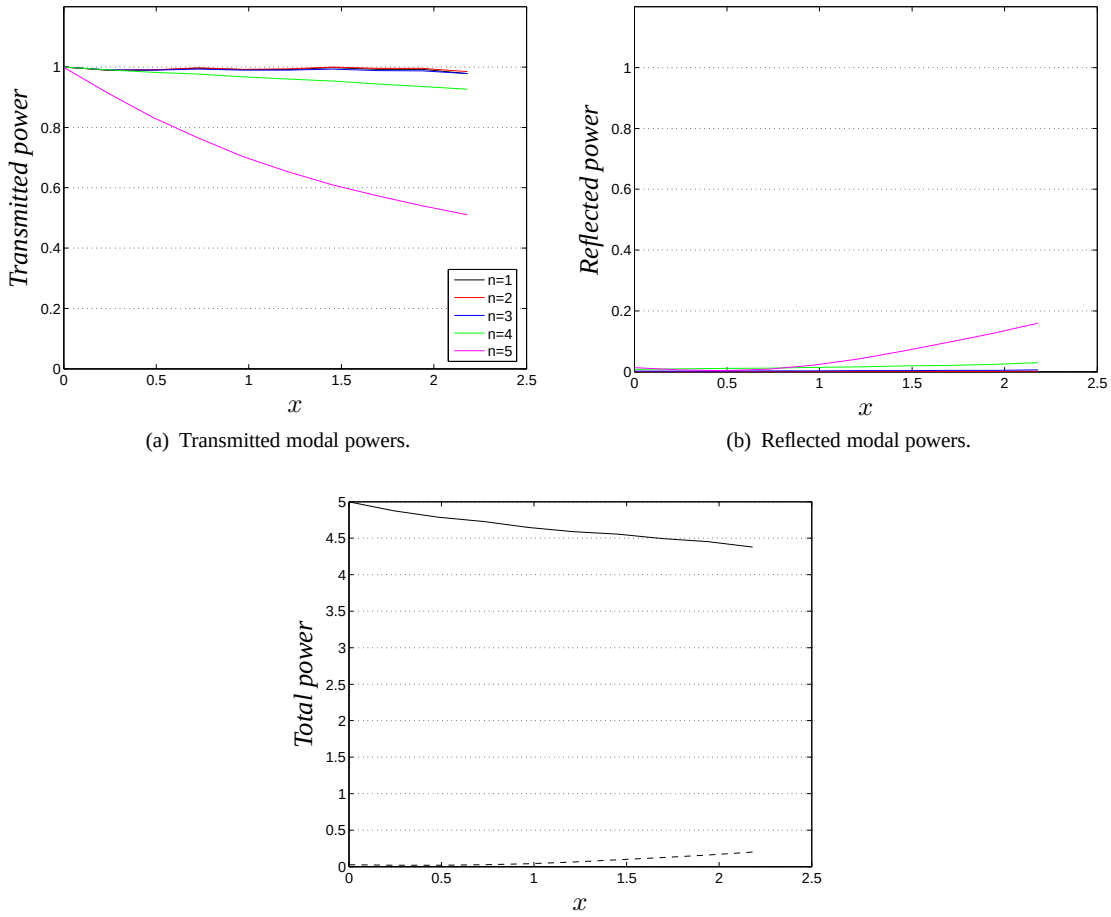


(a) Transmitted modal powers.

(b) Reflected modal powers.

(c) Total transmitted (—) and reflected (- -) powers.

FIGURE 5.16: *Axial variation in individual and summed modal powers from uniform duct CFD acoustic solutions on a viscous mean flow field, with a non-uniform inlet flow.*

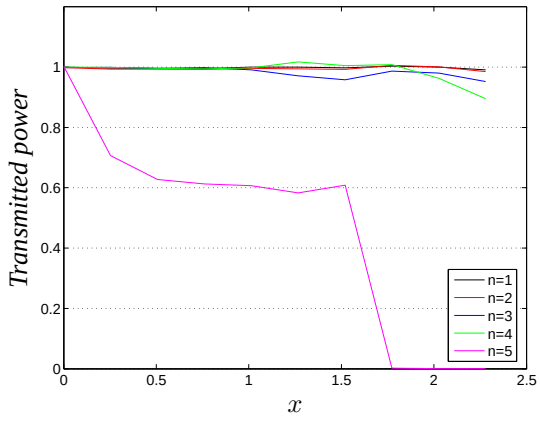


(a) Transmitted modal powers.

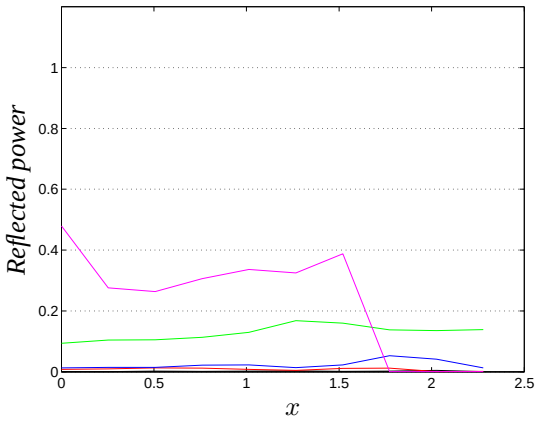


(b) Reflected modal powers.

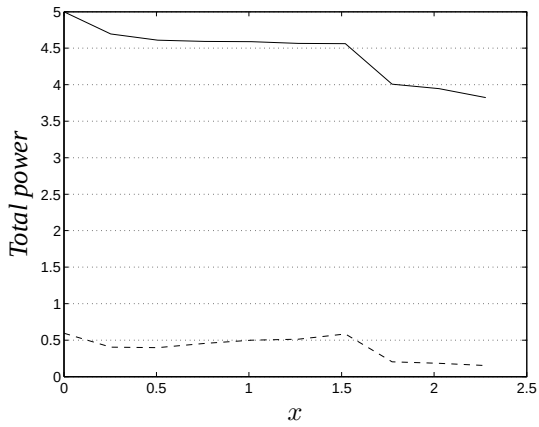


(c) Total transmitted (—) and reflected (- -) powers.

FIGURE 5.17: *Axial variation in individual and summed modal powers from curved duct CFD acoustic solutions on a viscous mean flow field, with a uniform inlet flow.*

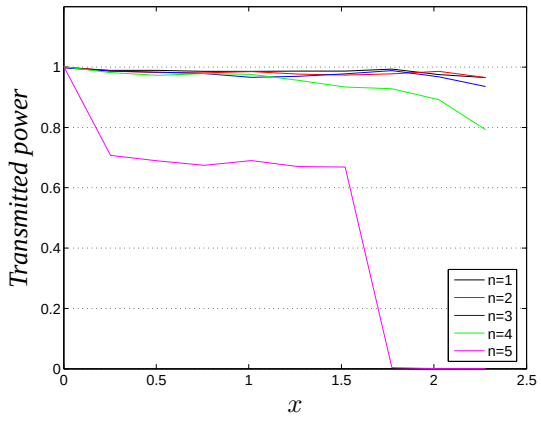


(a) Transmitted modal powers.

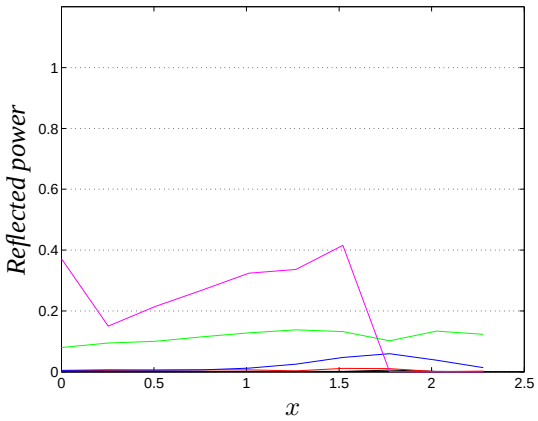


(b) Reflected modal powers.

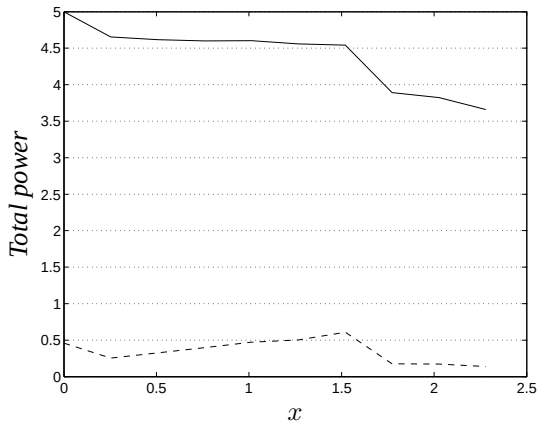


(c) Total transmitted (—) and reflected (- -) powers.

FIGURE 5.18: *Axial variation in individual and summed modal powers from curved duct CFD acoustic solutions on a viscous mean flow field, with a non-uniform inlet flow.*

## 5.4 Summary

- A series of inviscid and viscous steady flow CFD calculations were undertaken to investigate the characteristics of bypass duct flows. Both uniform and realistic curved ducts with uniform and realistic inlet flow profiles were considered at an approach engine power condition.
- The duct region around the turbine hump contains higher flow velocities with a negative general flow gradient. The outlet flow velocity is higher, due to mass flow continuity, but the general outlet profile remains similar to that at the inlet for this geometry. A boundary layer growth of 7 percent is observed for the conditions investigated.
- Acoustic solutions were obtained for the various base flows using a linear CFD solver. Incident acoustic perturbations were prescribed in terms of modes obtained from inviscid, parallel flow equations.
- Acoustic solutions on an Euler flow with uniform inlet flow were compared with an equivalent Finite Element solution. Qualitatively, the mode scattering compared very well. Transmitted modal powers must be corrected for mesh dissipation, which is not possible for the reflected power without prior knowledge of wave path lengths.
- Acoustic power flow was assessed using a decomposition of the CFD solution into eigenmodes of the Euler flow equations. The region around the turbine hump contains the most mode scattering. Non-uniform inlet flow cases have more scattering than for uniform inlet flow. The growing boundary layers cause reflection which is most prominent in the higher order modes.
- When comparing viscous and inviscid solutions is was found that the strongest differences in the scattering were found in the higher mode orders. However, differences in the more important low order modes are small. Thus, considerable computational savings can be achieved by using inviscid solutions with realistic inlet profiles, which will capture the most important scattering effects.

# Chapter 6

# Acoustic propagation in lined annular ducts with parallel sheared flow

This chapter outlines the theory and methods used to obtain acoustic eigenmode solutions of an axially uniform, lined annular duct containing an inviscid, parallel subsonic mean flow. Most of the related work on sound transmission in sheared flows was undertaken between the 1950s and 1980s, see for example the reviews in references [118, 2, 4]. In contrast to the case of no flow or uniform flow, there does not appear to be a general method for obtaining analytic solutions to the governing linearised Euler equations for arbitrary sheared flows (closed form solutions exist for linearly sheared flow [119, 120, 121, 122], parabolic flow [123, 124, 125] and exponential boundary layers [126]). The most common solution procedure is to obtain a second order ordinary differential equation in pressure, referred to as the Pridmore-Brown equation [50]. This is derived in the following section. Alternatively, the solution of two first order coupled equations in pressure and radial particle velocity was preferred by Tester [51], citing better convergence properties. One problem that arises in these formulations is the presence of a singularity when the mean flow gradient becomes infinite, as is the case for power law boundary layer profiles [127], or as the boundary layer thickness is reduced to slip flow conditions at the wall [51]. An alternative formulation in terms of pressure and particle displacement was derived by Smith and Morfey [128] for the problem of sound radiation from a wall source under a boundary layer. It is shown that the mean velocity gradient can be eliminated. The three formulations are outlined and assessed in the following sections, in light of the problem considered here.

The eigenvalue problem formed by the governing equations, applying the relevant boundary conditions, must be solved numerically. Four popular solution methods include shooting methods [115, 129, 130], the Galerkin method of weighted residuals [131], finite difference methods [132, 92, 133], and finite element or wave envelope methods [134, 135, 133]. With the exception of shooting methods, these solutions methods yield entire sets of eigenvalues in one calculation. Galerkin methods require a large basis function set in order to resolve higher order

modes, especially for impedance boundary conditions [131, 136]. Finite difference methods require specially modified matrix procedures in order to circumvent matrix conditioning problems [92, 133]. Shooting methods based on Runge-Kutta integration or finite difference marching methods require iterations in flow profile and wall impedance from an initial guess starting value. A shooting method has been chosen here to demonstrate the applicability of the eigenvalue tracking method used previously (see Chapter (2)). This provides useful information on the effect on the mode eigenvalues of modifying both the flow profile and the wall impedances.

## 6.1 Governing equations

In this work, modelling of acoustic propagation is based upon linearisation of the Euler equations, governing the motion of an inviscid, compressible, isentropic perfect gas. Gas flow through a prismatic circular duct of annular cross-section is considered, as shown in figure (6.1). Using cylindrical polar coordinates $\left(\tilde{r}, \tilde{\theta}, \tilde{x}\right)$, where $\tilde{}$ denotes the dimensional values. The non-uniform, steady mean flow is assumed to be parallel, such that the density $\rho_0$ and pressure $p_0$ are constant, and the velocity $\mathbf{U} = (0, 0, U_0(\tilde{r}))$ is arbitrarily nonuniform in the radial direction. For this mean flow, the linearised Euler equations, in non-dimensional form, are

$$\text{Acoustic continuity} \qquad \frac{D_0\hat{p}}{Dt} = -\nabla \cdot \hat{\mathbf{u}}\,, \tag{6.1}$$

$$\text{Acoustic momentum} \qquad \frac{D_0\hat{\mathbf{u}}}{Dt} + (\hat{\mathbf{u}} \cdot \nabla)\,\mathbf{M} = -\nabla \cdot \hat{p}\,, \tag{6.2}$$

non-dimensionalising as per Section (2.1), with the reference length scale being the outer duct radius $d$. The acoustic equation of state is $\hat{p} = c_0^2\hat{\rho}$, and the material derivative is defined as $D_0/Dt = \partial/\partial t + (\mathbf{M} \cdot \nabla)$. The following subsections detail how the field equations may be combined to obtain ordinary differential equations (ODEs) in pressure, pressure and particle velocity, and pressure and particle displacement. When combined with the wall boundary conditions these ODEs constitute the eigenvalue problem for the duct modes.

### 6.1.1 The Pridmore-Brown equation

Following Goldstein [137], taking the divergence of the momentum equation gives

$$\nabla^2\hat{p} + \frac{D_0}{Dt}\left(\nabla \cdot \hat{\mathbf{u}}\right) + \hat{\mathbf{x}}2\frac{\mathrm{d}M}{\mathrm{d}r}\frac{\partial\hat{u}}{\partial x} = 0\,, \tag{6.3}$$

and operating on the continuity equation with $D_0/Dt$ gives

$$\frac{D^2\hat{p}}{Dt^2} + \frac{D}{Dt}\left(\nabla \cdot \hat{\mathbf{u}}\right) = 0\,. \tag{6.4}$$

Subtracting equation (6.4) from equation (6.3) results in a single differential equation in two dependent unknowns given by

$$\nabla^2 \hat{p} - \frac{D_0 \hat{p}}{Dt} + \hat{\mathbf{x}} 2 \frac{\mathrm{d}M}{\mathrm{d}r} \frac{\partial \hat{v}}{\partial x} = 0 \,. \tag{6.5}$$

The radial acoustic particle velocity $\hat{v}$ is eliminated by forming the axial partial derivative of radial momentum equation to give

$$\frac{D_0}{Dt} \frac{\partial \hat{v}}{\partial x} = -\frac{\partial \hat{p}}{\partial x \partial r} \,. \tag{6.6}$$

Operating on equation (6.5) with $D_0/Dt$ and substituting equation (6.6) results in a single third order differential equation in pressure given by

$$\frac{D_0}{Dt} \left( \nabla^2 - \frac{D_0^2}{Dt^2} \right) \hat{p} - 2 \frac{\mathrm{d}M}{\mathrm{d}r} \frac{\partial^2 \hat{p}}{\partial x \partial r} = 0 \,. \tag{6.7}$$

Then, on assuming time-harmonic modes of the form

$$\hat{p}\,(r, \theta, x) = p\,(r)\, e^{-i(m\theta + kx)} \,, \tag{6.8}$$

equation (6.7) becomes

$$\frac{\mathrm{d}^2 p}{\mathrm{d}r^2} + \left[ \frac{1}{r} + \frac{2k}{k_0 - kM} \frac{\mathrm{d}M}{\mathrm{d}r} \right] \frac{\mathrm{d}p}{\mathrm{d}r} + \left[ (k_0 - kM)^2 - \frac{m^2}{r^2} - k^2 \right] p = 0 \,, \tag{6.9}$$

which is known as the Pridmore-Brown equation. The wall boundary conditions are determined from continuity of particle displacement at the walls, i.e.

$$\frac{\mathrm{d}p}{\mathrm{d}r} = -\frac{i}{k_0 Z_d} \left( k_0 - kM \right)^2 p \qquad \text{at} \quad r = 1 \,, \tag{6.10}$$

$$\frac{\mathrm{d}p}{\mathrm{d}r} = \frac{i}{k_0 Z_h} \left( k_0 - kM \right)^2 p \qquad \text{at} \quad r = h \,, \tag{6.11}$$

where $Z_h$ and $Z_d$ are the hub and casing wall impedances, respectively.

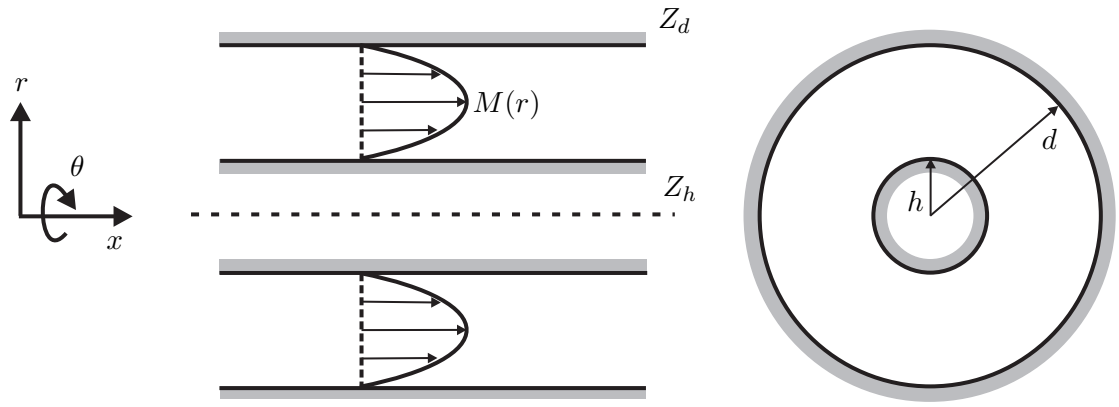


FIGURE 6.1: *Geometry for a lined annular duct containing arbitrary sheared flow.*

### 6.1.2 Pressure and particle velocity coupled ODEs

Coupled ODEs in pressure and radial particle velocity are obtained by eliminating axial and azimuthal velocity components from the continuity equation, which in expanded form is

$$i\left(k_0 - kM\right)p + \frac{1}{r}\frac{\partial(vr)}{\partial r} + \frac{imw}{r} - iku = 0\,. \tag{6.12}$$

The axial and azimuthal momentum equations are rearranged to give

$$u = \frac{1}{k_0 - kM}\left(kp + iv\frac{\mathrm{d}M}{\mathrm{d}r}\right)\,, \tag{6.13}$$

$$w = \frac{mp}{r\left(k_0 - kM\right)}\,. \tag{6.14}$$

Substituting into equation (6.12), and rearranging for $vr$ gives

$$\frac{\partial(vr)}{\partial r} = \left[\left(k_0 - kM\right)^2 - \frac{m^2}{r^2} - k^2\right]\frac{pr}{i\left(k_0 - kM\right)} - \frac{k}{k_0 - kM}\frac{\mathrm{d}M}{\mathrm{d}r}\left(vr\right)\,. \tag{6.15}$$

The radial momentum equation is rearranged for $p$ to give

$$\frac{\partial p}{\partial r} = \frac{-i\left(k_0 - kM\right)}{r}\left(vr\right)\,. \tag{6.16}$$

Together, equations (6.15) and (6.16) form the coupled first order ODEs to be solved for $p$ and $vr$. The wall boundary conditions are determined from continuity of particle displacement at the walls, i.e.

$$vr = \frac{r}{k_0 Z_d}\left(k_0 - kM\right)p \qquad \text{at} \quad r = 1\,, \tag{6.17}$$

$$vr = -\frac{r}{k_0 Z_h}\left(k_0 - kM\right)p \qquad \text{at} \quad r = h\,. \tag{6.18}$$

### 6.1.3 Pressure and particle displacement coupled ODEs

Coupled ODEs in pressure and particle displacement $\epsilon_r$ are obtained following the analysis of Smith [52], by eliminating radial particle velocity using the following expression

$$vr = \frac{D_0\left(\epsilon_r r\right)}{Dt} = \left(\epsilon_r r\right)i\left(k_0 - kM\right)\,. \tag{6.19}$$

Taking the radial derivative and rearranging for $\epsilon_r$ gives

$$\frac{\partial(\epsilon_r r)}{\partial r} = -\frac{1}{\left(k_0 - kM\right)^2}\left[i\left(k_0 - kM\right)\frac{\partial}{\partial r} + ik\frac{\mathrm{d}M}{\mathrm{d}r}\right]\left(vr\right)\,. \tag{6.20}$$

On substituting equation (6.15), the flow gradient term is eliminated, leading to the following

$$\frac{\partial(\epsilon_r r)}{\partial r} = \left[\frac{m^2}{r^2} + k^2 - (k_0 - kM)^2\right] \frac{pr}{(k_0 - kM)^2} \,. \tag{6.21}$$

Substituting equation (6.19) into the radial momentum equation gives

$$\frac{\partial p}{\partial r} = \frac{(k_0 - kM)^2}{r} (\epsilon_r r) \,, \tag{6.22}$$

which, together with equation (6.21), form coupled ODEs in pressure and particle displacement. The wall boundary conditions are determined from continuity of particle displacement at the walls, i.e.

$$\epsilon_r r = -\frac{ir}{k_0 Z_d} p \qquad \text{at} \quad r = 1 \,, \tag{6.23}$$

$$\epsilon_r r = \frac{ir}{k_0 Z_h} p \qquad \text{at} \quad r = h \,. \tag{6.24}$$

Note that the boundary conditions do not contain the eigenvalue $k$ or the mean flow Mach number $M$ at the wall.

## 6.2 Computational scheme

The eigenvalue problems set out in the previous section are solved for individual mode eigenvalues $k$ using a shooting method. The method for finding the eigenvalues is summarised as follows:

1. Select an initial value of $k$.
2. Specify values of the relevant wave variables at one of the walls which satisfy the boundary condition.
3. Use either an integration routine or a finite difference routine to compute the wave variables across the annulus, from the system of governing ODEs.
4. Calculate the error in the far wall boundary condition. If the error is below a given tolerance then the current choice of $k$ is kept, otherwise a new value of $k$ is found using Muller's iteration method [138].

In general, the method marches from the hub wall to the casing wall, except in the case of hydrodynamic surface waves. In this instance, the method marches from the wall *opposite* to that which the surface wave is attached. This is to avoid errors in the boundary condition calculation due to the exponential behaviour of the hydrodynamic surface wave eigenfunction. The initial value of pressure at the starting wall is set to be $p = 1 + 0i$, and the other wave variables are determined from the relevant boundary condition.

The initial value of $k$ is determined from a tracking scheme where the eigenvalue is tracked with systematic increments in mean flow profile and wall impedance. The impedance tracking method is similar to that described in Chapter (2). The tracking scheme for finding the eigenvalues of an annular duct containing an arbitrary non-uniform flow $M(r)$, with casing wall impedance $Z_d$ and hub wall impedance $Z_h$ is summarised as follows:

1. Select an initial value of $k$ to be the eigenvalue of either the no flow or uniform flow case with rigid walls.
2. Calculate new values of $k$ for increments in the mean flow profile, from the no flow or uniform flow condition to the required profile.
3. Calculate new values of $k$ for increments in the admittance of the wall from which the shooting method marches. The admittance is incremented from the rigid wall condition $\beta = 0 + i0$ to the nearly rigid wall condition $\beta = 1/(R + iX_\infty)$.
4. Calculate new values of $k$ for increments in the impedance of the wall from which the shooting method marches. The impedance is incremented from the nearly rigid wall condition $Z = R + iX_\infty$ to the required wall impedance $Z = R + iX$, where the resistance $R$ is held constant.
5. Steps (3) and (4) are repeated for the far wall.

The initial no flow or uniform flow eigenvalues for a duct with rigid walls are obtained from closed form solutions [136]. The mean flow profile is incremented by either modifying the coefficients of analytic flow profiles, or by using a windowing function for discrete flow profiles. The choice of windowing function generally depends upon the features of the chosen flow profile (e.g. boundary layers, flow value range, local flow gradients), and examples of functions used here include sine curve, Hermite polynomial and uniform increments.

An addition to the impedance tracking method used here is the refinement of the reactance contour from $X_\infty$ to $X$, around regions where the eigenvalue changes rapidly with impedance, as highlighted in Section (2.4). From Brambley and Peake [75], the contour is refined around $X = -2U_0/\left(1 - U_0^2\right)^{3/2}$, 0, and $2U_0/\left(1 - U_0^2\right)^{3/2}$, where $U_0$ is the mean flow velocity at the wall.

The shooting method is undertaken using a 4th order Runge-Kutta integration scheme [130]. Closed form solutions for the uniform flow case are used for a grid point refinement study. The error in the boundary condition using the exact eigenvalue is plotted in figure (6.2). Errors for solutions of the Pridmore-Brown equation, pressure and velocity ODEs, and pressure and displacement ODEs are shown to have order of magnitude differences. The boundary condition errors are measured in terms of pressure gradient, particle velocity and particle displacement for the three governing ODEs respectively. The order of magnitude difference in error is due to the choice of dependant variables. This is demonstrated in figure (6.3), where the error in the

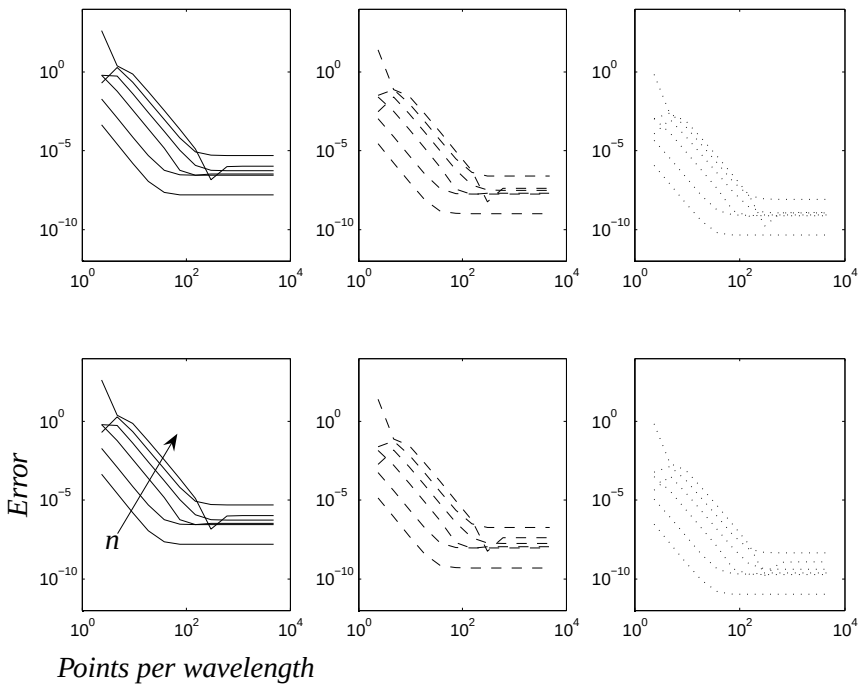


FIGURE 6.2: *Boundary condition error due to exact uniform flow, rigid duct eigenvalue $k^e$. Top row, downstream modes; Bottom row, upstream modes; —, Pridmore-Brown equation; - -, pressure and particle velocity ODEs; · · ·, pressure and particle displacement ODEs.* $k_0 = 30.94$, $M = 0.345$, $m = 4$, $n = 1$ *to* $6$, $\hbar = 0.569$.

eigenvalue obtained using each governing equation set is plotted against grid point refinement. The exact eigenvalue is used as an initial guess, and is iterated until the boundary condition error tolerance is met. Here, the tolerance is $10^{-8}$ for each case. This tolerance level must be set, for the velocity and displacement boundary conditions respectively, one or two orders of magnitude lower than for the pressure gradient condition.

The error in the eigenvalues for a lined duct is presented in figure (6.4) where the relevant tolerances are set. Each equation set is seen to exhibit similar convergence properties. The error increases for higher order modes due to the increasing number of oscillations in the mode eigenfunctions, which contribute larger gradient errors in the integration scheme.

## 6.3 Validation

Validation of the eigenvalue solver is undertaken using results from the literature, and is presented in the form of tables of eigenvalues $k/k_0$.

### 6.3.1 Power law mean flow profile

The results of Shankar [53] and Kousen [133] for a one-seventh power law flow profile are used to validate solutions based on pressure and displacement ODEs. A fourth order

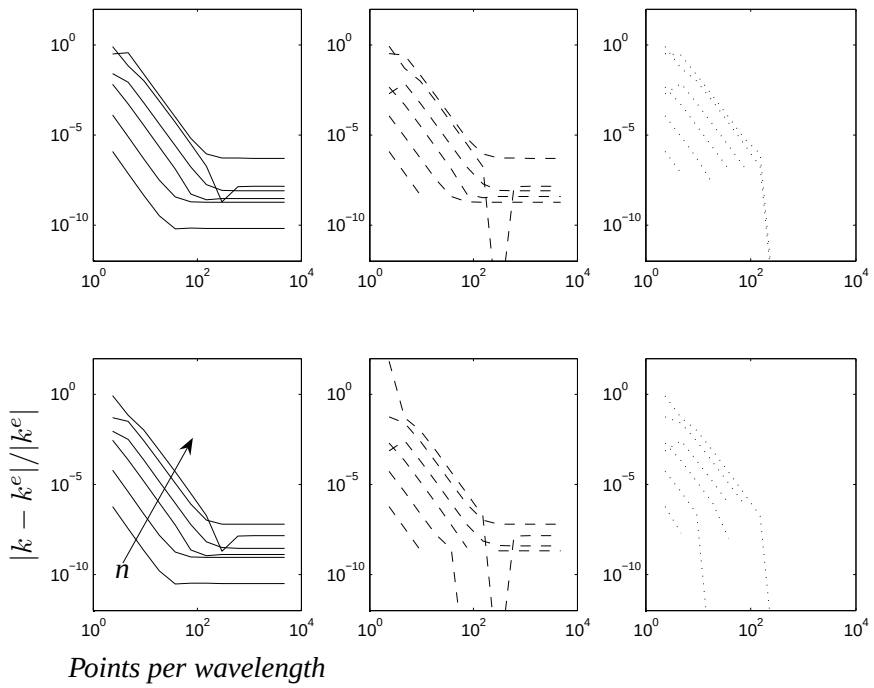


FIGURE 6.3: *Eigenvalue error for a rigid duct. Top row, downstream modes; Bottom row, upstream modes; —, Pridmore-Brown equation; - -, pressure and particle velocity ODEs; · · ·, pressure and particle displacement ODEs.* $k_0 = 30.94$, $M = 0.345$, $m = 4$, $n = 1$ *to* $6$, $\hbar = 0.569$.

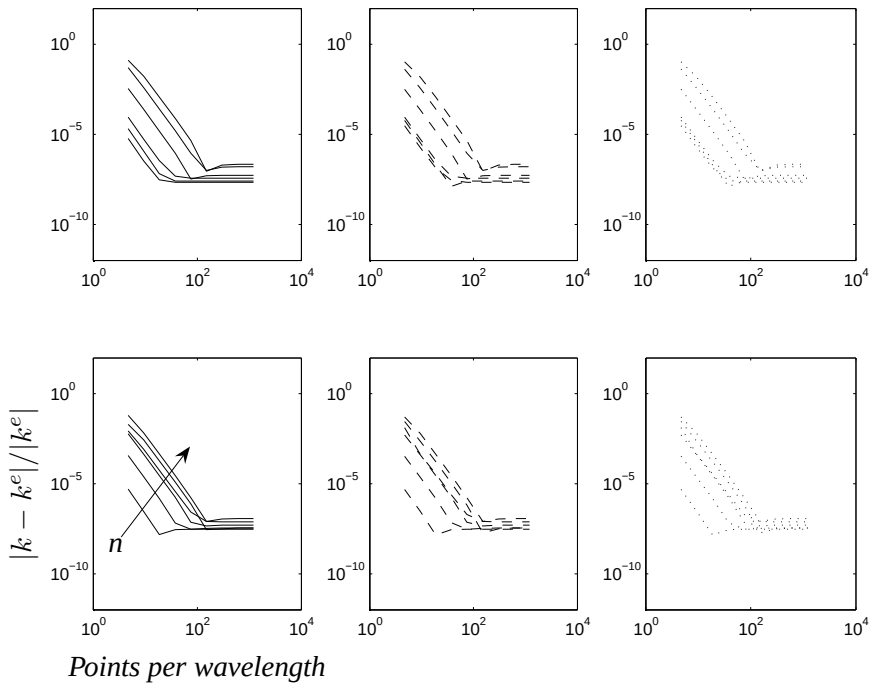


FIGURE 6.4: *Eigenvalue error for a lined duct. Top row, downstream modes; Bottom row, upstream modes; —, Pridmore-Brown equation; - -, pressure and particle velocity ODEs; · · ·, pressure and particle displacement ODEs.* $k_0 = 30.94$, $M = 0.345$, $m = 4$, $n = 1$ *to* $6$, $\hbar = 0.569$, $Z = 1 - 0.93i$.

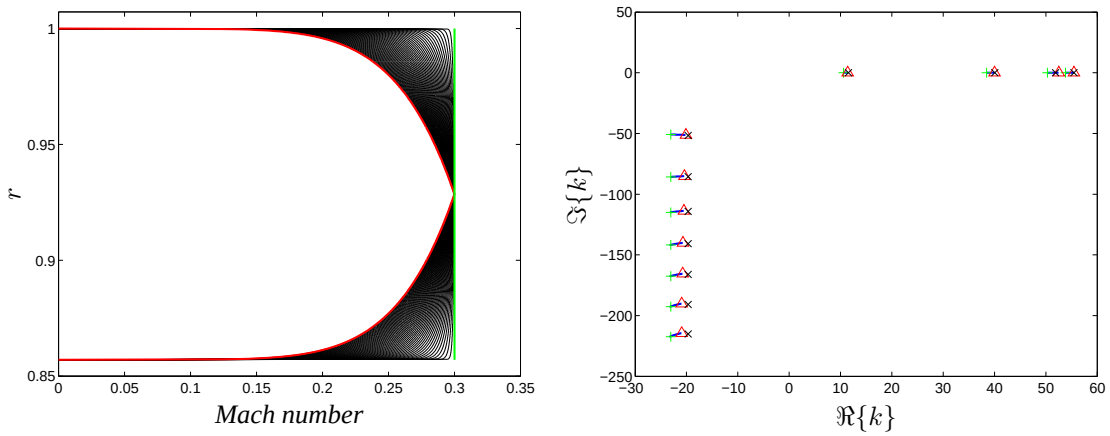


(a) Mach profile variation.

(b) Eigenvalue tracking.

FIGURE 6.5: *Mach profile variation and rigid duct eigenvalue tracking for one-seventh power law validation case.* $+$*, initial uniform flow eigenvalue;* $\triangle$*, final eigenvalue;* $\times$*, average uniform flow eigenvalue.* $k_0 = 70$*,* $m = 0$*,* $\hbar = 0.85714$*.*

Runge-Kutta integration was used by Shankar, and a spectral method was used by Kousen. It is noted that formulations used by Shankar and Kousen explicitly contain the flow gradient term (here it is infinite at the walls), which has been eliminated from the current formulation. The first case is for a rigid annular duct of hub-to-tip ratio $\hbar = 0.85714$, at a frequency $k_0 = 70$, for the first eleven downstream propagating non-spinning modes $m = 0$. The power law mean flow profile is given by

$$M(r) = 0.3 \times \left[1 - 2|\frac{h}{d-h} + 0.5 - \frac{rd}{d-h}|\right]^{\frac{1}{7}} , \tag{6.25}$$

with the variation in the flow profile used for tracking the eigenvalues shown in figure (6.5a). The tracking of the eigenvalues from the uniform slip profile $M = 0.3$ to the required profile is shown in figure (6.5b), and a comparison with results from the literature is given in Table (6.1). The eigenvalues compare very well. The eigenvalue tracking shows a trend to the right because, as the mean flow profile is varied, the mass flow rate is reduced. Eigenvalues calculated using the average Mach number $(M_{ave} = 0.2621)$ of the final flow profile are plotted for reference, and show that uniform flow assumption is fairly good, but becomes less accurate for higher order modes.

The second case is for a lined annular duct of hub-to-tip ratio $\hbar = \frac{2}{3}$, at a frequency $k_0 = 30$, for the first eleven downstream propagating non-spinning modes $m = 0$. Both hub and casing walls have an impedance of $Z = 3 - 1i$, and a comparison of eigenvalues is presented in table (6.2). The comparison is not as good as for the rigid case, and this is thought to be due to the effect of the flow gradient term in the reference solutions. The eigenvalue tracking is shown in figure (6.6b), where the average Mach number results are also plotted. The uniform flow assumption is again fairly good, but significant differences are found in the lowest order mode eigenfunction as shown in figure (6.6a). Such differences are important when considering modal decomposition of in-duct sources and modal scattered by liners.

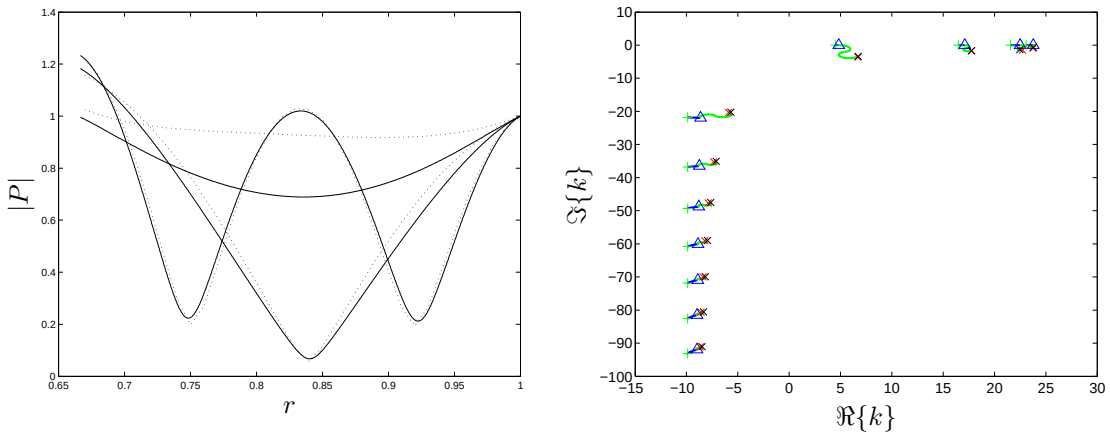


(a) Mode eigenfunction comparison.

(b) Eigenvalue tracking.

FIGURE 6.6: *Mode eigenfunctions and lined duct eigenvalue tracking for one-seventh power law validation case.* $+$*, initial uniform flow eigenvalue;* $\triangle$*, final rigid duct eigenvalue;* $\times$*, final lined duct eigenvalue;* $\times$*, average uniform flow eigenvalue;* —*, sheared flow;* $\cdots$*, uniform flow.* $k_0 = 30$, $m = 0$, $\hbar = 0.66667$, $Z = 3 - 1i$.

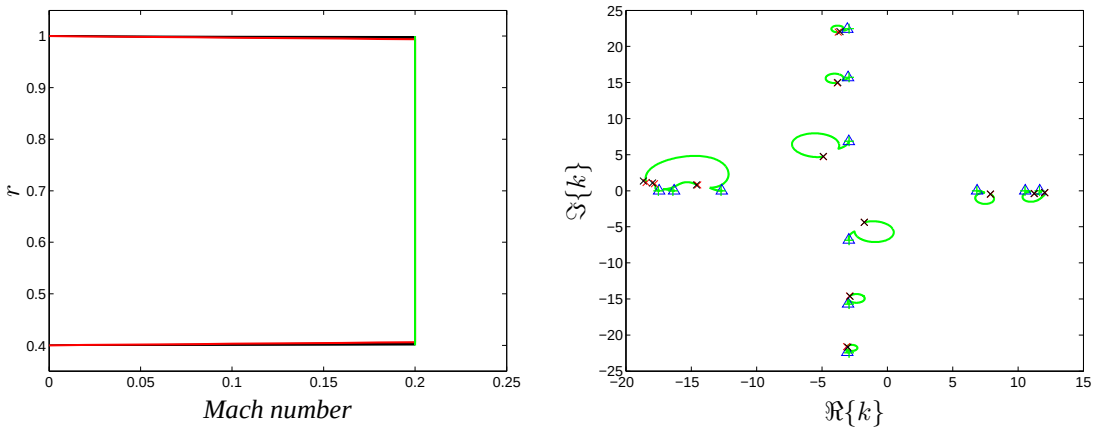


(a) Mach profile variation.

(b) Eigenvalue tracking.

FIGURE 6.7: *Mach profile variation and rigid duct eigenvalue tracking for linear boundary layer validation case.* $+$*, initial uniform flow eigenvalue;* $\triangle$*, final rigid duct eigenvalue;* $\times$*, final lined duct eigenvalue;* $\times$*, uniform flow eigenvalue.* $k_0 = 14.06667$, $m = 1$, $\hbar = 0.4$.

### 6.3.2 Linear boundary layer mean flow profile

The case of a lined duct containing a uniform mean flow profile with a linear boundary layer is validated against the results of Joshi *et al.* [139], obtained using a Runge-Kutta based shooting method. The Pridmore-Brown equation is solved for hub-to-tip ratio $\hbar = 0.4$, at a frequency $k_0 = 14.0667$, for the first six upstream and five downstream propagating spinning modes $m = 1$. A linear boundary layer of thickness $\delta = 0.01$ and a wall impedance $Z = 1.5 - 3i$ are specified on both hub and casing walls. The freestream Mach number is $M = 0.2$, with the iterations in flow profile shown in figure (6.7a), and eigenvalue tracking is shown in figure (6.7b). A comparison of eigenvalues from the literature, and for uniform flow $M = 0.2$, is presented in table (6.3), and demonstrate very good agreement.

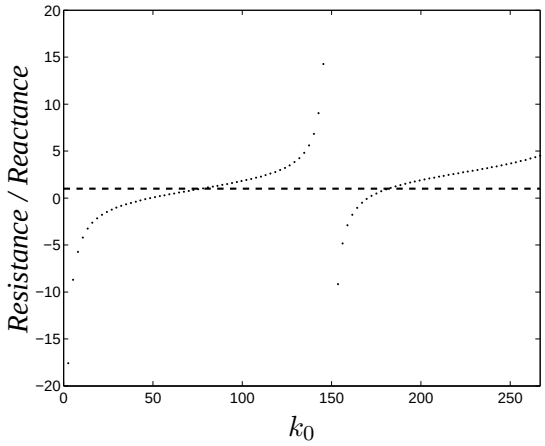


FIGURE 6.8: *Single-degree-of-freedom liner impedance. - -, face-sheet resistance; · · ·, reactance.* $R = 1$, $M_r = 0.012$, $D = 0.021$.

## 6.4 Effects of radial flow profile upon the mode spectrum

The non-uniformity of the mean flow profile affects both the eigenfunction and axial decay of the modes. In the previous chapter (5), it was demonstrated for a realistic bypass duct that the mean flow profile can be characterised into two parts: the core, and wall boundary layers. In the following subsections the effects of both upon the mode spectrum are demonstrated for realistic duct dimensions, mass flow rate, frequency and acoustic liner impedance. The casing $Z_d$ and hub $Z_h$ wall impedances are determined from the SDOF liner model given in equation (4.2). The non-dimensional liner parameters used here are face-sheet resistance $R = 1$, face-sheet mass inertance $M_r = 0.012$, and liner cavity depth $D = 0.021$. The frequency variation of the impedance is shown in figure (6.8).

### 6.4.1 Convergence to the slip flow case

A simplifying assumption often used in assessing acoustic liner performance in flow ducts is to obtain results based on the convected wave equation for uniform flow. The real flow non-uniformity and finite thickness boundary layers are thus ignored, and an unrealistic slip flow boundary condition is prescribed. The impact of this assumption has been discussed by several investigators [51, 54], with the common conclusion that the uniform flow assumption provides a good approximation in the limit of small boundary layer thickness $\delta = \hat{\delta}/d$. In this analysis, the limit $\delta \to 0$ is investigated by solving ODEs in pressure and particle displacement, since these do not involve the flow gradient $\mathrm{d}M/\mathrm{d}r$ (which will tend to infinity at the duct walls). The two flow profiles used here are linear and one-seventh power law

boundary layer profiles with uniform core flows, defined by

$$\begin{aligned} M(r) &= M_0 \left(\frac{r}{\delta}\right)^{\frac{1}{g}} && 0 \leq r \leq \delta \,, \\ &= M_0 && \delta \leq r \leq (1-\delta) \,, \\ &= M_0 \left(\frac{1-r}{\delta}\right)^{\frac{1}{g}} && (1-\delta) \leq r \leq 1 \,. \end{aligned} \tag{6.26}$$

where $M_0$ is the core flow Mach number, and $g$ defines the power. The linear boundary layer thickness is determined by equating the displacement thicknesses of the two profiles to give

$$\delta_g = \delta_1 = \frac{\delta_7}{4} \,. \tag{6.27}$$

In order to maintain accuracy, an expanding grid is used in the boundary layer, and a uniform grid in the core flow region. The lined duct eigenvalues are first obtained for a boundary layer thickness $\delta_7/(d-h) = 0.4$, then the eigenvalues are tracked in the limit $\delta \to 0$. The trajectories of the first few eigenvalues calculated for both profiles are shown in figures (6.9) and (6.10). All mode eigenvalues converge to the analytic uniform slip flow solutions. Rigid duct eigenfunctions in wave variables of pressure, radial particle displacement, radial and axial particle velocity are presented in figures (6.11) and (6.12) of the mode (0,0) for a series of boundary layer thicknesses as $\delta \to 0$. It can be seen that the rigid duct eigenfunctions also converge to the uniform slip flow solutions as $\delta \to 0$. The wall values of the axial particle velocity $u$ are related to the near wall values by the Doppler factor $k_0/\left(k_0 - Mk\right)$, which is consistent with the Ingard-Myers vortex sheet model [11, 57]. Similar plots are presented in figure (6.13) and (6.14) for the corresponding lined wall duct. Unlike the rigid duct case, the axial particle velocity is undefined at the walls when $\mathrm{d}M/\mathrm{d}r = \pm\infty$ and $v \neq 0$. The pressure eigenfunctions converge, and the velocity and displacement eigenfunctions are consistent, except for the Doppler-shifted wall values. The variation of the wave variables through the hub and casing boundary layers is presented in figures (6.15) and (6.16). As $\delta \to 0$ the pressure becomes uniform, and the radial particle velocity and displacement ratios at the edge of the boundary layer converge to the Doppler-shifted uniform slip flow values. The variation of the wave variables within the boundary layer is clearly dependent on the flow profile shape.

### 6.4.2 Boundary layer effects

Boundary layers affect acoustic propagation through refraction and convection. Previous studies have shown that, for a given boundary layer thickness, the profile shape has a strong effect upon the modes which is mainly due to the difference in mass flow rate and flow gradient. Prydz [54] and Nayfeh et al. [140] demonstrated that, by correlating on boundary layer displacement thickness, downstream propagation is essentially independent of flow profile, but upstream propagation is still profile dependent. Eigenvalue results obtained in the previous section for linear and one-seventh power law profiles are plotted in figure (6.17)

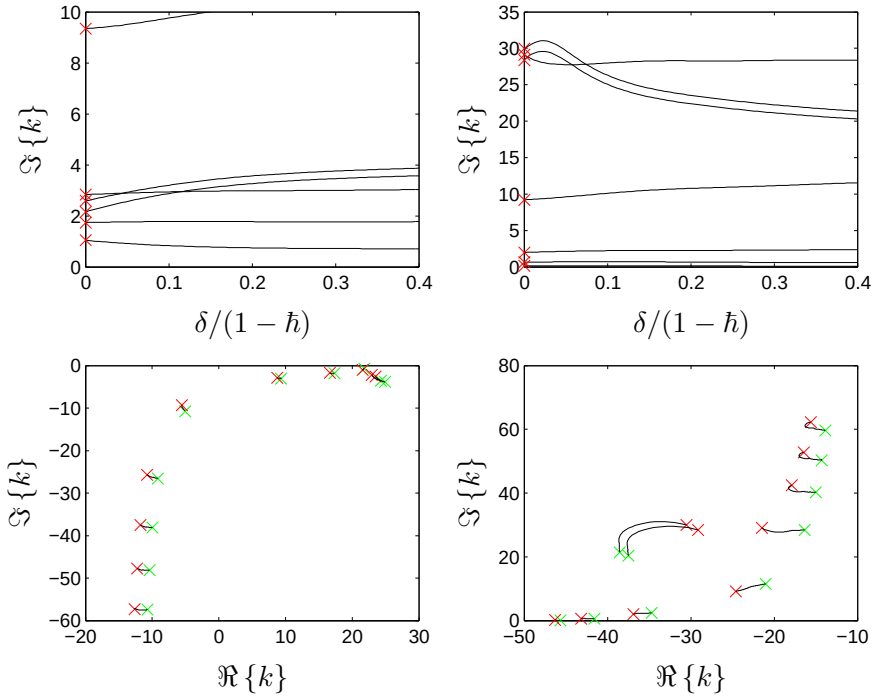


FIGURE 6.9: *Eigenvalue trajectories as* $\delta \to 0$ *for a* ***one-seventh power law*** *boundary layer profile. Left plots, downstream propagating modes; Right plots, upstream propagating modes;*×*, analytic uniform slip flow eigenvalues;*×*, initial eigenvalues.* $k_0 = 30.9435$, $\hbar = 0.569$, $Z = 1 - 0.9343i$, $M_0 = 0.345$.

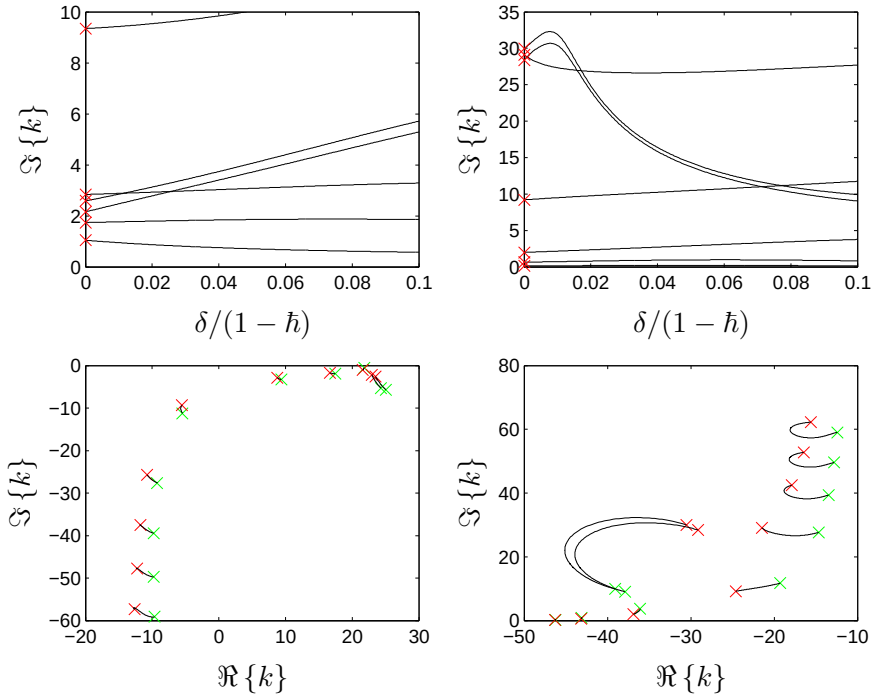


FIGURE 6.10: *Eigenvalue trajectories as* $\delta \to 0$ *for a* ***linear*** *boundary layer profile. Left plots, downstream propagating modes; Right plots, upstream propagating modes;*×*, analytic uniform slip flow eigenvalues;*×*, initial eigenvalues.* $k_0 = 30.9435$, $\hbar = 0.569$, $Z = 1 - 0.9343i$, $M_0 = 0.345$.

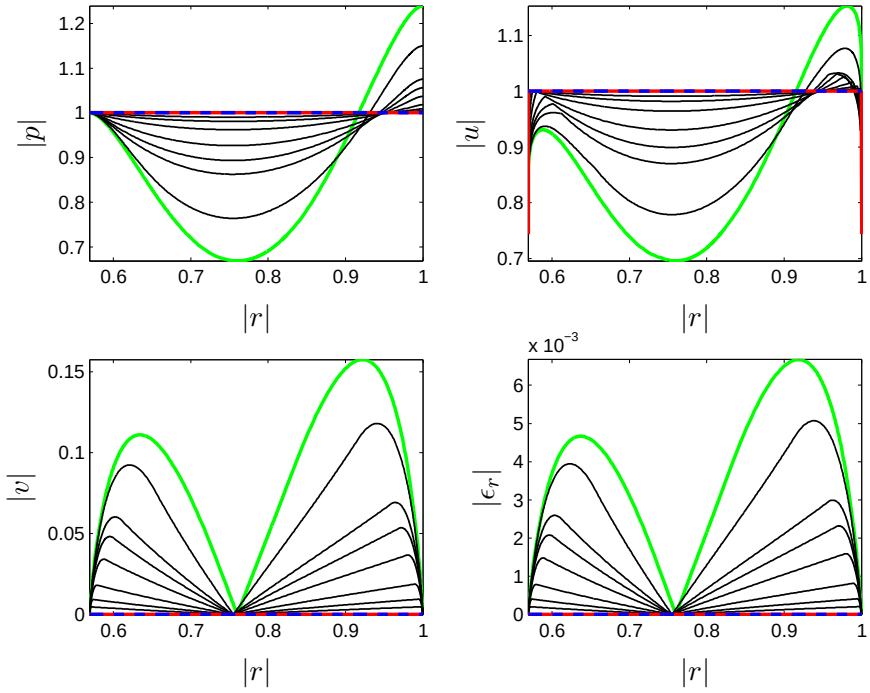


FIGURE 6.11: *Rigid duct mode* $(0,1)$ *eigenfunction as* $\delta \to 0$ *for a* ***one-seventh power law*** *boundary layer profile.* —*, initial eigenfunctions;* —*, intermediate eigenfunctions;* —*, final eigenfunctions;* ––*, analytic uniform slip flow eigenfunctions;* . $k_0 = 30.9435$, $\hbar = 0.569$, $M_0 = 0.345$.

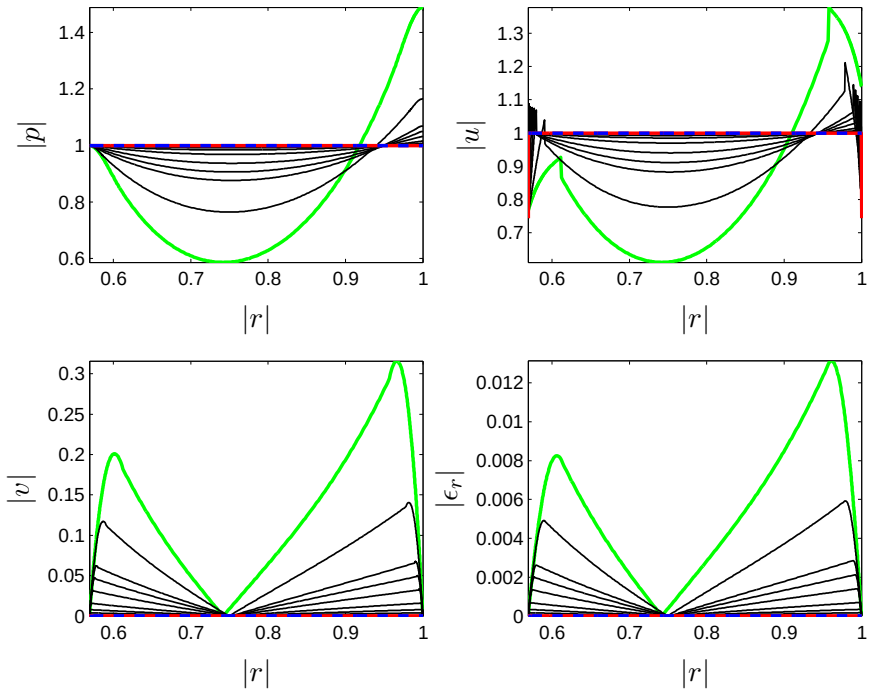


FIGURE 6.12: *Rigid duct mode* $(0,1)$ *eigenfunction as* $\delta \to 0$ *for a* ***linear*** *boundary layer profile.* —*, initial eigenfunctions;* —*, intermediate eigenfunctions;* —*, final eigenfunctions;* ––*, analytic uniform slip flow eigenfunctions;* . $k_0 = 30.9435$, $\hbar = 0.569$, $M_0 = 0.345$.

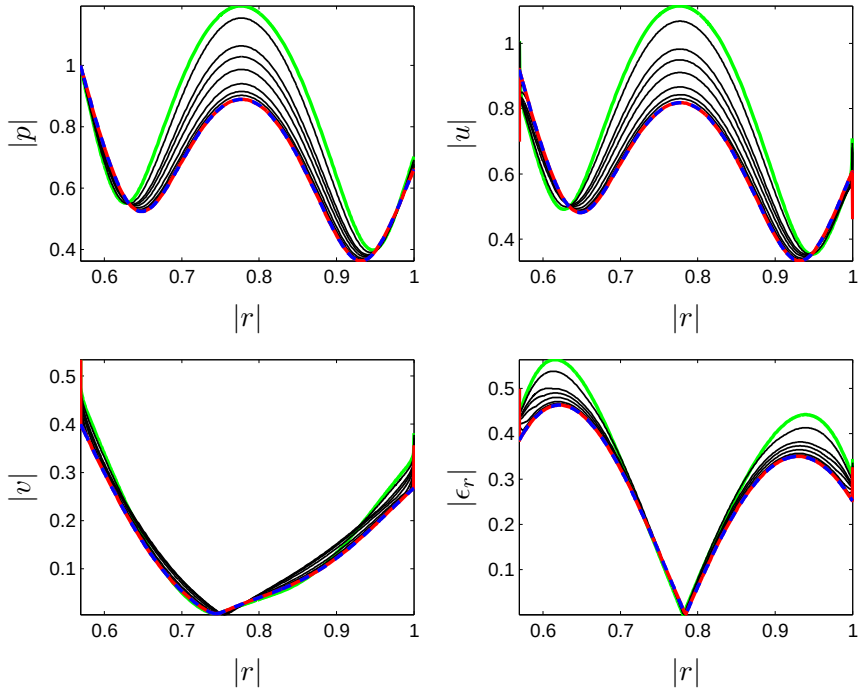


FIGURE 6.13: *Lined duct mode* $(0,1)$ *eigenfunction as* $\delta \to 0$ *for a* ***one-seventh power law*** *boundary layer profile.* —, *initial eigenfunctions;* —, *intermediate eigenfunctions;* —, *final eigenfunctions;* ––, *analytic uniform slip flow eigenfunctions;* . $k_0 = 30.9435$, $\hbar = 0.569$, $Z = 1 - 0.9343i$, $M_0 = 0.345$.

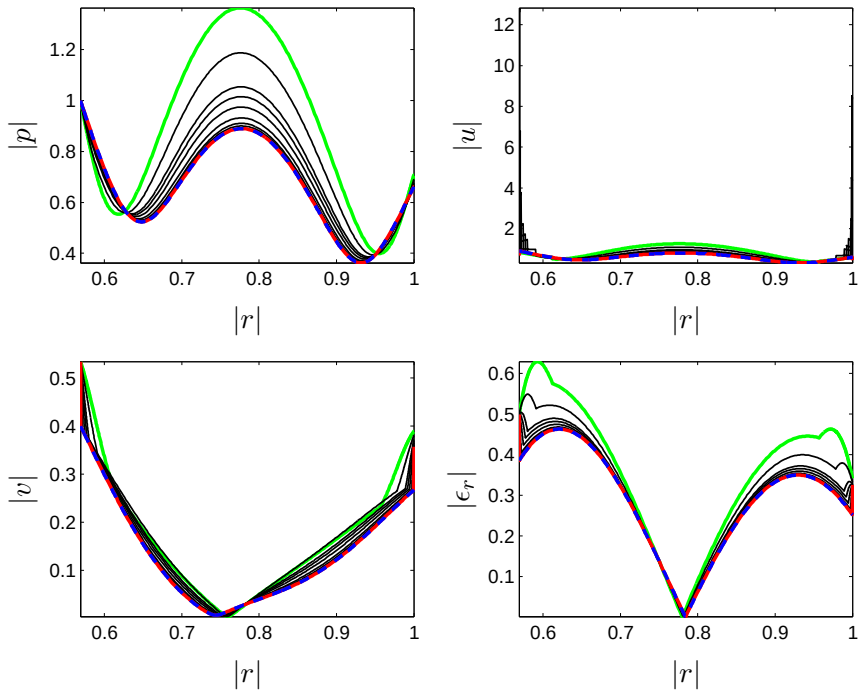


FIGURE 6.14: *Lined duct mode* $(0,1)$ *eigenfunction as* $\delta \to 0$ *for a* ***linear*** *boundary layer profile.* —, *initial eigenfunctions;* —, *intermediate eigenfunctions;* —, *final eigenfunctions;* ––, *analytic uniform slip flow eigenfunctions;* . $k_0 = 30.9435$, $\hbar = 0.569$, $Z = 1 - 0.9343i$, $M_0 = 0.345$.

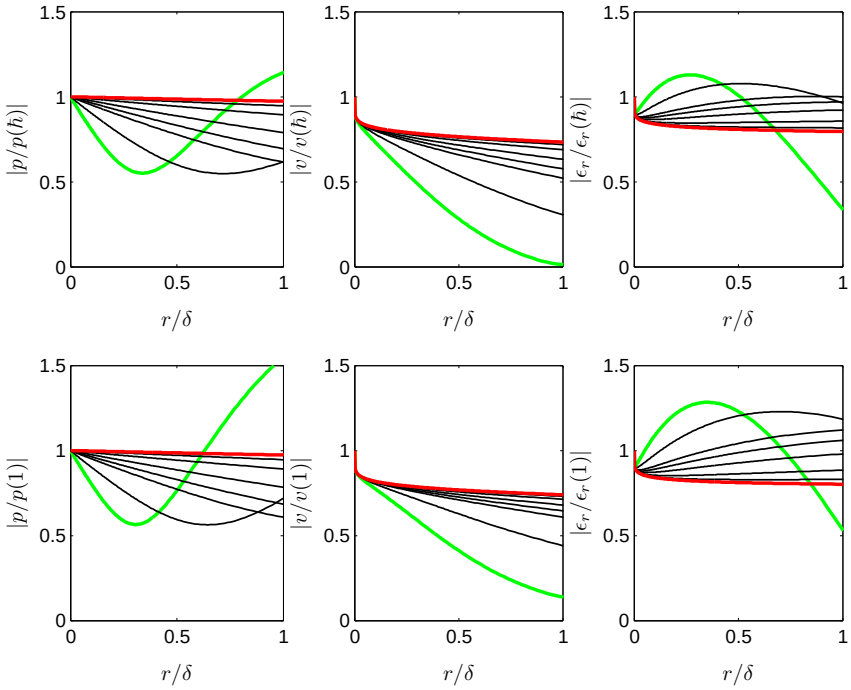


FIGURE 6.15: *Lined duct mode* $(0,1)$ *eigenfunction boundary layer variation as* $\delta \to 0$ *for a* ***one-seventh power law*** *boundary layer profile. Top row, hub boundary layer; Bottom row, casing boundary layer; —, initial eigenfunctions; —, intermediate eigenfunctions; —,* $0.00625\%$ *boundary layer eigenfunctions.* $k_0 = 30.9435$, $\hbar = 0.569$, $Z = 1 - 0.9343i$, $M_0 = 0.345$.

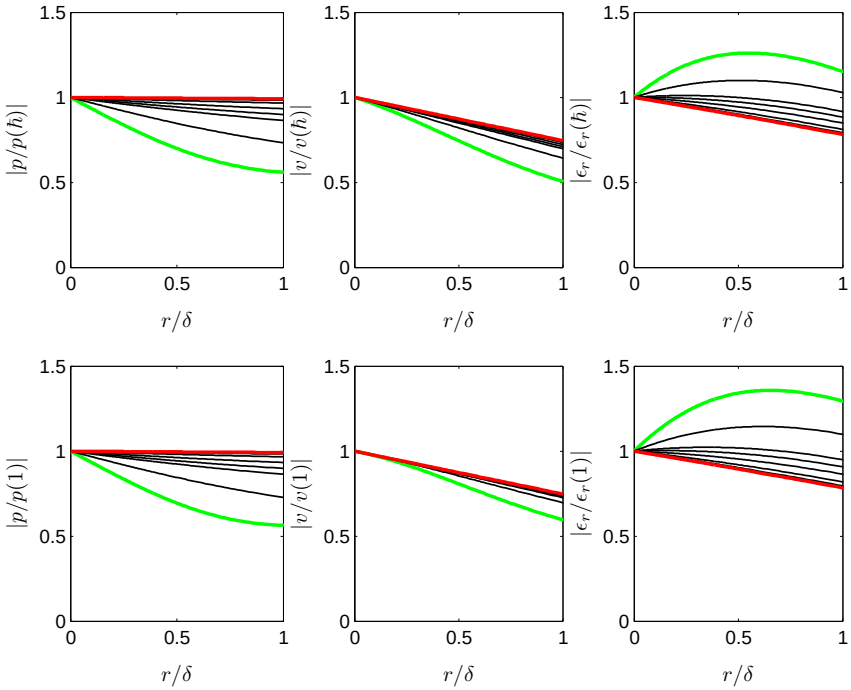


FIGURE 6.16: *Lined duct mode* $(0,1)$ *eigenfunction boundary layer variation as* $\delta \to 0$ *for a* ***linear*** *boundary layer profile. Top row, hub boundary layer; Bottom row, casing boundary layer; —, initial eigenfunctions; —, intermediate eigenfunctions; —,* $0.00625\%$ *boundary layer eigenfunctions.* $k_0 = 30.9435$, $\hbar = 0.569$, $Z = 1 - 0.9343i$, $M_0 = 0.345$.

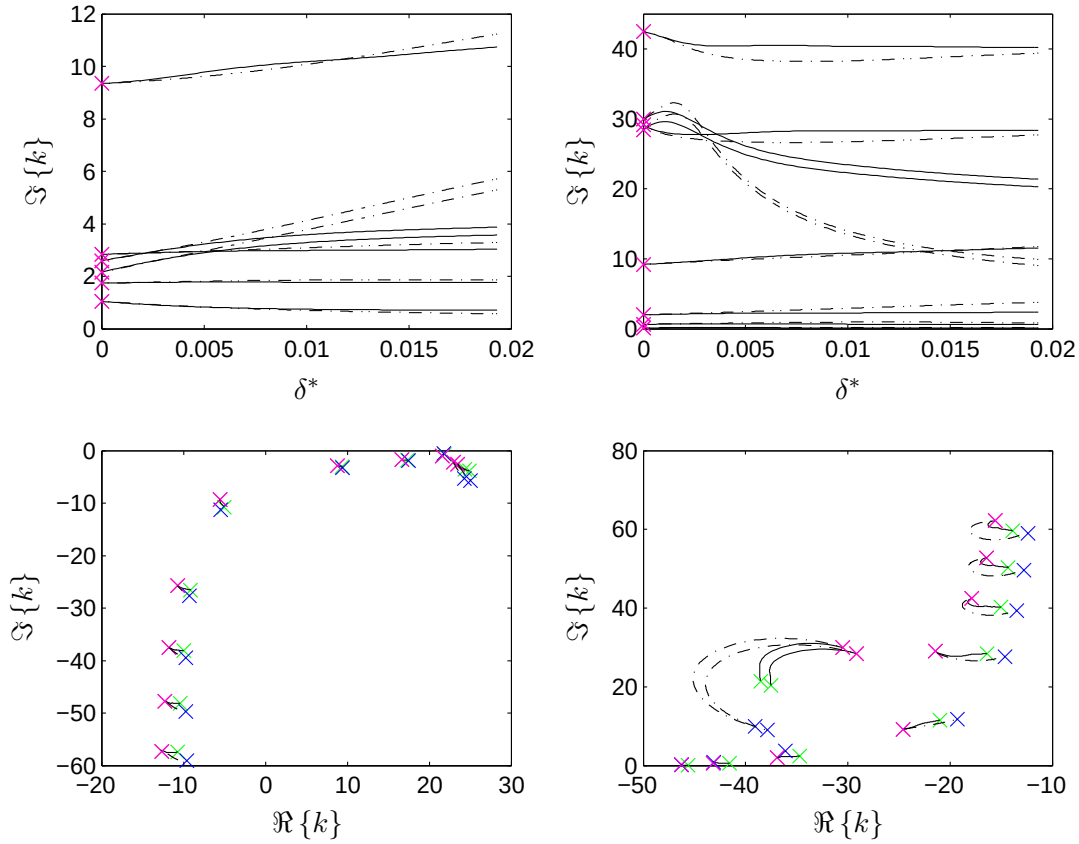


FIGURE 6.17: *Comparison of eigenvalue trajectories as $\delta^* \to 0$ for **linear** and **one-seventh power law** boundary layer profiles. Left plots, downstream propagating modes; Right plots, upstream propagating modes; —, $1/7$th power law profile; $-\cdot$, linear profile; $\times$, analytic uniform slip flow eigenvalues; $\times$, initial $1/7$th power law profile eigenvalues; $\times$, initial linear profile eigenvalues. $k_0 = 30.9435$, $\hbar = 0.569$, $Z = 1 - 0.9343i$, $M_0 = 0.345$.*

against non-dimensional displacement thickness $\delta^*$. It is seen that the upstream propagating modes do indeed depend strongly upon the profile shape, and the downstream modes correlate fairly well just on displacement thickness. The refractive effects upon mode axial decay are fairly intuitive, where thicker boundary layers result in refraction towards the liner giving higher downstream mode decay rates, and, conversely, lower upstream mode decay rates. The greatest variation is seen in the surface wave modes, of which the upstream modes show very strong sensitivity to flow profile. Such modes are localised at the wall, and so would be expected to depend strongly upon the boundary layer.

As the wavelength of sound becomes comparable to the boundary layer thickness it is expected that refraction effects will get stronger. This proves to be the case, as demonstrated in figure (6.18), where the axial decay rates of the first five non-spinning modes $m = 0$ are plotted over frequency up to 7BPF. Two linear boundary of thicknesses of $\delta_1/(1-\hbar) = 0.0125$ and $0.05$ are chosen, and the uniform slip flow values are plotted for reference. An increase in decay rates, compared to attenuation with uniform flow, occurs with increasing frequency for the low order downstream propagating modes, which is very strongly enhanced for the thicker

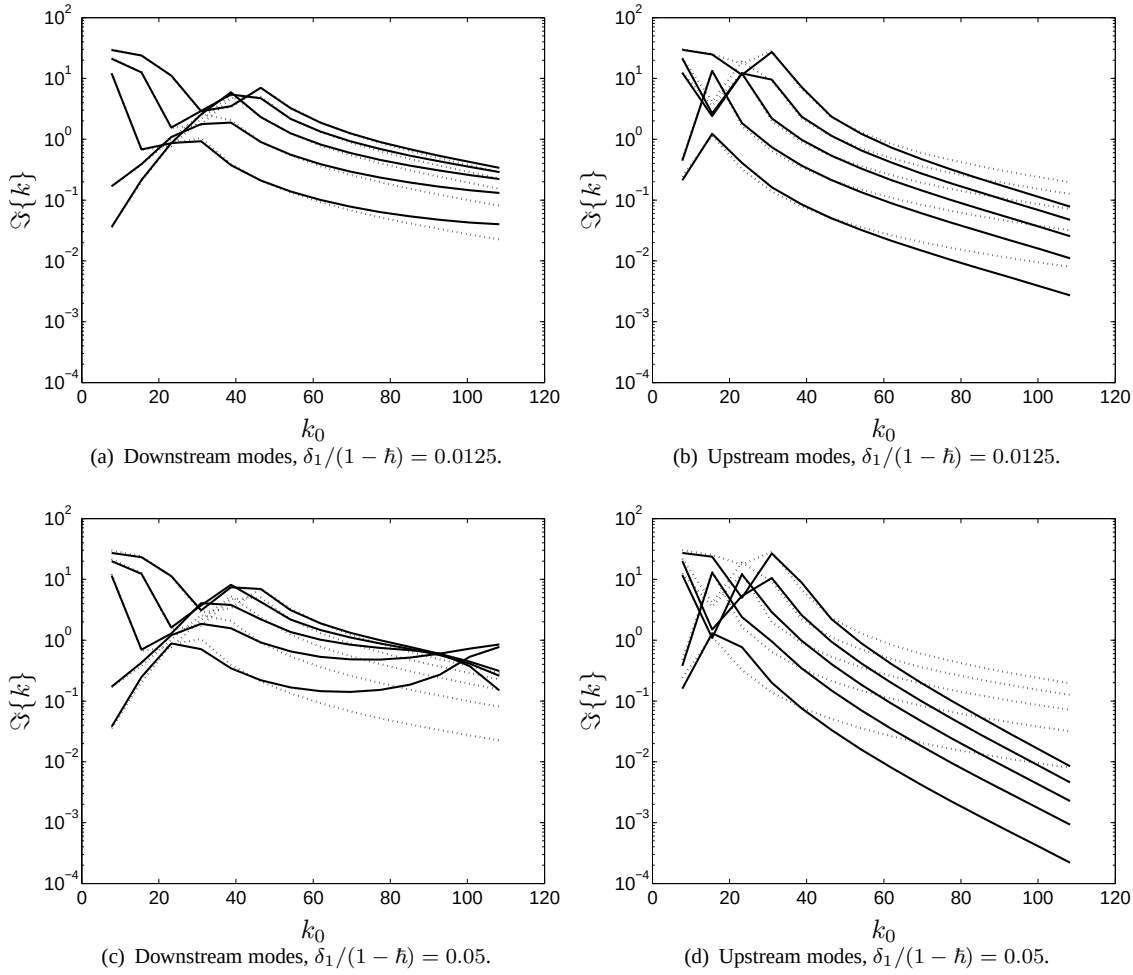


(a) Downstream modes, $\delta_1/(1-\hbar) = 0.0125$.

(b) Upstream modes, $\delta_1/(1-\hbar) = 0.0125$.

(c) Downstream modes, $\delta_1/(1-\hbar) = 0.05$.

(d) Upstream modes, $\delta_1/(1-\hbar) = 0.05$.

FIGURE 6.18: *Modal decay rate spectra for first five non-spinning $m = 0$ radial modes in a lined (SDOF liner impedance model) duct with **linear** boundary layer profiles. —, boundary layer flow, $\cdots$, uniform slip flow $M = 0.345$.*

boundary layer. Conversely, the decay rates of the upstream propagating modes decrease with increasing frequency, and this effect is also enhanced for the thicker boundary layer. These effects are maintained for spinning modes. An example for $m = 16$ modes, which are less well cut-on, is shown in figure (6.19). Refraction effects begin at a lower frequency for upstream propagation compared with downstream propagation due to shortening of the effective wavelength by mean flow convection.

### 6.4.3 General flow non-uniformity effects

The core flow profile is dependent upon flow conditions after the fan/OGV stage, and for the slowly varying geometry of the bypass duct, the initial core profile is generally maintained along the length of the duct. The greatest variation is to be expected at the turbine hump, where a large negative shear is seen. Two linear shear core flows of positive and negative gradient are assessed against the uniform flow case, with a slip flow condition prescribed at the walls as shown in figure (6.20). The variation of the axial decay rates with increasing frequency of

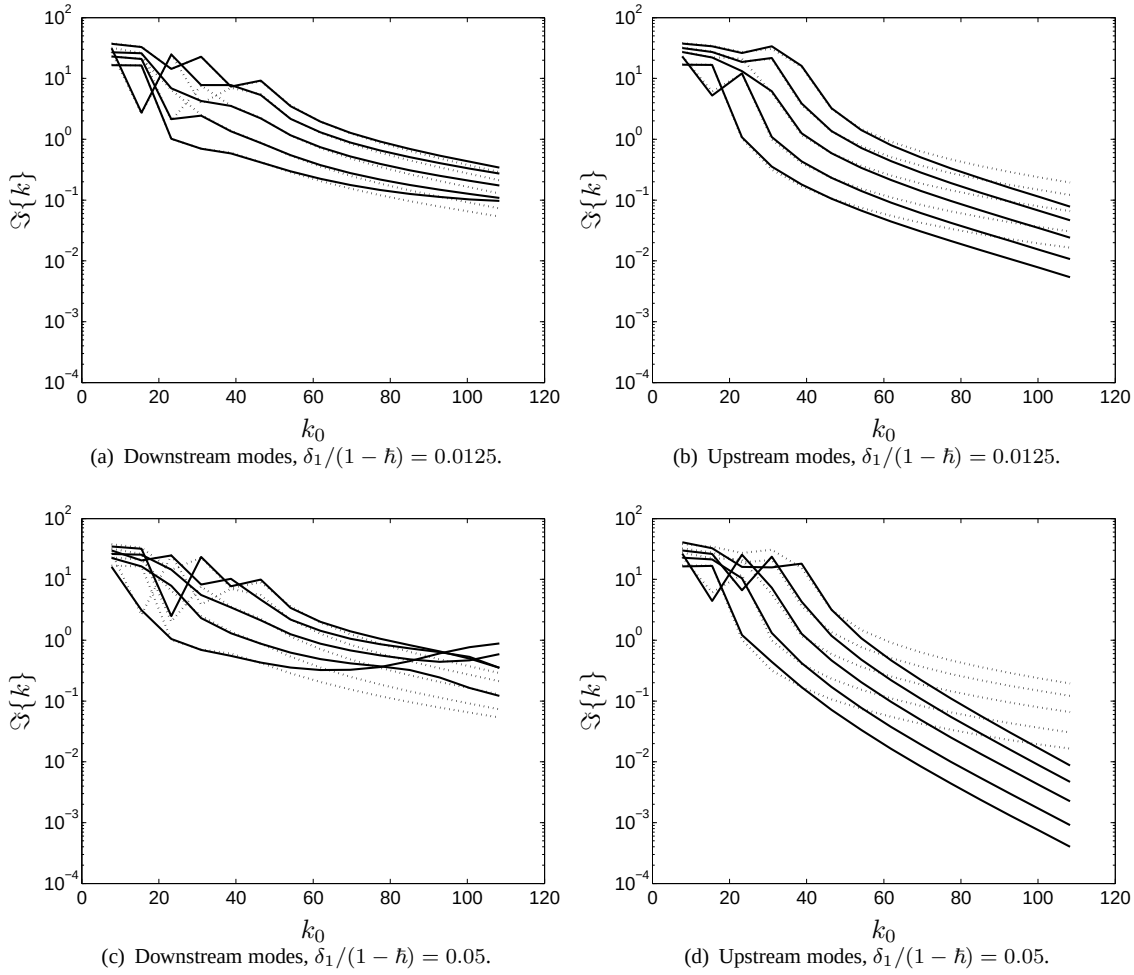


(a) Downstream modes, $\delta_1/(1-\hbar) = 0.0125$.

(b) Upstream modes, $\delta_1/(1-\hbar) = 0.0125$.

(c) Downstream modes, $\delta_1/(1-\hbar) = 0.05$.

(d) Upstream modes, $\delta_1/(1-\hbar) = 0.05$.

FIGURE 6.19: *Modal decay rate spectra for first five spinning $m = 16$ radial modes in a lined (SDOF liner impedance model) duct with **linear** boundary layer profiles. —, boundary layer flow, $\cdots$, uniform slip flow $M = 0.345$.*

non-spinning modes $m = 0$ relative to the uniform flow case is shown in figure (6.21). For the downstream propagating modes, decay rates for all but the lowest order mode decrease with increasing frequency. For the upstream propagating modes, as the frequency is increased, the decay rates also decrease, but appear to become independent of frequency at high frequencies. Both profiles produce near identical decay rates, which is due to the two-dimensional nature of the $m = 0$ case, whereby the difference in hub and casing liner area has no effect. The axial decay rates of the $m = 16$ spinning modes are plotted in figure (6.22). For positive shear flow, refraction of the downstream modes occurs towards the hub wall, which has a lower lined area, and thus the low order mode decay rates are less than for uniform flow. The upstream modes are refracted towards the casing wall, which has a higher lined area, and the decay rates are higher. The opposite is observed with negatively sheared flow. In general, the low order modes follow these expected trends, whilst the higher order modes are generally less affected by the core mean flow shear, compared with the boundary layer.

The realistic flow fields investigated in the previous chapter were found, overall, to have a general negative core flow shear gradient, with additional profile features due to the fan/OGV

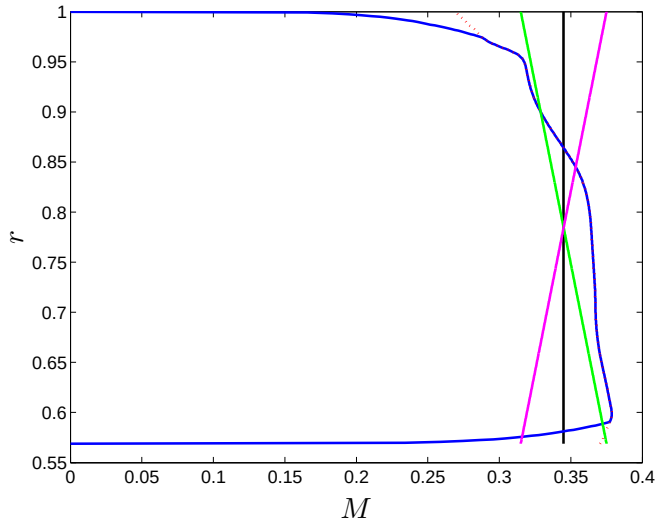


FIGURE 6.20: *Mean flow radial profiles. —, uniform flow $M = 0.345$; · · ·, realistic flow with slip; —, realistic flow with boundary layers; —, positively sheared linear flow; —, negatively sheared linear flow.*

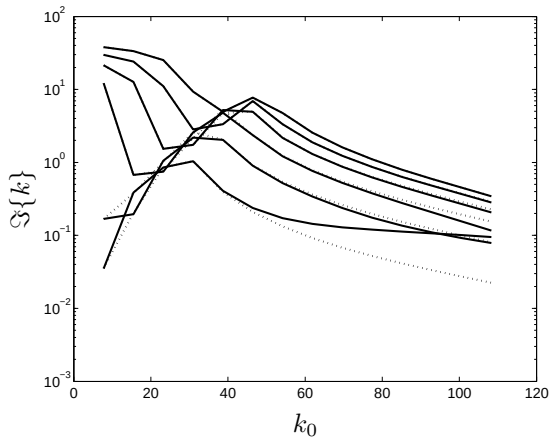


(a) Positively shear linear flow, downstream modes.

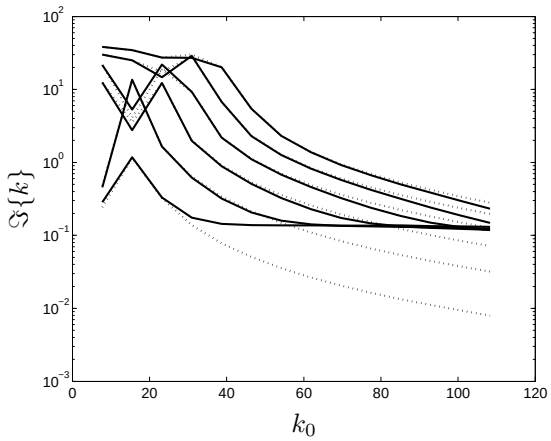


(b) Positively shear linear flow, upstream modes.

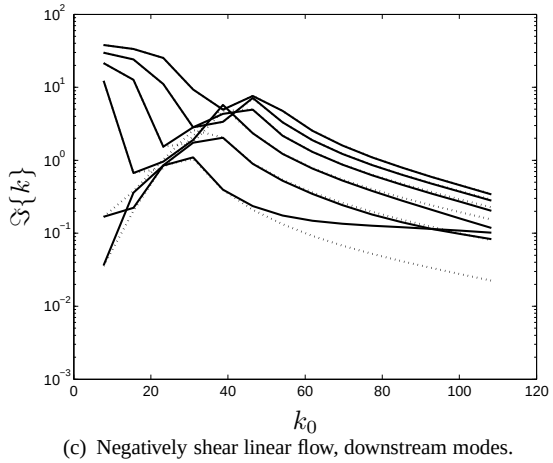


(c) Negatively shear linear flow, downstream modes.

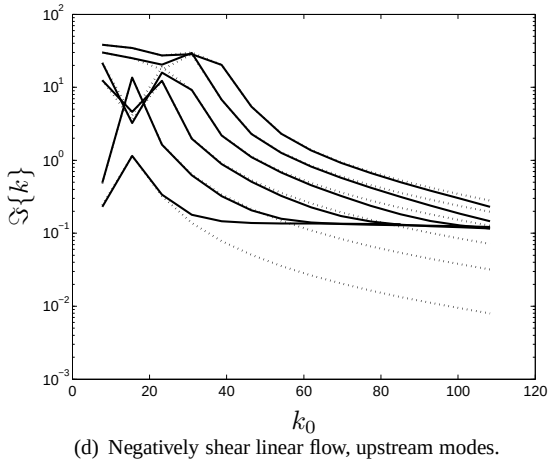


(d) Negatively shear linear flow, upstream modes.

FIGURE 6.21: *Modal decay rate spectra for first six non-spinning $m = 0$ radial modes in a lined (SDOF liner impedance model) duct with **linear** flow profiles. —, linear shear flow, · · ·, uniform slip flow $M = 0.345$.*

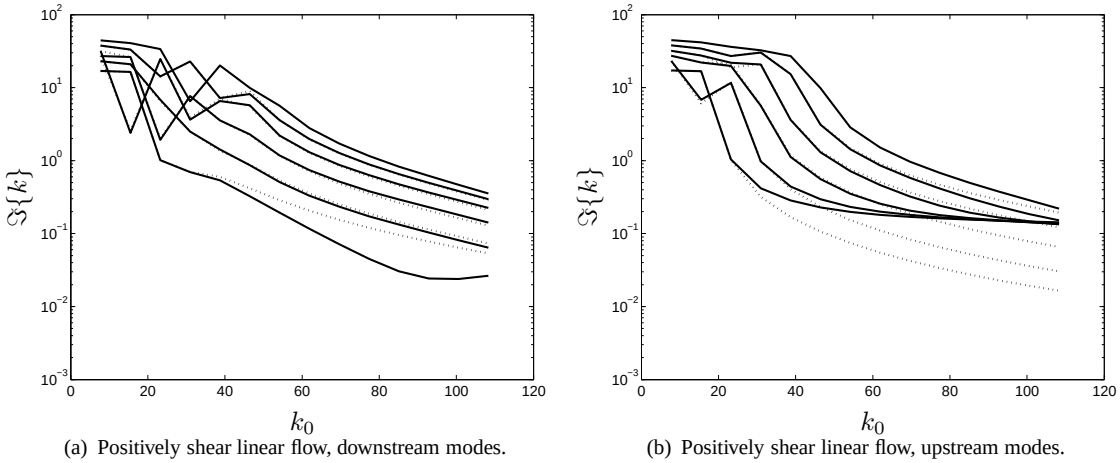


(a) Positively shear linear flow, downstream modes.

(b) Positively shear linear flow, upstream modes.

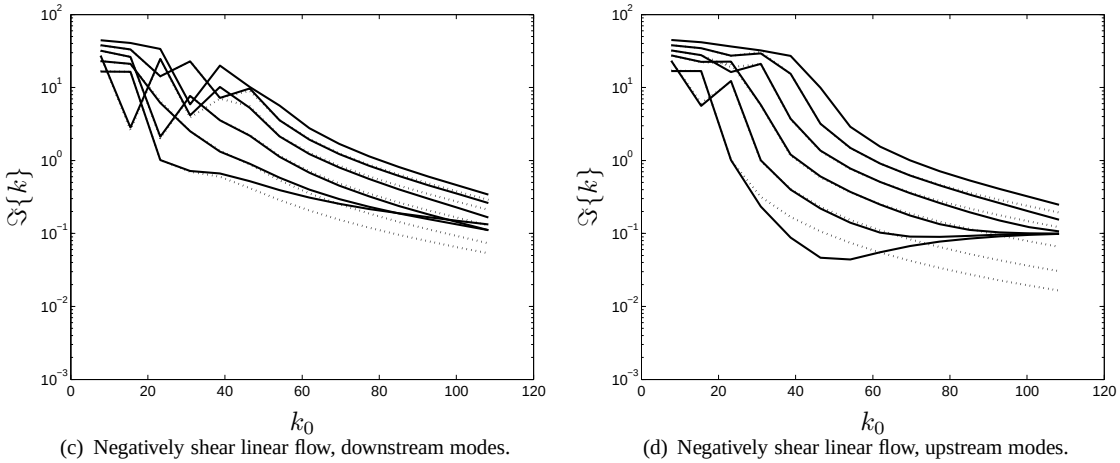


(c) Negatively shear linear flow, downstream modes.

(d) Negatively shear linear flow, upstream modes.

FIGURE 6.22: *Modal decay rate spectra for first six spinning $m = 16$ radial modes in a lined (SDOF liner impedance model) duct with **linear** flow profiles. —, linear shear flow, $\cdots$, uniform slip flow $M = 0.345$.*

stage. Decay rates and mode eigenfunctions for a realistic profile obtained from the CFD investigation, and modified to the current duct geometry, are assessed against uniform flow solutions. The realistic profile is assessed with both a slip condition and boundary layers, as shown in figure (6.20). Axial decay rates for the first six radial modes for $m = 0$ and $m = 16$ are shown in figure (6.23), and demonstrate the trends observed previously for negatively sheared linear flow. The downstream mode decay rates increase with frequency, compared with the uniform flow decay rates, with the lowest order modes being most affected. Upstream mode decay rates decrease with frequency relative to the uniform flow decay rates, and tend to converge at very high frequencies. The slip flow values converge towards a finite value, whilst the boundary layer flow values appear to continue on a downward trend. The presence of the boundary layer allows for total refraction of the upstream propagating waves in the limiting case when the wavelength is comparable to the boundary layer thickness, and with an appropriate incident wave angle [52]. When this occurs, waves may not reach the liner and thus no absorption occurs, which explains the downward trend seen for the decay rates at high frequency with boundary layer flows. However, for slip flows waves always reach the liner, thus some absorption should occur in the high frequency limit.

These results demonstrate that, ideally, realistic flow profiles should be used to assess acoustic mode propagation in ducts, in particular at high frequencies. This is particularly important for low order modes and surface waves, and at higher sound frequencies. The uniform slip flow assumption is valid for very thin boundary layers at low frequencies.

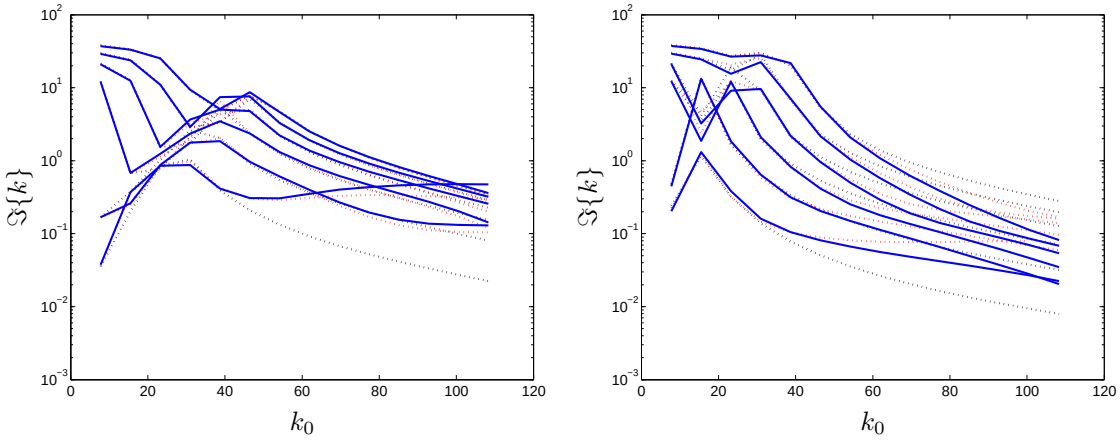


(a) Downstream modes, $m = 0$.




(b) Upstream modes, $m = 0$.

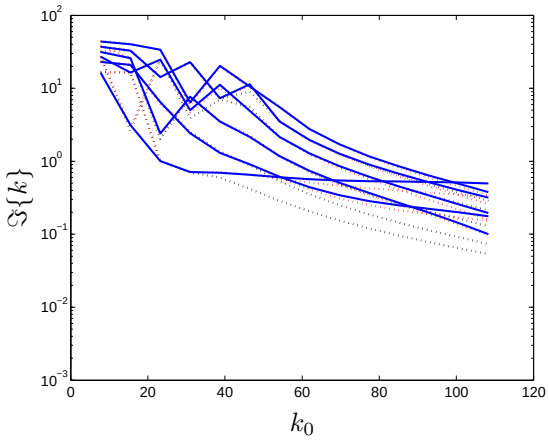


(c) Downstream modes, $m = 16$.

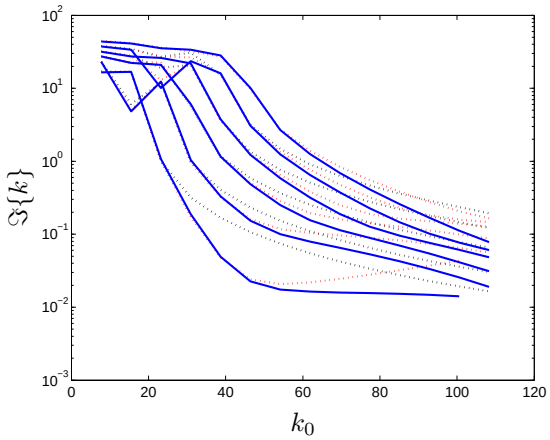


(d) Upstream modes $m = 16$.

FIGURE 6.23: *Modal decay rate spectra for first six radial modes in a lined (SDOF liner impedance model) duct with* ***realistic*** *flow profiles. —, realistic shear flow with boundary layers; · · ·, realistic shear flow with slip; · · ·, uniform slip flow* $M = 0.345$.

## 6.5 Summary

- Sets of governing equations for acoustic propagation in a lined annular duct containing an inviscid, parallel subsonic mean flow have been outlined. First order ODEs in pressure and particle displacement that are independent of flow gradient allow for solutions to be obtained for power law profiles typically used to describe turbulent boundary layer flows.
- An eigenvalue tracking procedure is described for obtaining the acoustic eigenmodes of the governing equations, and have been validated against results from literature.
- The convergence of solutions for boundary layer flows to those of the commonly used slip flow condition is demonstrated. A Doppler-factor is imparted to the velocity and displacement eigenmodes at the lined wall, which is consistent with the Ingard-Myers vortex sheet model.
- The downstream mode decay rates were found to correlate well on boundary layer displacement thickness, but variation of the wave variables through the boundary layer was found to strongly depend upon the flow profile.
- Refractive effects become stronger as the wavelength of sound becomes comparable to boundary layer thickness. Refractive effects upon upstream propagating modes begin to occur at lower frequency than downstream modes due to the shortening of the effective wavelength by the mean flow convection.
- The sign of the shear flow gradient in the core mean flow is found to have a strong effect on mode decay rates. For downstream propagating spinning modes, larger increases were obtained for refraction towards the casing compared with towards the hub, due to the higher casing lined area.
- All refraction effects were found to be strongest for the lowest order modes and surface waves.
- It was demonstrated that realistic flow profiles should be used to assess acoustic mode propagation in bypass ducts. The flow profile can have strong effects upon low order modes and surface waves, and on all modes at higher frequencies.

TABLE 6.1: *First eleven downstream propagating modes $k/k_0$ for a rigid duct with a one-seventh power law flow profile. $k_0 = 70$, $m = 0$, $\hbar = 0.85714$.*

| $n$ | Shankar [53] | Kousen [133] | Present |
|---|---|---|---|
| 1 | $0.79293$ | $0.79353$ | $0.79284$ |
| 2 | $0.75075$ | $0.75292$ | $0.75057$ |
| 3 | $0.57143$ | $0.57320$ | $0.57128$ |
| 4 | $-0.00969$ | $0.16437$ | $0.16268$ |
| 5 | $-0.28733 - 0.73219i$ | $-0.28357 - 0.73425i$ | $-0.28771 - 0.73197i$ |
| 6 | $-0.29118 - 1.21721i$ | $-0.28622 - 1.2198i$ | $-0.29167 - 1.21701i$ |
| 7 | $-0.29248 - 1.62569i$ | $-0.28766 - 1.6281i$ | $-0.29310 - 1.62548i$ |
| 8 | $-0.29519 - 2.00221i$ | $-0.28947 - 2.0055i$ | $-0.29598 - 2.00196i$ |
| 9 | $-0.29768 - 2.71665i$ | $-0.29035 - 2.3683i$ | $-0.29667 - 2.36480i$ |
| 10 | $-0.29768 - 2.71665i$ | $-0.29167 - 2.7209i$ | $-0.29891 - 2.71624i$ |
| 11 | $-0.29776 - 3.06414i$ | $-0.29243 - 3.0679i$ | $-0.29928 - 3.06360i$ |

TABLE 6.2: *First eleven downstream propagating modes $k/k_0$ for a lined duct with a one-seventh power law flow profile. $k_0 = 30$, $m = 0$, $\hbar = 0.66667$, $Z = 3 - 1i$.*

| $n$ | Shankar [53] | Kousen [133] | Present |
|---|---|---|---|
| 1 | $0.78698 - 0.00400i$ | $0.78093 - 0.00913i$ | $0.79214 - 0.02899i$ |
| 2 | $0.73438 - 0.02541i$ | $0.75079 - 0.03387i$ | $0.75795 - 0.05123i$ |
| 3 | $0.55840 - 0.03148i$ | $0.57267 - 0.03246i$ | $0.59171 - 0.05639i$ |
| 4 | $0.14308 - 0.07638i$ | $0.16875 - 0.06982i$ | $0.22225 - 0.11627i$ |
| 5 | $-0.23900 - 0.74173i$ | $-0.23734 - 0.72727i$ | $-0.19659 - 0.67792i$ |
| 6 | $-0.26149 - 1.21973i$ | $-0.25993 - 1.2120i$ | $-0.24519 - 1.17372i$ |
| 7 | $-0.26996 - 1.62627i$ | $-0.26860 - 1.6207i$ | $-0.26237 - 1.58836i$ |
| 8 | $-0.27669 - 2.00192i$ | $-0.27468 - 1.9983i$ | $-0.27379 - 1.96866i$ |
| 9 | $-0.27974 - 2.36439i$ | $-0.27813 - 2.3612i$ | $-0.28003 - 2.33418i$ |
| 10 | $-0.28359 - 2.71568i$ | $-0.28147 - 2.7139i$ | $-0.28625 - 2.68758i$ |
| 11 | $-0.28502 - 3.06304i$ | $-0.28361 - 3.0610i$ | $-0.28967 - 3.03649i$ |

TABLE 6.3: *First six upstream and five downstream propagating modes $k/k_0$ for a lined duct with a linear boundary layer flow profile. $k_0 = 14.06667$, $m = 1$, $\hbar = 0.4$, $Z = 1.5 - 3i$.*

| $n$ | Uniform flow $M = 0.2$ | Joshi *et al.* [139] | Present |
|---|---|---|---|
| 1+ | $0.79807 - 0.02667i$ | $0.8556 - 0.0200i$ | $0.85771 - 0.02033i$ |
| 2+ | $0.85523 - 0.01918i$ | $0.7969 - 0.0262i$ | $0.80106 - 0.02747i$ |
| 3+ | $0.56097 - 0.03354i$ | $0.5582 - 0.0337i$ | $0.56248 - 0.03392i$ |
| 4+ | $-0.12492 - 0.31080i$ | $-0.1308 - 0.3047i$ | $-0.12450 - 0.31137i$ |
| 5+ | $-0.20290 - 1.04009i$ | $-0.2000 - 1.0367i$ | $-0.20534 - 1.03813i$ |
| 1- | $-1.03765 + 0.05588i$ | $-1.0408 + 0.0536i$ | $-1.03035 + 0.05597i$ |
| 2- | $-1.27682 + 0.07593i$ | | $-1.26632 + 0.06888i$ |
| 3- | $-1.32670 + 0.09521i$ | $-1.3206 + 0.0801i$ | $-1.31128 + 0.08123i$ |
| 4- | $-0.34862 + 0.33685i$ | $-0.3584 + 0.3279i$ | $-0.34621 + 0.33552i$ |
| 5- | $-0.26979 + 1.06720i$ | $-0.2855 + 1.0593i$ | $-0.27248 + 1.06293i$ |
| 6- | $-0.25780 + 1.56806i$ | $-0.2828 + 1.5578i$ | $-0.26602 + 1.56185i$ |

# Chapter 7

# Axially-segmented liners in annular ducts with parallel sheared mean flow

In this chapter, the mode-matching theory of Chapter (3) is extended, in order to assess the performance of axially-segmented liners in annular ducts, containing parallel shear flows of arbitrary radial profile. It was demonstrated in the previous chapters that the non-uniformity of the mean flow can have a potentially strong effect upon the mode eigenfunctions and axial decay rates. In light of this, it is reasonable to assume that the attenuation performance of finite length acoustic liners may also be affected by the mean flow profile.

The sole example in the literature of mode-matching for sheared flows is that of Joshi et al. [139], where approximate modal solutions for boundary layer flows were used in a matching scheme based upon continuity of pressure and axial particle velocity across the liner interface planes. It was shown in Chapter (3) that this type of matching scheme does not ensure continuity of mass and momentum, and can lead to errors in predicted attenuation levels and scattering. In the scheme described here, the matching equations are derived from weighted integrals of the continuity and axial momentum equations. Benchmarking is undertaken against finite element solutions for uniform flow, since comparable sheared flow solutions are not currently available. However, at the present time, a strong research and development effort is progressing in the development of finite element methods (e.g. Discontinuous Galerkin Method [45], Galbrun's equation [46, 47]), which are applicable to solving the current problem, and for which the mode-matching method may provide validation cases.

## 7.1 Mode-matching method for annular ducts with parallel sheared mean flow

The analysis begins with the acoustic continuity and axial momentum equations for propagation in an inviscid, parallel sheared mean flow, given in cylindrical coordinates $(r, \theta, x)$

by

$$\left[ik_0 + M\frac{\partial}{\partial x}\right] p + \frac{1}{r}\frac{\partial vr}{\partial r} + \frac{1}{r}\frac{\partial w}{\partial \theta} + \frac{\partial u}{\partial x} = 0\,, \tag{7.1}$$

$$\left[ik_0 + M\frac{\partial}{\partial x}\right] u + v\frac{\mathrm{d}M}{\mathrm{d}r} + \frac{\partial p}{\partial x} = 0\,. \tag{7.2}$$

The weighted forms of the continuity and axial momentum equations over a control volume $V$ around the matching plane, respectively are

$$\int_V ik_0 Wp - v\frac{\partial W}{\partial r} - \frac{w}{r}\frac{\partial W}{\partial \theta}\mathrm{d}V$$
$$+ \int_V \nabla \cdot [Wv, Ww, WMp + Wu]\,\mathrm{d}V = 0\,, \tag{7.3}$$
$$\int_V ik_0 Wu + Wv\frac{\mathrm{d}M}{\mathrm{d}r}\mathrm{d}V + \int_V \nabla \cdot [0, 0, WMu + Wp]\,\mathrm{d}V = 0\,, \tag{7.4}$$

where $W = W(r, \theta)$. Following the analysis of section (3.4), six surface integrals are obtained from the second volume integral, and on taking the limit $\varepsilon \to 0$ (see Figure (3.2)) the following final matching equations are obtained

$$2\pi \int_\hbar^1 W(r)M\left[p(r)^{II} - p(r)^I\right] r\,\mathrm{d}r + 2\pi \int_\hbar^1 W(r)\left[u(r)^{II} - u(r)^I\right] r\,\mathrm{d}r$$

$$+2\pi\hbar\frac{W(\hbar)M(\hbar)}{ik_0}\left[\beta_2^{II}p(\hbar)^{II} - \beta_2^I p(\hbar)^I\right] + 2\pi\frac{W(1)M(1)}{ik_0}\left[\beta_1^{II}p(1)^{II} - \beta_1^I p(1)^I\right] = 0\,, \tag{7.5}$$

$$2\pi \int_\hbar^1 W(r)\left[p(r)^{II} - p(r)^I\right] r\,\mathrm{d}r + 2\pi \int_\hbar^1 W(r)M\left[u(r)^{II} - u(r)^I\right] r\,\mathrm{d}r = 0\,. \tag{7.6}$$

It is assumed that the weighting functions $W$ are finite over the duct cross-section, and that the flow gradient $\mathrm{d}M/\mathrm{d}r$ is also finite over the radial duct section, which excludes power law profiles from the analysis. The third and fourth terms of (7.5) are only present for flow profiles with wall slip conditions. The method is identical for both uniform and sheared flows. In the absence of flow, the matching equations reduce to those of continuity of pressure and axial particle velocity.

### 7.1.1 Expressions for in-duct sound power in sheared flow

The sound power transmission loss $\Delta_{PWL}$ is used to quantify the acoustic liner performance. For uniform flow, the form of axial intensity given by Morfey in equation (3.44) is used, but in fact is only valid for irrotational flows. The mode eigenfunctions in a uniform flow are orthogonal, and so the total sound power can be calculated as the sum of individual modal powers. In contrast to the case of uniform flow, the mode eigenfunctions in a sheared flow are

not orthogonal. Therefore, the total in-duct sound power may contain cross-term contributions due to interactions between different modes (however, Möhring [141] suggests that such cross-terms do not exist). However, in the course of this work, it has been found that the cross-term contributions are rather small, and subsequently are ignored in the analysis. In this work, the form of the axial intensity given by Möhring [142] is used,

$$I_{x\,m,n}^{\pm} = \frac{1}{2}\frac{k_0}{(k_0 - kM)^2}\left\{\frac{-k_0}{2\,(k_0 - kM)^2}\frac{\mathrm{d}M}{\mathrm{d}r}\frac{\mathrm{d}|p_{m,n}^{\pm}|^2}{\mathrm{d}r} + \left(kM + k\left(1 - M^2\right)\right)|p_{m,n}^{\pm}|^2\right\}. \tag{7.7}$$

The total sound power is found by integrating $I_x$ over the duct cross-section and summing over all the propagating modes, to give

$$W^{\pm} = 2\pi \sum_m \sum_n \int_{\hbar}^{1} I_{x\,m,n}^{\pm}(r) r dr. \tag{7.8}$$

The sound power transmission loss and the sound power reflection loss are then given by, respectively

$$\Delta_{\mathrm{PWL}} = 10\log_{10}\left[\frac{W^{+I}}{W^{+(S+1)}}\right], \tag{7.9}$$

$$\Delta_{\mathrm{PWLR}} = 10\log_{10}\left[\frac{W^{+I}}{(W^{+I} + W^{-I})}\right], \tag{7.10}$$

where the power reflection loss is a measure of the power reflected at the liner leading edge.

## 7.2 Validation

Validation of the method is undertaken comparing with Finite Element (FE) solutions obtained using the ACTRAN/TM solver, produced by Free Field Technologies [80]. The finite element solver provides solutions of the wave equation in terms of the velocity potential, requiring a potential mean flow to be specified. Therefore, a uniform mean flow is used for the validation case. The mode-matching method used here is identical to that for a uniform mean flow, the only difference for a sheared flow is that a different set of modes are used. It is noted that the mode eigenvalue solver has already been validated for sheared flows, so only a brief validation is included here.

The validation case is for a realistic geometry at approach conditions for an incident rotor-stator interaction mode. Specifically, the parameters used here are $k_0 = 30.9435$, $m = 4$, $n = 1$, $\hbar = 0.56897$, $Z_1 = Z_2 = 2.1463 - 1.07313i$, $l_I = l_{III} = 0.06788$, $l_{II} = 0.67879$, and $M = 0.345$. The values of pressure at the hub and casing walls obtained from the FE and mode-matching solutions are plotted in figure (7.1) over the axial extent of the duct. The agreement between the two methods is very good, except at the matching planes where a larger singularity in the wall pressure at the matching planes is predicted by the FE method. The

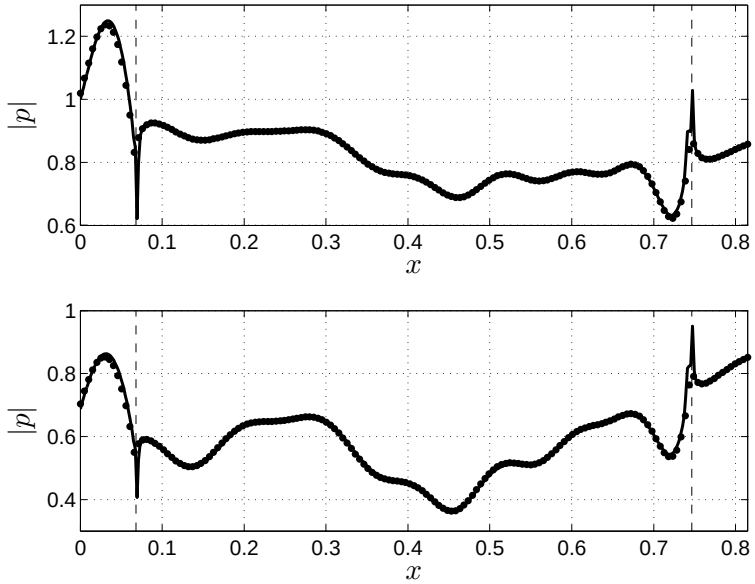


FIGURE 7.1: *Wall pressure comparison of FE and mode-matching solutions for a finite length lined duct with uniform flow. Top plot, casing wall pressure; Bottom plot, hub wall pressure; —, FE solution; •, mode-matching solution.*

radial pressure profile at the leading and trailing matching planes is plotted in figure (7.2), where the FE solution is compared against the mode-matching solutions constructed from rigid and also lined duct modes. The agreement is very good, except near the walls where oscillations in the mode-matching solutions are more noticeable. This behaviour has already been discussed in Chapter (3). A comparison of the scattered modal intensity is shown in figure (7.3) where multi-mode solutions have been obtained assuming equal energy per cut-on mode at $k_0 = 30.9435$. The agreement in the transmitted intensities is excellent, whilst small discrepancies occur in the reflected intensities for the less well cut-on modes.

## 7.3 Mode-matching with vortical modes

If the mean flow is uniform, a convenient decoupling of the acoustic and hydrodynamic (vortical) fields is possible (see Eversman [4]). However, if the flow is non-uniform this no longer applies. Since the acoustic and hydrodynamic fields are coupled, this theoretically requires both fields to be solved to form a complete solution of the unsteady field. In this case two distinct eigenmode spectra are present, consisting of pressure dominant acoustic modes, and velocity dominant vortical modes. The only modes that propagate upstream are acoustic modes, whilst both acoustic and vortical modes propagate downstream. The vortical modes form a continuous spectrum owing to the presence of a critical layer where $k_0 - kM(r) = 0$. The current method for solving the acoustic mode eigenvalues is not suitable for obtaining vortical mode eigenvalues since the eigenvalue equations are singular at the critical layer. Recent work by Vilenski and Rienstra [143, 115, 144] suggests that, for mean flows with wall

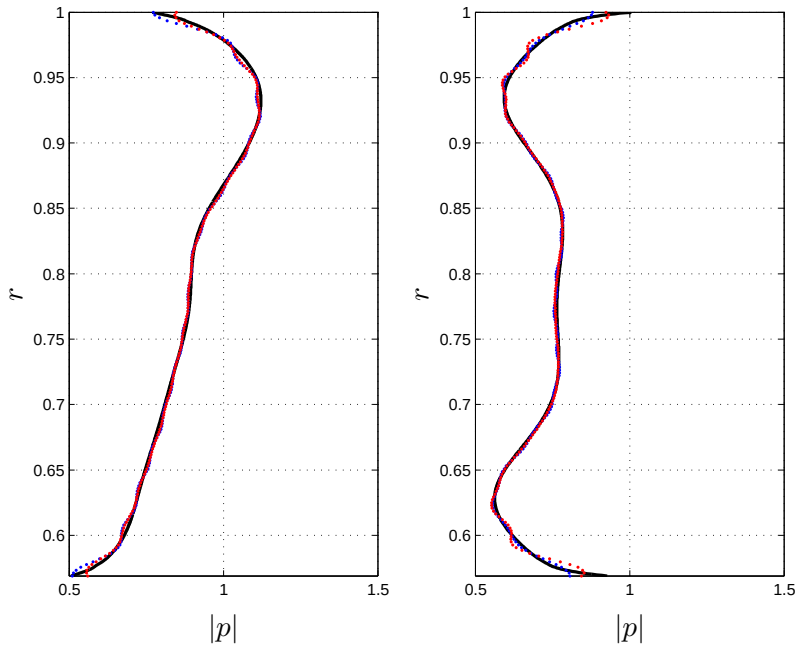


FIGURE 7.2: *Matching plane radial pressure profile comparison of FE and mode-matching solutions for a finite length duct with uniform flow. Left plot, leading matching plane $x = x^I$; Right plot, trailing matching plane $x = x^{II}$; —, FE solution; · · ·, mode-matching solution (rigid duct modes); · · ·, mode-matching solution (lined duct modes).*

slip conditions, there exist two vortical modes which have smooth eigenfunctions, and correspond to critical layers located at each wall. In addition, there is a continuum of vortical modes corresponding to critical layers inside the flow region, the eigenfunctions of which are not smooth having only two continuous derivatives at the critical point [144].

It is of interest to investigate the effect of such modes on the mode-matching procedure, since to obtain complete field solutions would theoretically require their inclusion. The inclusion of vortical modes in triple-plane pressure matching schemes was investigated by Vilenski [145] for modal decomposition of unsteady CFD solutions in rigid ducts. It was suggested that the inclusion of some of the wall localised vortical modes can improve the near wall accuracy of the matching. The presence of a continuous spectrum means that modal analysis is not strictly applicable to the hydrodynamic spectrum, however, in the discrete model a set of discrete mode solutions exist and depend upon the number of grid points. In the discrete model, the vortical modes are defined at $k = k_0/M(r_*)$, with possible multiplicity depending on the flow profile. For slip flows the continuous spectrum is bounded in a region defined by the maximum and minimum Mach numbers to be $k_0/max[M(r_*)] \leq k \leq k_0/min[M(r_*)]$. For profiles with no-slip wall conditions, the upper limit is unbounded.

In this work, the vortical modes are solved by expanding the Pridmore-Brown equation in a small region around the critical layer [146]. This leads to an ODE valid in the neighbouring region, which is solved using the method of Frobenius [147]. This analytic solution is then used to find the value of the pressure at the critical point. The mode eigenfunction over the whole duct section is then obtained by matching the numerical solution of the Pridmore-Brown

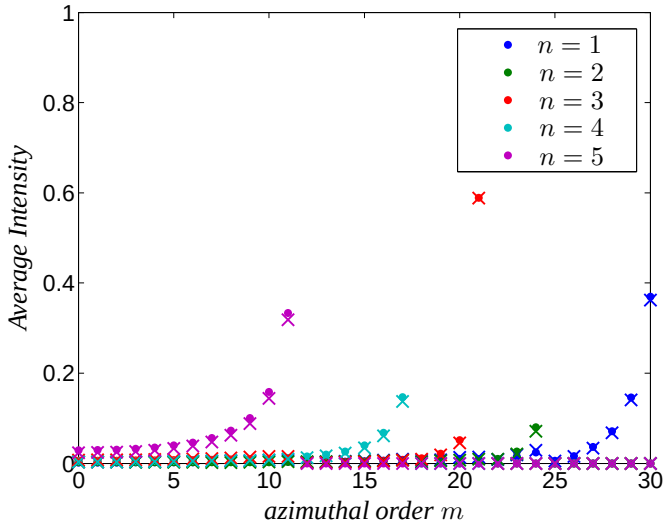


(a) Reflected modal intensity.

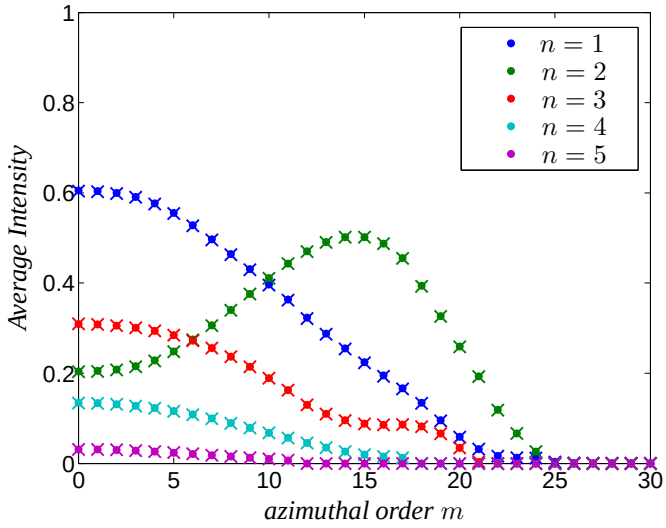


(b) Transmitted modal intensity.

FIGURE 7.3: *Comparison of scattered modal intensities from FE and mode-matching solutions for a finite length duct with uniform flow.* $\times$*, mode-matching solution;* $\bullet$*, FE solution.*

equation (obtained using Runge-Kutta integration) at the edges of the small region bounding the critical layer, to the analytic solution. Examples of the vortical mode pressure and axial particle velocity eigenfunctions are presented in figure (7.4) for the linear shear flow profile shown in figure (7.5). The pressure eigenfunctions have maxima at the critical point and decay rapidly away from there, remaining pressure-less across the remaining duct section. For critical points at the wall, the pressure eigenfunctions are finite at the wall and decay rapidly away from the wall. However, the axial particle velocity eigenfunctions, which are required in the mode-matching scheme, are discontinuous at the critical point for critical layers not located at the walls. This poses a problem for mode-matching with such modes, since the axial particle velocity is undefined at the critical layers. In an attempt to circumvent this problem, the critical points are defined to be mid-way between pairs of grid points. An example of the pressure field contour obtained from the mode-matching solution using this method is shown in figure (7.6),

and is compared against solutions including only acoustic modes, and including the two wall vortical modes. Here, the vortical modes in the lined sections are assumed to be independent of the wall impedance, since they are almost incompressible. In fact, when the critical point is at the wall this turns out to be true since $k_0 - kM\left(r_*\right) = 0$, and from the boundary condition

$$\frac{\mathrm{d}p}{\mathrm{d}r} = \pm\frac{i}{k_0 Z}\left(k_0 - kM\left(r_*\right)\right)^2 p = 0 \quad \Rightarrow \frac{\partial p}{\partial r} = 0\,, \tag{7.11}$$

whilst the mode is pressure-less at the opposite wall. The pressure and axial particle velocity radial matching profiles at the matching planes are shown in figure (7.7) where ten vortical modes are included. The velocity field includes un-physical singularities, and the pressure field is subsequently quite different from the case without vortical modes. Matching profile plots for solutions when only the wall vortical modes are included are shown in figure (7.8). In this case the matching dramatically improves. Oscillations that are present away from the walls, in the solutions with only acoustic modes, are reduced when the wall vortical modes are included. This effect is similar to that seen in Chapter (3) when including the hydrodynamic surface wave mode. The differences in the power transmission loss for solutions including zero, ten, and only wall vortical modes are compared in figure (7.9). The power losses very slightly increase when the wall vortical modes are included, whilst larger variation is seen when ten vortical modes are included, but this result has an un-physical velocity field.

A case of further interest is that where the incident disturbance is a vortical mode. Contours of the three pressure fields due to incident vortical modes of unit amplitude located on both hub and casing, on only the casing, and in mid-duct are shown in figure (7.10). When the incident vortical modes are located at critical points on (or near) the walls there is scattering of energy into acoustic modes at the liner leading and trailing edges. From a mathematical viewpoint, this occurs due to the wall terms in the matching equation (7.5) for continuity of mass. Note that for flows with no wall slip conditions this term is zero, and no scattering into acoustic modes would occur. The magnitude of the reflected and transmitted acoustic powers is very small. These results demonstrate that, for a rotational flow, the interaction of acoustic and vortical modes occurs at the liner edges resulting in both shed vorticity and a transfer of energy between acoustic and vortical modes. Whether this represents a net production of acoustic power (i.e. a source) at the liner edges is unclear since a method to calculate the acoustic power of the pressure-coupled vortical modes is as yet unknown [69].

The results presented here show that the inclusion of vortical modes is only justified for vortical modes located at the walls, and the effect upon the scattered acoustic power is minimal for typical applications. Therefore, in the following sections, analysis of finite length liners in duct with sheared flows is undertaken with only acoustic modes included in the mode-matching scheme.

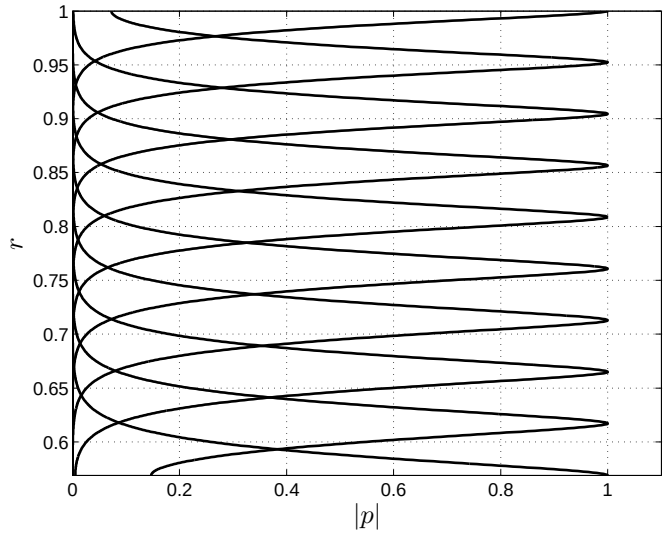


(a) Pressure eigenfunctions.

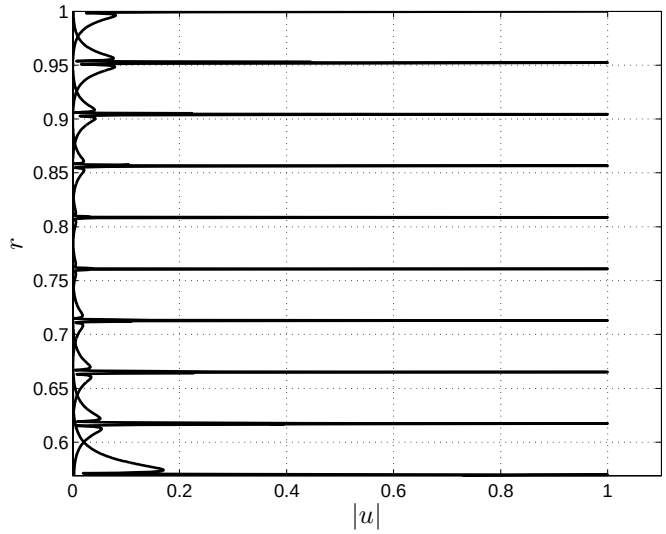


(b) Axial particle velocity eigenfunctions.

FIGURE 7.4: *Ten hydrodynamic mode pressure and axial particle velocity eigenfunctions for* $m = 0$ *at* $k_0 = 30.94355$ *for a linear shear flow (negative gradient).*$\hbar = 0.56$.

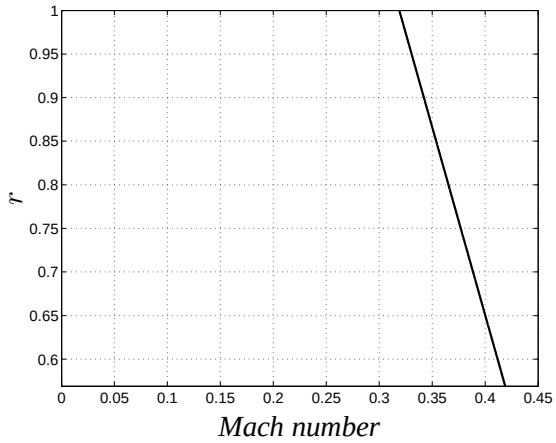


FIGURE 7.5: *Linear shear profile with negative gradient and wall slip conditions.*

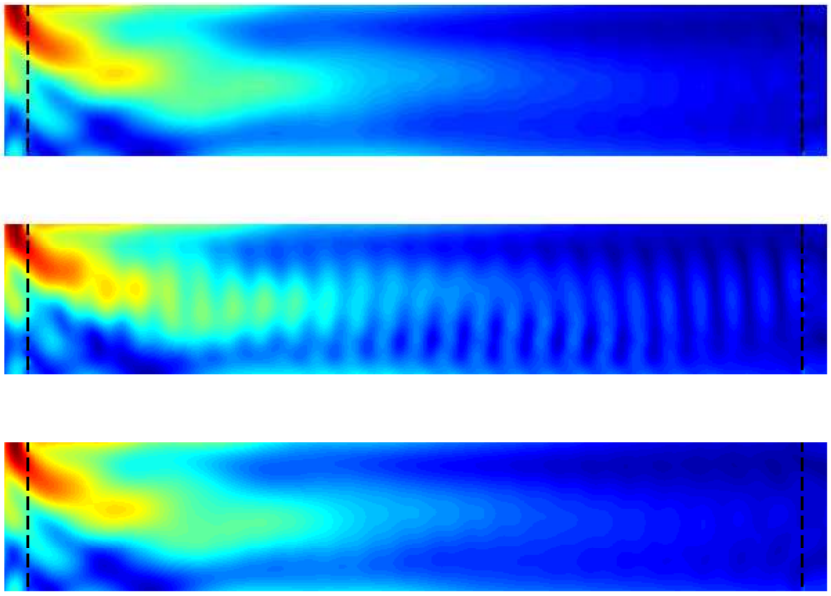

FIGURE 7.6: *Pressure field contours due to single mode source* $(0, 1)$ *at* $k_0 = 30.94355$ *for a finite length lined duct with a linear sheared flow (negative gradient). Location of the leading and trailing edges of the liner is indicated by vertical dashed lines. Top plot, acoustic modes only; Middle plot, with 10 vortical modes; Bottom plot, with 2 wall vortical modes.* $R = 1$, $M_r = 0.012$, $D = 0.021$, $l_I = l_{III} = 0.067879$, $l_{II} = 2.226446$, $\hbar = 0.56897$.

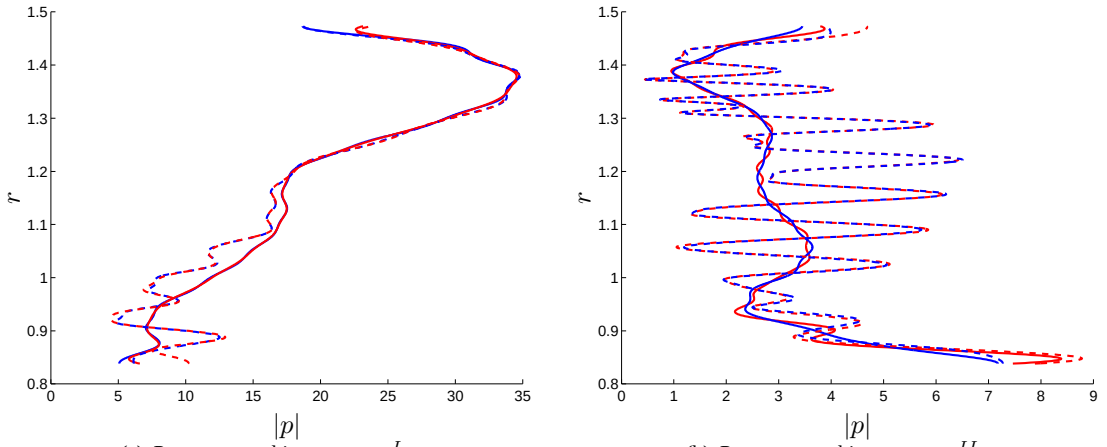


(a) Pressure matching at $x = x^I$.

(b) Pressure matching at $x = x^{II}$.

(c) Axial particle velocity matching at $x = x^I$.

(d) Axial particle velocity matching at $x = x^{II}$.

FIGURE 7.7: *Pressure and axial particle velocity matching plane profiles for* $m = 0$ *at* $k_0 = 30.94355$ *for a linear shear flow (negative gradient). —, acoustic modes only; −−, including 10 vortical modes; Blue lines, rigid duct modes; Red lines, lined duct modes.*$\hbar = 0.56897$.

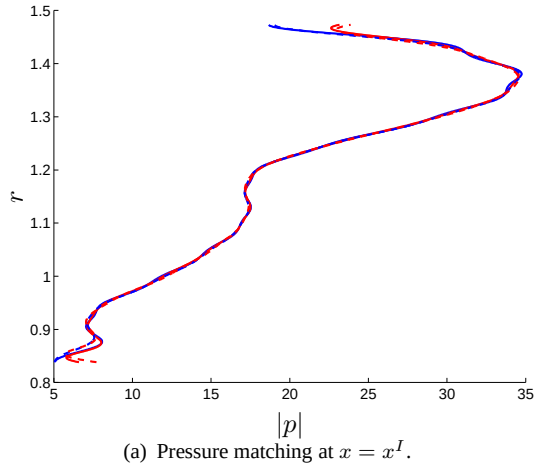


(a) Pressure matching at $x = x^I$.

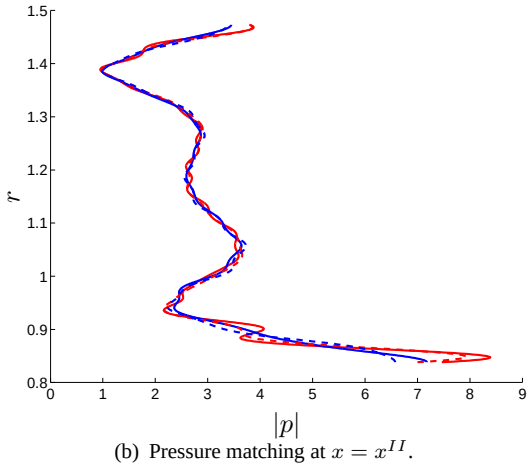


(b) Pressure matching at $x = x^{II}$.

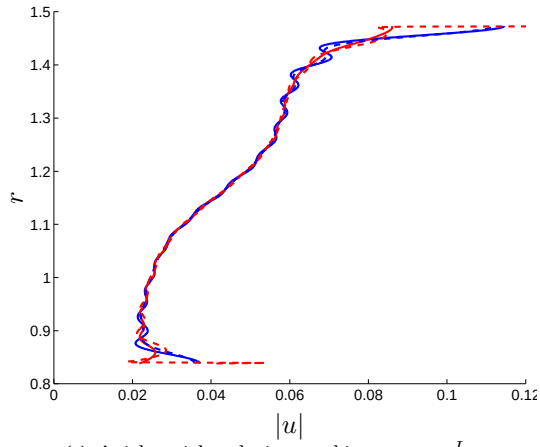


(c) Axial particle velocity matching at $x = x^I$.

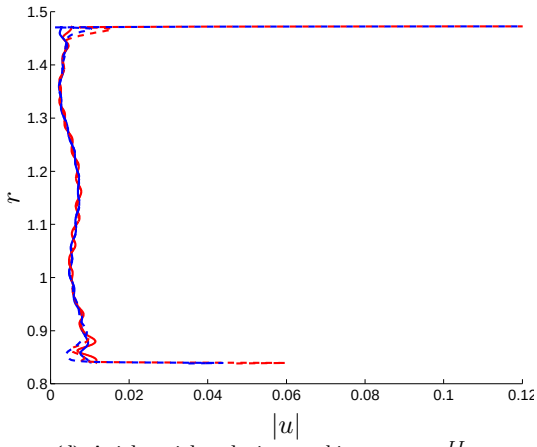


(d) Axial particle velocity matching at $x = x^{II}$.

FIGURE 7.8: *Pressure and axial particle velocity matching plane profiles for* $m = 0$ *at* $k_0 = 30.94355$ *for a linear shear flow (negative gradient). —, acoustic modes only; −−, including 2 wall vortical modes; Blue lines, rigid duct modes; Red lines, lined duct modes.*$\hbar = 0.56897$.

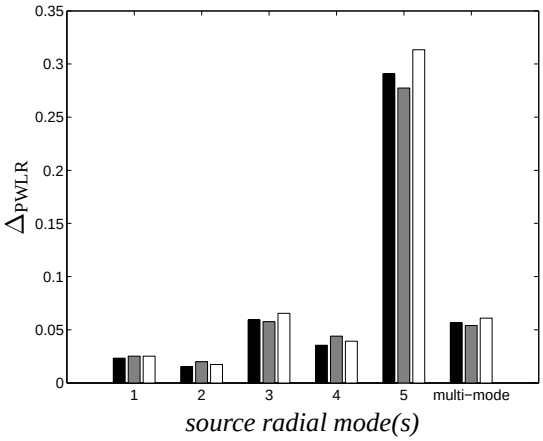


(a) Reflection loss, $m = 0$.

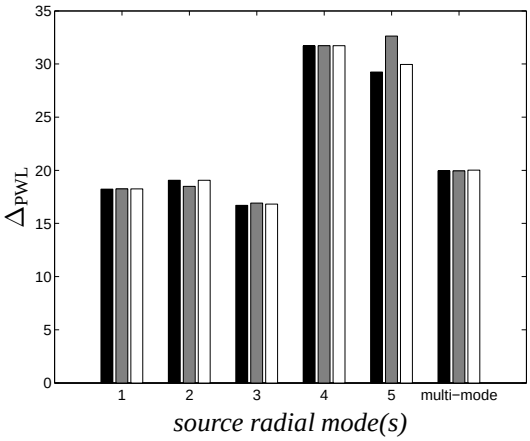


(b) Transmission loss, $m = 0$.

FIGURE 7.9: *Comparison of power reflection and transmission loss for single and multi-mode sources* $m = 0$ *at* $k_0 = 30.94355$ *for a linear shear flow (negative gradient).* ■*, acoustic modes only;* ■*, including 10 vortical modes;* □*, including 2 wall vortical modes.* $R = 1$, $M_r = 0.012$, $D = 0.021$, $l_I = l_{III} = 0.067879$, $l_{II} = 2.226446$, $\hbar = 0.56897$.

FIGURE 7.10: *Pressure field contours due to vortical mode sources at* $k_0 = 30.94355$ *for a finite length lined duct with a linear sheared flow (negative gradient). Location of the leading and trailing edges of the liner is indicated by vertical dashed lines. Top plot, 2 incident vortical modes located at hub and casing ; Middle plot, single incident vortical mode located at casing; Bottom plot, single incident vortical mode located mid-duct.* $R = 1$, $M_r = 0.012$, $D = 0.021$, $l_I = l_{III} = 0.067879$, $l_{II} = 2.226446$, $\hbar = 0.56897$.

## 7.4 Summary

- A mode-matching scheme for acoustic propagation in lined annular ducts containing an inviscid, parallel sheared flow is presented.
- Validation of the scheme has been successfully undertaken against finite element solutions for finite length liners in ducts with uniform flow.
- Solutions of the mode-matching scheme including vortical modes have been investigated for slip flow profiles. It is found that the inclusion of vortical modes corresponding to critical points at the walls could improve the matching procedure. The inclusion of mid-duct vortical modes is found to produce un-physical results.
- The transfer of energy between incident acoustic and vortical disturbances is demonstrated to result in the transfer of energy between near wall vortical modes and acoustic modes.

# Chapter 8

# Analysis of axially-segmented liners in annular ducts with parallel sheared mean flow

It was demonstrated in Chapter (6) that the mean flow profile can have a strong effect on both the mode eigenfunctions and the mode decay rates in rigid and lined ducts. In this chapter the effects of flow profile upon the modal scattering and attenuation performance of finite length liners are assessed. Again, realistic geometry and approach conditions are used where $\hbar = 0.56897$.

## 8.1 Convergence to the slip flow case

Full assessment of the limit $\delta \to 0$ is not possible in the current formulation since the flow gradient $\mathrm{d}M/\mathrm{d}r$ must be finite. Here, a linear boundary layer profile is used to investigate convergence to the uniform slip flow case to the limit of a very small boundary layer thickness $\delta/(1-\hbar) \to 0.003125$. The parameters used are identical to the validation case, and the source consists of equal energy per cut-on mode for azimuthal order $m = 4$. The variation of the power transmission loss $\Delta_{PWL}$ and the power reflection loss $\Delta_{PWLR}$ with boundary layer thickness are presented in figure (8.1), where the corresponding FE solution for uniform flow is plotted for reference. The power losses are seen to converge to the uniform slip flow solutions. With uniform flow, the difference between mode-matching and FE solutions is very small, and were already shown to converge with increasing number of modes in the matching and FE mesh refinement in Chapter (3).

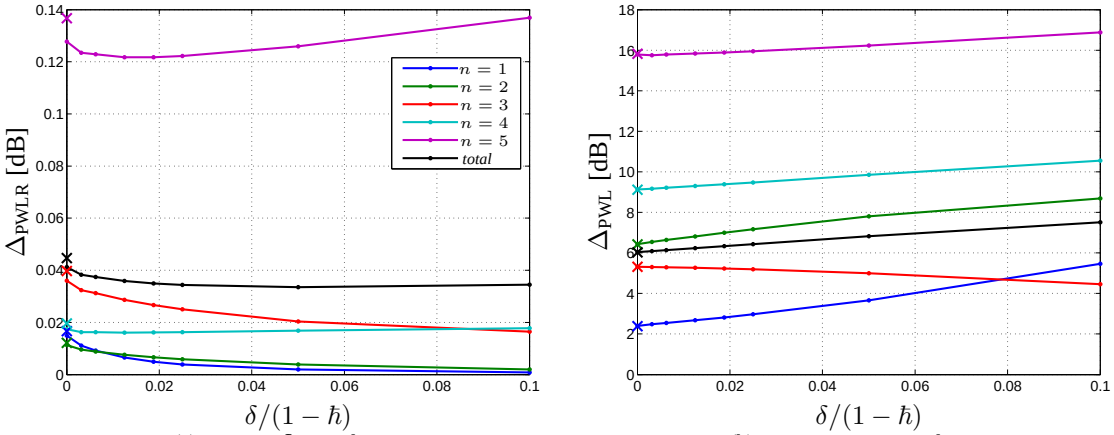


(a) Power reflection loss. (b) Power transmission loss.

FIGURE 8.1: *Convergence of power transmission and reflection loss for a finite length duct with a linear boundary layer mean flow in the limit $\delta \to 0$. $-\bullet-$, mode-matching solution; $\times$, FE uniform flow solution.*

## 8.2 Boundary layer effects

The effects of boundary layers upon modal scattering and power attenuation are investigated by comparing mode-matching solutions for uniform flow with those obtained for two linear boundary layer profiles of thickness $\delta/(1-\hbar) = 0.0125$ and 0.05, representing thin and thick boundary layers, respectively. The sound power transmission loss spectra for multi-mode sources for $m = 0$ and $m = 16$ are compared in figure (8.2). The low frequency ($k \sim 2 \times$ BPF) attenuation peak shifts to lower frequency as the boundary layer thickness increases, which is mainly due to the reduction in the mass flow rate. At higher frequencies, the attenuation is seen to increase with boundary layer thickness. Additionally, the attenuation rates for sources $m = 0$ and $m = 16$ are comparable at high frequency where many modes are propagating.

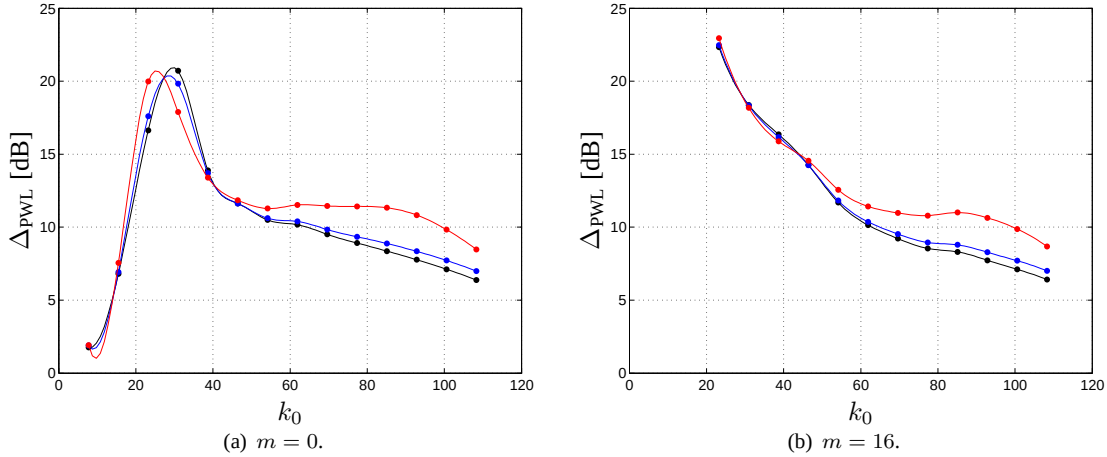


(a) $m = 0$. (b) $m = 16$.

FIGURE 8.2: *Effect of boundary layer thickness upon sound power transmission loss frequency response for multi-mode sources at $m = 0$ and $m = 16$ in a lined duct of finite length. $-\bullet-$, uniform flow $M = 0.345$; $-\bullet-$, thin linear boundary layer $\delta/(1-\hbar) = 0.0125$; $-\bullet-$, thick linear boundary layer $\delta/(1-\hbar) = 0.05$. $R = 1$, $M_r = 0.012$, $D = 0.021$, $l_I = l_{III} = 0.067879$, $l_{II} = 2.226446$, $\hbar = 0.56897$.*

The scattered modal intensities for multi-mode sources $m = 0$ and $m = 16$ are plotted in figure (8.3) at $k_0 = 30.94$, near the peak power attenuation, and in figure (8.4) at $k_0 = 85.09$, in the frequency region where refraction effects are stronger. At the lower frequency, the scattering behaviour is consistent for each boundary layer, with most transmitted energy contained in modes $n = 1$ and $n = 3$. The absolute level differences are mainly due to the change in mass flow rate, resulting in less attenuation as the boundary layer thickness increases. However, at the higher frequency, stronger flow gradient effects upon the mode eigenfunctions and eigenvalues cause large changes in the scattering pattern. As the boundary layer thickness is increased, the least well attenuated mode changes from $n = 1$ to $n = 3$. Pressure contour plots for the incident modes $(0, 1)$ and $(16, 1)$ at $k_0 = 85.09$ are shown in figure (8.5) for each flow profile. The pressure field for the uniform flow case with the plane wave incident mode $(0, 1)$ is almost symmetric about the annulus center-line. However, when a boundary layer is introduced the pressure field becomes highly asymmetric, and in fact become very similar to the cases with incident modes $(16, 1)$. When a boundary layer is introduced, the incident mode eigenfunction $(0, 1)$ is more affected than mode $(16, 1)$, as demonstrated in figure (8.6). For the thick boundary layer, the modes $(0, 1)$ and $(16, 1)$ are almost indistinguishable, and thus the modal scattering patterns due to each are very similar.

## 8.3 General flow non-uniformity effects

The effects of general flow non-uniformity are investigated by comparing mode scattering and power attenuation calculations for the series of flow profiles presented in figure (8.7). The flow profiles have been adjusted so that the mass flow rate for each is approximately equal, with an equivalent average Mach number of $M = 0.345$. An SDOF liner is modelled using equation (4.2), with identical parameters to those used previously to give the impedance spectrum shown in figure (6.8). The power transmission loss spectra for multi-mode sources at azimuthal orders $m = 0$ and $m = 4$ are presented in figure (8.8) for each flow profile, and for configurations where there is a liner on the hub, casing or both. Power transmission loss values are obtained at frequency intervals of $k_0 = 0.5 \times BPF = 7.74$.

The inclusion of a boundary layer leads to an increase in attenuation compared with the wall slip profiles, at frequencies greater than $k_0 = 60$. When only the casing is lined, flow profiles with negative core flow gradients produce higher attenuation rates since sound is refracted towards the lined wall. Conversely, when only the hub is lined, flow profiles with positive flow gradients produce higher attenuation rates. The multi-modal attenuation of the spinning modes is slightly higher than for the non-spinning modes.

The corresponding power transmission loss spectra for a single mode source $n = 1$ are presented in figure (8.9). It is noted that the source mode pressure is more localised at the outer wall for the spinning mode $m = 4$, compared with the non-spinning mode $m = 0$. Where both walls are lined, the attenuation rates are substantially higher for flows with non-uniform core

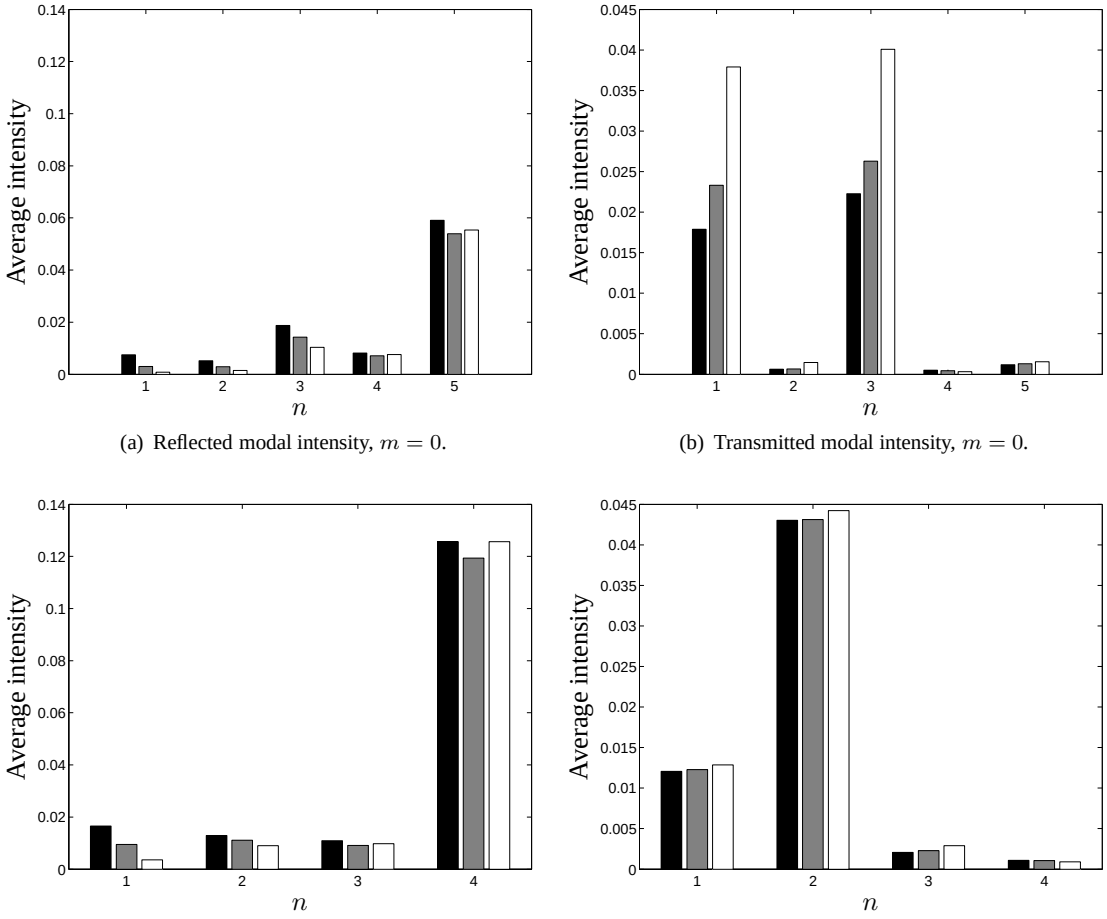


(a) Reflected modal intensity, $m = 0$.

(b) Transmitted modal intensity, $m = 0$.

(c) Reflected modal intensity, $m = 16$.

(d) Transmitted modal intensity, $m = 16$.

FIGURE 8.3: *Effect of boundary layer thickness upon modal scattering for multi-mode sources* $m = 0$ *and* $m = 16$ *at* $k_0 = 30.94355$ *in a lined duct of finite length.* ■*, uniform flow* $M = 0.345$*;* ■*, thin linear boundary layer* $\delta/(1-\hbar) = 0.0125$*;* □*, thick linear boundary layer* $\delta/(1-\hbar) = 0.05$*.* $R = 1$*,* $M_r = 0.012$*,* $D = 0.021$*,* $l_I = l_{III} = 0.067879$*,* $l_{II} = 2.226446$*,* $\hbar = 0.56897$*.*

profiles, and are again generally highest for those with negative core flow gradients. When only the casing is lined, higher attenuation is obtained for profiles with negative core flow gradients, and for the spinning mode source. Conversely, when only the hub is lined, higher attenuation is obtained for profiles with positive core flow gradients, and for the non-spinning mode source.

In order to investigate the physical mechanisms behind the observed trends in power attenuation, further analysis of the mode scattering and modal power attenuation for each flow profile is conducted for sources at $k_0 = 2 \times BPF = 30.94$, where five radial modes are cut-on. The axial decay rates of the cut-on, downstream propagating modes for each flow profile, with one or both walls lined, are given in Table (8.1) for $m = 0$, and Table (8.2) for $m = 4$. An estimate of the transmission loss is given for each case, given by

$$\Delta_{m,n} = -20\Im\{k_{m,n}\} l_{II} \log_{10} e \,, \tag{8.1}$$

where $k_{m,n}$ is the eigenvalue of the Least Attenuated Mode (LAM), and $l_{II}$ is the

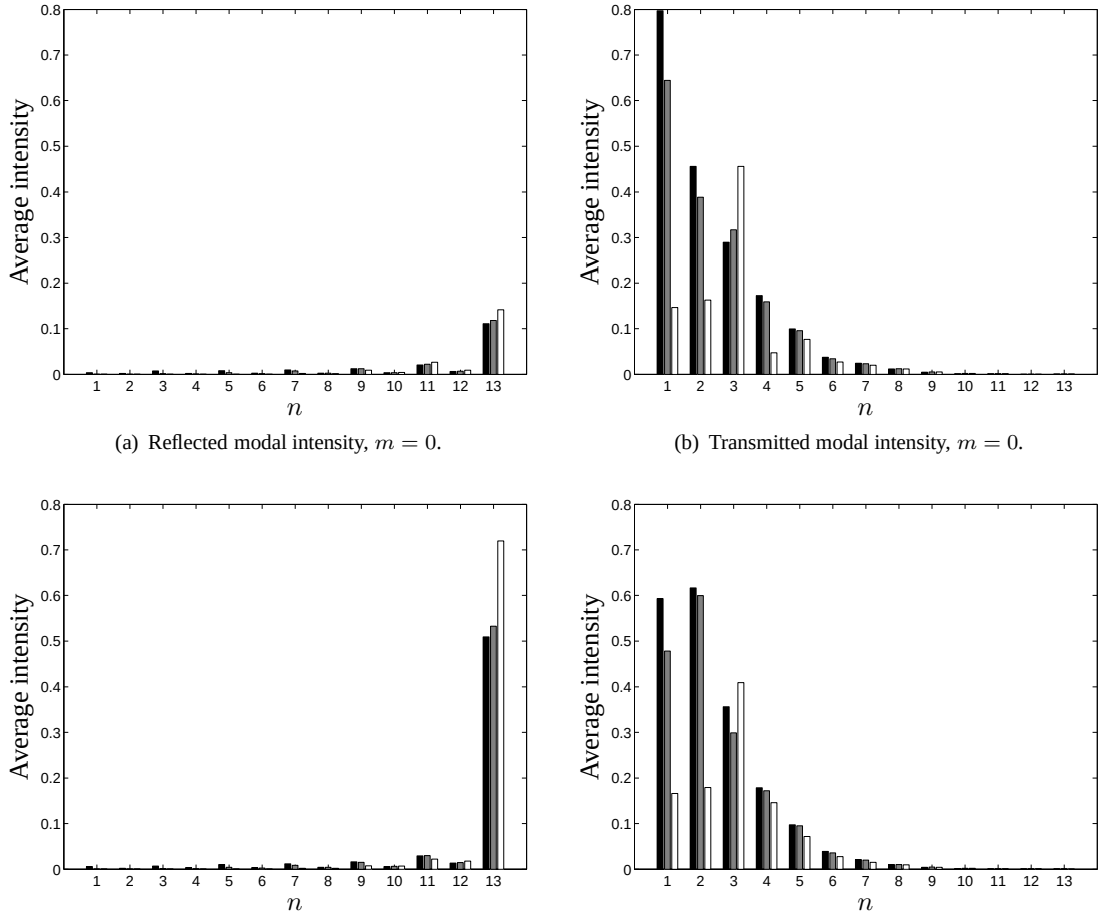


(a) Reflected modal intensity, $m = 0$.

(b) Transmitted modal intensity, $m = 0$.

(c) Reflected modal intensity, $m = 16$.

(d) Transmitted modal intensity, $m = 16$.

FIGURE 8.4: *Effect of boundary layer thickness upon modal scattering for multi-mode sources* $m = 0$ *and* $m = 16$ *at* $k_0 = 85.094754$ *in a lined duct of finite length.* ■*, uniform flow* $M = 0.345$*;* ■*, thin linear boundary layer* $\delta/(1-\hbar) = 0.0125$*;* □*, thick linear boundary layer* $\delta/(1-\hbar) = 0.05$*.* $R = 1$*,* $M_r = 0.012$*,* $D = 0.021$*,* $l_I = l_{III} = 0.067879$*,* $l_{II} = 2.226446$*,* $\hbar = 0.56897$*.*

non-dimensional liner length. The mode ordering is such that the least attenuated mode is not necessarily $n = 1$. In these examples, quasi-surface waves (in the sense that the eigenfunctions are tending to appear similar to a surface wave) are present, and are typically of low mode order, but have higher decay rates than the lowest order acoustic modes. It is seen that, with the exception of the quasi-surface wave modes, the decay rates for ducts lined on both walls are much higher than for those with only one wall lined. The lowest least attenuated mode decay rates are found when one wall is lined, and the core flow gradient is such that sound is refracted away from the lined wall. The surface wave mode decay rates are strongly affected by the flow profile, but are quite insensitive to the impedance of the wall opposite to which they are localised.

The power transmission loss due to each of the five cut-on modes as individual sources $(m, n) = (m, 1)$ to $(m, 5)$, and also as a multi-mode source, are given in Table (8.3) for the non-spinning mode $m = 0$, and Table (8.4) for the spinning mode $m = 4$. The transmission loss values are much higher when both walls are lined since the least attenuated mode changes

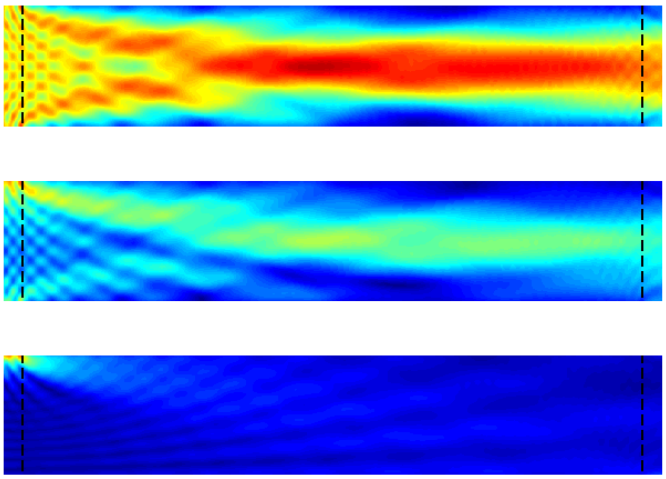

(a) Pressure field, $(0, 1)$.

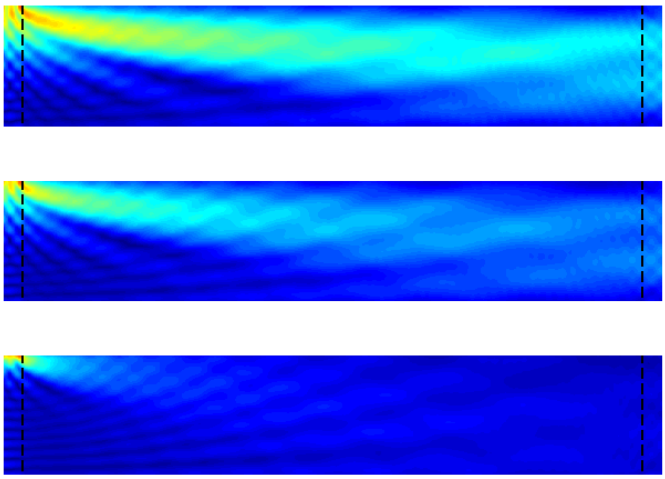

(b) Pressure field, $(16, 1)$.

FIGURE 8.5: *Pressure field contours due to single mode source* $(m, 1)$ *at* $k_0 = 85.094754$ *for a finite length lined duct with uniform and linear boundary layer flows. Location of the leading and trailing edges of the liner is indicated by vertical dashed lines. Top plot, uniform slip flow* $M = 0.345$*; Middle plot, thin linear boundary layer* $\delta/(1-\hbar) = 0.0125$*; Bottom plot, thick linear boundary layer* $\delta/(1-\hbar) = 0.05$*.* $R = 1$*,* $M_r = 0.012$*,* $D = 0.021$*,* $l_I = l_{III} = 0.067879$*,* $l_{II} = 2.226446$*,* $\hbar = 0.56897$*.*

from either mode $(m, 1)$ or $(m, 2)$ to $(m, 3)$ which has a higher decay rate. In addition, the modes $(m, 1)$ and $(m, 2)$ are both quasi-surface wave modes when both walls are lined, thus any energy scattered into these modes is more heavily attenuated.

Contour plots of the pressure fields with incident modes $(0, 1)$ and $(4, 1)$ are shown in figure (8.10) for a uniform flow. Examples are shown for configurations with one or both walls lined. These plots demonstrate the scattering of incident modes by the acoustic liner. When both walls are lined a fairly symmetric sound field is seen for the plane wave mode case, whereas higher pressure levels are seen towards the casing for the spinning mode case. Contour plots for cases with either the hub or casing wall lined demonstrate the effect of the liner on the pressure field, with the blue areas, indicating low pressure values, adjacent to the lined wall. The average modal and total intensities, (averaged over the duct cross-section), of the transmitted modes for

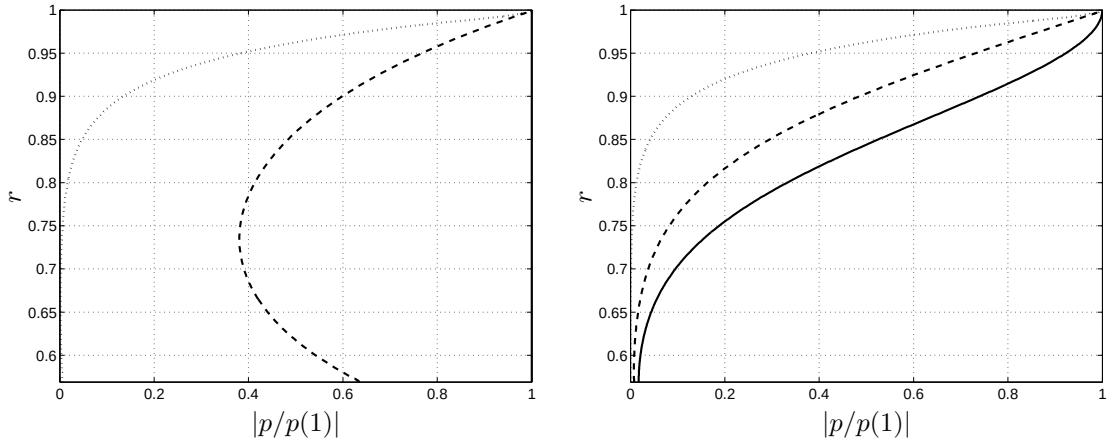


(a) Incident mode eigenfunctions, $(0, 1)$. (b) Incident mode eigenfunctions, $(16, 1)$.

FIGURE 8.6: *Comparison of incident mode eigenfunctions at* $k_0 = 85.094754$. *—, uniform slip flow* $M = 0.345$*; −−, thin linear boundary layer* $\delta/(1 - \hbar) = 0.0125$*; · · ·, thick linear boundary layer* $\delta/(1 - \hbar) = 0.05$. $\hbar = 0.56897$.

the case where both walls are lined are presented in figure (8.11) (top row). Six intensities are plotted for each transmitted mode radial order, which correspond (from left to right) to the levels with a single mode source ($(m, 1)$ to $(m, 5)$), and a multi-mode source $(m, 1 \rightarrow 5)$. In addition, the acoustic pressure radial eigenfunctions of downstream propagating modes $(m, 1)$ to $(m, 5)$, in the rigid (middle row) and lined ducts (bottom row), are shown. From the pressure field contour plots, it is clear that after scattering, the field owing to the plane wave source is more oscillatory, indicating that a large amount of scattering occurs. This is confirmed by observing the transmitted intensities, where most energy in the trailing duct section is contained in modes $(0, 1)$ and $(0, 3)$. A similar scattering pattern is observed for the spinning mode case.

Contour plots of the pressure field for cases with a positive core shear flow gradient are shown in figure (8.12). Here, there is a significant change in the pressure field when only the hub or the casing are lined. The pressure fields are similar when both walls are lined or only the hub is

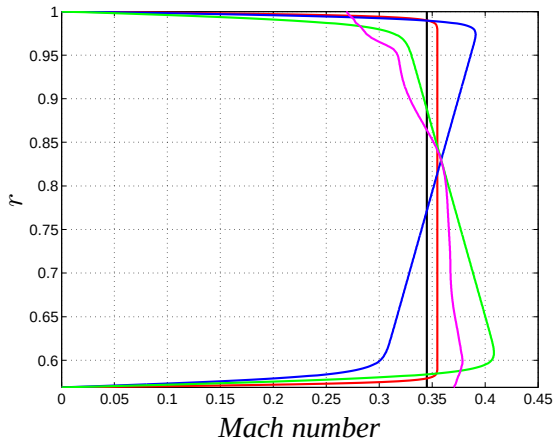


FIGURE 8.7: *Mean flow profiles with equal mass flow rate used in the mode scattering and power attenuation study. —, uniform flow* $M = 0.345$*; —, boundary layer flow; —, positively sheared linear flow; —, negatively sheared linear flow; —, realistic flow with wall slip conditions.*

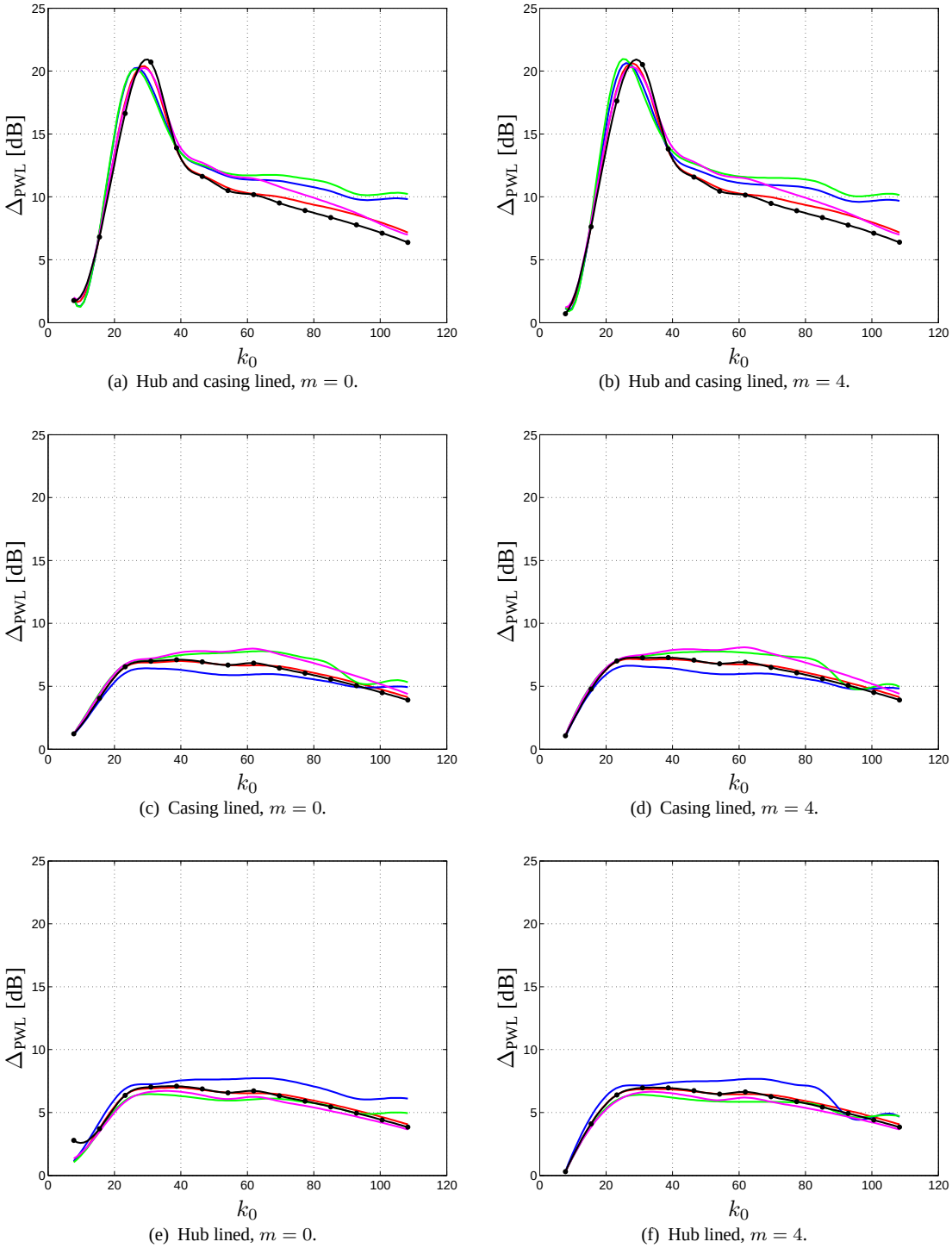


(a) Hub and casing lined, $m = 0$.

(b) Hub and casing lined, $m = 4$.

(c) Casing lined, $m = 0$.

(d) Casing lined, $m = 4$.

(e) Hub lined, $m = 0$.

(f) Hub lined, $m = 4$.

FIGURE 8.8: *Power transmission loss spectra for multi-mode sources $m = 0$ and $m = 4$ for a finite length duct with various flow profiles. Flow profile key as figure (8.7). $R = 1$, $M_r = 0.012$, $D = 0.021$, $l_I = l_{III} = 0.067879$, $l_{II} = 2.226446$, $\hbar = 0.56897$.*

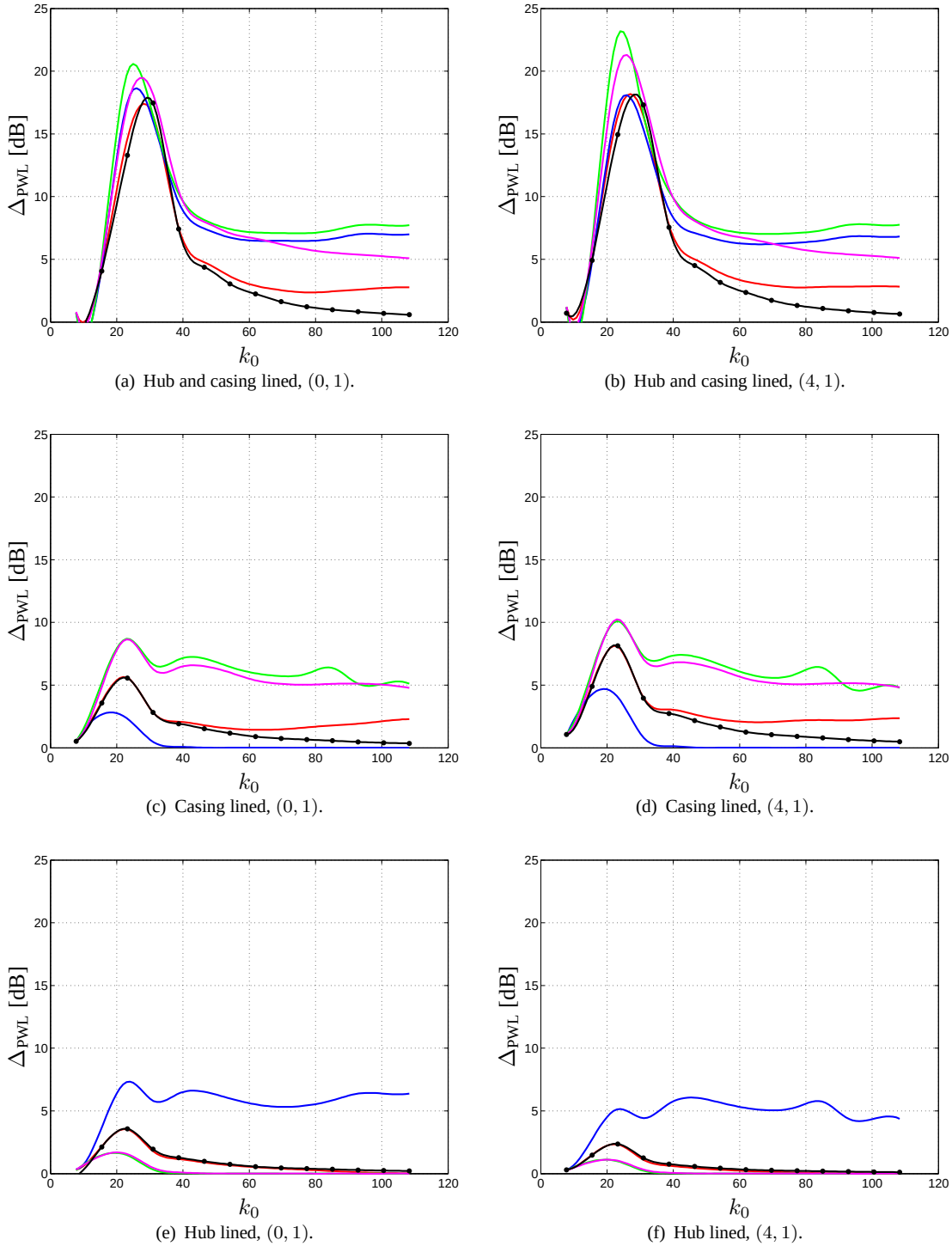


(a) Hub and casing lined, $(0, 1)$.

(b) Hub and casing lined, $(4, 1)$.

(c) Casing lined, $(0, 1)$.

(d) Casing lined, $(4, 1)$.

(e) Hub lined, $(0, 1)$.

(f) Hub lined, $(4, 1)$.

FIGURE 8.9: *Power transmission loss spectra for single mode sources* $(0, 1)$ *and* $(4, 1)$ *for a finite length duct with various flow profiles. Flow profile key as figure (8.7).* $R = 1$, $M_r = 0.012$, $D = 0.021$, $l_I = l_{III} = 0.067879$, $l_{II} = 2.226446$, $\hbar = 0.56897$.

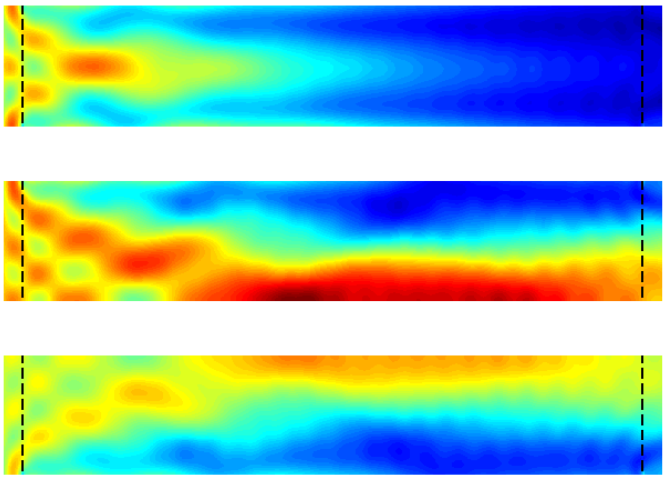

(a) Pressure field, $(0, 1)$.

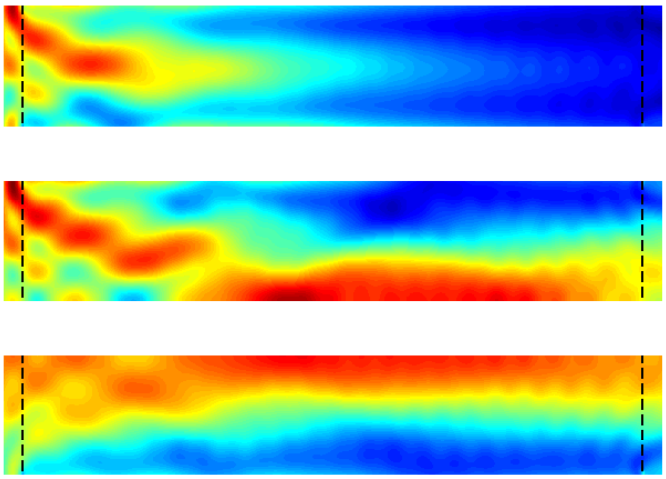

(b) Pressure field, $(4, 1)$.

FIGURE 8.10: *Pressure field contours due to single mode source* $(m, 1)$ *at* $k_0 = 30.94355$ *for a finite length lined duct with uniform flow. Location of the leading and trailing edges of the liner is indicated by vertical dashed lines. Top plot, both walls lined; Middle plot, only casing lined; Bottom plot, only hub lined.* $R = 1$, $M_r = 0.012$, $D = 0.021$, $l_I = l_{III} = 0.067879$, $l_{II} = 2.226446$, $\hbar = 0.56897$.

lined, because the incident wave is refracted towards the hub by the positive flow gradient. When only the casing is lined, a higher pressure is maintained along the rigid hub wall due to the lack of absorption. The opposite is seen when the flow gradient is negative, as shown in figure (8.13).

Considering the linear shear flow with a positive gradient, when only the casing is lined, the predicted transmission loss for incident mode $(0, 1)$ is 0.48 dB, and for mode $(0, 2)$ is 10.41 dB. However, when only the hub is lined, the predicted transmission loss for incident mode $(0, 1)$ is 5.81 dB, and for mode $(0, 2)$ is 2.81 dB. The transmitted intensities and mode eigenfunctions for these cases are presented in figures (8.14) and (8.15) respectively. It is seen that, when only the casing is lined, the mode eigenfunctions for $(0, 1)$ in the rigid duct, and $(0, 2)$ in the lined duct are very similar. Thus, for incident mode $(0, 1)$, there is very little scattering observed in the pressure field contour plot of figure (8.12a). In addition, since mode

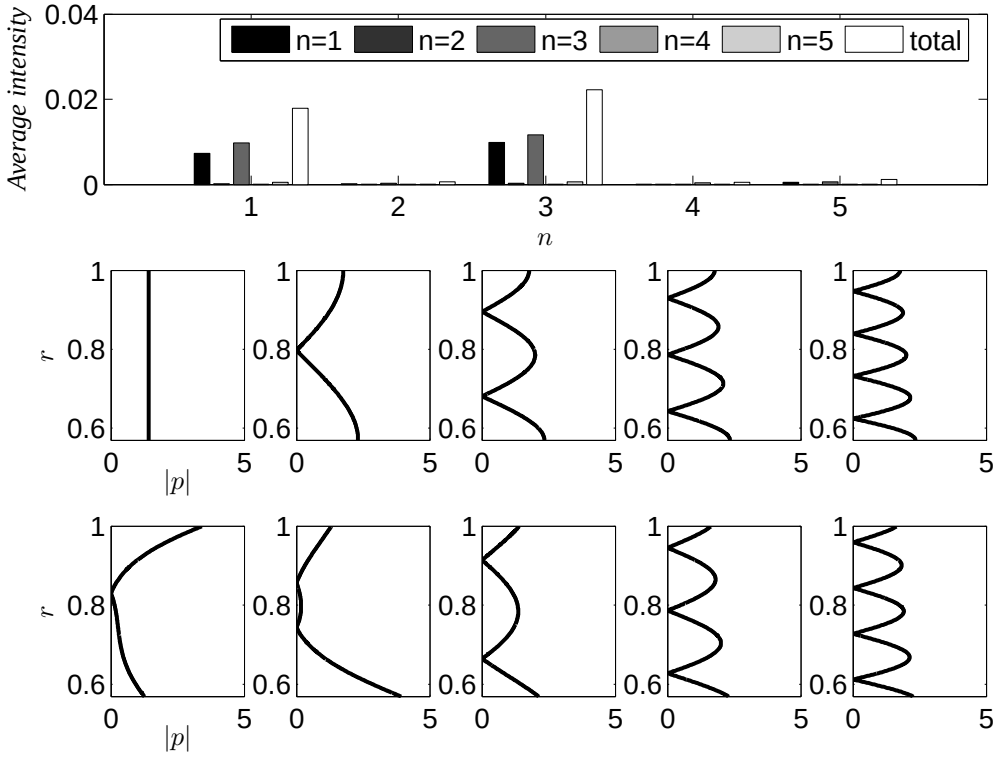


(a) Incident mode, $(0, n)$.

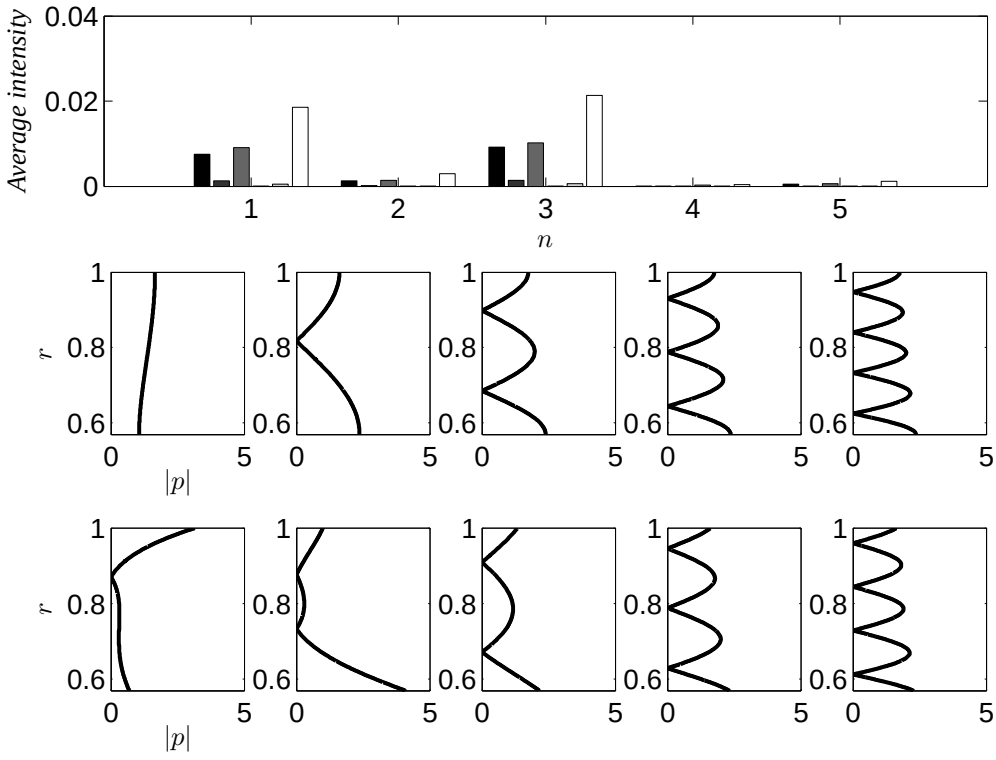


(b) Incident mode, $(4, n)$.

FIGURE 8.11: *First five downstream mode eigenfunctions and transmitted modal intensities due to single mode source* $(m, n)$ *at* $k_0 = 30.94355$ *for a finite length lined duct with uniform flow. Top plot, transmitted mode intensities; Middle plot, rigid duct eigenfunctions; Bottom plot, lined duct eigenfunctions.* $R = 1$, $M_r = 0.012$, $D = 0.021$, $l_I = l_{III} = 0.067879$, $l_{II} = 2.226446$, $\hbar = 0.56897$.

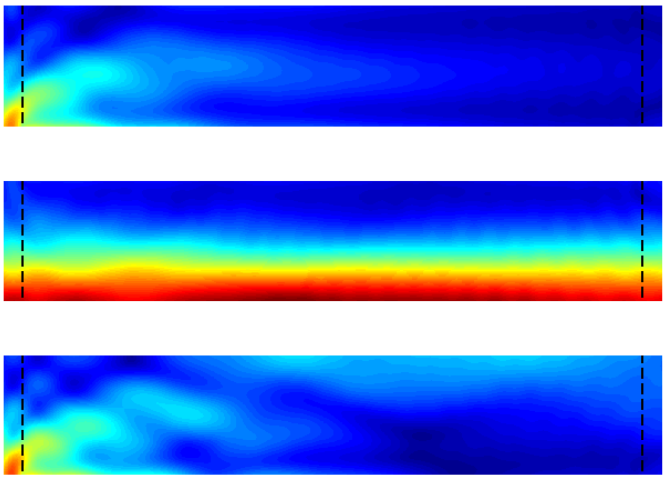

(a) Pressure field, $(0, 1)$.

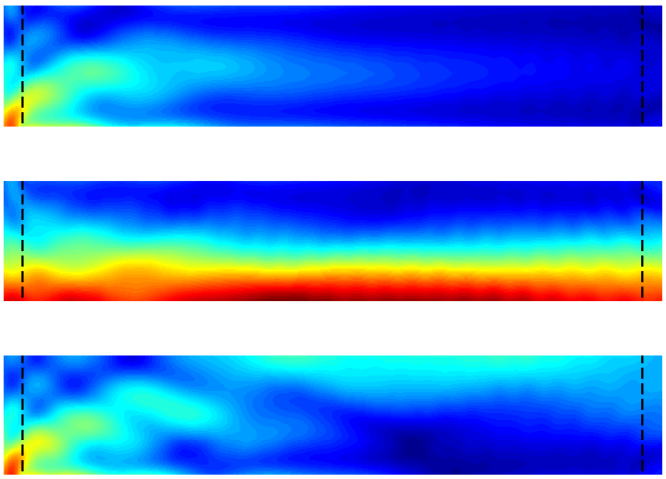

(b) Pressure field, $(4, 1)$.

FIGURE 8.12: *Pressure field contours due to single mode source* $(m, 1)$ *at* $k_0 = 30.94355$ *for a finite length lined duct with a linear sheared flow (positive gradient). Location of the leading and trailing edges of the liner is indicated by vertical dashed lines. Top plot, both walls lined; Middle plot, only casing lined; Bottom plot, only hub lined.* $R = 1$, $M_r = 0.012$, $D = 0.021$, $l_I = l_{III} = 0.067879$, $l_{II} = 2.226446$, $\hbar = 0.56897$.

$(0, 2)$ is the least attenuated mode in the lined section, there is very little attenuation of the incident energy. In contrast, the transmission loss of incident mode $(0, 2)$ is much higher due to scattering, since the rigid duct eigenfunction does not closely resemble any of the lined duct eigenfunctions. Also a similar pattern occurs comparing the situation for the case where only the hub is lined (see Figure (8.15)). Here, it is mode $(0, 2)$ in the rigid duct and mode $(0, 1)$ in the lined section which are most similar. Thus, most of the transmitted energy remains in mode $(0, 2)$ in the trailing rigid section, and little attenuation is observed since the lined duct mode $(0, 1)$ is the least attenuated mode. The transmission loss of incident mode $(0, 1)$ in this case is now higher since more scattering occurs. The same features are observed for the spinning mode cases. When the linear flow profile has a negative shear gradient a similar scenario occurs, but the roles of the liner locations are reversed.

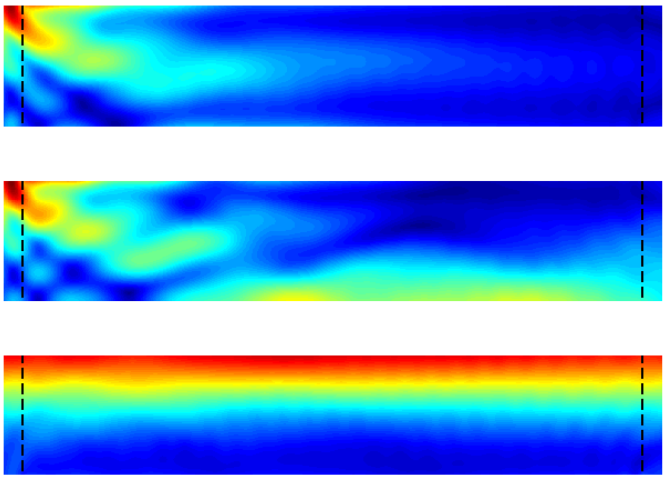

(a) Pressure field, $(0, 1)$.

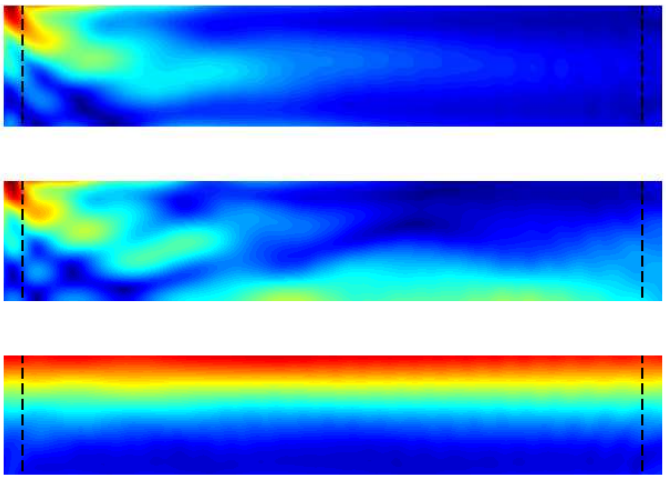

(b) Pressure field, $(4, 1)$.

FIGURE 8.13: *Pressure field contours due to single mode source* $(m, 1)$ *at* $k_0 = 30.94355$ *for a finite length lined duct with a linear sheared flow (negative gradient). Location of the leading and trailing edges of the liner is indicated by vertical dashed lines. Top plot, both walls lined; Middle plot, only casing lined; Bottom plot, only hub lined.* $R = 1$, $M_r = 0.012$, $D = 0.021$, $l_I = l_{III} = 0.067879$, $l_{II} = 2.226446$, $\hbar = 0.56897$.

## 8.4 Finite length effects

The acoustically lined area within a realistic bypass duct is likely to consist of various liners of different lengths. It was shown by Unruh [26] that liner performance, particularly at low frequency, can be strongly affected by finite length tuning effects, whereby axial standing waves are produced in short liners by strong reflections at the leading and trailing liner edges. The variation of power transmission loss with liner length is shown in figure (8.16) for a symmetrically lined duct at $k_0 = 2 \times BPF = 30.94$ for the various flow profiles in figure (8.7). Results for both multi-mode and single mode sources are shown. Since the gradients of the curves in each plot are not constant, as would be expected from infinite lined duct theory, this indicates that finite length effects are significant. In fact, some of the curves have strong changes in gradient as the liner length is varied. Strong differences between the flow profiles

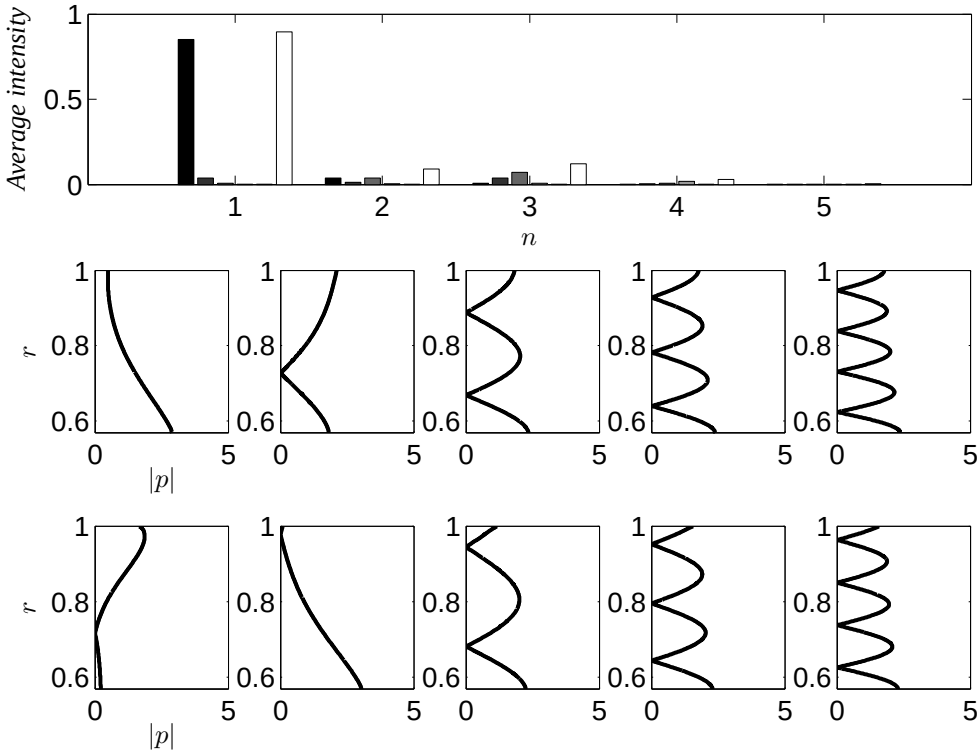


(a) Incident mode, $(0, n)$.

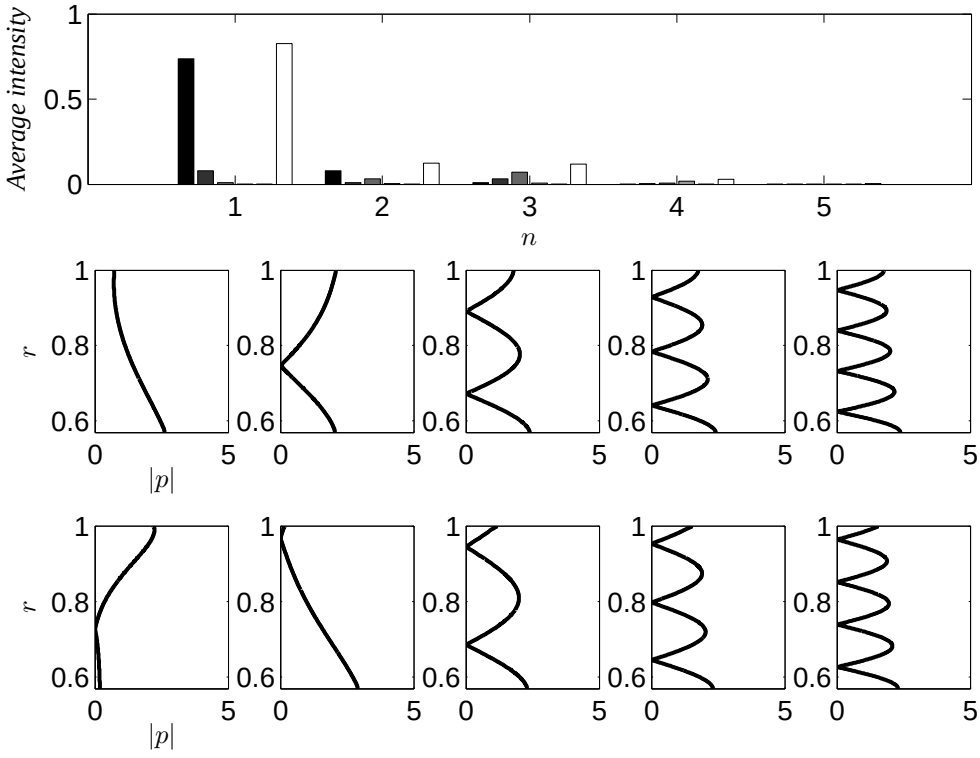


(b) Incident mode, $(4, n)$.

FIGURE 8.14: *First five downstream mode eigenfunctions and transmitted modal intensities due to single mode source* $(m, n)$ *at* $k_0 = 30.94355$ *for a finite length duct with only casing lined, with linear shear flow (positive gradient). Top plot, transmitted mode intensities; Middle plot, rigid duct eigenfunctions; Bottom plot, lined duct eigenfunctions.* $R = 1$, $M_r = 0.012$, $D = 0.021$, $l_I = l_{III} = 0.067879$, $l_{II} = 2.226446$, $\hbar = 0.56897$.

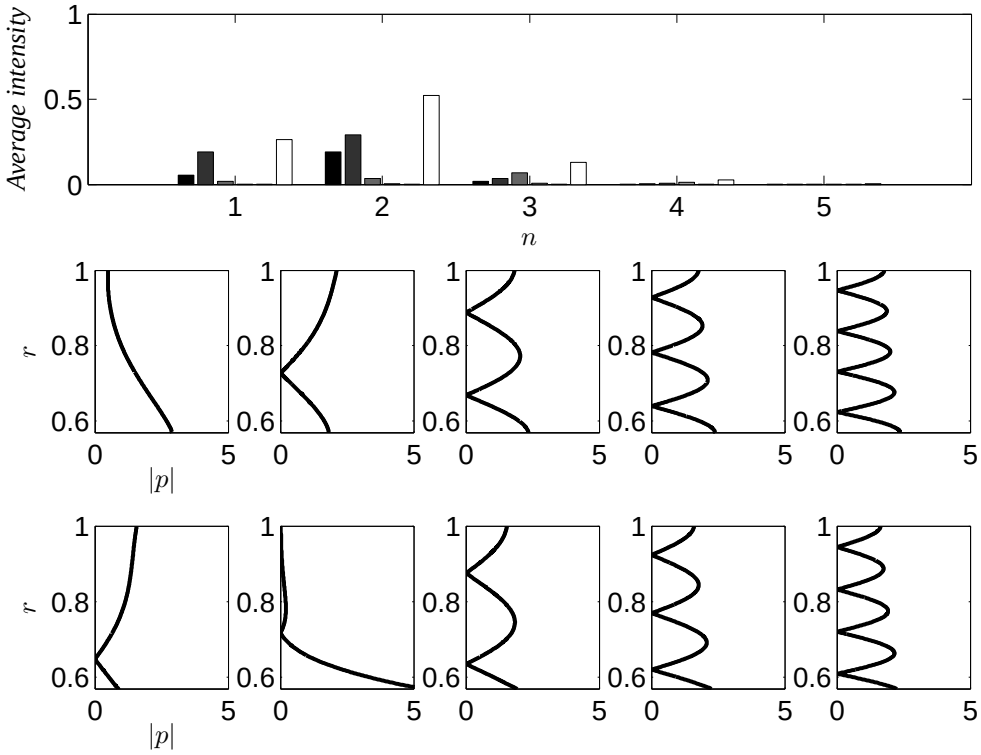


(a) Incident mode, $(0, n)$.

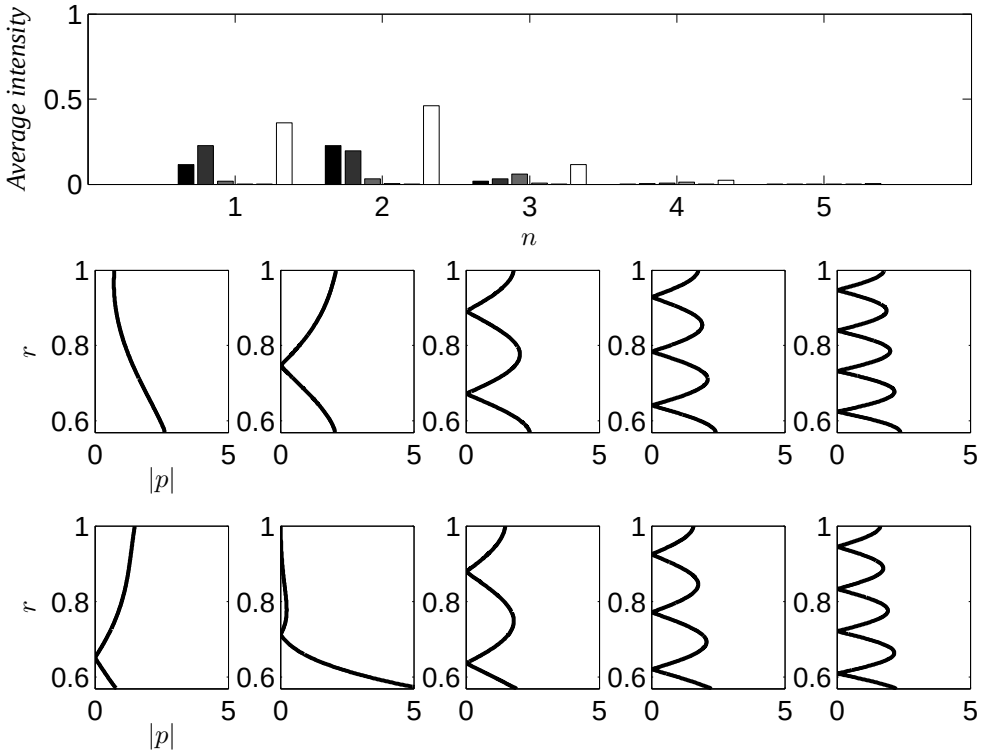


(b) Incident mode, $(4, n)$.

FIGURE 8.15: *First five downstream mode eigenfunctions and transmitted modal intensities due to single mode source* $(m, n)$ *at* $k_0 = 30.94355$ *for a finite length duct with only hub lined, with linear sheared flow (positive gradient). Top plot, transmitted mode intensities; Middle plot, rigid duct eigenfunctions; Bottom plot, lined duct eigenfunctions.* $R = 1$, $M_r = 0.012$, $D = 0.021$, $l_I = l_{III} = 0.067879$, $l_{II} = 2.226446$, $\hbar = 0.56897$.

are only seen for the two lowest order modes $(4,1)$ and $(4,2)$. In both of these cases the negatively sheared flows are distinctly different from the rest.

The reflection loss for each case is plotted in figure (8.17). Distinct oscillations are seen, which reduce in strength as the liner length is increased, and are strongest for the least well cut-on incident mode $(4,5)$. The wavelength of the oscillation corresponds to half the wavelength of the excitation frequency. The wall slip flow profiles have consistently higher reflection losses than the profiles without wall slip.

## 8.5 The effect of sheared flow upon optimum liner performance

In this section, the effect of sheared flow upon optimum bypass duct liner performance is briefly assessed. In the preceding work, it was seen that sheared flow has a potentially strong effect, when compared with the uniform flow assumption, on the mode eigenfunctions and decay rates, and the scattering and power attenuation of finite length liners. The low order radial modes were most affected by the mean flow shear, whilst the effects on multi-mode propagation were not as strong. The effect of the mean flow profiles used previously, shown in figure (8.7), on the optimum wall impedance is assessed here for a multi-mode source $m = 4$, and a single mode source $(m = 4, n = 1)$. Contour plots of sound power transmission loss are calculated for resistance values $0.4 \leq R \leq 5$, and reactance values $-5 \leq X \leq 3$.

The uniform flow solution $M = 0.345$ is used as the baseline case in each comparison. Contour plots for multi-mode and single mode sources are shown in figure (8.18) at frequencies of $k_0 = 2 \times \text{BPF} = 30.94$ and $k_0 = 5.5 \times \text{BPF} = 85.09$, where there are five and thirteen cut-on modes, respectively. Both hub and casing walls have the same impedance. At $k_0 = 30.94$ the optimum impedance for the multi-mode case $Z = 1.32 - 1i$ is identical to that for $n = 1$. At $k_0 = 85.09$ the optimum impedance for the multi-mode case is $Z = 2.24 - 1i$, and for $n = 1$ it is $Z = 1.32 - 3.4i$. For higher order incident modes the trend in impedance is to higher resistance values, whilst reactance values tend to zero.

### 8.5.1 Single impedance optimisation

Figure (8.19) shows the multi-mode power transmission loss contours at $k_0 = 30.94$ for a uniform flow, realistic flow with slip, and linear shear flows (positive and negative gradients) with boundary layers. For each case the optimum reactance is located at around $X = -1$, whilst the optimum resistance slightly increases for the non-uniform flows. The attenuation levels show only weak variation between the flow profiles. The same plots, but for a single mode $(4,1)$ source, are shown in figure (8.20). A similar shift in the optimum is seen for each non-uniform flow to a higher resistance and lower reactance than the uniform flow case. Differences of around 2 to 4 dB are seen in the attenuation levels between the flow cases, with the highest levels achieved for the negatively sheared linear flow profiles. The multi-mode and

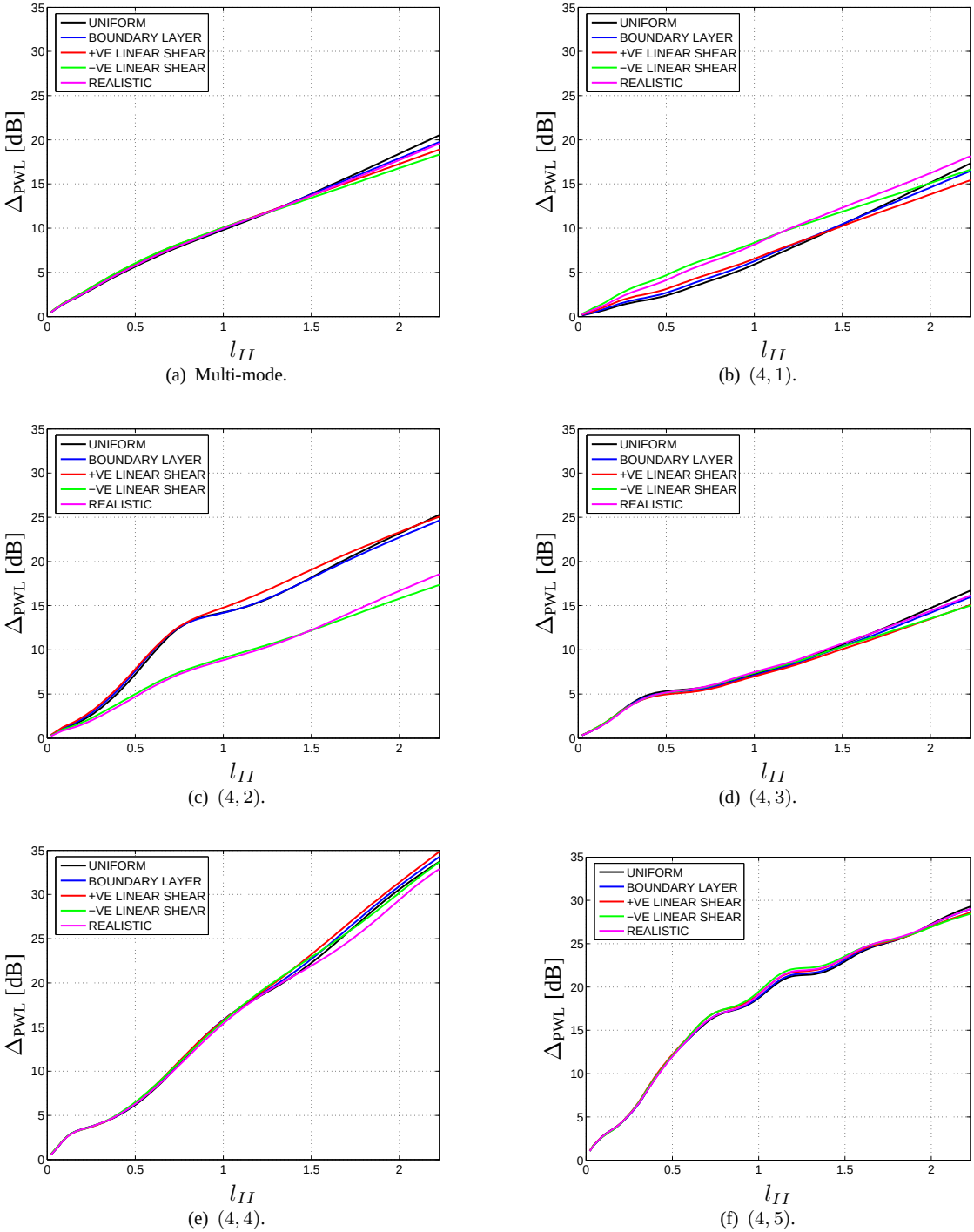


(a) Multi-mode. (b) $(4, 1)$. (c) $(4, 2)$. (d) $(4, 3)$. (e) $(4, 4)$. (f) $(4, 5)$.

FIGURE 8.16: *Variation of power transmission loss with liner length for single mode and multi-mode sources for various flow profiles. Flow profiles as figure (8.7).* $k_0 = 30.94355$, $R = 1$, $M_r = 0.012$, $D = 0.021$, $l_I = l_{III} = 0.067879$, $\hbar = 0.56897$.

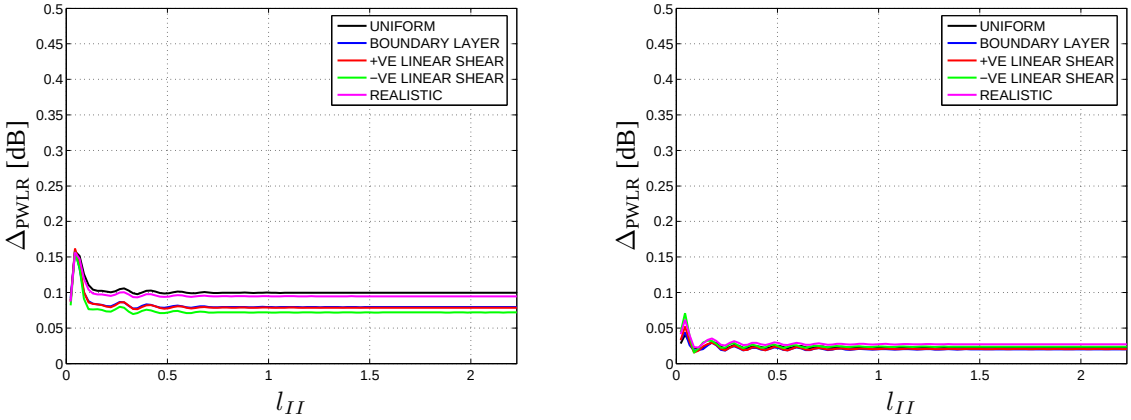


(a) Multi-mode. (b) $(4, 1)$.

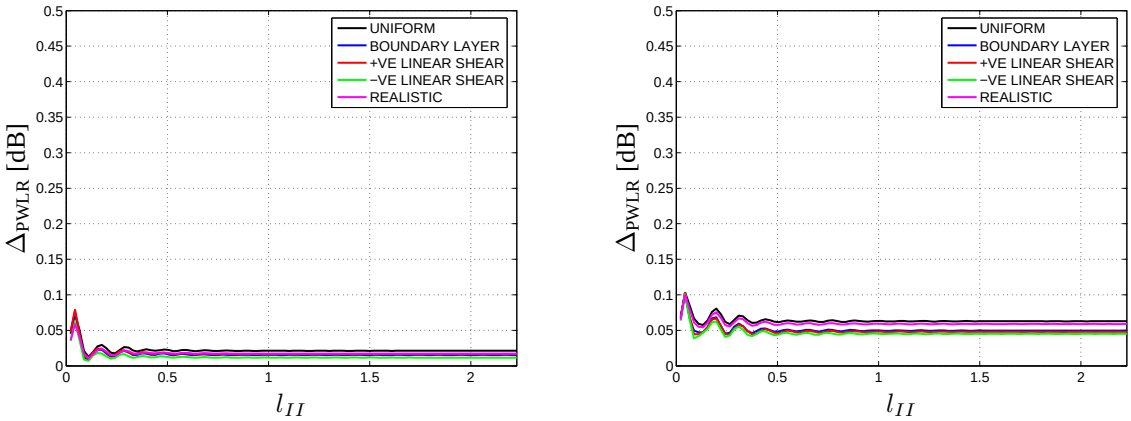


(c) $(4, 2)$. (d) $(4, 3)$.

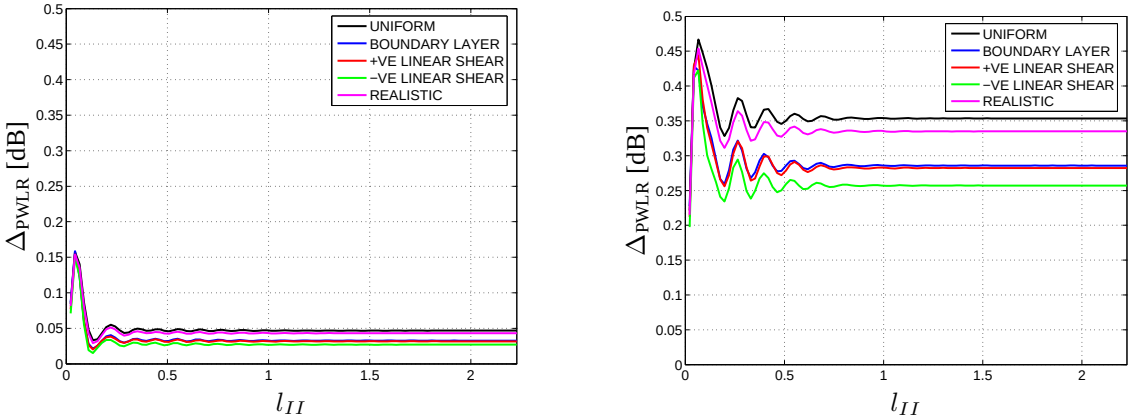


(e) $(4, 4)$. (f) $(4, 5)$.

FIGURE 8.17: *Variation of power reflection loss with liner length for single mode and multi-mode sources for various flow profiles. Flow profiles as figure (8.7).* $k_0 = 30.94355$, $R = 1$, $M_r = 0.012$, $D = 0.021$, $l_I = l_{III} = 0.067879$, $\hbar = 0.56897$.

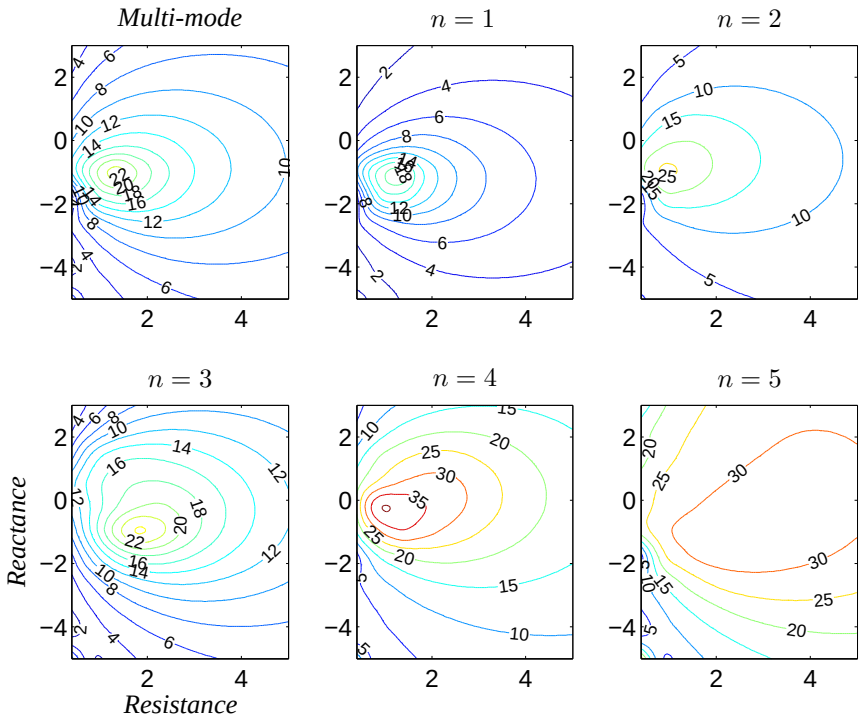


(a) $k_0 = 2 \times \text{BPF} = 30.94355$.

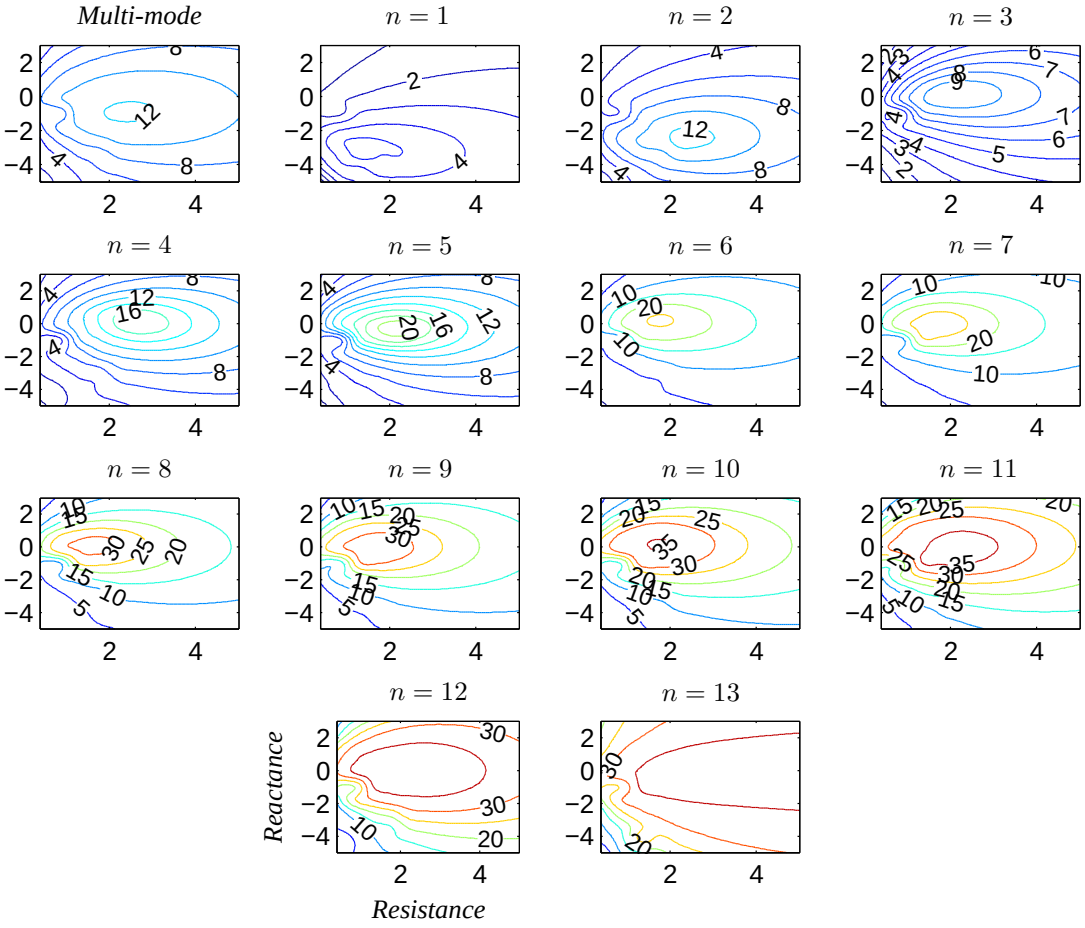


(b) $k_0 = 5.5 \times \text{BPF} = 85.09475$.

FIGURE 8.18: *Contour plots of $\Delta_{PWL}$ over resistance and reactance for multi-mode and single mode sources with uniform flow $M = 0.345$. $m = 4$, $l_I = l_{III} = 0.067879$, $l_{II} = 2.226446$, $\hbar = 0.56897$.*

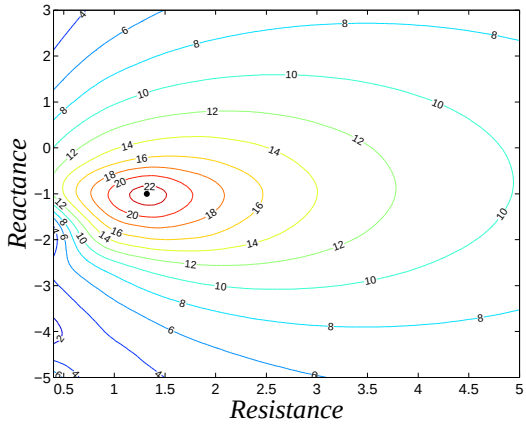


(a) Uniform flow.

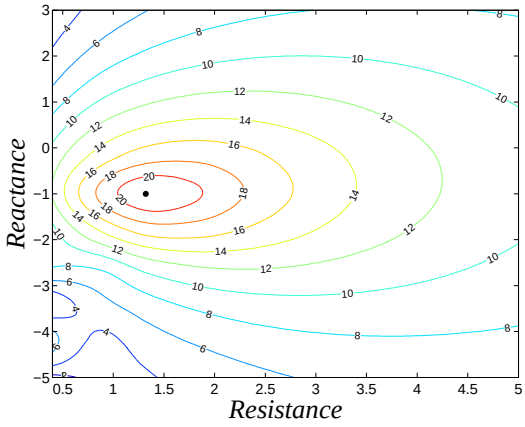


(b) Realistic flow with slip.

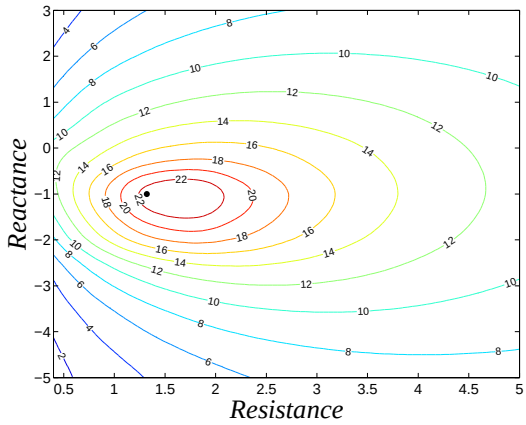


(c) Linear shear flow (positive gradient) with boundary layers.

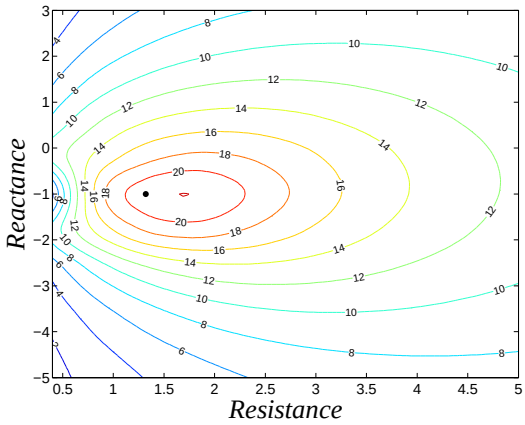


(d) Linear shear flow (negative gradient) with boundary layers.

FIGURE 8.19: *Contour plots of $\Delta_{PWL}$ over resistance and reactance for a multi-mode source at $k_0 = 2 \times BPF = 30.94355$. Uniform flow optimum indicated by •. $m = 4$, $l_I = l_{III} = 0.067879$, $l_{II} = 2.226446$, $\hbar = 0.56897$.*

single mode power transmission loss contours for the boundary layer flow profile are compared with the uniform flow case in figure (8.21) at the higher frequency of $k_0 = 5.5 \times \text{BPF} = 85.09$. For the multi-mode source, the optimum resistance and reactance are slightly higher. Stronger differences are seen in the case of a single mode source. Here, the optimum resistance is much higher than the uniform flow case, at around $R = 3.1$, and the reactance is lower, at around $X = -4.1$. The attenuation levels are around double those of the uniform flow case.

### 8.5.2 Casing wall impedance optimisation

It was found in the preceding sections that the direction of the mean flow gradient can have a strong effect upon the attenuation performance of the hub and casing liners. It is therefore of interest to investigate the optimisation of the hub and casing wall impedances for the different flow profiles. The approach taken here is to fix the hub impedance at the values obtained for the optimum impedance of the symmetrically lined case (in the previous subsection). The optimisation of the casing impedance is then undertaken as previously using contour plots. It is

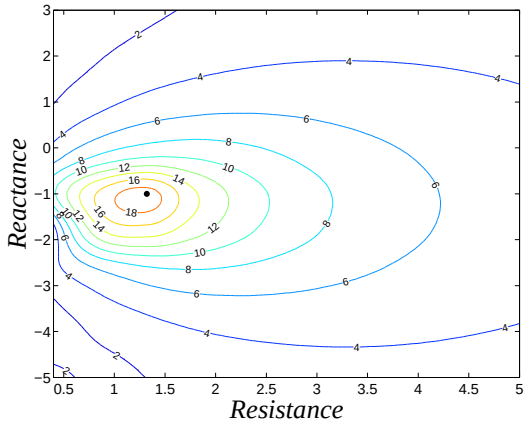


(a) Uniform flow.

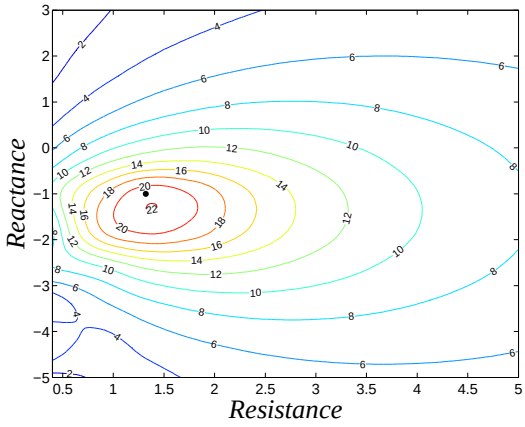


(b) Realistic flow with slip.

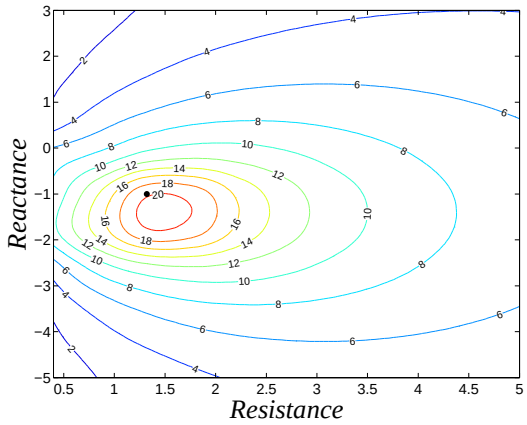


(c) Linear shear flow (positive gradient) with boundary layers.

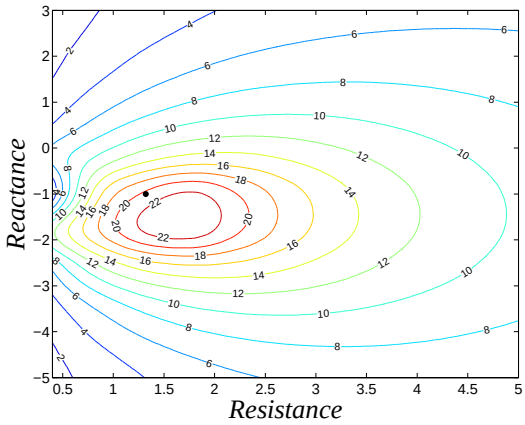


(d) Linear shear flow (negative gradient) with boundary layers.

FIGURE 8.20: *Contour plots of $\Delta_{PWL}$ over resistance and reactance for a single mode $(4,1)$ source at $k_0 = 2 \times BPF = 30.94355$. Uniform flow optimum indicated by $\bullet$. $m = 4$, $l_I = l_{III} = 0.067879, l_{II} = 2.226446, \hbar = 0.56897$.*

noted that the value of impedance obtained is, in general, not the global optimum, but will give indication of whether the flow profile has a strong effect or not.

Contour plots of the multi-mode power transmission loss over the casing impedance at $k_0 = 30.94$ are shown in figure (8.22). The optimum casing reactances do not change drastically from the symmetrically lined optima, whilst the trends in the resistance are towards higher resistance for negatively sheared flows, and lower resistance for positively sheared flows. In addition, when comparing figures (8.19) and (8.22), the attenuation levels for each profile are seen to increase by the order of 2 to 4 dB in the asymmetrically lined case. The highest attenuation levels occur for the positively sheared linear flow profile.

Contour plots of the single mode $(4,1)$ power transmission loss over the casing impedance at $k_0 = 30.94$ are shown in figure (8.23). Here the optimum casing impedances do not change significantly from the symmetrically lined optimum. By using an asymmetric liner the attenuation levels increase over the symmetric case by around 2 dB for the uniform, realistic and negatively shear linear flow profiles. However, this increases to between 4 and 6 dB over the casing impedance range for the positively sheared linear flow profile.

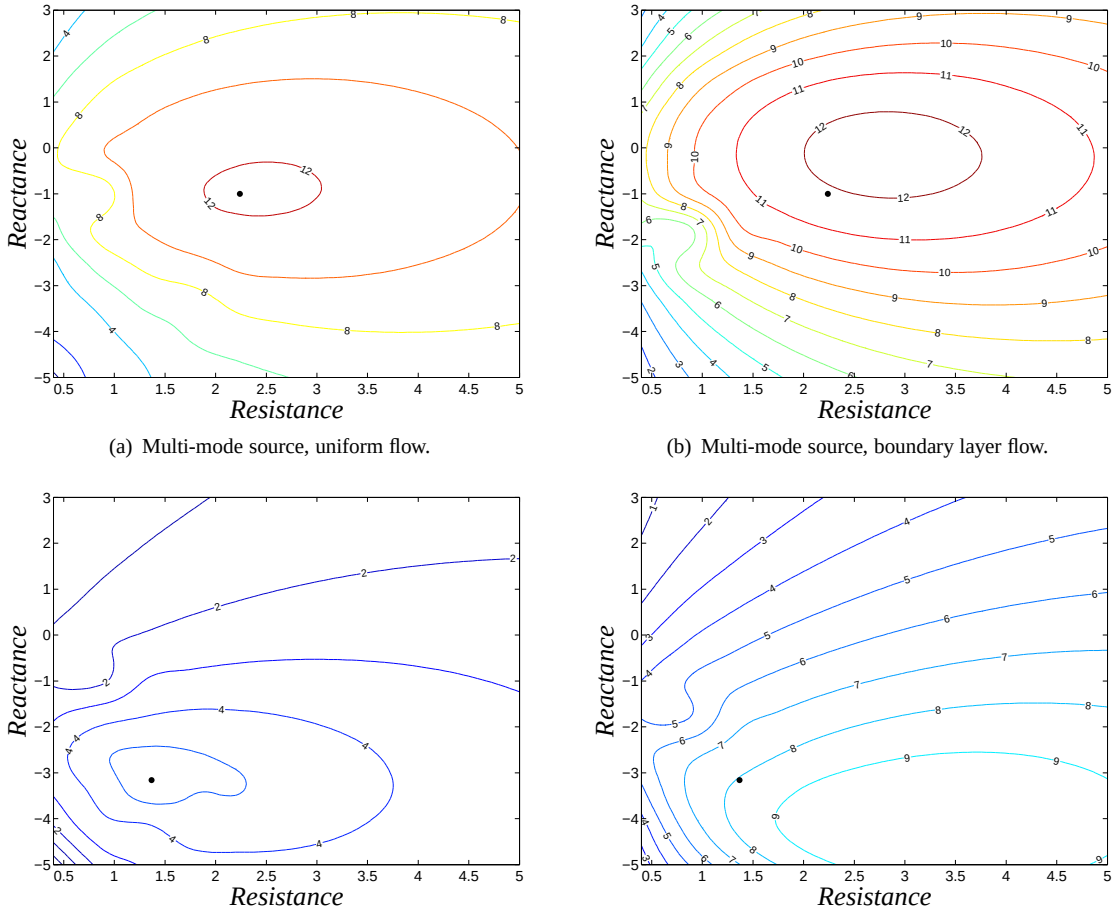


(a) Multi-mode source, uniform flow.

(b) Multi-mode source, boundary layer flow.

(c) Single mode $(4, 1)$ source, uniform flow.

(d) Single mode $(4, 1)$ source, boundary layer flow.

FIGURE 8.21: *Contour plots of $\Delta_{PWL}$ over resistance and reactance for a single mode $(4, 1)$ and multi-mode sources at $k_0 = 5.5 \times BPF = 85.09475$. Uniform flow optimum indicated by* •. $m = 4, l_I = l_{III} = 0.067879, l_{II} = 2.226446, \hbar = 0.56897$.

Finally, contour plots of the multi-mode and single mode $(4, 1)$ power transmission loss at $k_0 = 5.5 \times \text{BPF} = 85.09$ are shown in figure (8.24) for uniform and boundary layer flow profiles. The results show virtually no change in the optimum casing impedance and attenuation levels compared with those of the symmetrically lined case, indicating that these profiles may be suitably modelled using symmetrically lined ducts when undertaking impedance optimisation.

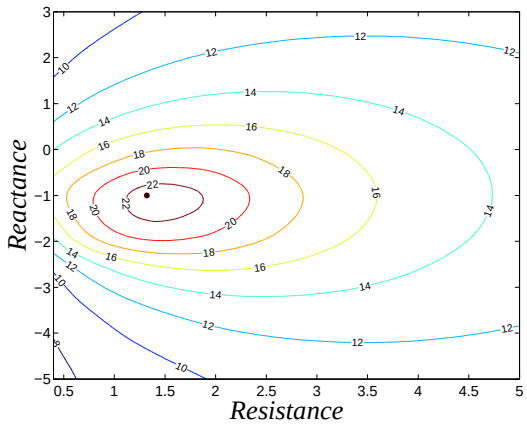


(a) Uniform flow.

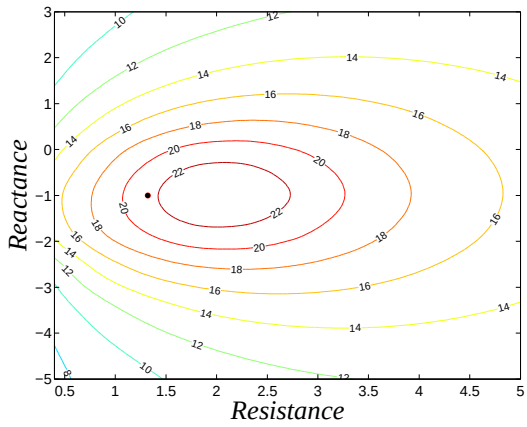


(b) Realistic flow with slip.

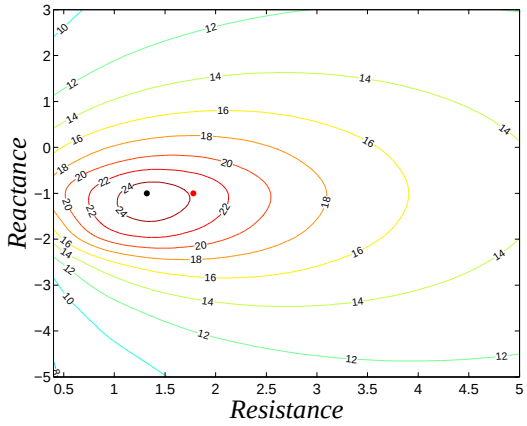


(c) Linear shear flow (positive gradient) with boundary layers.

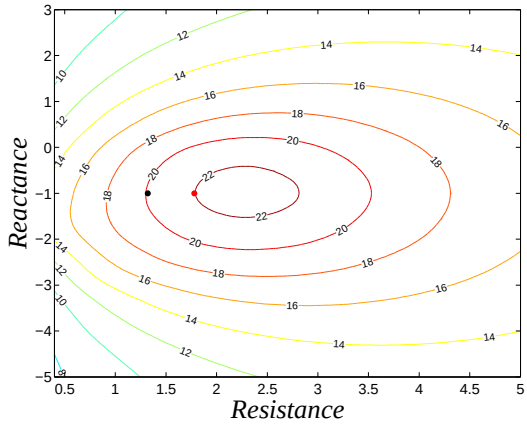


(d) Linear shear flow (negative gradient) with boundary layers.

FIGURE 8.22: *Contour plots of $\Delta_{PWL}$ over casing wall resistance and reactance for a multi-mode source at $k_0 = 2 \times BPF = 30.94355$. Uniform flow optimum indicated by • and hub impedance indicated by •. $m = 4, l_I = l_{III} = 0.067879, l_{II} = 2.226446, \hbar = 0.56897$.*

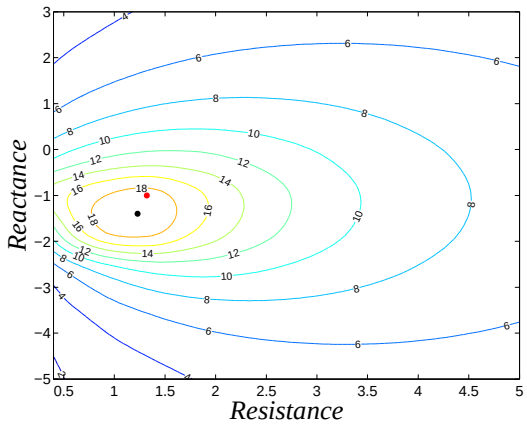


(a) Uniform flow.

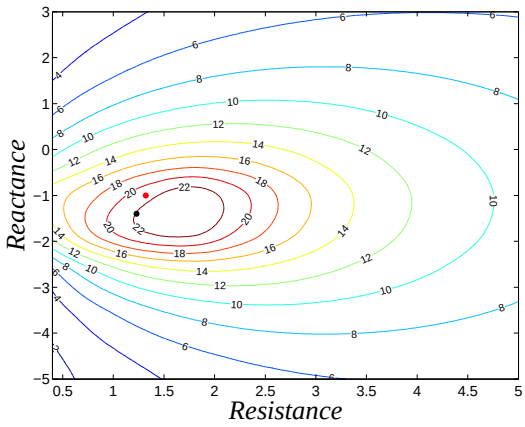


(b) Realistic flow with slip.

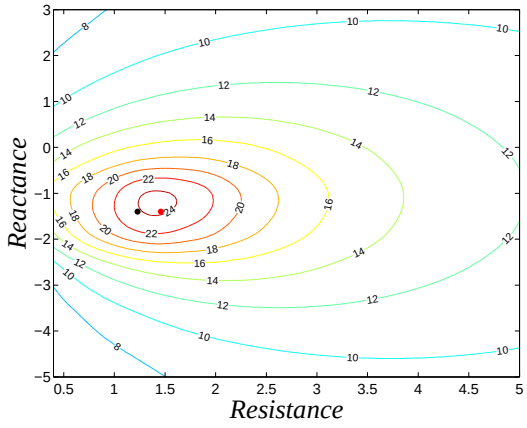


(c) Linear shear flow (positive gradient) with boundary layers.

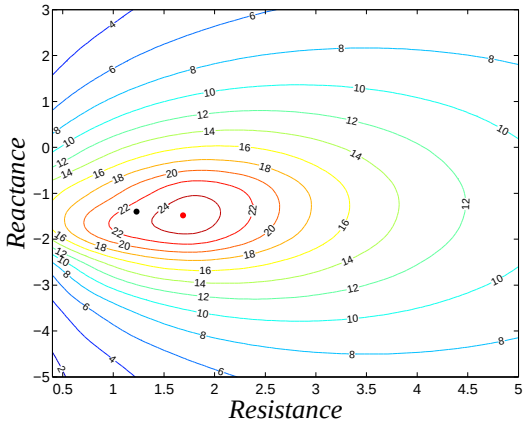


(d) Linear shear flow (negative gradient) with boundary layers.

FIGURE 8.23: *Contour plots of $\Delta_{PWL}$ over casing wall resistance and reactance for a single mode $(4,1)$ source at $k_0 = 2 \times BPF = 30.94355$. Uniform flow optimum indicated by • and hub impedance indicated by •. $m = 4$, $l_I = l_{III} = 0.067879$, $l_{II} = 2.226446$, $\hbar = 0.56897$.*

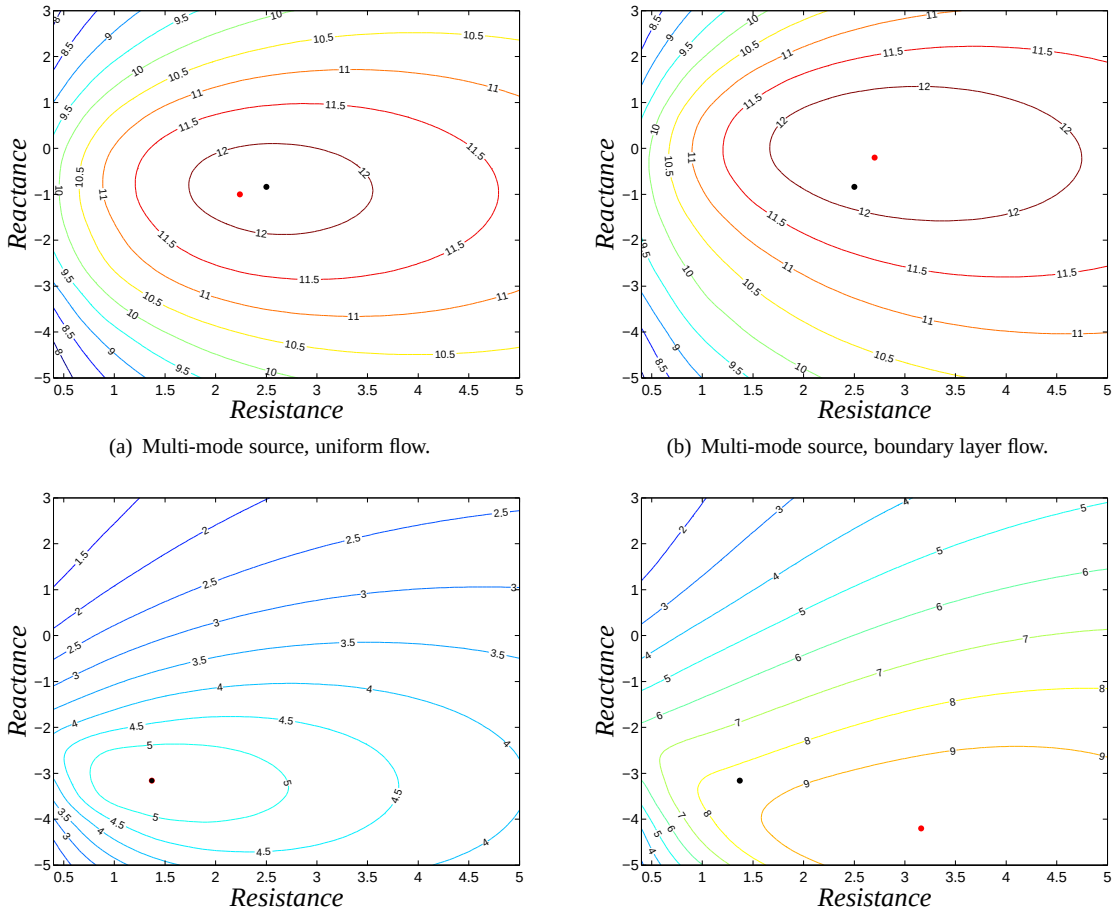


(a) Multi-mode source, uniform flow.

(b) Multi-mode source, boundary layer flow.

(c) Single mode $(4, 1)$ source, uniform flow.

(d) Single mode $(4, 1)$ source, boundary layer flow.

FIGURE 8.24: *Contour plots of $\Delta_{PWL}$ over casing wall resistance and reactance for a single mode $(4, 1)$ and multi-mode sources at $k_0 = 5.5 \times BPF = 85.09475$. Uniform flow optimum indicated by $\bullet$ and hub impedance indicated by $\bullet$.* $m = 4$, $l_I = l_{III} = 0.067879$, $l_{II} = 2.226446$, $\hbar = 0.56897$.

## 8.6 Summary

- The convergence of solutions with thin boundary layers to the slip flow case is demonstrated.
- The presence of boundary layers is shown to increase power transmission loss at high frequencies. The pattern of modal scattering is shown to vary with boundary layer thickness.
- The effects of several flow profiles upon liner attenuation and scattering have been investigated. Higher power attenuation occurs where the mean flow gradient refracts sound towards the liner. Strong variations in attenuation have been noted between individual modal sources, depending upon flow profile and liner location, particularly for the lowest order radial modes.
- Identical trends are seen for multi-mode sources, but smaller changes in power transmission loss occur due to the lower sensitivity of higher order modes to changes in flow profile.
- Finite length effects upon power attenuation are found to be most significant for single incident mode sources. Differences between flow profiles are found only to be significant for the lowest order modes.
- A brief assessment of the effects of flow profile on the optimum liner impedance at a single frequency is made using contour plots, against the baseline case of uniform flow. The change in the optimum impedance of a symmetric liner for several flow profiles is found to be fairly small. It is found that asymmetric liners could provide higher attenuation rates, depending on the direction of the mean flow shear gradient.
- Attenuation levels over the impedance plane are found to be potentially much higher for sheared flows, particularly for single mode sources. In the examples used, the highest attenuation levels are found for positively sheared flow.

TABLE 8.1: *Predicted axial decay rates $\Im\{k\}$ of modes $(0,1 \rightarrow 5)$ at $k_0 = 2 \times BPF = 30.94355$ in a lined annular duct with various flow profiles. The transmission loss for the least attenuated mode (LAM) is also listed.*

| | | | | | $\Im\{k\}$ | | | $\Delta_{m,n}$ [dB] |
|---|---|---|---|---|---|---|---|---|
| Mean flow profile | Casing | Hub | $(0,1)$ | $(0,2)$ | $(0,3)$ | $(0,4)$ | $(0,5)$ | (LAM) |
| Uniform | Lined | Lined | -2.59 | -2.16 | -1.04 | -1.74 | -2.84 | 20.17 |
| | Lined | Rigid | -2.56 | -0.09 | -0.51 | -0.87 | -1.60 | 1.71 |
| | Rigid | Lined | -0.08 | -2.28 | -0.59 | -0.93 | -1.68 | 1.63 |
| Uniform with | Lined | Lined | -2.93 | -2.56 | -0.92 | -1.77 | -2.88 | 17.81 |
| boundary layer | Lined | Rigid | -2.91 | -0.07 | -0.50 | -0.89 | -1.61 | 1.39 |
| | Rigid | Lined | -0.07 | -2.61 | -0.58 | -0.95 | -1.69 | 1.28 |
| Linear shear with | Lined | Lined | -2.83 | -3.81 | -0.80 | -1.81 | -2.97 | 15.56 |
| boundary layer | Lined | Rigid | -2.83 | -0.03 | -0.49 | -0.90 | -1.64 | 0.51 |
| (positive gradient) | Rigid | Lined | -0.10 | -3.81 | -0.53 | -0.99 | -1.76 | 1.87 |
| Linear shear with | Lined | Lined | -3.97 | -2.81 | -0.79 | -1.82 | -2.96 | 15.23 |
| boundary layer | Lined | Rigid | -3.97 | -0.09 | -0.48 | -0.92 | -1.65 | 1.75 |
| (negative gradient) | Rigid | Lined | -0.02 | -2.80 | -0.54 | -0.99 | -1.71 | 0.38 |
| Realistic flow with | Lined | Lined | -3.26 | -1.97 | -0.99 | -1.74 | -2.85 | 19.20 |
| wall slip | Lined | Rigid | -3.26 | -0.10 | -0.48 | -0.88 | -1.62 | 1.91 |
| | Rigid | Lined | -0.03 | -2.05 | -0.62 | -0.93 | -1.66 | 0.61 |

TABLE 8.2: *Predicted axial decay rates $\Im\{k\}$ of modes $(4,1 \rightarrow 5)$ at $k_0 = 2 \times BPF = 30.94355$ in a lined annular duct with various flow profiles. The transmission loss for the least attenuated mode (LAM) is also listed.*

| | | | | | $\Im\{k\}$ | | | $\Delta_{m,n}$ [dB] |
|---|---|---|---|---|---|---|---|---|
| Mean flow profile | Casing | Hub | $(0,1)$ | $(0,2)$ | $(0,3)$ | $(0,4)$ | $(0,5)$ | (LAM) |
| Uniform | Lined | Lined | -2.64 | -2.27 | -1.05 | -1.79 | -2.96 | 20.32 |
| | Lined | Rigid | -2.63 | -0.11 | -0.51 | -0.88 | -1.68 | 2.14 |
| | Rigid | Lined | -0.07 | -2.37 | -0.62 | -0.98 | -1.78 | 1.32 |
| Uniform with | Lined | Lined | -3.00 | -2.68 | -0.92 | -1.82 | -3.00 | 17.73 |
| boundary layer | Lined | Rigid | -2.99 | -0.09 | -0.50 | -0.90 | -1.69 | 1.78 |
| | Rigid | Lined | -0.05 | -2.72 | -0.59 | -1.00 | -1.79 | 1.04 |
| Linear shear with | Lined | Lined | -2.91 | -3.93 | -0.80 | -1.85 | -3.09 | 15.50 |
| boundary layer | Lined | Rigid | -2.91 | -0.04 | -0.50 | -0.92 | -1.72 | 0.72 |
| (positive gradient) | Rigid | Lined | -0.08 | -3.94 | -0.54 | -1.02 | -1.86 | 1.58 |
| Linear shear with | Lined | Lined | -4.04 | -2.95 | -0.77 | -1.87 | -3.07 | 14.89 |
| boundary layer | Lined | Rigid | -4.04 | -0.12 | -0.48 | -0.93 | -1.72 | 2.22 |
| (negative gradient) | Rigid | Lined | -0.01 | -2.93 | -0.54 | -1.03 | -1.81 | 0.29 |
| Realistic flow with | Lined | Lined | -3.33 | -2.06 | -1.00 | -1.80 | -2.97 | 19.30 |
| wall slip | Lined | Rigid | -3.33 | -0.12 | -0.49 | -0.89 | -1.70 | 2.39 |
| | Rigid | Lined | -0.02 | -2.12 | -0.65 | -0.98 | -1.76 | 0.45 |

TABLE 8.3: *Predicted sound power transmission loss for non-spinning modes $m = 0$ at $k_0 = 2 \times BPF = 30.94355$ in a lined annular duct with various flow profiles. Single mode $\Delta_{PWL_{0,n}}$ and multi-mode $\Delta_{PWL_0}$ transmission loss values are listed.*

| | | | Incident mode $\Delta_{\mathrm{PWL}_{m,n}}$ [dB] | | | | | $\Delta_{\mathrm{PWL}_m}$ [dB] |
|---|---|---|---|---|---|---|---|---|
| Mean flow profile | Casing | Hub | $(0,1)$ | $(0,2)$ | $(0,3)$ | $(0,4)$ | $(0,5)$ | $(0,1 \rightarrow 5)$ |
| Uniform | Lined | Lined | 17.47 | 32.10 | 16.52 | 33.02 | 29.34 | 20.71 |
| | Lined | Rigid | 2.83 | 5.16 | 8.78 | 14.60 | 23.68 | 7.00 |
| | Rigid | Lined | 1.95 | 6.65 | 9.80 | 15.46 | 24.22 | 7.02 |
| Uniform with | Lined | Lined | 16.46 | 31.71 | 15.80 | 33.55 | 29.05 | 19.89 |
| boundary layer | Lined | Rigid | 2.83 | 4.78 | 8.74 | 14.85 | 23.86 | 6.88 |
| | Rigid | Lined | 1.79 | 6.58 | 9.79 | 15.74 | 24.43 | 6.92 |
| Linear shear with | Lined | Lined | 16.07 | 21.45 | 15.00 | 33.72 | 28.61 | 18.84 |
| boundary layer | Lined | Rigid | 0.48 | 10.41 | 9.13 | 15.22 | 24.58 | 6.42 |
| (positive gradient) | Rigid | Lined | 5.81 | 2.81 | 8.90 | 15.93 | 24.17 | 7.24 |
| Linear shear with | Lined | Lined | 16.47 | 18.86 | 14.75 | 33.82 | 28.42 | 18.49 |
| boundary layer | Lined | Rigid | 6.66 | 2.45 | 8.24 | 15.13 | 23.74 | 7.12 |
| (negative gradient) | Rigid | Lined | 0.33 | 11.32 | 9.90 | 16.28 | 25.05 | 6.46 |
| Realistic flow with | Lined | Lined | 18.19 | 20.58 | 15.88 | 32.73 | 29.02 | 19.87 |
| wall slip | Lined | Rigid | 6.28 | 2.78 | 8.24 | 14.64 | 23.50 | 7.21 |
| | Rigid | Lined | 0.46 | 11.93 | 10.49 | 15.60 | 24.77 | 6.64 |

TABLE 8.4: *Predicted sound power transmission loss for spinning modes $m = 4$ at $k_0 = 2 \times BPF = 30.94355$ in a lined annular duct with various flow profiles. Single mode $\Delta_{PWL_{4,n}}$ and multi-mode $\Delta_{PWL_4}$ transmission loss values are listed.*

| | | | Incident mode $\Delta_{\mathrm{PWL}_{m,n}}$ [dB] | | | | | $\Delta_{\mathrm{PWL}_m}$ [dB] |
|---|---|---|---|---|---|---|---|---|
| Mean flow profile | Casing | Hub | $(0,1)$ | $(0,2)$ | $(0,3)$ | $(0,4)$ | $(0,5)$ | $(0,1 \rightarrow 5)$ |
| Uniform | Lined | Lined | 17.32 | 25.29 | 16.71 | 33.70 | 29.30 | 20.51 |
| | Lined | Rigid | 3.97 | 4.38 | 8.67 | 14.70 | 23.77 | 7.26 |
| | Rigid | Lined | 1.26 | 8.60 | 10.37 | 15.99 | 24.75 | 6.96 |
| Uniform with | Lined | Lined | 16.46 | 24.63 | 15.96 | 34.25 | 29.00 | 19.75 |
| boundary layer | Lined | Rigid | 4.03 | 3.95 | 8.67 | 14.95 | 23.97 | 7.12 |
| | Rigid | Lined | 1.11 | 8.62 | 10.27 | 16.24 | 24.94 | 6.85 |
| Linear shear with | Lined | Lined | 15.42 | 25.07 | 15.07 | 34.84 | 28.59 | 18.89 |
| boundary layer | Lined | Rigid | 0.84 | 9.07 | 9.23 | 15.41 | 24.89 | 6.57 |
| (positive gradient) | Rigid | Lined | 4.42 | 3.36 | 9.32 | 16.33 | 24.55 | 7.14 |
| Linear shear with | Lined | Lined | 16.62 | 17.34 | 15.02 | 33.64 | 28.45 | 18.32 |
| boundary layer | Lined | Rigid | 7.33 | 2.70 | 8.09 | 15.18 | 23.76 | 7.39 |
| (negative gradient) | Rigid | Lined | 0.23 | 11.18 | 10.20 | 16.71 | 25.48 | 6.41 |
| Realistic flow with | Lined | Lined | 18.14 | 18.56 | 16.16 | 32.88 | 29.00 | 19.56 |
| wall slip | Lined | Rigid | 7.08 | 2.99 | 8.15 | 14.70 | 23.55 | 7.50 |
| | Rigid | Lined | 0.32 | 12.54 | 10.97 | 16.15 | 25.32 | 6.61 |

# Chapter 9

# Conclusions and future work

## 9.1 Overall conclusions

The initial motivation for this work was the requirement to predict the performance of acoustic liners in the bypass duct of modern high bypass ratio turbofan engines. Such predictions are required by the Noise Engineering department at Rolls-Royce in order to optimise the acoustic liner configuration and, ultimately, to assess the impact of the rear fan noise source on the total engine noise.

In this study, a series of computationally inexpensive modal methods have been developed, which are suitable for use in intensive liner optimisation studies or as preliminary design tools. To place this work in context, since the 1970s, predictions of bypass duct acoustic liner performance have typically been based upon interpolation over tables of modal decay rates obtained from idealised uniform duct models with uniform flow. At the present time, efforts are being made to integrate Finite Element methods into the prediction process. These represent the most mature of the various numerical methods, and are based on the solution of the convected Helmholtz equation for axisymmetric curved ducts containing an irrotational mean flow. However, these methods are computationally expensive and limited to the low or mid frequency range.

The fidelity and computational expense of the mode-matching methods developed here are placed in between the modal decay rate methods and FE methods. A key advantage of the mode-matching methods is the ability to assess the impact of discontinuities in the wall impedance on the sound field, or from an engineering perspective, the effect upon the attenuation performance of the finite liner length. In-depth analysis of the scattering problem has been possible since the methods directly calculate the modal amplitudes. To obtain this information from FE solutions requires the use of suitable wave-splitting methods. The optimisation study carried out in Chapter (4) has shown that, by scattering the modal power with specific liner segments, it is possible to obtain potentially large improvements in the

attenuation of tonal noise. In the bypass duct, this could be used to improve the attenuation of important rotor-stator interaction tones.

The prediction of broadband noise attenuation using numerical methods is limited by the high propagating mode density at mid to high frequencies. The broadband noise source is typically modelled by assuming an equal energy distribution per uncorrelated cut-on mode, which may number in the hundreds or thousands at the highest frequencies of interest. This requires many computations which means that the faster modal methods developed here are suitable. Although the methods are based upon idealised geometry, they have been shown to provide a good approximation to experimental results for broadband noise sources. The optimisation of liners to maximise the attenuation of broadband noise requires a range of frequencies to be considered. The analysis of Chapter (4) suggests that it is difficult to obtain improvements over the attenuation due to an optimised uniform liner by using axially-segmented liners, across the frequency range of interest. Improvements are possible at discrete frequencies, but the benefits fall off sharply with increasing frequency. This is due to the increase in propagating mode density at high frequency, which appears to smear out any benefits from mode scattering by additional liner segments.

A key problem encountered in the optimisation study of Chapter (4) was the inadequacy of the optimisation strategies used for obtaining axially-segmented liner designs. Each of the design parameters (resistance, reactance or liner depth, and liner length) may have a significant effect upon the topology of the multi-dimensional objective function surface, which necessitates an efficient global search of the design space. This is a common scenario encountered in design optimisation when searching a high dimensional parameter space for the global optimum design. The current method used at Rolls-Royce to obtain bypass duct liner designs involves the use of tables of modal decay rates and contour plots of approximate far-field SPL attenuation for individual liner segments of fixed length. This method is effectively a series of two dimensional optimisation problems where the liner lengths are fixed, and liner scattering and length effects are ignored. Thus obtaining the global optimum is very unlikely. The study undertaken here improves both the modeling and optimisation process, however, it is clear that more work needs to be done to develop both the optimisation algorithms and the search strategy, in order to search the design space efficiently and to improve confidence that the design achieved is the global optimum. A feature of the work which could be exploited in practise is the use of optimised asymmetric liner segments. The work presented in section (8.5) demonstrated that such configurations can provide attenuation benefits over symmetric liner segments, depending upon the mean gradient of the core flow and the source description. Such effects are only captured by using models based on the real annular geometry, and require a higher dimensional parameter space to be searched.

The real mean flow field within the bypass duct consists of growing boundary layers and a non-uniform radial profile which varies with the axial curvature of the duct walls. The region around the turbine hump contains most variable region of flow in the duct. Simplified acoustic models based on the uniform slip flow assumption miss the potentially important effects of the

flow non-uniformity, which include changes to the scattering and power attenuation by the convection and refraction of sound. The slip flow assumption has been shown to be valid only for very thin boundary layers, which may not be the case in the bypass duct where boundary layer thicknesses of up to 7% were predicted in the CFD solutions in Chapter (5).

The sheared flow modal methods developed in this work provide the Rolls-Royce Noise Engineering department with the means to better predict the bypass duct liner attenuation performance. Since the mean flow profile varies between engine designs, the methods may be used to provide engine specific predictions. The eigenvalue solver may be used to provide tables of modal decay rates, or the mode-matching scheme may be used to replace the interpolation methods. The mean flow profile can have a strong effect upon the mode eigenfunctions, particularly for low order modes. This means that the modal decomposition of a source description, for example from a CFD solution at an axial plane, can be strongly dependent upon the mean flow. This can have implications for matching strategies where modal descriptions from CFD solutions are required, with particular application to tonal noise (e.g. buzzsaw noise) propagation predictions using hydrid CAA/FE methods. An example of the application of the sheared flow mode matching method would be to model the propagation of rotor-stator interation noise in the bypass duct, where the source description is obtained by modal decomposition of a fan/OGV stage CFD calculation.

## 9.2 Future work

This section outlines related topics and applications in which further investigation may benefit from the work undertaken in the current study.

The methods developed here for predicting acoustic liner attenuation are suitable for intensive optimisation studies. Optimisation of multiple liner segments involves, potentially, a very large design parameter set. Such parameters include facing sheet porosity and thickness, cavity depth and septum height and segment length. For such a large parameter space, it is the search algorithm process which can become the most problematic part of the optimisation. Initial attempts have been made to improve the search process for multiple liner segments by using hybrid methods [108, 100], and the propagation methods developed here could be used in further work in this area.

Recent work on specialised finite element methods for acoustic propagation in rotational flows [45, 46, 47] is ongoing and the sheared flow mode-matching method developed here could be used as a method for benchmarking purposes.

A useful extension of the current mode-matching methods would be to allow for circular duct with no centre body for application to the inlet duct. The mean flow field in the inlet is not as non-uniform as the bypass duct, but the current work has shown that the effect of sheared mean flow is stronger for upstream propagating sound. Such an extension would be useful in

assessing the impact of the deep fan case liner located in front of the fan to reduce reflections that could induce fan flutter. It is possible that the flow non-uniformity in this region of annular geometry (due to the presence of the spinner) could have a strong impact upon the optimum fan case and inlet liner design parameters.

# Appendix A

# Details of the rectangular duct mode-matching equations

The terms $a_{ln}$ and $c_{ln}^{\pm}$ are obtained from the integrals in equations (3.17) and (3.18), respectively. Taking advantage of the orthogonality of the mode eigenfunctions, the above integrals are evaluated to give,

$$\begin{aligned} a_{ln} &= 2 && l = n = 0, \\ &= 1 && l = n \neq 0, \\ &= 0 && l \neq 0, \end{aligned} \tag{A.1}$$

$$\begin{aligned} c_{ln}^{\pm} &= 1 && \mu_{m,n} = \kappa_{m,l} \neq 0\ , \\ &= R_{m,n}^{\pm II} \frac{2\sin(\mu_{m,n})}{\mu_{m,n}} && \kappa_{m,l} = 0, \mu_{m,n} \neq \kappa_{m,l}\ , \\ &= \cos(\kappa_{m,l}) R_{m,n}^{\pm II} \left[ \frac{\sin(\kappa_{m,l} + \mu_{m,n})}{\kappa_{m,l} + \mu_{m,n}} + \frac{\sin(\kappa_{m,l} - \mu_{m,n})}{\kappa_{m,l} - \mu_{m,n}} \right] \\ &\quad + \sin(\kappa_{m,l}) S_{m,n}^{\pm II} \left[ \frac{\sin(\kappa_{m,l} - \mu_{m,n})}{\kappa_{m,l} - \mu_{m,n}} - \frac{\sin(\kappa_{m,l} + \mu_{m,n})}{\kappa_{m,l} + \mu_{m,n}} \right] && \mu_{m,n} \neq \kappa_{m,l}\ . \end{aligned} \tag{A.2}$$

The combined matrix equation for the continuity of pressure and axial particle velocity at a rigid-lined impedance discontinuity at $x^I$ is given by,

$$\left(\begin{array}{c|c} \mathbf{a}_1^+ & \mathbf{a}_1^+ \\ \hline \mathbf{b}_1^+ & \mathbf{b}_1^+ \end{array}\right) \left(\begin{array}{c} \mathbf{A}^{+I} \\ \hline \mathbf{A}^{-I} \end{array}\right) = \left(\begin{array}{c|c} \mathbf{c}_1^+ & \mathbf{c}_1^+ \\ \hline \mathbf{d}_1^+ & \mathbf{d}_1^+ \end{array}\right) \left(\begin{array}{c} \mathbf{A}^{+II} \\ \hline \mathbf{A}^{-II} \end{array}\right)\ . \tag{A.3}$$

The matrix elements are given by the following

$$\mathbf{a}_1^{\pm} = \begin{bmatrix} a_{1\,1}e^{-ik_1^{\pm}x^I} & 0 & \dots & 0 \\ 0 & a_{2\,2}e^{-ik_2^{\pm}x^I} & \ddots & \vdots \\ \vdots & \ddots & \ddots & 0 \\ 0 & \dots & 0 & a_{N_I\,N_I}e^{-ik_{N_I}^{\pm}x^I} \end{bmatrix}, \tag{A.4}$$

$$\mathbf{c}_1^{\pm} = \begin{bmatrix} c_{1\,1}^{\pm}e^{-i\alpha_1^{\pm}x^I} & c_{1\,2}^{\pm}e^{-i\alpha_2^{\pm}x^I} & \dots & c_{1\,N_{II}}^{\pm}e^{-i\alpha_{N_{II}}^{\pm}x^I} \\ c_{2\,1}^{\pm}e^{-i\alpha_1^{\pm}x^I} & c_{2\,2}^{\pm}e^{-i\alpha_2^{\pm}x^I} & \dots & c_{2\,N_{II}}^{\pm}e^{-i\alpha_{N_{II}}^{\pm}x^I} \\ \vdots & \vdots & & \vdots \\ c_{N_I\,1}^{\pm}e^{-i\alpha_1^{\pm}x^I} & c_{N_I\,2}^{\pm}e^{-i\alpha_2^{\pm}x^I} & \dots & c_{N_I\,N_{II}}^{\pm}e^{-i\alpha_{N_{II}}^{\pm}x^I} \end{bmatrix}, \tag{A.5}$$

$$\mathbf{b}_1^{\pm} = \begin{bmatrix} b_{1\,1}e^{-ik_1^{\pm}x^I} & 0 & \dots & 0 \\ 0 & b_{2\,2}e^{-ik_2^{\pm}x^I} & \ddots & \vdots \\ \vdots & \ddots & \ddots & 0 \\ 0 & \dots & 0 & b_{N_I\,N_I}e^{-ik_{N_I}^{\pm}x^I} \end{bmatrix}, \tag{A.6}$$

$$\mathbf{d}_1^{\pm} = \begin{bmatrix} d_{1\,1}^{\pm}e^{-i\alpha_1^{\pm}x^I} & d_{1\,2}^{\pm}e^{-i\alpha_2^{\pm}x^I} & \dots & d_{1\,N_{II}}^{\pm}e^{-i\alpha_{N_{II}}^{\pm}x^I} \\ d_{2\,1}^{\pm}e^{-i\alpha_1^{\pm}x^I} & d_{2\,2}^{\pm}e^{-i\alpha_2^{\pm}x^I} & \ddots & \vdots \\ \vdots & \ddots & \ddots & \vdots \\ d_{N_I\,1}^{\pm}e^{-i\alpha_1^{\pm}x^I} & \dots & \dots & d_{N_I\,N_{II}}^{\pm}e^{-i\alpha_{N_{II}}^{\pm}x^I} \end{bmatrix}, \tag{A.7}$$

$$\mathbf{A}^{+I} = \begin{bmatrix} A_1^{+I} \\ \vdots \\ A_{N_I}^{+I} \end{bmatrix}, \quad \mathbf{A}^{-I} = \begin{bmatrix} A_1^{-I} \\ \vdots \\ A_{N_I}^{-I} \end{bmatrix}, \quad \mathbf{A}^{+II} = \begin{bmatrix} A_1^{+II} \\ \vdots \\ A_{N_{II}}^{+II} \end{bmatrix}, \quad \mathbf{A}^{-II} = \begin{bmatrix} A_1^{-II} \\ \vdots \\ A_{N_{II}}^{-II} \end{bmatrix}. \tag{A.8}$$

# Appendix B

# Details of the Wiener-Hopf solution for a uniform symmetric liner in the absence of a mean flow

The mathematical formulation summarised here is from Koch [28], where a single even mode excitation is assumed. The kernel function for even modes is given by

$$\mathfrak{K}^s(\xi) = \frac{\hat{\gamma}\sin(\hat{\gamma}/2) - \frac{ik_0 2d\cos(\hat{\gamma}/2)}{Z^{II}}}{\hat{\gamma}\sin(\hat{\gamma}/2)}\ , \tag{B.1}$$

where $\hat{\gamma} = \left[(k_0 2d)^2 - (k_z 2d)^2 - \xi^2\right]^{1/2}$. The split function for left-running modes is given by

$$\mathfrak{K}^s_+(\xi) = \mathfrak{K}^s(0)\prod_{n=0}^{N_c}\frac{1+\xi/-\alpha_{m,2n}2d}{1-\xi/\delta_{k_x}k_{x_{m,2n}}2d}\prod_{n=N_c+1}^{N}\frac{1+\xi/-\alpha_{m,2n}2d}{1+\xi/\delta_{k_x}k_{x_{m,2n}}2d}\ , \tag{B.2}$$

and the split function for right-running modes follows as

$$\mathfrak{K}^s_-(\xi) = \mathfrak{K}^s_+(-\xi)/\mathfrak{K}^s(0)\ . \tag{B.3}$$

The transmission and reflection factors given in equations (3.49) and (3.50) are found after the decomposition of the generalised Wiener-Hopf equation, and application of the residue theorem to solve all decomposition integrals. The various coefficients that result are now defined. The coefficients $Q_{2n}$ and $P_{2n}$ are given by

$$Q_{2n} = \frac{\kappa^2_{m,2n}e^{-il^{II*}\alpha_{m,2n}2d}\mathfrak{K}^s_+(-\alpha_{m,2n}2d)^2}{-\alpha_{m,2n}2d\left[1+\frac{ik_0 d}{Z^{II}}+\frac{\kappa^2_{m,2n}Z^{II}}{i2k_0}\right]}\ , \tag{B.4}$$

$$P_{2n} = \frac{\kappa_{m,2n}^2 e^{-il^{II*}\alpha_{m,2n}2d}\mathfrak{K}_-^s\left(\alpha_{m,2n}2d\right)^2}{-\alpha_{m,2n}2d\left[1+\frac{ik_0d}{Z^{II}}+\frac{\kappa_{m,2n}^2 Z^{II}}{i2k_0}\right]} \,. \tag{B.5}$$

The correction term $C_{2n}^{(1)}$ is found by solving the following complex general system of linear equations

$$\left(\begin{bmatrix}1 & 0 & \dots & 0\\ 0 & 1 & \ddots & \vdots\\ \vdots & \ddots & \ddots & 0\\ 0 & \dots & 0 & 1\end{bmatrix} - \begin{bmatrix}A_0^0 & A_1^0 & \dots & A_N^0\\ A_0^1 & \ddots & \ddots & A_N^1\\ \vdots & \ddots & \ddots & \vdots\\ A_0^N & \dots\dots & & A_N^N\end{bmatrix}\begin{bmatrix}G_0^0 & G_1^0 & \dots & G_N^0\\ G_0^1 & \ddots & \ddots & G_N^1\\ \vdots & \ddots & \ddots & \vdots\\ G_0^N & \dots\dots & & G_N^N\end{bmatrix}\right)\begin{bmatrix}C_{2s}^{(1)}\\ \vdots\\ \vdots\\ C_{2N}^{(1)}\end{bmatrix} = \begin{bmatrix}B^0\\ \vdots\\ \vdots\\ B^N\end{bmatrix} \,. \tag{B.6}$$

The matrix elements are given by the following

$$A_n^s = \frac{P_{2n}}{-\alpha_{m,2s}2d - \alpha_{m,2n}2d} \,, \tag{B.7}$$

$$B^s = -\frac{\hat{E}_{m,2r}k_0 2d}{\left(-\alpha_{m,2s}2d + \delta_{k_x}k_{x_{m,2r}}2d\right)\mathfrak{K}_+^s\left(-\kappa_{m,2r}2d\right)} \,, \tag{B.8}$$

$$G_n^s = \frac{Q_{2n}}{-\alpha_{m,2s}2d - \alpha_{m,2n}2d} \,. \tag{B.9}$$

Solution of the linear system can be achieved using standard techniques, and for the purposes of the work here this is done computationally using the IMSL Fortran Numerical Library routine LSACG, which utilises LU factorisation and iterative refinement routines. The correction term $C_{2n}^{(2)}$ is then given by

$$\mathbf{C^{(2)}} = -\mathbf{G}\mathbf{C^{(1)}} \,. \tag{B.10}$$

# Appendix C

# Figures

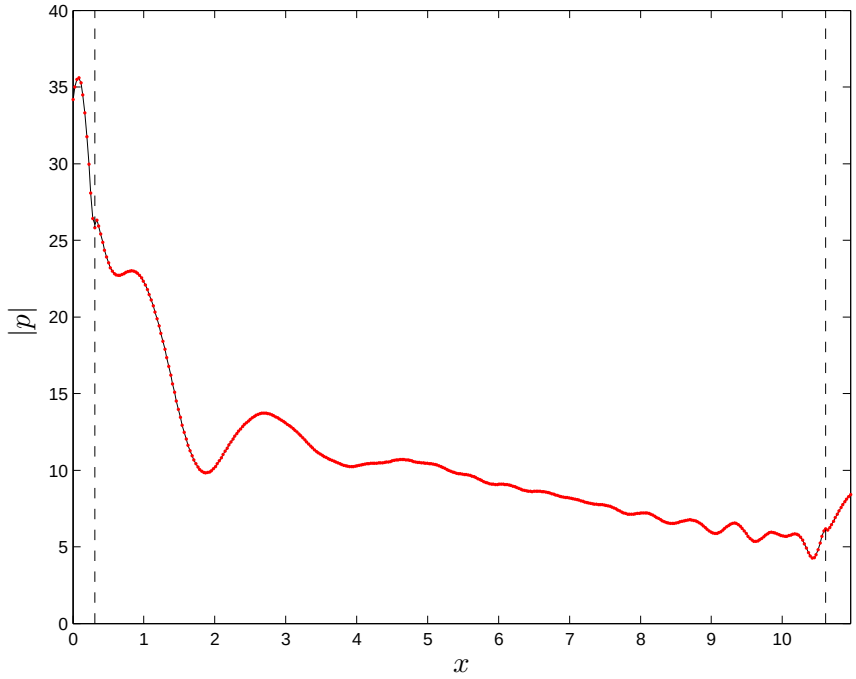


(a) Top wall pressure

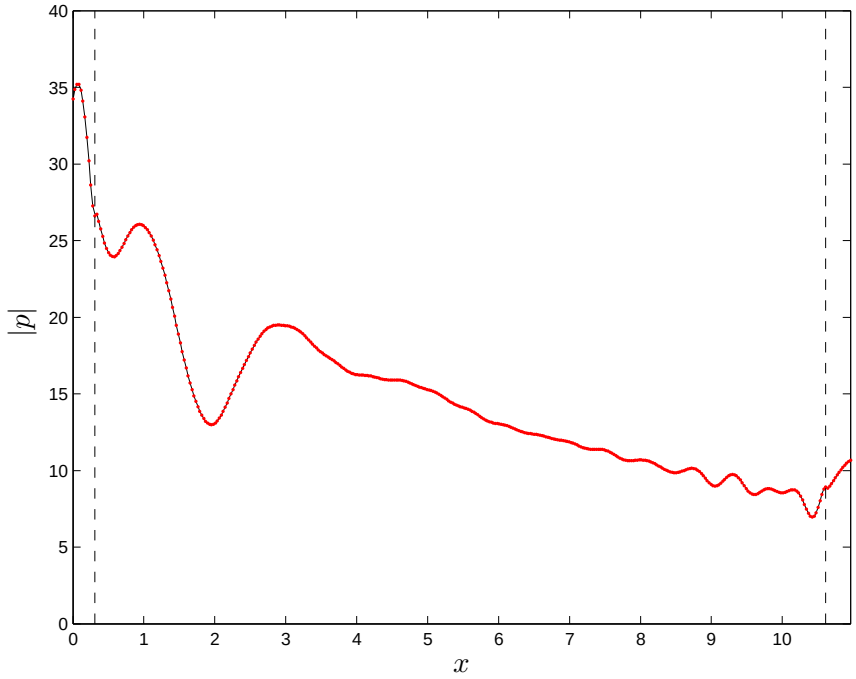


(b) Bottom wall pressure

FIGURE C.1: *Case 2: Comparison of 2D mode matching and finite solutions for a single asymmetric liner without flow. Liner interface matching planes indicated by dashed lines. Solid line, finite element solution;* •, *$p$-$u$ mode matching solution.*

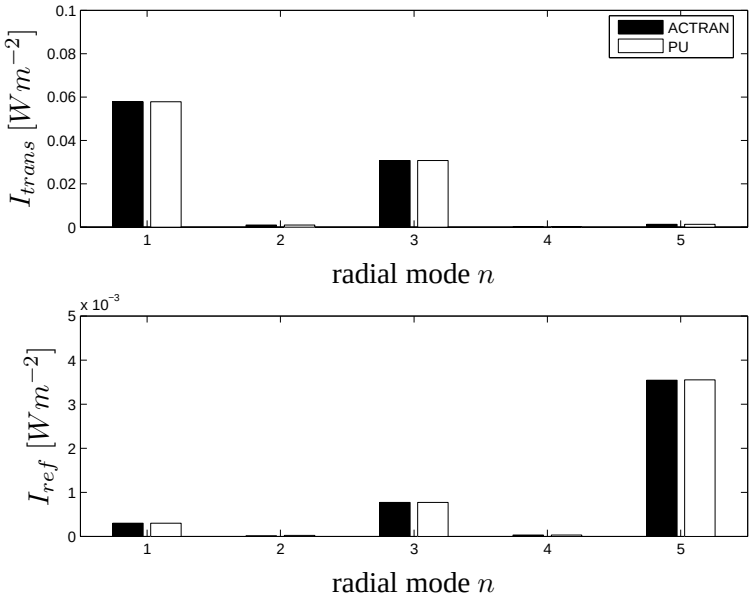


FIGURE C.2: *Case 2: Comparison of scattered modal intensities from mode matching and finite element methods due to an incident plane wave of unit intensity. Top plot, Transmitted modal intensity; Bottom plot, Reflected modal intensity.*

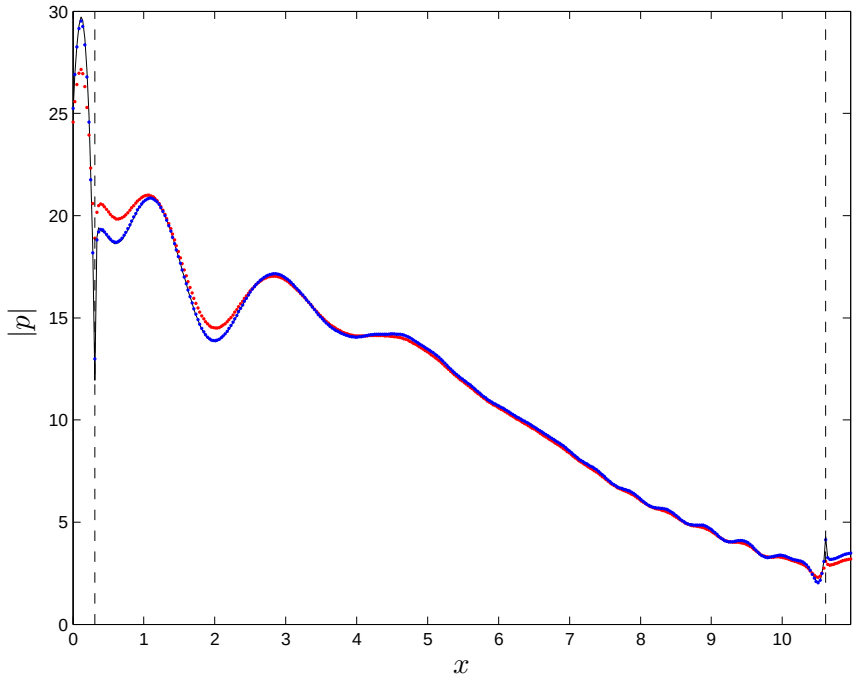


(a) Top wall pressure

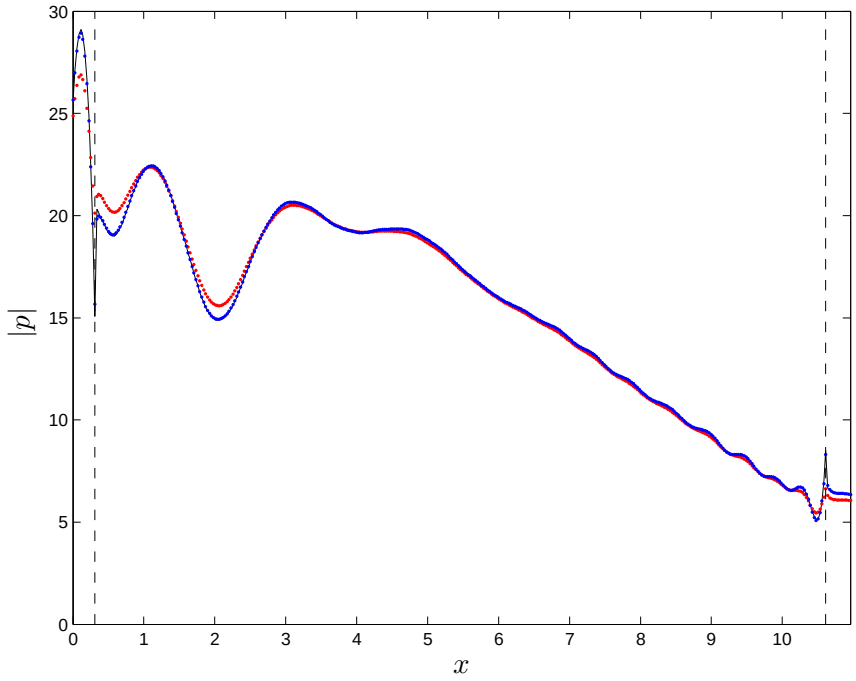


(b) Bottom pressure

FIGURE C.3: *Case 5: Comparison of 2D mode matching and finite solutions for a single asymmetric liner with flow. Liner interface matching planes indicated by dashed lines. Solid line, finite element solution;* ●, *$p$-$u$ mode matching solution;* ●, *mass-momentum mode matching solution.*

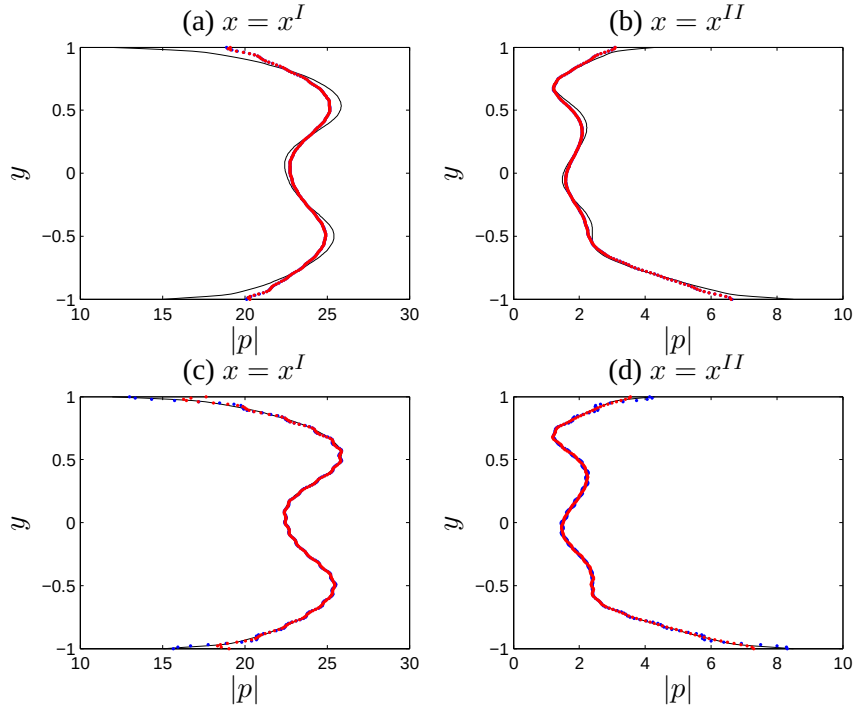


FIGURE C.4: *Case 5: Comparison of mode matching and finite element radial pressure solutions at liner interface matching planes. (a,b,c), $p$-$u$ matching; (d,e,f), mass-momentum matching ; Solid line, finite element solution; ●, mode matching solution (lefthand segment modes); ●, mode matching solution (righthand segment modes).*

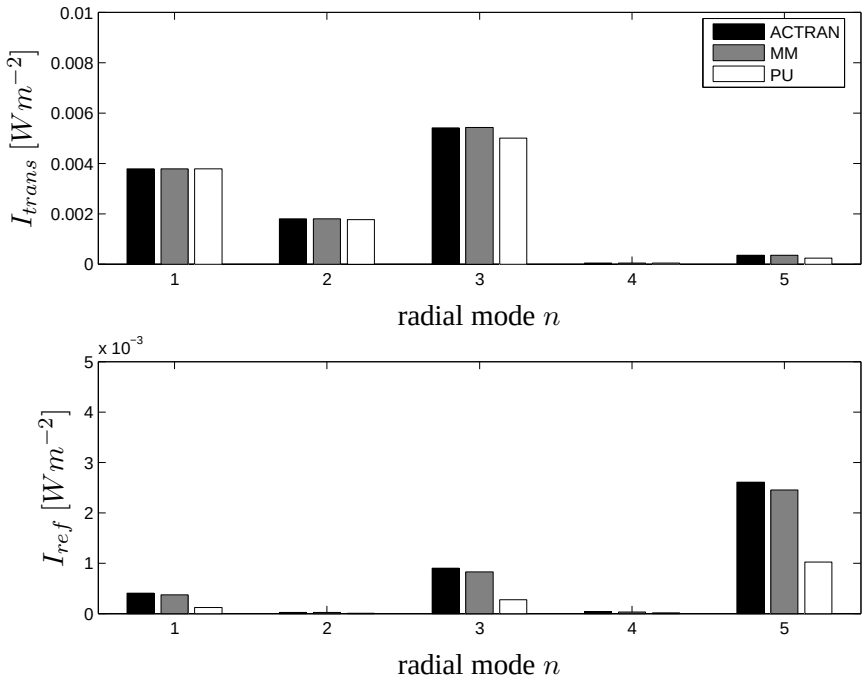


FIGURE C.5: *Case 5: Comparison of scattered modal intensities from mode matching and finite element methods due to an incident plane wave of unit intensity. Top plot, Transmitted modal intensity; Bottom plot, Reflected modal intensity.*

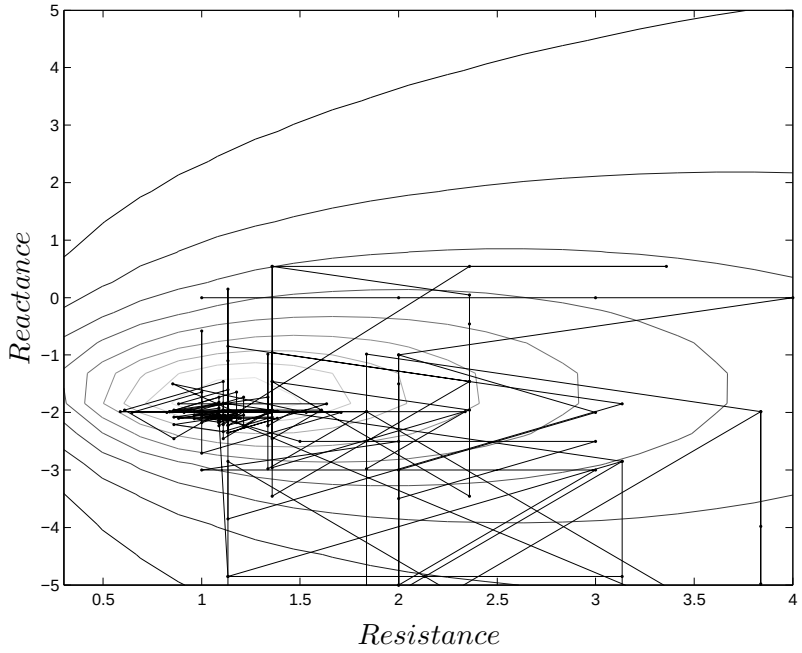


(a) DHC search pattern.

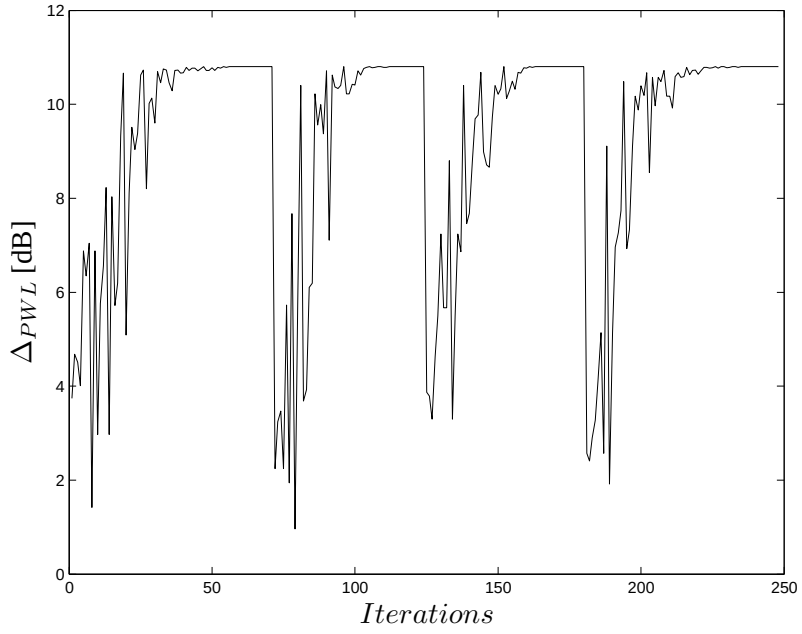


(b) DHC convergence.

FIGURE C.6: *Example of the dynamic hill climber search pattern and convergence for a single symmetric liner segment due to incident plane wave mode.* $k_0 = 8.7268$, $l_{II} = 10$, $M = 0.4$.

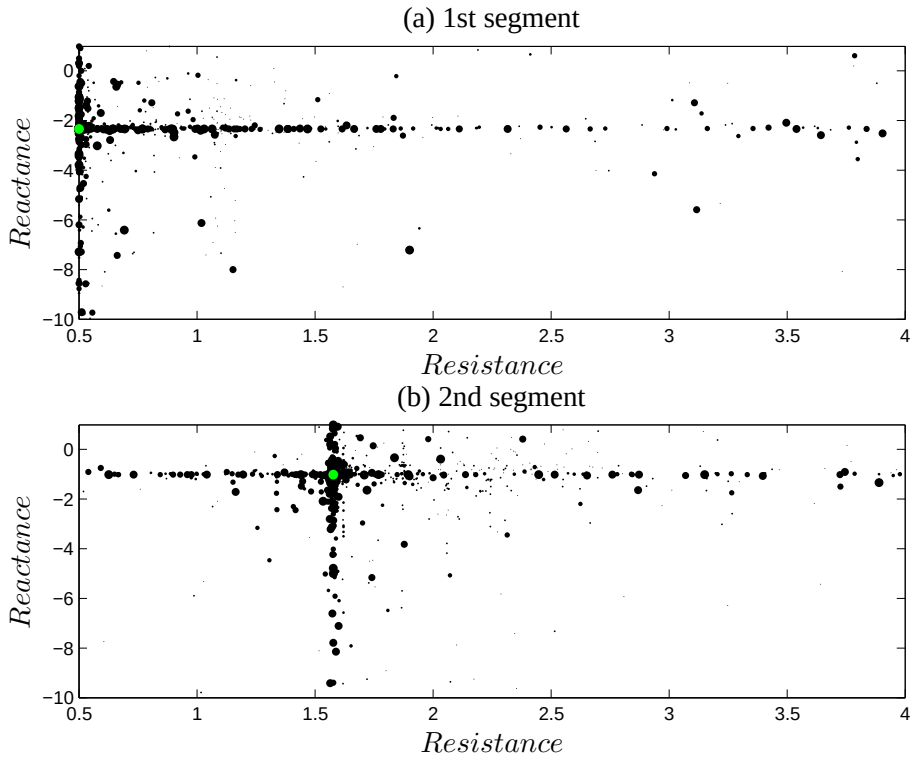


(a) ASA search pattern, where larger dot size indicates higher iteration number and green indicates optimum design point.

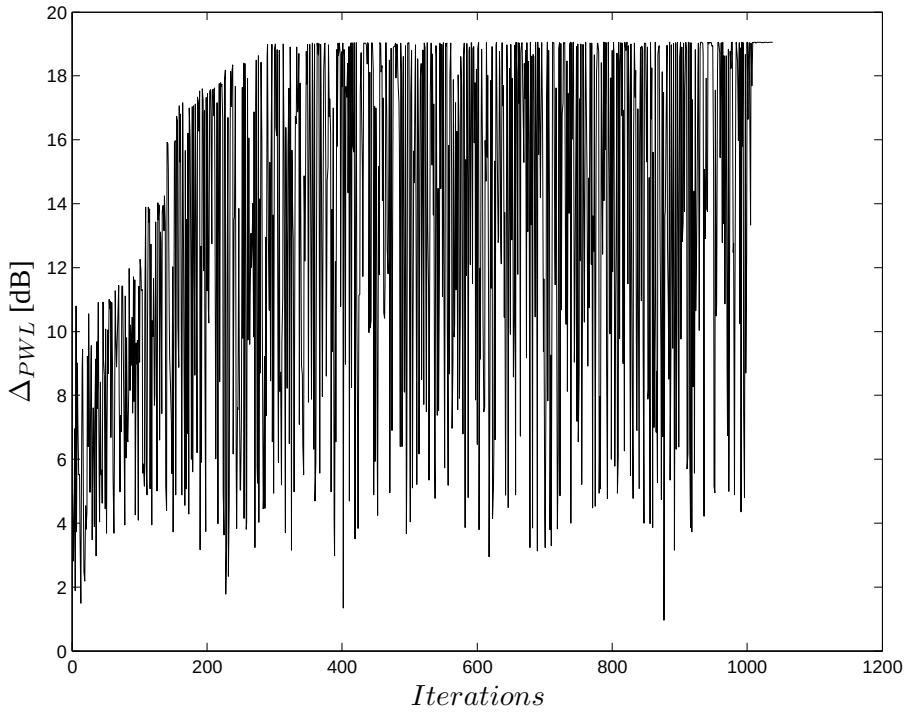


(b) ASA convergence.

FIGURE C.7: *Example of the adaptive simulated annealing search pattern and convergence for a single symmetric liner segment due to incident plane wave mode.* $k_0 = 8.7268$, $l_{II} = l_{III} = 5$, $M = 0.4$.

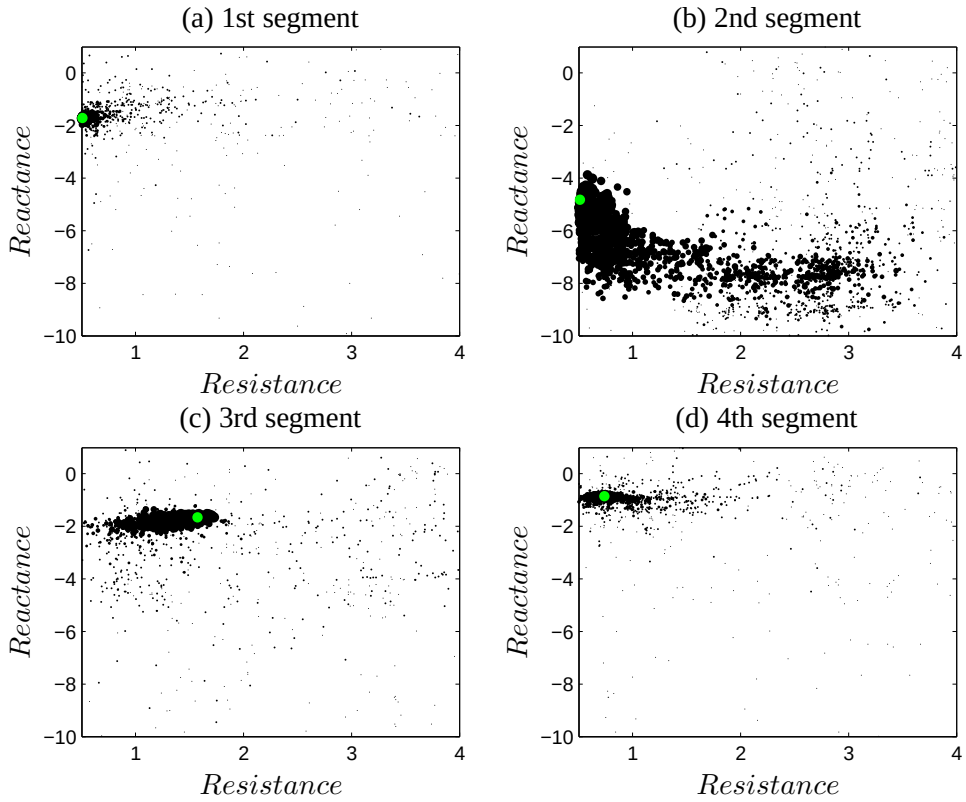


(a) ARMOGA search pattern, where larger dot size indicates later generation and green indicates optimum design point.

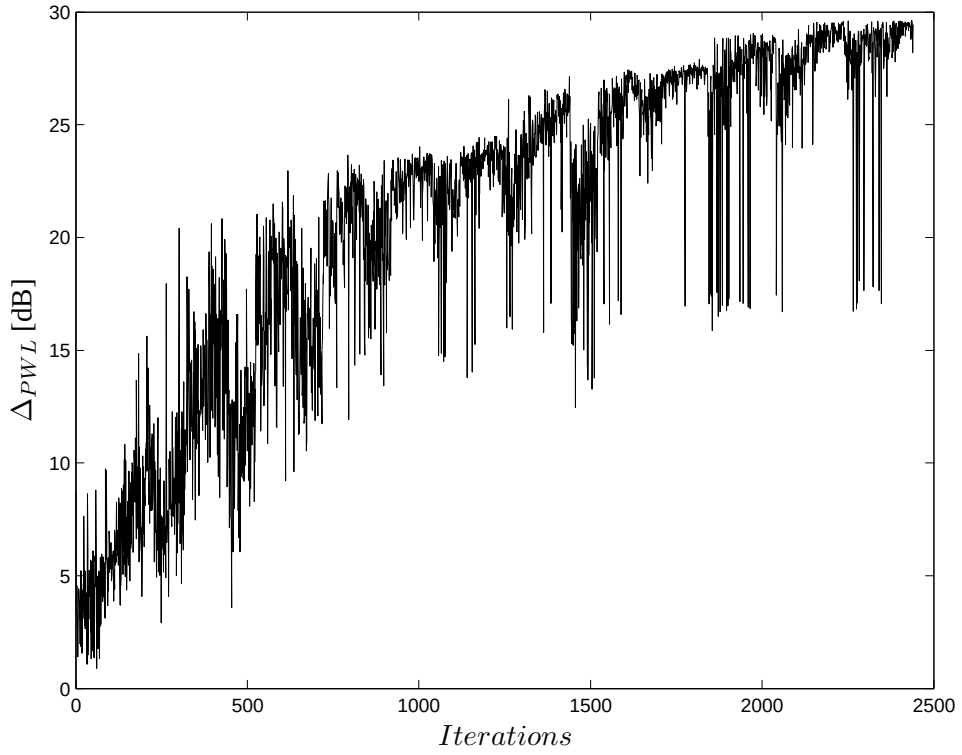


(b) ARMOGA convergence.

FIGURE C.8: *Example of the adaptive range multiobjective genetic algorithm search pattern and convergence for a single symmetric liner segment due to incident plane wave mode.* $k_0 = 8.7268, l_{II} = l_{III} = l_{IV} = l_V = 2.5, M = 0.4$.

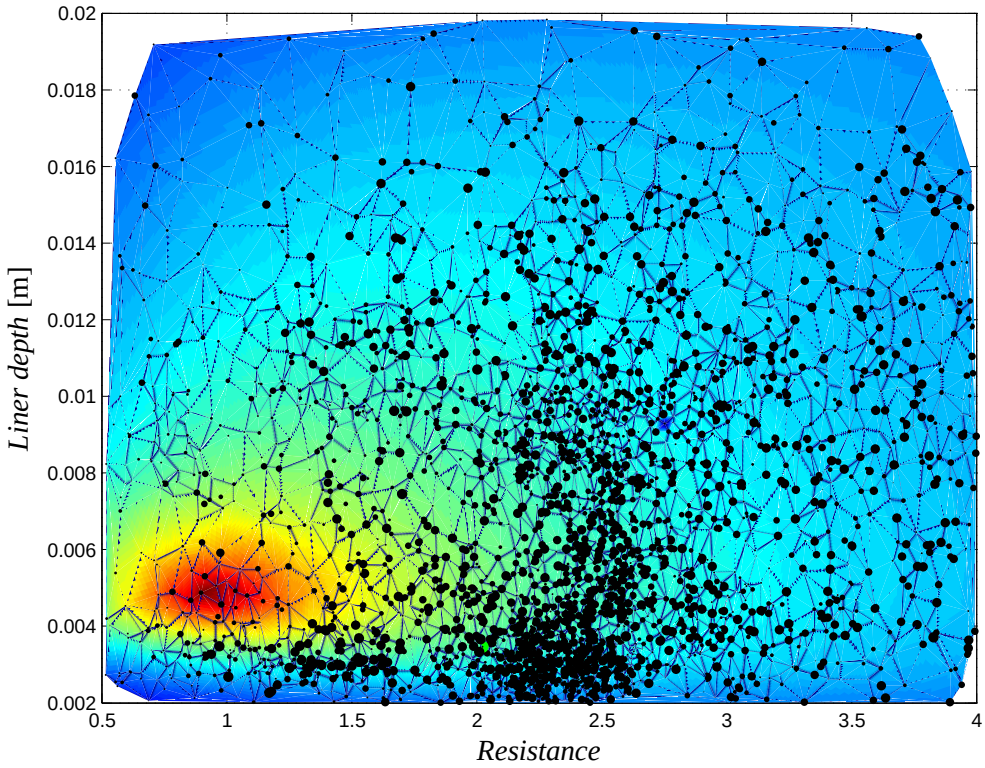


(a) $\Delta_{RS}$ cost function.

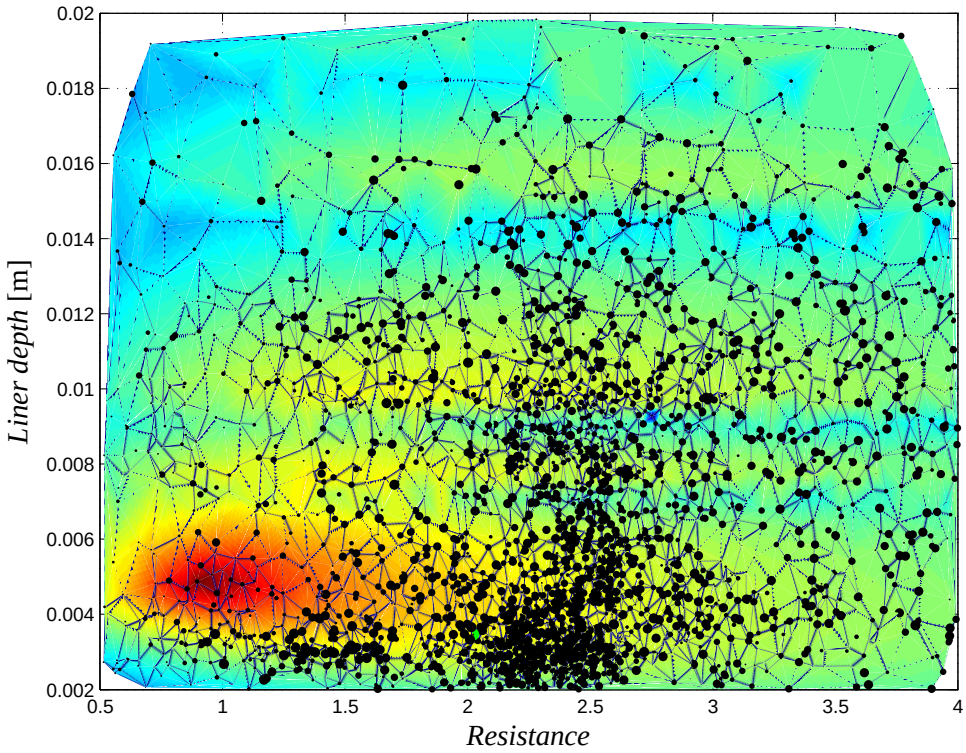


(b) Combine frequency cost function.

FIGURE C.9: *Adaptive range multiobjective genetic algorithm search pattern for a single symmetric liner segment due to multi-mode source and rotor-stator interaction tonal source (Contours constructed using Delaunay interpolation).* $l_{liner} = 10$, $M = 0.4$.

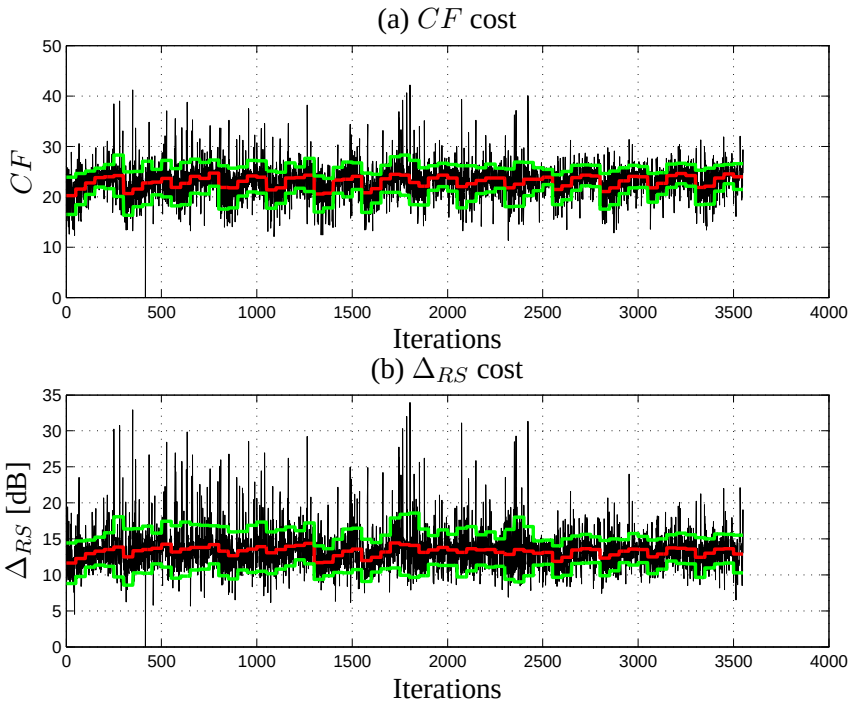


FIGURE C.10: *Adaptive range multiobjective genetic algorithm convergence for a single symmetric liner segment due to multi-mode source and rotor-stator interaction tonal source. —, Population cost function mean; —, Population cost function standard deviation bounds;* $l_{liner} = 10$, $M = 0.4$.

# Bibliography


[1] C. J. Brooks, “Prediction and control of sound propagation in turbofan inlet and bypass ducts.” EngD mini-thesis, Institute of Sound and Vibration Research, University of Southampton, United Kingdom, 2005.

[2] A. H. Nayfeh, J. E. Kaiser, and D. P. Telionis, “Acoustics of aircraft engine-duct systems.,” *AIAA Journal*, vol. 13, no. 2, pp. 130 – 153, 1975.

[3] P. G. Vaidya and P. D. Dean, “State of the art of duct acoustics,” in *AIAA 4th Aeroacoustics Conference*, no. AIAA-77-1279, (Atlanta, Georgia), AIAA, 1977.

[4] W. Eversman, “Theoretical models for duct acoustic propagation and radiation,” in *Aeroacoustics of flight vehicles: Theory and practise, volume 2: Noise control* (H. Hubbard, ed.), pp. 101 – 163, NASA, 1991.

[5] L. L. Beranek, *Acoustics*. McGraw-Hill electrical and electronic engineering series, 1954.

[6] J. M. Tyler and T. G. Sofrin, “Axial flow compressor noise,” in *SAE Aeronautic meeting transactions, vol. 70*, no. SAE-345D, pp. 309 – 332, SAE, 1962.

[7] W. Eversman, “The effect of mach number on the tuning of an acoustic lining in a flow duct,” *J. Acoust. Soc. Am. (USA)*, vol. 48, no. 2, pt.1, pp. 425 – 8, 1970.

[8] S.-H. Ko, “Sound attenuation in lined rectangular ducts with flow and its application to the reduction of aircraft engine noise,” *J. Acoust. Soc. Am. (USA)*, vol. 50, no. 6, pt.1, pp. 1418 – 32, 1971.

[9] D. Snow and M. Lowson, “Attenuation of spiral modes in a circular and annular lined duct,” *J. Sound Vib. (UK)*, vol. 25, no. 3, pp. 465 – 77, 1972.

[10] R. Yurkovich, “Attenuation of acoustic modes in circular and annular ducts in the presence of uniform flow,” in *AIAA 7th Fluid and Plasma Dynamics Conference*, (Palo Alto, California), AIAA, 1974.

[11] K. U. Ingard, “Influence of fluid motion past a plane boundary on sound reflection, absorption and transmission,” *J. Acous. Soc. Amer. (USA)*, vol. 31, no. 7, pp. 1035 – 1036, 1959.

[12] R. E. Motsinger, R. E. Kraft, and J. W. Zwick, "Optimization of suppression for two element treatment liners for turbomachinery exhaust ducts," NASA CR 134997, General Electric Company, April 1976.

[13] C. T. Molloy and E. Honigman, "Attenuation of sound in lined circular ducts," *Journal of the Acoustical Society of America*, vol. 16, no. 4, pp. 267 – 272, 1945.

[14] P. M. Morse and K. U. Ingard, *Theoretical Acoustics*. McGraw-Hill, 1968.

[15] R. Rogers, "The attenuation of sound tubes," *J. Acous. Soc. Amer. (USA)*, vol. 11, no. 4, pp. 480 – 484, 1940.

[16] E. J. Rice, *Aerodynamic noise*. University of Toronto Press, 1969.

[17] D. R. A. Christie, "Theoretical attenuation of sound in a lined duct: some computer calculations," *J. Sound Vib. (UK)*, vol. 17, no. 2, pp. 283 – 6, 1971.

[18] F. Mechel, "Modal solutions in circular and annular ducts with locally or bulk reacting lining," *Acta Acustica (Stuttgart)*, vol. 84, no. 2, pp. 201 – 222, 1998.

[19] W. Eversman, "Computation of axial and transverse wave numbers for uniform two-dimensional ducts with flow using a numerical integration scheme," *J. Sound Vib. (UK)*, vol. 41, no. 2, pp. 252 – 5, 1975. Errata, vol. 47, no. 1, 1976, p. 125.

[20] W. Eversman, "Initial values for the integration scheme to compute the eigenvalues for propagation in ducts," *J. Sound Vib. (UK)*, vol. 50, no. 1, pp. 159 – 62, 1977.

[21] B. Tester, "The propagation and attenuation of sound in lined ducts containing uniform or 'plug' flow," *J. Sound Vib. (UK)*, vol. 28, no. 2, pp. 151 – 203, 1973.

[22] S. W. Rienstra, "A classification of duct modes based on surface waves," *Wave Motion*, vol. 37, no. 2, pp. 119 – 135, 2003.

[23] S. W. Rienstra, "Hydrodynamic instabilities and surface waves in a flow over an impedance wall," in *Proceedings of the IUATM symposium Aero- and hydro-acoustics*, (Lyon, France), pp. 483 – 490, Springer-Verlag, 1985.

[24] L. Cremer, "Theory regarding the attenuation of sound transmitted by air in a rectangular duct with an absorbing wall, and the maximum attenuation constant produced during this process. (in german.)," *Acustica*, vol. 3, pp. 249 – 263, 1953.

[25] B. Tester, "The optimization of modal sound attenuation in ducts, in the absence of mean flow," *J. Sound Vib. (UK)*, vol. 27, no. 4, pp. 477 – 513, 1973.

[26] J. Unruh, "Finite length tuning for low frequency lining design," *J. Sound Vib. (UK)*, vol. 45, no. 1, pp. 5 – 14, 1976.

[27] J. F. Unruh and I. R. Price, "Experimental verification of a finite length tuning concept for acoustic lining design," *Journal of Sound and Vibration*, vol. 49, no. 3, pp. 393 – 402, 1976.

[28] W. Koch, "Attenuation of sound in multi-element acoustically lined rectangular ducts in the absence of mean flow," *J. Sound Vib. (UK)*, vol. 52, no. 4, pp. 459 – 96, 1977.

[29] W. Koch and W. Mohring, "Eigensolutions for liners in uniform mean flow ducts," *AIAA J. (USA)*, vol. 21, no. 2, pp. 200 – 13, 1983.

[30] R. Mittra and S. W. Lee, *Analytical Techniques in the Theory of Guided Waves*. MacMillan Series in Electrical Science, 1971.

[31] D. Lansing and W. Zorumski, "Effects of wall admittance changes on duct transmission and radiation of sound," *J. Sound Vib. (UK)*, vol. 27, no. 1, pp. 85 – 100, 1973.

[32] R. E. Motsinger, R. E. Kraft, and J. W. Zwick, "Design of optimum acoustic treatment for rectangular ducts with flow.," *American Society of Mechanical Engineers (Paper)*, no. 76-GT-113, pp. 15 –, 1976.

[33] J. D. Patterson, D. T. Sawdy, and R. J. Beckemeyer, "Experimental-analytical correlation of optimum duct acoustic liner performance.," *American Society of Mechanical Engineers (Paper)*, no. 76-GT-126, pp. 12 –, 1976.

[34] J. D. Patterson, D. T. Sawdy, and R. J. Beckemeyer, "Analytical and experimental studies of an optimum multisegment phased liner noise suppression concept," NASA CR 134960, Boeing, May 1976.

[35] W. E. Zorumski, "Acoustic theory of axisymmetric multisectioned ducts," TR R-419, NASA Langley Research Center, 1974.

[36] J. Barros and M. Moser, "Acoustic effects of broadening and contracting transition between ducts of different cross-section. part i: Theoretical treatment," *Acta Acustica (Stuttgart)*, vol. 89, no. 3, pp. 416 – 425, 2003.

[37] J. Barros and M. Moser, "Acoustic effects of broadening and contracting transition between ducts of different cross-section. part ii. numerical results and measurements," *Acta Acust. United With Acust. (Germany)*, vol. 90, no. 2, pp. 221 – 31, 2004.

[38] V. J. T. Hii, *Effective computation of acoustic propagation in turbofan aero-engine ducts*. PhD thesis, Institute of sound and vibration research, University of Southampton, United Kingdom, 2005.

[39] K. J. Baumeister, "Generalized wave envelope analysis of sound propagation in ducts with stepped noise source profiles and variable axial impedance," in *AIAA 2nd Aero-Acoustics Conference*, (Hampton, Virginia), AIAA, 1975.

[40] K. Baumeister, "Evaluation of optimized multisectioned acoustic liners," *AIAA J. (USA)*, vol. 17, no. 11, pp. 1185 – 92, 1979.

[41] A. N. Abdelhamid, "Acoustic propagation in two dimensional flow ducts with asymmetric liners," in *AIAA 4th aeroacoustics conference*, no. AIAA-77-1283, (Atlanta, Georgia), AIAA, 1977.

[42] M. Ochmann and U. Donner, "Investigation of silencers with asymmetrical lining. i: theory," *Acta Acust. (France)*, vol. 2, no. 4, pp. 247 – 55, 1994.

[43] M. Ochmann, "Calculation of the sound transmission loss of silencers with asymmetrical lining in rectangular ducts," in *Noise-93*, (St. Petersburg, Russia), pp. 181 – 186, 1993.

[44] F. P. Mechel, "Why are silencers symmetrical?," in *Noise control conference*, (Warsaw, Poland), pp. 65 – 71, 1976.

[45] N. Chevaugeon, J.-F. Remacle, X. Gallez, P. Ploumhans, and S. Caro, "Efficient discontinuous galerkin methods for solving acoustic problems," vol. 1, (Monterey, CA, United States), pp. 295 – 313, 2005.

[46] J.-F. Mercier, A.-S.-B. Dhia, E.-M. Duclairoir, and G. Legendre, "Time-harmonic acoustic propagation in the presence of a shear flow," *Journal of Computational and Applied Mathematics*, vol. 204, no. 2, pp. 428 – 39, 2007.

[47] G. Gabard, F. Treyssede, and M. B. Tahar, "A numerical method for vibro-acoustic problems with sheared mean flows," *Journal of Sound and Vibration*, vol. 272, no. 3-5, pp. 991 – 1011, 2004.

[48] X. Zhang, X. Chen, C. L. Morfey, and B. J. Tester, "Computation of fan noise radiation through a realistic engine exhaust geometry with flow," in *9th AIAA/CEAS Aeroacoustics conference and exhibit*, (Hilton Head, South Carolina), 2003.

[49] Y. Ozyoruk and V. Ahuja, "Numerical simulation of fore and aft sound fields of a turbofan," *AIAA Journal*, vol. 42, no. 10, pp. 2028 – 34, 2004.

[50] D. C. Pridmore-Brown, "Sound propagation in a fluid flowing through an attenuating duct," *Journal of Fluid Mechanics*, vol. 4, pp. 393 – 406, 1958.

[51] B. Tester, "Some aspects of 'sound' attenuation in lined ducts containing inviscid mean flows with boundary layers," *Journal of Sound and Vibration*, vol. 28, no. 2, pp. 217 – 45, 1973.

[52] M. G. Smith, *Sound radiation from a vibrating surface under a boundary layer*. PhD thesis, Institute of Sound and Vibration Research, University of Southampton, United Kingdom, 2004.

[53] P. Shankar, "Acoustic refraction and attenuation in cylindrical and annular ducts," *Journal of Sound and Vibration*, vol. 22, no. 2, pp. 233 – 46, 1972.

[54] R. A. Prydz, "Boundary layer considerations for optimization of acoustic liners for aircraft engine ducts.," *SAE Preprints*, no. 760896, pp. 16 –, 1976.

[55] W. Eversman, "Energy flow criteria for acoustic propagation in ducts with flow," *J. Acoust. Soc. Am. (USA)*, vol. 49, no. 6, pt.1, pp. 1717 – 22, 1971.

[56] W. Eversman, M. D. Nelsen, D. Armstrong, and O. J. Hall, "Design of acoustic linings for ducts with flow," *J. Aircraft*, vol. 51, no. 1, pp. 23 – 54, 1972.

[57] M. Myers, "On the acoustic boundary condition in the presence of flow," *Journal of Sound and Vibration*, vol. 71, no. 3, pp. 429 – 34, 1980.

[58] W. H. Press, B. P. Flannery, S. A. Teukolsky, and W. T. Vetterling, *Numerical recipes: The art of scientific programming*. Cambridge University Press, 1986.

[59] S. J. Perkins and A. B. Parry, "Cut-off in annular ducts with axial and swirl flow," Rolls-Royce Powerplant Technology Memorandum INM05050, Rolls-Royce plc., December 1991.

[60] M. G. Smith, "Acoustic propagation in annular ducts with swirling mean flow," Rolls-Royce Noise Department Report INR90089, Rolls-Royce plc., May 1980.

[61] C. L. Morfey, "Rotating pressure patterns in ducts: their generation and transmission," *J. Sound Vib. (UK)*, vol. 1, no. 1, pp. 60 – 87, 1964.

[62] M. Abramowitz and I. A. Stegun, *Handbook of mathematical functions*. National Bureau of Standards, Dover Publications Inc., 1964.

[63] E. J. Rice, "Modal propagation angles in ducts with soft walls and their connection with supressor performance," in *AIAA 5th Aeroacoustics Conference*, (Seattle, Washington), AIAA, 1979.

[64] A. McAlpine, R. Astley, V. Hii, N. Baker, and A. Kempton, "Acoustic scattering by an axially-segmented turbofan inlet duct liner at supersonic fan speeds," *Journal of Sound and Vibration*, vol. 294, no. 4-5, pp. 780 – 806, 2006.

[65] A. Cummings, "High frequency ray acoustics models for duct silencers," *J. Sound Vib. (UK)*, vol. 221, no. 4, pp. 681 – 708, 1999.

[66] S. W. Rienstra, "The acoustics of a lined duct with flow," NLR Technical Report NLR TR 87002 U, National Aerospace Laboratory NLR, The Netherlands, 1987.

[67] R. Astley, V. Hii, and G. Gabard, "A computational mode matching approach for propagation in three-dimensional ducts with flow," *Collection of Technical Papers - 12th AIAA/CEAS Aeroacoustics Conference*, vol. 3, pp. 1652 – 1674, 2006.

[68] W. Möhring and W. Eversman, "Conversion of acoustic energy by lossless liners.," *Journal of Sound and Vibration*, vol. 82, no. 3, pp. 371 – 381, 1982.

[69] M. Quinn and M. Howe, "On the production and absorption of sound by lossless liners in the presence of mean flow," *Journal of Sound and Vibration*, vol. 97, no. 1, pp. 1 – 9, 1984.

[70] A. E. Heins and H. Feshbach, "The coupling of two acoustic ducts," *Journal of Mathematics and Physics*, vol. 26, pp. 143 – 155, 1947.

[71] S. W. Rienstra and N. Peake, "Modal scattering at an impedance transition in a lined flow duct," *Collection of Technical Papers - 11th AIAA/CEAS Aeroacoustics Conference*, vol. 1, pp. 676 – 694, 2005.

[72] R. Nijboer, "Sound diffraction by the splitter in a turbofan rotor-stator gap swirling flow," *Proceedings of the Tenth International Congress on Sound and Vibration*, pp. 629 – 636, 2003.

[73] R. J. Nijboer, "Sound diffraction by the splitter in a turbofan rotor-stator gap swirling flow," NLR Technical Report NLR-TP-2003-220, National Aerospace Laboratory NLR, April 2003.

[74] S. W. Rienstra and B. J. Tester, "An analytic green's function for a lined circular duct containing uniform mean flow," *Collection of Technical Papers - 11th AIAA/CEAS Aeroacoustics Conference*, vol. 4, pp. 2738 – 2755, 2005.

[75] E. Brambley and N. Peake, "Classification of aeroacoustically relevant surface modes in cylindrical lined ducts," *Wave Motion*, vol. 43, no. 4, pp. 301 – 310, 2006.

[76] C. Morfey, "Acoustic energy in non-uniform flows," *J. Sound Vib. (UK)*, vol. 14, no. 2, pp. 159 – 70, 1971.

[77] O. Ryshov and G. Shefter, "On the energy of acoustic waves propagating in a moving media," *J. appl. Math. Mech.*, vol. 26, p. 1293, 1962.

[78] S. W. Rienstra and N. Peake, "Modal scattering at an impedance transition in a lined flow duct," in *11th AIAA/CEAS Aeroacoustics Conference (26th AIAA Aeroacoustics Conference)*, (Monterey, California), AIAA, 2005.

[79] B. Noble, *Methods based on the Wiener-Hopf technique for the solution of partial differential equations*. Pergamon Press, 1988.

[80] F. field technologies, *Actran-tm 2006 users' manual*. FFT, Louvain-la-Neuve, Belgium, 2006.

[81] W. Koch, "Radiation of sound from a two-dimensional lined duct," *Journal of Sound and Vibration*, vol. 55, no. 2, pp. 255 – 274, 1977.

[82] R. J. Astley, A. Agarwal, K. R. Holland, P. F. Joseph, R. Sugimoto, R. H. Self, M. G. Smith, and B. J. Tester, "Predicting and reducing aircraft noise," in *14th International congress on sound and vibration*, (Cairns, Australia), ICSV14, 2007.

[83] R. Mani, "Noise due to interaction of inlet turbulence with isolated stators and rotors," *Journal of Sound and Vibration*, vol. 17, no. 2, pp. 251 – 60, 1971.

[84] W. Watson, J. Robinson, M. Jones, and T. Parrott, "Computational study of optimum and off-design performance of checkerboard liners," in *Collection of Technical Papers - 10th AIAA/CEAS Aeroacoustics Conference*, vol. 3, (Manchester, United Kingdom), pp. 2606 – 2617, 2004.

[85] F. Pan and J. Coupland, "An integrated optimization system for low noise nacelle design," in *Collection of Technical Papers - 11th AIAA/CEAS Aeroacoustics Conference*, vol. 3, pp. 1826 – 1841, 2005.

[86] E. J. Rice, "Optimum wall impedance for spinning modes - a correlation with mode cutoff ratio.," *Journal of Aircraft*, vol. 16, no. 5, pp. 336 – 343, 1979.

[87] A. J. Kempton, C. J. Brooks, A. McAlpine, and C. R. McAleer, "Andante wp3.2 report on optimised bypass-duct liner design - d3.2.1," Rolls-Royce Internal Noise Report INR90519, Rolls-Royce plc., 2006.

[88] R. Sugimoto, R. J. Astley, L. De Mercato, K. R. Holland, and V. Jurdic, "Prediction methods for propagation in bypass ducts and comparision with measured data," in *11th AIAA/CEAS aeroacoustics conference*, no. AIAA 2005-3059, (Monterey, USA), AIAA, 2005.

[89] R. E. Motsinger and R. E. Kraft, "Design and performance of duct acoustic treatment," in *Aeroacoustics of flight vehicles: Theory and practise, volume 2: Noise control* (H. Hubbard, ed.), pp. 165 – 206, 1991.

[90] J. Coupland, A. Wilson, N. Pollard, S. Uellenberg, C. Breard, and J. Diamond, "Demonstration of a cfd-caa methodology to predict buzz-saw noise propagation to the aircraft," in *13th AIAA/CEAS aeroacoustics conference*, no. AIAA 2007-3517, (Rome, Italy), AIAA, 2007.

[91] L. Enghardt, U. Tapken, O. Kornow, and F. Kennepohl, "Acoustic mode decomposition of compressor noise under consideration of radial flow profiles," in *Collection of Technical Papers - 11th AIAA/CEAS Aeroacoustics Conference*, vol. 1, (Monterey, CA, United States), pp. 437 – 449, 2005.

[92] M. D. Dahl and D. L. Sutliff, "Numerical technique for analyzing rotating rake mode measurements in a duct with passive treatment and shear flow," in *13th AIAA/CEAS aeroacoustics conference*, no. AIAA 2007-3679, (Rome, Italy), AIAA, 2007.

[93] C. Lowis and P. Joseph, "A focused beamformer technique for separating rotor and stator-based broadband sources," in *Collection of Technical Papers - 12th AIAA/CEAS Aeroacoustics Conference*, vol. 6, pp. 3973 – 3986, 2006.

[94] C. Lowis and P. Joseph, "Determining the strength of rotating broadband sources in ducts by inverse methods," *Journal of Sound and Vibration*, vol. 295, no. 3-5, pp. 614 – 632, 2006.

[95] G. Zlavog and W. Eversman, "Statistical distributions for acoustic power of broad band noise in lined ducts," in *Collection of Technical Papers - 11th AIAA/CEAS Aeroacoustics Conference*, vol. 2, (Monterey, CA, United States), pp. 1258 – 1274, 2005.

[96] G. Zlavog and W. Eversman, "A statistically based computational approach for tonal and broadband noise attenuation," in *Collection of Technical Papers - 11th AIAA/CEAS Aeroacoustics Conference*, vol. 2, (Monterey, CA, United States), pp. 1275 – 1290, 2005.

[97] G. Zlavog and W. Eversman, "A statistical approach to optimum design of inlet acoustic treatment," vol. 3, (Cambridge, MA, United States), pp. 1577 – 1601, 2006.

[98] M. J. T. Smith, "Quietening a quiet engine - the rb211 demonstrator programme.," *SAE Preprints*, no. 760897, pp. 17 –, 1976.

[99] B. J. Tester, *Sound attenuation in lined ducts containing subsonic mean flow*. PhD thesis, Institute of sound and vibration research, University of Southampton, United Kingdom, 1972.

[100] L. Lafronza, A. McAlpine, A. Keane, and R. Astley, "Response surface method optimization of uniform and axially segmented duct acoustics liners," *Journal of Aircraft*, vol. 43, no. 4, pp. 1089 – 102, 2006.

[101] C. J. Brooks, "Axially-segmented acoustic liners for turbofan engine bypass ducts: A method for preliminary design iterations and optimisation," in *Institute of Acoustics Spring Conference 2006*, (University of Southampton, Southampton, United Kingdom), 2006.

[102] B. Tester, "The propagation and attenuation of sound in lined ducts containing uniform or 'plug' flow," *Journal of Sound and Vibration*, vol. 28, no. 2, pp. 151 – 203, 1973.

[103] D. Yuret, "From genetic algorithms to efficient optimisation.," MIT Artificial Intelligence Laboratory Report 1569, MIT Artificial Intelligence Laboratory, May 1994.

[104] L. Ingber, "Simulated annealing: Practise versus theory.," *Mathl. Comput. Modelling*, vol. 18, no. 11, pp. 29 – 57, 1993.

[105] A. J. Keane and P. B. Nair, *Computational approaches for aerospace design*. John Wiley and Sons Ltd., Chichester, 2005.

[106] M. Arakawa and I. Hagiwara, "Development of adaptive real range (arrange) genetic algorithms," *JSME International Journal, Series C (Mechanical Systems, Machine Elements and Manufacturing)*, vol. 41, no. 4, pp. 969 – 77, 1998.

[107] S. Obayashi and D. Sasaki, "Multi-objective optimization for aerodynamic designs by using armogas," in *Proceedings - Seventh International Conference on High Performance Computing and Grid in Asia Pacific Region, HPCAsia 2004*, (Tokyo, Japan), pp. 396 – 403, 2004.

[108] L. Lafronza, A. McAlpine, A. J. Keane, and R. J. Astley, "Computer-aided liner optimisation for broadband noise," in *10th AIAA/CEAS aeroacoustics conference*, no. AIAA-2004-3029, (Manchester, United Kingdom), AIAA, 2004.

[109] Y. Zhao and P. Morris, "The prediction of fan exhaust noise propagation," in *12th AIAA/CEAS Aeroacoustics conference*, (Cambridge, Massachusetts), 2006.

[110] R. Leneveu, B. Schiltz, S. Caro, and J. Manera, "Parallel dgm scheme for lee applied to 3d realistic exhaust problems," (Rome, Italy), 2007.

[111] P. Moinier, J.-D. Muller, and M. Giles, "Edge-based multigrid and preconditioning for hybrid grids," *AIAA Journal*, vol. 40, no. 10, pp. 1954 – 60, 2002/10/.

[112] B. Lapworth, "Hydra-cfd : A framework for collaborative cfd development," in *International Conference on Scientific and Engineering Computation (IC-SEC)*, (Singapore), 2004.

[113] N. C. Ovenden and S. W. Rienstra, "In-duct matching strategies," TurboNoiseCFD Workpackage 2 deliverable D2.4, Eindhoven University of Technology, 2002.

[114] J. Coupland, "Private communication," 2006.

[115] G. Vilenski and S. W. Rienstra, "Acoustic modes in a ducted shear flow," in *Collection of Technical Papers - 11th AIAA/CEAS Aeroacoustics Conference*, vol. 4, (Monterey, CA, United States), pp. 2786 – 2805, 2005.

[116] P. Moinier and M. Giles, "Eigenmode analysis for turbomachinery applications," *Journal of Propulsion and Power*, vol. 21, no. 6, pp. 973 – 8, 2005.

[117] A. G. Wilson, "Turbomachinery noise source cfd models for low noise aircraft designs," TurboNoiseCFD Workpackage 1 deliverable TurboNoiseCFD-RR-01-WP1-01, Rolls-Royce plc., 2001.

[118] W. Mohring, E.-A. Muller, and F. Obermeier, "Problems in flow acoustics," *Reviews of Modern Physics*, vol. 55, no. 3, pp. 707 – 24, 1983.

[119] M. Goldstein and E. Rice, "Effect of shear on duct wall impedance," *Journal of Sound and Vibration*, vol. 30, no. 1, pp. 79 – 84, 8 Sept. 1973.

[120] J. Scott, "Propagation of sound waves through a linear shear layer," *AIAA Journal*, vol. 17, no. 3, pp. 237 – 44, 1979.

[121] S. Koutsoyannis, "Characterization of acoustic disturbances in linearly sheared flows," *Journal of Sound and Vibration*, vol. 68, no. 2, pp. 187 – 202, 1980/01/22.

[122] S. Koutsoyannis, K. Karamcheti, and D. Galant, "Acoustic resonances and sound scattering by a shear layer," *AIAA Journal*, vol. 18, no. 12, pp. 1446 – 54, 1980.

[123] G. Gogate and M. Munjal, "Analytical solution of the laminar mean flow wave equation in a lined or unlined two-dimensional rectangular duct," *Journal of the Acoustical Society of America*, vol. 92, no. 5, pp. 2915 –, 1992.

[124] G. Gogate and M. Munjal, "Analytical solution of sound propagation in lined or unlined circular ducts with laminar mean flow," *Journal of Sound and Vibration*, vol. 160, no. 3, pp. 465 – 84, 1993.

[125] J.-C. Valiere, R. Boucheron, and H. Bailliet, "Analytical solution of multimodal acoustic propagation in circular ducts with laminar mean flow profile," *Journal of Sound and Vibration*, vol. 292, no. 3-5, pp. 504 – 18, 2006.

[126] L. Campos and P. Serrao, "On the acoustics of an exponential boundary layer," *Philosophical Transactions of the Royal Society London, Series A (Mathematical, Physical and Engineering Sciences)*, vol. 356, no. 1746, pp. 2335 – 78, 1998.

[127] W. Eversman, "Representation of a 1/n power law boundary layer in the sheared flow acoustic transmission problem," *Journal of Sound and Vibration*, vol. 24, no. 4, pp. 459 – 69, 1972.

[128] M. Smith and C. Morfey, "Directivity and sound power radiated by a source under a boundary layer," *AIAA Journal*, vol. 44, no. 11, pp. 2630 – 5, 2006.

[129] P. Mungur and G. Gladwell, "Acoustic wave propagation in a sheared fluid contained in a duct," *Journal of Sound and Vibration*, vol. 9, no. 1, pp. 28 – 48, 1969.

[130] P. Mungur and H. E. Plumbee, "Propagation and attenuation of sound in a soft walled annular duct containing a sheared flow," NASA technical report NASA SP-207, NASA, Washington, 1969.

[131] J. Unruh and W. Eversman, "The transmission of sound in an acoustically treated rectangular duct with boundary layer," *Journal of Sound and Vibration*, vol. 25, no. 3, pp. 371 – 82, 1972.

[132] G. A. Wynne and H. E. Plumbee, "Calculation of eigenvalues of the finite difference equations describing sound propagation in a duct carrying sheared flow," in *79th meeting of the Acoustical Society of America*, 1970.

[133] K. A. Kousen, "Eigenmodes of ducted flows with radially-dependant axial and swirl components," NASA contract report NASA CR-1999-208881, United Technologies Corporation, 1999.

[134] R. Astley and W. Eversman, "A finite element formulation of the eigenvalue problem in lined ducts with flow," *Journal of Sound and Vibration*, vol. 65, no. 1, pp. 61 – 74, 1979.

[135] R. J. Astley and W. Eversman, "Finite element duct eigenvalue problem: An improved formulation with hermitian elements and no-flow condensation.," *Journal of Sound and Vibration*, vol. 69, no. 1, pp. 13 – 25, 1980.

[136] C. J. Brooks and A. McAlpine, "Sound transmission in ducts with sheared mean flow," in *13th AIAA/CEAS aeroacoustics conference*, 2007. AIAA-2007-3545.

[137] M. E. Goldstein, *Aeroacoustics*. New York: McGraw-Hill Book Company, Inc., 1976.

[138] D. E. Muller, "A method for solving algebraic equations using an automatic computer," *Mathematical Tables and other Aids to Computation (MTAC)*, vol. 10, pp. 208 – 215, 1956.

[139] M. C. Joshi, R. E. Kraft, and S. Y. Son, "Analysis of sound propagation in annular ducts with segmented treatment and sheared flows," in *AIAA 20th Aerospace sciences meeting*, no. AIAA-82-0123, (Orlando, Florida), AIAA, 1982.

[140] A. Nayfeh, J. Kaiser, and B. Shaker, "Effect of mean-velocity profile shapes on sound transmission through two-dimensional ducts," *Journal of Sound and Vibration*, vol. 34, no. 3, pp. 413 – 23, 1974.

[141] W. Mohring, "Energy conservation, time-reversal invariance and reciprocity in ducts with flow," *Journal of Fluid Mechanics*, vol. 431, pp. 223 – 37, 2001.

[142] W. Mohring, "Energy flux in duct flow," *Journal of Sound and Vibration*, vol. 18, pp. 101 – 9, 8 Sept. 1971.

[143] G. G. Vilenski and S. W. Rienstra, "On hydrodynamic and acoustic modes in a ducted shear flow with wall lining," *Journal of Fluid Mechanics*, vol. 583, pp. 45 – 70, 2007.

[144] G. Vilenski and S. W. Rienstra, "Numerical study of acoustic modes in ducted shear flow," *J. Sound Vib. (UK)*, vol. 307, no. 3, pp. 610–626, 2007.

[145] G. Vilenski, "Mode matching in engine ducts with vortical flows," in *Collection of Technical Papers - 12th AIAA/CEAS Aeroacoustics Conference*, vol. 4, (Cambridge, MA, United States), pp. 2325 – 2335, 2006.

[146] A. McAlpine, "Private communication," 2007.

[147] L. Campos, J. Oliveira, and M. Kobayashi, "On sound propagation in a linear shear flow," *Journal of Sound and Vibration*, vol. 219, no. 5, pp. 739 – 770, 1999.